

A portable picocell antenna for 5G

Présentée le 2 juillet 2021

Faculté des sciences et techniques de l'ingénieur
Groupe microondes et antennes
Programme doctoral en génie électrique

pour l'obtention du grade de Docteur ès Sciences

par

Danelys RODRÍGUEZ AVILA

Acceptée sur proposition du jury

Dr S.-R. Cherkaoui, président du jury
Prof. A. Skrivervik, directrice de thèse
Prof. Ö. Aydin Civi, rapporteuse
Prof. A. Sharaiha, rapporteur
Prof. C. Dehollain, rapporteuse

Yo vivo de preguntar, saber no puede ser lujo.
—"El escaramujo" Silvio Rodríguez—

A mis padres...

Acknowledgements

I would like to thank the members of the jury Prof. Özlem Aydin Civi, Prof. Ala Sharaiha, Prof. Catherine Dehollain, and the jury president Prof. Sidi-Rachid Cherkaoui for participating in the oral exam of this thesis and for the fruitful scientific discussion that took place during it. Having a jury formed by a majority of female Professors was certainly an inspiration during my exam. I would also like to acknowledge Armasuisse for their financial support through the project Antennas for 5G. The fabrication of the prototypes presented in this work was possible due to the excellent job of the staff in two workshops from EPFL, Jean-Marc Buchs and Jean-Marie Barblan from ACI, and Alfred Thomas and Claude Cheseaux from ATPR. I would like to specially express my gratitude to Claude Cheseaux for his positive attitude during a complicated fabrication process and his dedication to also teaching me throughout. I would also like to acknowledge the help and advice received from Santiago, Miroslav, Ismael, Jovanche, Mehdi, Tjiang, Tomislav, Rafal, and David during the thesis.

I want to express my immense gratitude to my supervisor Anja Skrivervik for giving me the privilege of doing my PhD in such a scientific environment, for all the effort that implied letting me have this opportunity, and for your inspiration and support. One priceless feature of my PhD life has been experiencing the family-harmony that Juan Mosig created in LEMA and it has been maintained in MAG with Anja Skrivervik. I would like to thank Juan, the lab secretaries (Eulalia, Daniela and Mercedes) and all the LEMA and MAG members for that, especially to Maria, Jovanche, Michael, Joana, Hamed, Mina, Santiago, Ismael and Denys. Thanks to my officemates Anton and Miroslav, with whom I spent most of the PhD working hours, for all the discussions, jokes and nice atmosphere that lighten all the hard days.

At such an international University, I have enjoyed the rich cultural diversity received from many friends outside the lab: Orion, Angela, Nicolas, Jonathan, Nevena, Baha, Patricia, Aida, Vahid, Adriana, Giselle and Alberto.

I would also like to thank my professors in Cuba, especially Prof. Francisco Marante for his guidance and support during the year previous to my PhD.

The curious thing about moving abroad is that one ends up having many families in each place. I would like to thank those friends that I consider family in Switzerland: my dear Ismael, Jonathan and the Trujillo-Berger family (Bea, Ebert, Momo, Malik and Edith). Thank you to all my beloved family in Spain, “los Monzuitos”, for making me feel home even when I was still so far from my Cuban family and for all their support to me and my sister, you are certainly

an incredible gift! Thank you to all my friends that are always with me wherever I go, Jenny, Yunniel, Quevedo, Yanet, Yanelys and Aimeé.

An extra effort during these years was commuting for many hours, but it was all worth it just to meet you every day. You are my home and that's the most precious thing I could ask for. Thank you for always being there for me and for giving sense to all this love, David.

To my beloved parents Martha and Carlos for all your devotion and effort in my education, for being one of the most important motivations for me everyday, to my dear sister Daylin for being my oldest friend, thank you for your company and your happiness, and to my grandparents Marta and Ruben, my aunts Maylen and Vivian, and my cousin Alessandra. You have all shaped my will, you have made me feel brave and have taught me everything that has allowed me to arrive here.

Bern, 27 February 2021

D. R. A.

Abstract

Deployable emergency communication systems are a backbone solution for replacing damaged network infrastructures and/or providing high-end services in case of an emergency event. It is important that such systems are up-to-date with the latest mobile network technology, for enabling connectivity to users and profiting from its enhanced capabilities. The advent of 5G promises higher data rates, lower latencies, and improved quality of services when compared to previous generations. To achieve that, mm-Waves have been identified as a key element due to the wide available spectrum. The implementation of deployable emergency communication systems compatible with 5G mm-Waves technologies, thus benefiting from its prospective advantages, is of great interest. This thesis focuses on 5G mm-Waves antenna design for this kind of application. The high network capacity demand, the unfavorable channel conditions at mm-Waves, and the still underdeveloped related radio frequency (RF) technology define a group of challenging requirements on the antenna design. While directive antennas are required to mitigate the attenuation with distance at these bands, omnidirectional coverage still needs to be provided. In addition, wide bandwidth operation, high efficiency, and low cost and power consumption are desired. In this context, antennas with multibeam forming capabilities have been widely acknowledged as a key enabling technology to support 5G wireless communications, representing an attractive solution to provide omnidirectional coverage while supporting Multiple Input Multiple Output (MIMO) techniques.

In this thesis, the design and implementation of a broadband efficient multibeam antenna for a portable picocell station are investigated. The picocell scenario in the context of emergency communications is studied and the antenna link budget is calculated considering mm-Waves propagation properties and available information on the upcoming standard. This leads to the definition of the design requirements and a preliminary antenna architecture that consists of an $M \times N$ sectorial antenna fed by a hybrid beamforming network (HBFN). This architecture is a promising approach for making multibeam antennas cost- and energy-efficient according to the latest research. The synthesis of the HBFN was realized considering the design constraints in elevation and azimuth such that the subarray, fed by an analog beamforming network, provides a csc^2 pattern shape in elevation while M subarrays are controlled by a digital beamforming network to generate multiple orthogonal beams in azimuth. The antenna subarray was designed, fabricated, and measured. Based on this, a study of the antenna array

beamsteering capabilities in azimuth was carried out. After investigating the main parameters involved in improving its performance, the subarray design was optimized accordingly. The proposed antenna consists in a 12x6 array that works at 26 GHz with an impedance bandwidth higher than 12%. The radiation pattern shape in elevation is preserved over 7.3% of bandwidth. The antenna gain is superior to 10 dBi along the band of interest with a maximum value of 15 dBi. Simulated and measured results were compared, and the antenna beamsteering performance was tested for different sets of constraints indicating promising capabilities for a wide range of deployment scenarios. The proposed and validated design meets the requirements of the targeted applications on a practical low-profile implementation.

Key words: subarray, mm-Waves antennas, suspended strip line (SSL), feeding network, beamforming, cosecant squared pattern, multibeam antenna (MBA), antenna synthesis, picocell

Résumé

Les systèmes de communication d'urgence déployables sont une solution fondamentale pour remplacer les infrastructures réseau endommagées et / ou fournir des services de qualité en cas d'urgence. Il est important que ces systèmes soient à jour par rapport à la dernière technologie de réseau mobile pour permettre la connectivité aux utilisateurs et profiter de ses capacités améliorées. L'avènement de la 5G promet des débits de données plus élevés, des latences plus faibles et une qualité de services améliorée par rapport aux générations précédentes. Pour y parvenir, les ondes millimétriques (mmWave) ont été identifiées comme un élément clé en raison du large spectre disponible. La mise en œuvre de systèmes de communication d'urgence déployables compatibles avec les technologies 5G mmWave bénéficie ainsi de ses avantages prospectifs et est d'un grand intérêt. Cette thèse se concentre sur la conception d'antennes 5G mmWave pour ce type d'applications. La demande de capacité de réseau élevée, les conditions de canal défavorables pour le spectre de mmWave et la technologie RF associée encore sous-développée définissent des défis à lever en matière de conception d'antenne. Bien que les antennes directives soient nécessaires pour réduire l'atténuation avec la distance dans ces bandes, une couverture omnidirectionnelle doit être fournie. De plus, un fonctionnement à large bande passante, un rendement élevé, un faible coût et une faible consommation d'énergie sont fortement souhaités. Dans ce contexte, les antennes dotées de capacités de formation multifaisceaux ont été largement reconnues comme une technologie clé permettant de prendre en charge les communications sans fil 5G, ce qui représente une solution intéressante pour fournir une couverture omnidirectionnelle tout en prenant en charge les techniques MIMO (Multiple Input Multiple Output – entrées multiples, sorties multiples). Cette thèse aborde la conception et la mise en œuvre d'une antenne multifaisceaux efficace à large bande pour une station pico-cellulaire portable. Le scénario pico-cellulaire dans le contexte des communications d'urgence est étudié et le bilan de liaison d'antenne est calculé en tenant compte des propriétés de propagation des ondes mm et des informations disponibles sur les normes en cours de développement. Cela conduit à la définition des contraintes de conception et à une architecture d'antenne préliminaire qui consiste en une antenne MxN alimentée par un réseau hybride de formation de faisceaux (HBFN). Cette architecture est une approche prometteuse pour rendre les antennes multifaisceaux économiques et éco-énergétiques selon l'état de l'art. La synthèse du HBFN a été réalisée en tenant compte des contraintes de conception en élévation et azimut telles

que le sous-réseau (alimenté par un réseau de formation de faisceau analogique) fournit un diagramme csc^2 en élévation tandis que M sous-réseaux sont contrôlés par un réseau de formation de faisceau numérique pour générer plusieurs faisceaux orthogonaux en azimut. Le sous-réseau d'antenne a été conçu, fabriqué et mesuré. Puis, une étude des capacités de pointage du faisceau du réseau d'antennes en azimut a été réalisée. Après avoir étudié les principaux paramètres impliqués dans l'amélioration des performances de rayonnement, le sous-réseau a été optimisé. L'antenne proposée consiste en un réseau 12×6 fonctionnant à 26 GHz avec une largeur de bande d'impédance supérieure à 12%. La forme du diagramme de rayonnement en élévation est préservée sur 7,3% de la bande passante. Le gain d'antenne est supérieur à 10 dBi dans la bande d'intérêt avec une valeur maximale de 15 dBi. Les résultats simulés et mesurés ont été comparés et les performances de direction du faisceau de l'antenne ont été testées pour différents ensembles de contraintes indiquant des capacités prometteuses pour un large éventail de scénarios de déploiement. L'antenne proposée et validée dans cette thèse répond aux exigences des applications ciblées sur une mise en œuvre ad hoc et à profil bas.

Contents

Acknowledgements	i
Abstract (English/Français)	iii
List of Figures	ix
List of Tables	xv
Acronyms	xvii
1 Introduction	1
1.1 Brief overview of mobile network generations	1
1.2 Current state of mobile communications	2
1.3 General introduction to the 5G mobile network generation	3
1.3.1 Requirements	3
1.3.2 Key enabling concepts	4
1.3.3 Key enabling technologies and their challenges	13
1.4 Motivation	25
1.5 Research problem definition and objectives	25
1.6 Organization of the thesis	26
2 Scenario and design requirements	29
2.1 Scenario and Link budget analysis	29
2.1.1 Link budget parameters	29
2.1.2 Link budget analysis	33
2.2 Definition of the picocell antenna architecture	34
2.2.1 State of the art on antennas for 5G base stations	34
2.2.2 Antenna architecture	43
2.2.3 Subarray antenna and ABFN requirements	44
2.2.4 Multibeam antenna and DBFN requirements	45
3 Synthesis of the hybrid beamforming network	47
3.1 Introduction to hybrid beamforming architectures	47
3.2 Antenna pattern synthesis	49
3.2.1 Analytical methods	49

3.2.2	Numerical methods	49
3.2.3	Global optimization methods	50
3.2.4	Methods based in convex optimization	50
3.3	Synthesis of the proposed Hybrid BFN	53
3.3.1	Optimization problem in elevation. csc^2 subarray	53
3.3.2	Optimization problem in azimuth. Sectorial antenna	57
4	Cosecant-squared pattern shaped subarray	65
4.1	Subarray specifications	65
4.2	Transmission line	67
4.3	Antenna element	68
4.4	Subarray synthesis	69
4.4.1	Analog beamforming in elevation	71
4.5	Subarray fabrication and results	78
5	Multibeam antenna fed by hybrid beamforming network	89
5.1	Overview of the MBA design requirements and limitations	89
5.2	Relevant design parameters	91
5.2.1	Impact of the number of subarrays	92
5.2.2	Impact of the subarray width	93
5.2.3	Impact of the subarray pattern in azimuth	94
5.2.4	Optimized subarray design	97
5.3	Multiple beam antenna implementation and results	101
6	Conclusions and future work	113
6.1	Summary	113
6.2	Perspective and future work	116
A	Appendix A	117
B	Appendix B	129
	Bibliography	161
	Curriculum Vitae	163

List of Figures

1.1	Current 2G, 3G, 4G and LTE-A spectrum allocations [4]	2
1.2	Cooper's law of spectral efficiency [12]	4
1.3	Spectrum of interest for bands n257 and n258 in various locations [17]	7
1.4	Propagation loss predicted by the Friis equation [18]	8
1.5	Millimeter-wave propagation characteristics: a) atmospheric absorption [4], b) rain attenuation [20]	8
1.6	a) Propagation effects influencing mm-Waves propagation [19], b) foliage penetration loss [20]	9
1.7	General schematic of the potential 5G architecture	14
1.8	a) Full duplex FDD node with half duplex UEs b) half duplex FDD c) half duplex TDD d) Full duplex FDD node with full duplex FDD UEs and e) Full duplex TDD node with full or half duplex FDD UEs.	20
1.9	OFDMA concept [32]	21
1.10	SDMA concept [59]	22
1.11	Spatial division multiple access based on 60 GHz transceiver beamforming [61]	22
1.12	NOMA when SIC is used at UE [65]	23
1.13	Comparison of NOMA and OFDMA for downlink [65]	23
1.14	Antenna Training: Beam Steering for Link Alignment [9]	24
1.15	Emergency communication scenario [70]	26
1.16	Picocell scenario	27
2.1	Measured Path Loss Exponent (n) for 28 GHz outdoor cellular channels a) In Suwon, Korea [78] and b) New York, Manhattan [4]	31
2.2	RMS delay spread as a function of TX-RX separation for all links using all possible pointing angles at 28 GHz in New York City [4]	32
2.3	Picocell scenario	33
2.4	a) perspective view of the multibeam antenna b) 4x4 magnetoelectric-dipole antenna array [88].	35
2.5	a) Flat lens for 2D beamsteering b) Switched-beam antenna array [89].	35
2.6	a) 8x10 patch array with Butler matrix [85] b) 4x6 Butler matrix cascaded with the antenna array [86].	36
2.7	a) 4x4 Butler matrix b) Geometry of the dielectric-loaded stepped slot antenna [87].	37

2.8	a) Model of the switched-beam antenna b) RRS with highlighted group of slots forming a beam in different directions [90].	37
2.9	a) 6-way series parallel power divider b) 6×5 proximity-coupled planar array 2.9.	38
2.10	a) Side view of the proposed CP antenna array b) Geometry of the two types of CP antenna elements [92].	38
2.11	Front view of the TFSIW-excited dual-polarized antenna [93].	39
2.12	a) 64×4 Antenna array b) 1×4 antenna subarray [94].	39
2.13	4×8 planar antenna array [95].	40
2.14	Transceiver architecture proposed in [94].	40
2.15	Modem used in the DMBA antenna proposed in [95]	41
2.16	Typical array configurations for antennas for mobile network communications [9]	43
2.17	$M \times N$ antenna array in a segmented configuration	44
2.18	Sketch of an antenna array fed by hybrid beamforming network	44
2.19	Diagram of parameters defining coverage in vertical plane	45
2.20	Subarray with required csc^2 pattern in elevation	45
2.21	Antenna array with multibeam forming capabilities in azimuth	46
3.1	HBFN architecture in mm-Waves systems a) fully connected b) partially connected [100]	47
3.2	Fully connected HBFN a) with phase shifters b) with switches[100]	49
3.3	Convex function [128]	51
3.4	Lower and upper bounded constraint mask	52
3.5	Diagram of the proposed HBFN	53
3.6	csc^2 mask	54
3.7	Diagram of a generic analytical linear array illustrating the subarray in elevation	55
3.8	Synthesized pattern for arrays with different number of elements N . Legend refers to N	56
3.9	Synthesized pattern for arrays with different distances between elements $d(\lambda)$. Legend refers to $d(\lambda)$	56
3.10	Synthesized patterns for arrays with different beamwidths (HPBW). Legend refers to HPBW in degrees	57
3.11	Diagram of the regions defined by A_{tar} , A_{HPBW} and A_{SLL}	58
3.12	Multibeam antenna mask integrating constraints C_1 , C_2 and C_3	59
3.13	Flow diagram of the DBFN synthesis algorithm	60
3.14	Diagram of a generic sectorial antenna illustrating the MBA in azimuth	60
3.15	Antenna architectures for different number of sectors M	61
3.16	Sketch illustrating the rotation and translation of the antenna elements forming a sectorial array	61
3.17	Synthesized patterns for different antenna architectures, given by a variation of the number of elements, targeting a) 90° , b) 105° , c) 120° and d) 135° . Legend refers to number of sector (M)	63

3.18 Synthesized patterns for different antenna architectures, given by a variation of the subarray width, targeting a) 90° , b) 97° and c) 105° . Legend refers to subarray width (sub_a) in mm	64
4.1 Summary of the subarray synthesis specifications	66
4.2 Subarray architectures with adequate features to be used as starting point in the studied application, a) slotted WG antenna b) multilayer printed antenna . . .	67
4.3 Suspended strip line geometry	67
4.4 Antenna element geometry	69
4.5 Exploded view of the antenna element	70
4.6 Radiating element results: a) S_{11} b) Realized gain and gain radiation pattern for 26 GHz	70
4.7 Subarray layout with feeding port located after a) the third antenna element, b) the second antenna element, and c) the fourth antenna element	71
4.8 Radiating elements of the subarray fed by ideal ports	72
4.9 Synthesized patterns for layouts a, b, and c	72
4.10 Synthesized pattern for the selected subarray layout (layout c)	73
4.11 considered feeding line topologies	73
4.12 Selected subarray layout and feeding line topology	74
4.13 WG-SSL transition a) top view b) dimensions c) geometry d) bottom view	74
4.14 WG-SSL transition power ratio and S_{11} parameters	75
4.15 Divider r21 a) geometry b) dimensions c) top view d) bottom view	75
4.16 Divider r22 a) geometry b) dimensions c) top view d) bottom view	76
4.17 Power ratio and S_{11} parameters of a) divider r21 b) divider r22	76
4.18 Phase shifters configurations a) 180° phase meander b) U-shape shifter	77
4.19 Feeding network equivalent S-model	77
4.20 Feeding network designed in HFSS	78
4.21 Proposed subarray: a) exploded view of the subarray and b) fabricated subarray. Technical drawings detailing the subarray parts are included in the Appendix. .	78
4.22 Subarray WG feeding port	79
4.23 Subarray feeding line holder	80
4.24 Subarray metallic thin layers	80
4.25 Subarray pcb parts	81
4.26 Assembled subarray	81
4.27 Subarray TRL calibration set	82
4.28 Simulated and measured S_{11} of the subarray	82
4.29 Simulated and measured radiation pattern of the subarray at 26.5 GHz	82
4.30 Simulated and measured realized gain of the subarray as a function of frequency	83
4.31 Measure radiation pattern at 24.25 GHz, 25 GHz, 26 GHz and 26.5 GHz and 27.5 GHz	83
4.32 Picocell scenario with a section of the measured radiation pattern in polar coordinates at 26.5 GHz. The antenna height h is 2 m	84

4.33 a) Radiation pattern distribution versus distance at 26.5 GHz b) Received power versus distance at 26.5 GHz	84
4.34 a) Radiation pattern distribution versus distance at 24.25 GHz b) Received power versus distance at 24.25 GHz	85
4.35 a) Radiation pattern distribution versus distance at 27.5 GHz b) Received power versus distance at 27.5 GHz	85
4.36 Measured radiation pattern of the subarray: range (shaded) of the copolarized and cross polarized patterns at the band 24.75-26.75 GHz and mean (solid) of the copolarized and cross polarized patterns at the band 24.75-26.75 GHz . . .	86
4.37 Received power vs distance for LOS $n_{pmin} = 2.22$ and $n_{pmax} = 2.45$ at the band 24.75 GHz - 26.75 GHz (shaded) and worst case within this band (solid)	86
5.1 Summary of the MBA synthesis specifications a) studied picocell scenario b) top view of the MBA antenna c) constraint mask in azimuth d) testing set of constraints S_0	90
5.2 Synthesized pattern of an array based on Subarray ₀ for constraints S_0 targeting a) 90° b) 105°	91
5.3 Antenna architectures (based on Subarray ₀) having a) 4 b) 8 c) 12 and d) 18 sectors. Targets defined in S'_0 are included	92
5.4 Synthesized patterns, given the variation of the number of sectors, targeting a) 90° b) 105° c) 120° b) 135°. Legend refers to number of sectors M	93
5.5 12-sector antenna architectures (based on Subarray ₀) having different subarray width sub _a	94
5.6 Synthesized patterns, given the variation of the subarray width, targeting a) 90° b) 105° c) 120° b) 135°. Legend refers to subarray width sub _a in mm	95
5.7 12-sector antenna architecture based on antenna elements with different beamwidths (HPBW = [46°, 56°, 66°, 76°])	95
5.8 Synthesized patterns for arrays based on antenna elements with different beamwidths, targeting a) 90° b) 105° with constraint $C_2 = 40^\circ$. Legend refers to the antenna element beamwidth HPBW in degrees	96
5.9 Synthesized patterns for arrays based on antenna elements with different beamwidths, targeting a) 90° b) 105° with constraint $C_2 = 60^\circ$. Legend refers to the antenna element beamwidth HPBW in degrees	96
5.10 Geometry of Subarray _{HPBW}	97
5.11 Comparison between the radiation patterns in azimuth of Subarray _{HPBW} and Subarray ₀	98
5.12 Synthesized patterns of a 12-sector antenna based on Subarray ₀ and Subarray _{HPBW} targeting a) 90° b) 105°	98
5.13 12-sector antenna architectures (based on Subarray _{HPBW}) having different subarray width sub _a	99
5.14 Synthesized patterns, given the variation of the subarray width, targeting a) 90° b) 105° c) 120° b) 135°. Legend refers to subarray width sub _a in mm	99

5.15 Evolution of the design process to reduce the subarray width	100
5.16 Comparison of Subarray ₀ and Subarray _{opt} geometries	101
5.17 Synthesized pattern of arrays based on Subarray ₀ and Subarray _{opt} for constraints S ₀ targeting a) 90° b) 105°	101
5.18 Optimized subarray Subarray _{opt}	102
5.19 Fabricated section of the proposed multibeam antenna. An exploded view of the subarray in central position is provided. Technical drawings detailing the subarray parts are included in the Appendix B.	102
5.20 lateral subarrays: (left) exploded view and (right) fabricated parts. Technical drawings detailing the subarray parts are included in the Appendix B.	103
5.21 Feeding port of the lateral subarrays	103
5.22 Subarray PCB parts	104
5.23 Antenna array mounted on the 3D printed support a) front view b) back view .	105
5.24 Measurement set-up in the MAG anechoic chamber containing the multibeam antenna array mounted on 3D printed support a) front view b) back view	106
5.25 Simulated and measured S ₁₁	107
5.26 Simulated and measured radiation pattern at 25.9 GHz	107
5.27 Simulated and measured realized gain as a function of frequency	107
5.28 Measured radiation pattern of the optimized subarray: range (shaded) of the copolarized and crosspolarized patterns at the band 24.9-26.8 GHz and mean (solid) of the copolarized and crosspolarized patterns at the band 24.9-26.8 GHz	108
5.29 Received power vs distance for LOS npmin = 2.22 and npmax = 2.45 at the band 24.75 GHz - 26.75 GHz (shaded) and worst case within this band (solid)	108
5.30 Multiple beamforming a) in a continuous target range b) with arbitrary targets	110
5.31 Synthesized AP _{MBA} considering the set of constraints S ₃ with a) C ₂ = 20° b) C ₂ = 40° c) C ₂ = 60°	111
5.32 Top view of the 12-sector antenna specifying targets C ₁ considered in S ₄	111
5.33 Synthesized AP _{MBA} considering the set of constraints S ₄ with a) C ₂ = 20° b) C ₂ = 40° c) C ₂ = 60°	112

List of Tables

1.1	Evolution of mobile generations [1]–[3]	1
1.2	Technical requirements for 5G proposed in [11]	4
1.3	Technological approaches and their contribution to the mobile network capacity according to [12]	5
1.4	Small base stations parameters given in 3GPP Release 15 [11]	5
1.5	NR Operating bands [17]	7
1.6	MIMO techniques inspired from [33]	12
1.7	5G channel measurements, inspired from [48]	17
1.8	Comparison of General 5G models, inspired from [48]	18
1.9	Review of MBA architectures	19
2.1	Small base stations parameters given in 3GPP Release 15 [11]	30
2.2	28 GHz losses due to different environment conditions at 200 m [1]	30
2.3	Picocell requirements.	33
2.4	Consumed power by various mm-Waves front-end devices [97]	41
2.5	Comparison among the up-to-date passive MBAs for mm-Waves applications (*Referred to both, impedance and pattern shape bandwidths)	42
2.6	Comparison among the up-to-date phased arrays MBAs and DMBA for mm-Waves applications (*Referred to both, impedance and pattern shape bandwidths)	42
2.7	Subarray requirements.	45
2.8	Multibeam antenna requirements	46
3.1	Minimum radius and distance between subarrays for a given number of sectors	61
3.2	Minimum radius and distance between subarrays for a given subarray width	62
4.1	Summary of the subarray design parameters	66
4.2	w_0 in amplitude and phase	72
4.3	Power ratio per node	73
5.1	Minimum radius and distance between subarrays for a given number of sectors	92
5.2	Minimum radius and distance between subarrays for a given subarray width	94
5.3	Minimum radius and distance between subarrays for different subarray width	100
5.4	Features of subarrays Subarray_0 and $\text{Subarray}_{\text{opt}}$ compared to the required design parameters	109

Acronyms

1G 1st Generation.

2G 2nd Generation.

3G 3rd Generation.

3GPP 3rd Generation Partnership Project.

4G 4th Generation.

5G 5th Generation.

ABFN Analog Beamforming Network.

ADC Analog-to-Digital Converter.

AoA Angle-of-Arrival.

BFN Beamforming Network.

BPSK Binary Phase-Shift Keying.

BS Base Station.

C-RAN Cloud Radio Access Network.

CDMA Code-Division Multiple Access.

CP Circular Polarization.

D2D Device-to-Device Communications.

DAC Digital-to-Analog Converter.

DBFN Digital Beamforming Network.

DFT Direct Fourier Transform.

DMBA Digital Multibeam Antenna.

DSP Directional Self Pursuing Protocol.

EE Energy Efficiency.

ERFS Electromechanical Radio Frequency Switch.

FD Full Duplex.

FDD Frequency-Division Duplexing.

FDMA Frequency-Division Multiple Access.

FFT Fast Fourier Transform.

FPGA Field-Programmable Gate Array.

HBFN Hybrid Beamforming Network.

HD Half Duplex.

HetNets Heterogeneous Networks.

HFSS High-Frequency Structure Simulator.

HST High Speed Trains.

I/Q In-Phase/Quadrature.

IFFT Inverse Fast Fourier Transform.

IoT Internet of Things.

LHCP Left-Handed Circular Polarization.

LO Local Oscillator.

LOS Line-of-Sight.

LTCC Low-Temperature Co-Fired Ceramics.

LTE Long-Term Evolution.

M2M Machine-to-Machine Communications.

MAC Medium Access Control Layer.

MAG Microwaves and Antennas Group.

MBA Multibeam Antenna.

- MBS** Microcell Base Station.
- MIMO** Multiple-Input and Multiple-Output.
- MQAM** Quadrature Amplitude Modulation.
- MUSA** Multi-User Shared Access.
- NFV** Network Functions Virtualization.
- NLOS** Non-Line-of-Sight.
- NOMA** Non-Orthogonal Multiple Access.
- NR** New Radio.
- OFDM** Orthogonal Frequency-Division Multiplexing.
- OFDMA** Orthogonal Frequency-Division Multiple Access.
- OMA** Orthogonal Multiple Access.
- PCB** Printed Circuit Board.
- PDMA** Pattern-Division Multiple Access.
- PHY** Physical Layer.
- PL** Path Loss.
- PLE** Path Loss Exponent.
- PSK** Phase-Shift Keying.
- Q-D** Quasi Deterministic.
- QPSK** Quadrature Phase-Shift Keying.
- RAT** Radio Access Technologies.
- RF** Radio Frequency.
- RHCP** Right-Handed Circular Polarization.
- RMS** Root Mean Square.
- RRS** Radiating Reconfigurable Structure.
- RSMA** Resource Spread Multiple Access.
- RX** Receiver.

- SCMA** Sparse Code Multiple Access.
- SDMA** Space-Division Multiple Access.
- SDN** Software-Defined Network.
- SE** Spectral Efficiency.
- SIC** Successive Interference Cancellation.
- SIW** Substrate Integrated Waveguide.
- SLL** Sidelobe Level.
- SNR** Signal-to-Noise Ratio.
- SSL** Suspended Stripline.
- SVD** Singular Value Decomposition.
- TDD** Time-Division Duplexing.
- TDMA** Time-Division Multiple Access.
- TE** Transverse Electric.
- TEM** Transverse Electromagnetic.
- TFSIW** T-Type Folded Substrate Integrated Waveguide.
- TM** Transverse Magnetic.
- TRL** Through-Reflect-Line.
- TX** Transmitter.
- UE** User Equipment.
- ULA** Uniform Linear Array.
- V2V** Vehicle-to-Vehicle Communications.
- VNA** Vector Network Analyzer.
- VNF** Virtual Network Function.
- WCDMA** Wideband Code-Division Multiple Access.
- WG** Waveguide.

1 Introduction

1.1 Brief overview of mobile network generations

The development of mobile communications has experienced exponential growth during the last decades. A brief look at the past can better depict that from 1G to 4G, the beginning of each generation has been driven by an accumulation of requirements that the preceding generations were unable to fulfill. Additionally, new technologies and applications have shaped the rise of each mobile generation building up the current mobile communications (see Table 1.1).

Table 1.1 – Evolution of mobile generations [1]–[3]

Generation	Services	Enabling technologies	Limitations
1G	Analog radio transmission technology	<ul style="list-style-type: none">• Cellular concept• Mobility• TDMA	<ul style="list-style-type: none">• Security (Eavesdropping)• Poor spectral efficiency• Incompatibility• Increasing demand of customers
2G	Digital radio transmission technology (phone calls and messaging services)	<ul style="list-style-type: none">• Hierarchical cell structures (macrocells and small cells)• Ciphering of data• CDMA• FDD	<ul style="list-style-type: none">• Limited data rates• Difficulty to enable data browsing, email and fax access
3G	Digital transmission technology (phone call, messaging, data, multimedia and global roaming services)	<ul style="list-style-type: none">• WCDMA• HSUPA/HSDPA• EVDO• TDD• Higher order modulations (QPSK, QAM)• MIMO	<ul style="list-style-type: none">• Power hungry and costly network infrastructure
4G	IP services (voice, data, multimedia)	<ul style="list-style-type: none">• OFDMA/SC-FDMA• Higher order MIMO• Carrier aggregation (CA)• Coordinated multipoint (CoMP)	<ul style="list-style-type: none">• Unable to support the increasing traffic demand and applications within IoT

1.2 Current state of mobile communications

Nowadays mobile networks are placed in a range of the microwave spectrum that goes from 700 MHz to 2690 MHz. The current distribution is shown in Figure 1.1, where the highest bandwidth does not exceed 200 MHz [4]. The heterogeneous character of the network in terms of technologies is also appreciable, as it covers a considerable variety of techniques among the different mobile generations.

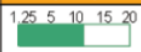


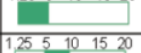
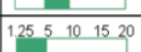

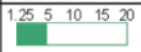


Band	Uplink (MHz)	Downlink (MHz)	Carrier Bandwidth (MHz)
700 MHz	746-763	776-793	
AWS	1710-1755	2110-2155	
IMT Extension	2500-2570	2620-2690	
GSM 900	880-915	925-960	
UMTS Core	1920-1980	2110-2170	
GSM 1800	1710-1785	1805-1880	
PCS 1900	1850-1910	1930-1990	
Cellular 850	824-849	869-894	
Digital Dividend	470-854		

Figure 1.1 – Current 2G, 3G, 4G and LTE-A spectrum allocations [4]

This means that many different frequency bands with different behaviors in terms of propagation, cell sizes, signal processing, and bandwidths coexist in the current mobile generation. This, in a way, has been due to the growing mobile technology and also to the reuse of the current infrastructure when a new generation appears. The significant growth of traffic in mobile communications, the increased bandwidth and data rates demanded by the emerging devices (e.g., smartphones, tablets, laptops) and applications (e.g. augmented reality, Internet of Things (IoT) and Machine-to-Machine Communications (M2M)) have drawn the attention of the telecommunication industry worldwide. For example, Cisco anticipates that the overall mobile data traffic is expected to grow to 77 exabytes per month by 2022, nearly 46 percent increase compared to 2017 [5]. The major problem is that the current technologies (3G, 4G) cannot fulfill the increasing demand. The first attempts to overcome those limitations were focused on reusing and efficiently sharing the microwave spectrum, with techniques as spectrum reallocation and cognitive radio [6]. However, in addition to the cost and complexity of the implementation of these techniques, their narrow bandwidths prevent their scalability [7]. In 2012, 3GPP (3rd Generation Partnership Project) started standardization of technologies referred to as LTE-B (evolution of LTE/LTE-A). This solution proposes the use of higher frequency bands in various deployments for both indoor and outdoor small cells [8]. This idea emerged as the suitable answer to develop what will be the 5th Generation of mobile

technologies, a new era in mobile communications.

1.3 General introduction to the 5G mobile network generation

This section summarizes the main requirements, key enabling concepts, and technologies linked to 5G. The key enabling technologies have been grouped according to their effect in the 5G mobile network architecture, and PHY and MAC layers.

1.3.1 Requirements

Aiming to meet the desired network capacity, both, industry and academic researchers have defined a group of requirements for 5G systems [9], [10]:

Data rate

The data rate for a user in a real network environment is expected to be 1 Gbps and in the best case scenario have a peak value higher than 10 Gbps. These figures are around 10x the data rate values in current 4G networks. Additionally, at the cell edge, where the user is equally distant from multiple base stations, 0.1 Gbps to 1 Gbps data rates are required. This is about 100x improvement with respect to 4G networks. The aggregate data rate (also known as area capacity) is a network indicator that refers to the available bandwidth per unit area. An increment of 1000x compared to 4G has been specified.

Latency

The round trip latency is defined as the time it takes to send a signal and receive acknowledgement at the transmitter. This parameter is currently around 10 ms in 4G systems and the general consensus is that this quantity will need to decrease 10x, leading to a 5G networks latency of 1ms.

Connection density

5G will need to enable 10 000 or more connected devices (10-100x higher than 4G) to support the M2M services and IoT, apart from the expected mobile user density.

Energy and cost efficiency

The transition to 5G should be economically and ecologically sustainable. Considering that the per-link data rates are expected to increase 10-100x, is necessary that the consumed power and cost per bit is at least 100-10x reduced.

Table 1.2 summarizes the specific technical requirements for 5G proposed in [11].

Table 1.2 – Technical requirements for 5G proposed in [11]

Metric	Requirement	Comments
Peak Data Rate	DL: 20 Gb/s UL: 10 Gb/s	Single eMBB mobile in ideal scenarios assuming all resources utilized
Peak Spectral Efficiency	DL: 30b/s/Hz UL: 15 b/s/Hz	Single eMBB mobile in ideal scenarios assuming all resources utilized
User Experienced Data Rate	DL: 100 Mb/s UL: 50 Mb/s	5% CDF of the eMBB user throughput
Area Traffic Capacity	Indoor hotspot DL: 10 Mb/s/m ²	eMBB
User Plane Latency	eMBB: 4ms URLLC: 1ms	Single user for small IP packets, for both DL and UL (eMBB and URLLC)
Control Plane Latency	20ms (encouraged to consider 10ms)	Transition from Idle to active (eMBB and URLLC)
Connection Density	1M devices per km ²	For mMTC
Reliability	99.9999 % success prob.	32 L2 bytes within 1ms at cell edge
Bandwidth	> 100 MHz; up to 1GHz in > 6 GHz	Carrier aggregation allowed

1.3.2 Key enabling concepts

In 1997 Martin Cooper made an observation, claiming that “The wireless capacity has doubled every 30 months over the last 104 years”, which translates into approximately a million-fold increase since 1975 (see Figure 1.2). The technological approaches that contribute to overcoming such increment of the wireless network capacity were also added, together with their effect in such increment (see Table 1.3).

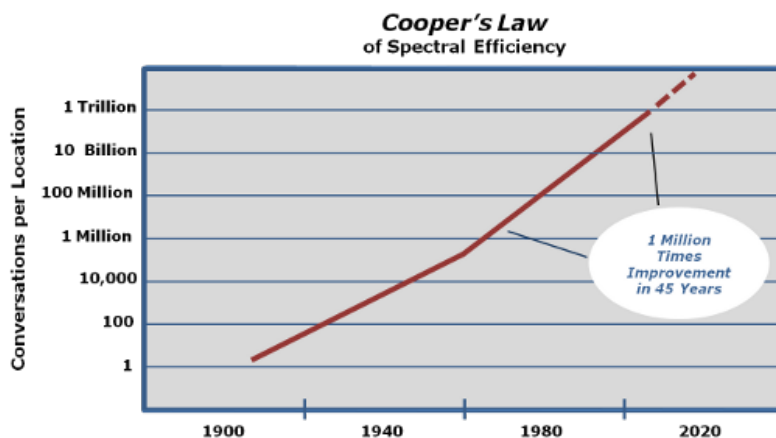


Figure 1.2 – Cooper's law of spectral efficiency [12]

It has been later specified that, at some point, further densification will no longer be able to provide exponentially increasing data rates (see [13] for more details). The technological approaches specified in Table 1.3 can be organized in three key enabling concepts:

Table 1.3 – Technological approaches and their contribution to the mobile network capacity according to [12]

Technological approaches	Increase figure
Reduced cell sizes and transmit distance	1600 times
Wider spectrum	25 times
Better modulation schemes and higher frequency division	10 times

- (A) Network densification.
- (B) Increasing bandwidth.
- (C) Increasing spectral efficiency.

The main enabling technologies proposed to meet the 5G requirements are commonly based on developing and efficiently combining such concepts. Due to their relevance during the rest of the section, they will be described before addressing each specific enabling technology.

A) Network densification. Small cells

Small cells are low-power wireless access points that operate in licensed, shared or unlicensed spectrum and cover a range of 10 meters to a few kilometers. They are deployed at indoor and outdoor environments, such as homes, enterprises, urban and rural public spaces. Currently, small cells come in a variety of coverage profiles (increasing in size from femto-cells to micro/metro cells) and transmission power characteristics. In the release 15 from 3GPP including the new radio (NR) specifications for 5G, small base stations are classified as: Medium-Range Base Station intended for microcell scenarios and Local Area Base Stations intended for picocell scenarios. Some of their parameters are summarized in Table :

Table 1.4 – Small base stations parameters given in 3GPP Release 15 [11]

	Medium Range BS (microcells)	Local Area BS (picocells)
BS-UE minimum distance from the ground	5m	2m
BS-UE minimum coupling loss	53 dB	45 dB
Base station output power*	≤ 38 dBm	≤ 24 dBm

*This power is defined per antenna and carrier

On the other side, femtocells are low-power small cells with reduced upfront cost to the service provider compared to other small cells deployments [14]. In LTE-A, they are typically installed in indoor environments, covering a few tens meters and operating in bands below 6 GHz. Recently, they have been proposed to be used in outdoor scenarios for offloading mobile macrocells in densely populated areas and public transportation vehicles [15]. They have been proposed in [13] to work jointly with Wi-Fi as complementary technologies for taking

advantage of both forms of connectivity while enhancing the data throughput and network reliability.

The benefits of shrinking the cell size are the efficient spatial reuse of spectrum and the reduction in the number of users competing from the same cell resources. However, some challenges arise with such densification:

- Preserving the base station densification gains (effective increase in data rate relative to the increase in network density).
- Coordinating and properly distributing such heterogeneous radio resources.
- Affording expensive network infrastructure (installation, maintenance, and backhaul).

B) Increasing bandwidth. mm-Waves spectrum

Until recently, the vast spectrum range in mm-Waves (20 GHz - 300 GHz) has remained barely occupied (military, radar, and backhaul applications) due to its limited propagation characteristics (high attenuation with distance, high sensitivity to blockage, and high atmospheric absorption – compared to microwaves–). This has also had a negative effect in the development of the RF technologies at mm-Waves, where especially the semiconductors and ADC and DAC converters are still costly and power demanding [16]. However, using the mm-Waves spectrum has been presented as one of the main solutions to address the required traffic capacity and data rates figures in 5G. This constitutes a paradigm shift in the new mobile generation, bringing a manifold of challenging tasks on the study of the mm-Waves propagating media and the development of the required infrastructure and technologies to properly take advantage of the attractive idle spectrum above 6 GHz. The considered bands for 5G are usually divided into two categories, below and above 6 GHz (see Table 1.5). Most of the bands below 6 GHz overlap with LTE to allow dual connectivity¹. Above 6 GHz, bands up to 40 GHz have been proposed in the release 15 from 3GPP [17]. The frequency range between 24.25-29.5 GHz is being actively studied, however the considered bands are different in various regions (see Figure 1.3) [17].

Pathloss

Considering the Friis formula for free space (Equation 1.1) and the relation between the antenna gain and its effective aperture (Equation 1.2); as the frequency increases, the pathloss remains unchanged if the antenna aperture at one end of the link is kept constant.

$$\frac{P_r}{P_t} = \left(\frac{\lambda}{4\pi R} \right)^2 G_t G_r \quad (1.1)$$

¹Users can receive data simultaneously from different nodes in a heterogeneous network

Table 1.5 – NR Operating bands [17]

NR operating band	Uplink (UL) and Downlink (DL) operating band BS transmit/receive UE transmit/receive $FUL_{low} - FUL_{high}$ $FDL_{low} - FDL_{high}$	Duplex Mode
n77	3.3 GHz – 4.2GHz	TDD
n78	3.3 GHz – 3.8GHz	TDD
n79	4.4 GHz – 5.0 GHz	TDD
n257	26.5 GHz – 29.5 GHz	TDD
n258	24.25 GHz – 27.5 GHz	TDD
n260	37.0 GHz – 40.0 GHz	TDD
n261	27.5 GHz – 28.35 GHz	TDD

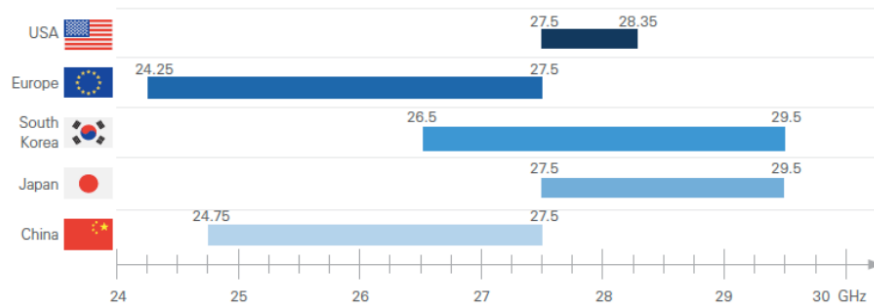


Figure 1.3 – Spectrum of interest for bands n257 and n258 in various locations [17]

$$G = \frac{4\pi A_e}{\lambda^2} \quad (1.2)$$

with A_e related to the physical area A_p through the aperture efficiency e_{AP} , $A_e = e_{AP} A_p$

Maintaining the antenna aperture as the frequency increases is possible by using antenna arrays. This was tested in [18] using a patch antenna at 3 GHz and an antenna array at 30 GHz of the same physical size. Results in Figure 1.4 shown a similar propagation loss when using each antenna at the receiving link end. Additionally, when array antennas at 30 GHz were used at both transmitting and receiving ends, due to the increased gain, the measured propagation loss was 20 dB smaller than that of the 3 GHz patch antenna case.

The measurement campaigns testing transmission links at mm-Waves realized by [4] also shown that the path loss exponent is close to free space conditions when line-of-sight (LOS) conditions are established. However, this might not always be possible and some other factors such as blockage, path loss attenuation and absorption due to different atmospheric conditions in the transmission medium need to be taken into account, [19].

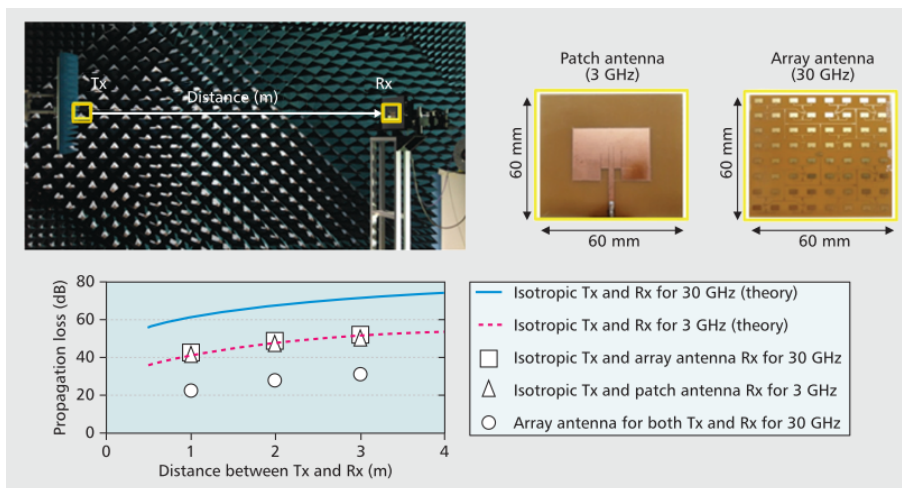


Figure 1.4 – Propagation loss predicted by the Friis equation [18]

Atmospheric, rain and foliage absorptions

Mm-Waves traveling through the atmosphere can be absorbed by molecules of oxygen, water vapor, and other atmospheric constituents yielding propagation losses. These losses are greater at certain frequencies, coinciding with the mechanical resonant frequencies of the gas molecules. Some of the most critical absorption peaks in the considered bands for 5G occur at 24 GHz and 60 GHz. Figure 1.5 a) show the attenuation caused by water vapour and oxygen [20].

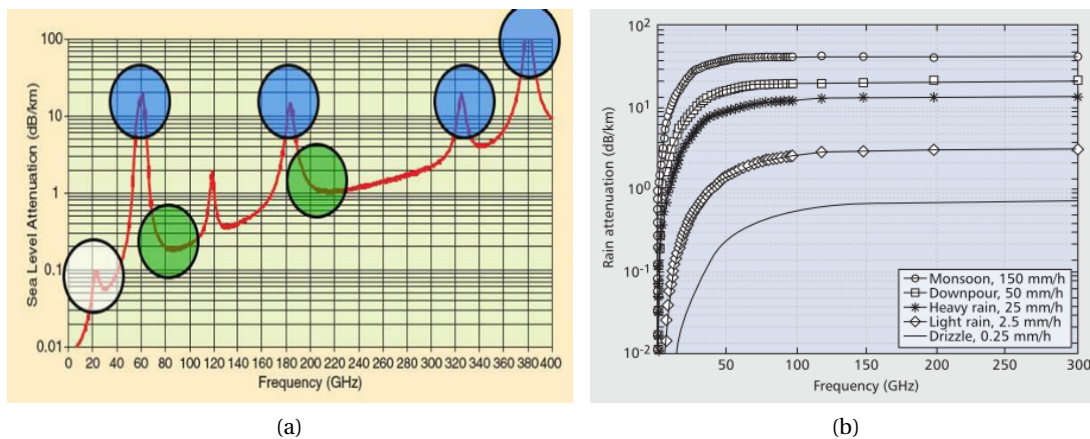


Figure 1.5 – Millimeter-wave propagation characteristics: a) atmospheric absorption [4], b) rain attenuation [20]

Attenuation due to rain is another factor to consider at these bands, since raindrops being roughly the same size as the wavelengths, might cause signal scattering. Figure 1.5 b) shows the attenuation in dB per km for different rain densities.

Blocking, Scattering and Diffraction

The short wavelengths of mm-Waves present reduced diffraction and less specular reflection than microwaves. This reduces the power intensity at the receiver, making mm-Waves more susceptible to blockages. Figure 1.6 a) depicts such propagation effects influencing the signal propagation at mm-Waves.

A group of measurement campaigns has been realized to analyze the signal outage in outdoor and indoor scenarios [4], [18]. To evaluate blocking, the signal penetration and reflection properties were measured for different common building materials (clear and tinted glasses, brick, wall, or concrete). Results show that most of the materials, especially tinted glass and brick are highly reflective and present significant penetration losses. Additionally, according to propagation measurements in [21], [22] it has been also demonstrated that the human body and the movement of people creates a significant obstruction and shadowing effect at mm-Waves. The advantage is that such resistance to penetration at mm-Waves might have a positive effect on the isolation of indoor and outdoor networks.

Given the mm-Waves propagation properties, the channel multipath characteristics have been studied for mitigating the obstruction of LOS and non-line-of-sight (NLOS) links. The measurements realized in [4], [23] exhibited a pathloss at least 40 dB smaller in an NLOS link, compared to the presence of LOS. This yields the consideration of mm-Waves propagation as a bimodal channel depending on the possibility of establishing LOS or NLOS links [2], [10].

On the other hand, foliage losses can be empirically predicted regarding the foliage depth as presented in [20]. The penetration loss for various foliage depth between 5-40m was plotted in Figure 1.6 b).

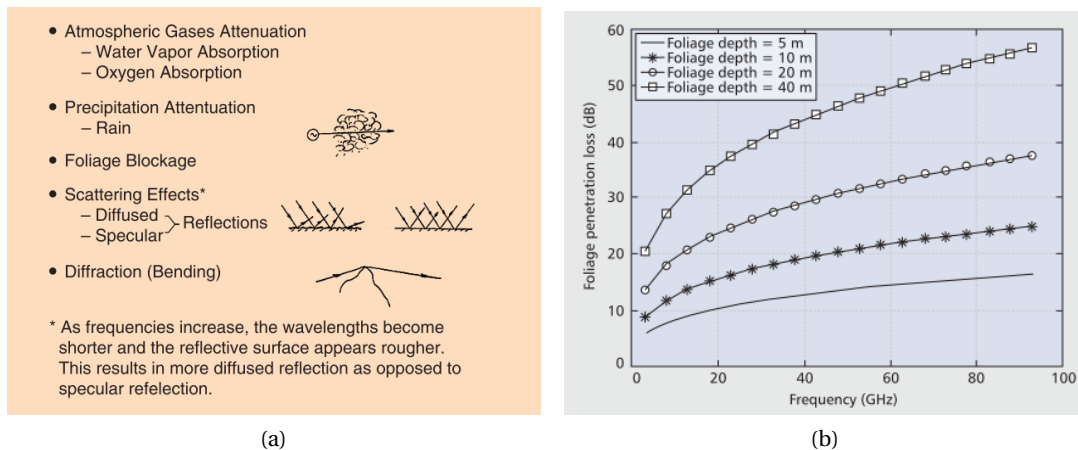


Figure 1.6 – a) Propagation effects influencing mm-Waves propagation [19], b) foliage penetration loss [20]

C) Increasing the spectral efficiency

The spectral efficiency describes the traffic density that can be achieved per unit bandwidth and unit area, i.e. increasing the number of bits/s/Hz per node. Once the area and bandwidth covered by a network provider are fixed, increasing the spectral efficiency can be achieved by implementing higher-level modulation schemes, multiple access techniques and MIMO diversity via polarization and/or angular disposition.

Waveforms and Modulation schemes

Current modulations schemes (BPSK /QPSK and M-QAM) are designed to generate a constellation of symbols such that a certain number of symbols (i.e. 2 symbols in BPSK and 64 in 64-QAM) can be transmitted in a designated carrier. Their main goal is to transmit as much data into the least amount of spectrum possible while still providing acceptable Bit Error Rates (BERs). The 5G modulation and waveforms have some commonalities with LTE but, combined with MIMO, aim to have much higher spectral efficiency. 5G supports QPSK, 16 QAM, and 256 QAM with the same constellation mapping as LTE.

In addition, in 5G an OFDM-based waveform is supported. OFDM is a signal waveform or modulation technique that divides the spectrum into closely spaced orthogonal subcarriers (each one modulated with the selected N-PSK and M-QAM modulation scheme). The subcarriers are transmitted in parallel and then an Inverse Fast Fourier Transform (IFFT) is performed on the frequency-domain to produce the orthogonal OFDM symbols in time domain. Both, Cyclic Prefix OFDM (CP-OFDM) for multicarrier transmission and Direct Fourier Transform spread OFDM (DFT-S-OFDM) for single stream transmissions are supported. In 5G, both CP-OFDM- and DFT-S-OFDM-based waveforms are mandatory for user equipment (UE) [17]. The first one consists of inserting a CP, generally a copy of part of the last transmitted symbol, between symbols to prevent inter-symbol interferences due to multipath delays in the propagation. The DFT-S-OFDM waveform is a single carrier each symbol is transmitted over the entire bandwidth.

Multiple access techniques

With these techniques, users can access and share the available spectrum resources. In the already established 2G, 3G and 4G techniques, users are multiplexed using different time slots (TDMA), modulation codes (CDMA), carriers (FDMA) or orthogonal carriers (OFDMA).

Various multiple access techniques have been considered and thoroughly researched to support the expecting demands of 5G mobile communications. According to [28] they should offer:

- Flexibility, i.e. one solution with adaptive settings for various applications.
- Interference control between users and systems in adjacent frequency bands.
- Coexistence with other technologies, e.g. with MIMO.

The existing orthogonal multiple access (OMA) concepts and their potential benefits, e.g. no-intra cell interference and simple receiver implementation, have been studied and evaluated at the mm-Waves. The radio access technology of the 4G, i.e. Orthogonal Frequency Division Multiple Access (OFDMA), Single-carrier Frequency Division Multiple Access (SC-FDMA), are regarded as a baseline for mm-Waves communications. The key telecommunication providers and equipment manufacturers, such as Samsung Electronics, Ericsson, Qualcomm Technologies, Huawei, Nokia and DOCOMO have outlined the suitability of OFDMA based technology for the 5G [24]–[29]. In fact, OFDM-inspired waveforms (Filtered OFDM, Single Carrier OFDM, Filter Bank MultiCarrier, Single Carrier Frequency Division Multiplexing, etc.) and those that can coexist with LTE/LTE-A are seen as a way to smoothly introduce and deploy the forthcoming 5G technology [24], [25], [30]. The other ongoing research on multiple access techniques for 5G is focused on developing non-orthogonal (NOMA) methods that will tackle the issues of spectral efficiency and massive connectivity at the expense of the hardware complexity [31], [32]. The question of whether these non-orthogonal-based systems can be put into practice has been raised. More details about multiple access techniques considered for 5G are summarized in Section 1.3.3 C.

MIMO

MIMO refers to a collection of signal processing techniques that have been developed to enhance the performance of wireless communication systems using multiple antennas at the transmitter, receiver, or both. By using a multiplicity of antennas, diversity (for redundancy) or multiplexing can be performed in MIMO by spacing, cross-polarization and/or angular disposition. This enables statistical independence to the channel matrix where multiple spatial dimensions become available for signaling and the spectral efficiency increases accordingly. According to [33], MIMO schemes can be categorized as diversity techniques, multiplexing schemes, multiple access methods, beamforming, and multi-functional MIMO arrangements. They are summarized in Table 1.6.

These techniques exploit the use of multiple antennas for enhancing the BER performance, the system throughput, the reuse of radio resources, the coverage area and SNR or a combination of them. MIMO communication was introduced in 3G in a 2x2 configuration [34]. In LTE, MIMO was leveraged to two-to-four antennas per mobile device and up to eight per BS sector. However, MIMO implementations in 3G and 4G are limited by the antenna form factor. As demonstrated in [35], having a larger number of antennas per BS, reduces the correlation between signals and the processing required at both ends of the communications. Such large-scale antenna systems can be deployed at mm-Waves and the implementation of MIMO in those systems is known as massive MIMO. The realization of massive MIMO requires meeting some challenges regarding the antenna system design implementation, the adequate channel model estimations, the proper coexistence of MIMO systems with the heterogeneous network architecture and the reduction of interference among pilots from different cells which could reduce the channel estimation quality.

The enabling technologies proposed to meet the aforementioned requirements can be grouped

Table 1.6 – MIMO techniques inspired from [33]

MIMO techniques	Concept	Methods
Diversity	Multiple antennas transmit/receive encoded replicas of the same information sequence. The goal is to improve BER performance. Antennas spaced far from each other to increase fading independence	<u>Receive Diversity:</u> Maximum Ratio Combining (MRC) Equal Gain Combining (EGC) Selection Combining (SC) <u>Transmit Diversity:</u> Spherical-Time Block Codes (STBC) Space Time Spreading (STS) Space-Time Trellis Codes (STTC) Linear Dispersion Code (LDC) Quasi-orthogonal STBC
Multiplexing	Multiple antennas are used for increasing the number of bits per symbol that can be transmitted in a given bandwidth to a single user	Space Division Multiplexing (Bell Labs Layered Space-Time (BLAST))
Multiple Access	Multiple antennas are employed for supporting multiple users	Space Division Multiple Access (SDMA)
Beamforming	Multiple antennas are used to increase the BF gain for mitigating path loss and interfering signals effects	Beamforming networks for SNR gain Beamforming networks for interference suppression
Multi-functional MIMO	A combination of more than one MIMO techniques	Layered Steered Space-Time Codes (LSSTC). Layered Steered Space-Time Spreading (LSSTS)

regarding the 5G:

- (A) Network architecture.
- (B) Physical layer (PHY).
- (C) Mac layer (MAC).

They are summarized in Section 1.3.3.

1.3.3 Key enabling technologies and their challenges

A) Network architecture

The network architecture is key to the understanding of 5G and the related upcoming technologies. The 5G network architecture will coexist with the current 3G/4G infrastructure where the already-deployed base station (BS) and microcell base stations (MBS) will be reused and reconfigured.

As wireless telecommunications evolved from cellular technology towards 4G the central role has always been assigned to the base station. Namely, the BSs are the main communication and controlling hubs for all the traffic occurring in a given area around the BS. Furthermore, currently existing networks are based on a homogenous macro-centric cellular planning process, i.e. each BS has similar transmitted powers, antenna patterns, backhaul connectivity, etc. [79]. Additionally, the locations of the base stations are carefully designed so that they ensure reliable coverage in a given area and reduced interference between neighboring BSs.

The low latency and high data rate requirements for 5G and the prevised small cells network densification have shifted the traditional homogenous BS-centric network paradigm. Technologies and concepts such as Heterogeneous Networks (HetNets), user-centric-based base stations, splitting of user and control planes, and Cloud Radio Access Network (C-RAN) have emerged to overcome such limitations and redefine the 5G network architecture.

Heterogeneous networks (HetNets)

The combination of different cell types (e.g. macro, pico and/or femtocells) and different Radio Access Technologies (RATs) such as (3G, 4G and Wi-Fi) in a cellular network is referred to as a heterogeneous network or HetNet. The small cells deployment and their coexistence with the existing macrocell infrastructure considerably improve the network capacity, spectrum reuse flexibility, and connectivity. As a result, operators can provide a more consistent customer experience compared to homogeneous networks. Figure 1.7 illustrates a general schematic of the potential outlook of the future HetNet 5G network architecture.

The heterogeneous characteristics of the 5G cellular network bring a group of issues that need to be sorted out such as the coordination and interference management among macrocells and small cells, as well as the efficient user-base station association. Additionally, the power supply and backhaul of dense small cell areas need to be considered. Regarding interferences between macro and second-tier cells the use of reverse Time Division Duplex has been proposed in [36] where downlink and uplink are alternatively assigned to base stations and small cells. With the same goal, Qualcomm proposes the implementation of interference management techniques at both communication ends (base station and user device) [36]. In [37] association methods via static biasing towards small cells and blanking of a percent of the macrocell transmissions have been addressed. For a smart coupling between multiple RATs, frequency scheduling algorithms and frequency reuse techniques have been considered [38]. Energy and spectral efficiency have been addressed in [39], [40] to provide a green HetNet.

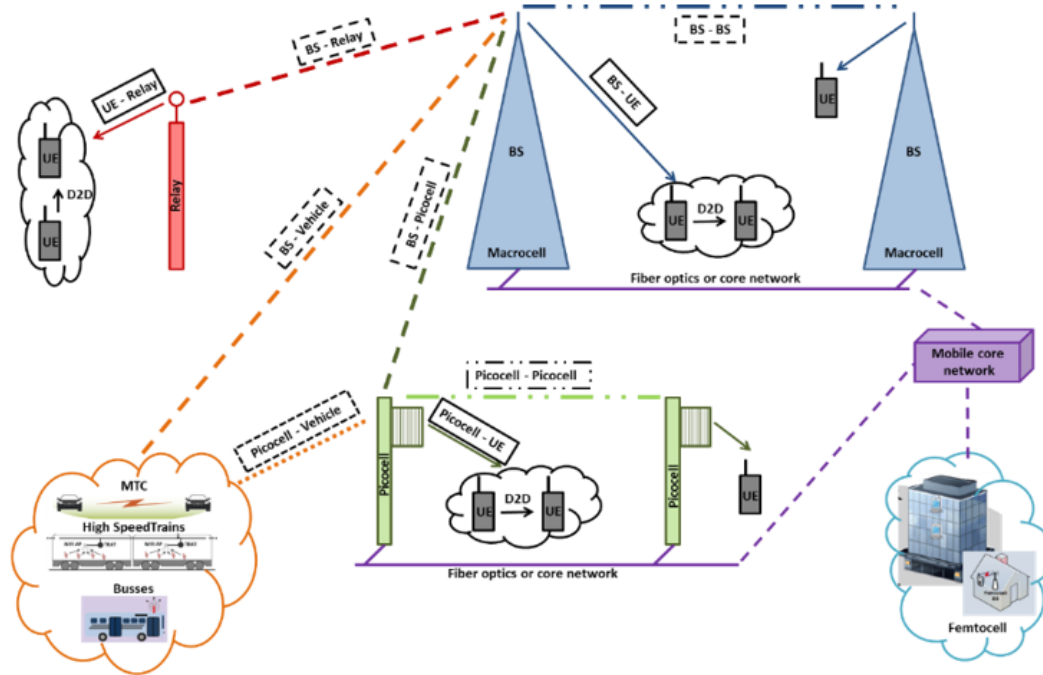


Figure 1.7 – General schematic of the potential 5G architecture

Device centric network. Device-to-Device communications (D2D)

Another concept to meet the 5G latency and data rates requirements is the shift from base-station-centric network to user-centric network. The idea is that users are actively used for storage, relaying and content-delivering instead of being only the end of the network architecture.

During the first mobile network generations it was considered that calls between two parties would be generally realized from non-close proximity. However, after the arrival of the internet, co-located users share content (e.g. photos and videos) or interact with each other (networking or video games). D2D communications propose to handle local communication in a more efficient manner [41]. In that regard, four main types of device-level communications have been specified: device relaying with base station controlled link formation, direct D2D communication with BS controlled link formation, device relaying with device controlled link formation, direct D2D communications with device controlled link formation. They include the cases where a device is used as a relay or it is one of the communications ends. In addition, they also specify in which plane the control link is established.

Although D2D communications are considered an important facilitator for applications requiring low latency, various open issues are still being investigated. They include the integration of D2D communications in the 5G heterogeneous network, the design of D2D-enabled devices, and the adequate management of security and interference. Regarding security, closed access and open access have been addressed. In close access, a user can communicate via encrypted D2D only with devices from a certain reliable self-created list, otherwise communication

through the BS needs to be executed [42]. In open access, where a device serves as a relay for other devices without any restrictions, implementing the research developed for Machine to Machine (M2M) communications has been suggested in [2]. Regarding interference management, [43] claims that the use of dedicated spectrum different from the BS-UE links might be a solution to avoid interferences and extra overheads for control and channel estimation. On the other hand, only a few researchers have proposed protocols for the implementation of D2D communications [44]. Considering the D2D-enabled devices, a built prototype for D2D communications has been presented by Qualcomm in cellular networks which can be used in different scenarios such as social networking and content sharing. Although D2D communications are not in a mature state yet, it should be taken into account that this technology is being studied since 4G for public safety applications [41], [45]. The interest that it has obtained from the standardization bodies, industry and academia shows that D2D will be part of future cellular communications.

Cloud-based Networking, NFV and SDN

In the traditional network, services are provided by a manifold of physical devices and equipment dedicated to specific service functions. Such service components are deployed by network operators depending on the network topology and the service location. This infrastructure has led to a rigid and highly specialized hardware-dependent network with complex and expensive scalability. Meeting the increasing data rates and storage demands implies continuously purchasing and deploying new equipment, and training the necessary personal dedicated to operating and managing it.

Cloud computing (or cloud based-networking), Network Function Virtualization (NFV) and Software Defined Network (SDN) have been proposed to address these drawbacks.

Cloud computing proposes moving data to the cloud to enable network access from anywhere and via a variety of platforms. According to [46], with cloud computing, a pool of computing resources (e.g. networks, servers, storage, applications and services) can be accessed with minimal management effort or service provider interaction.

NFV uses virtualization technology to decouple the network functions from the hardware infrastructure. This means that a network function, such as a firewall, can be implemented as an instance of plain software. Accordingly, a given service can be decomposed into a set of Virtual Network Functions (VNFs). This brings more flexibility and scalability to the network capabilities and services since VNFs may be relocated and instantiated at different network locations without requiring the purchase or installation of new hardware. Additionally, new services can be more dynamically deployed over the same physical platform.

SDN proposes a simplified solution to handle the highly-dense and heterogeneous mobile network by splitting the network's control logic (the control plane) from the corresponding routers and switches that forward the traffic (the data plane). In the control plane, controllers use information about capacity and demand obtained from the data plane to set up and tear down flows and paths in the network. Additionally, SDN proposes a centralized controller and view of the network so that the network is programmable by external applications or services provided by the network operator (e.g. energy-efficient networking, traffic/security moni-

toring, and mobility management). This facilitates the flow of large data without incurring control plane overhead, reduces hardware constraints and ease the cooperation among nodes for efficient management of the network density and diversity [46], [47].

These technologies are considered as some of the most relevant advances in the current mobile communications since they represent a paradigm shift in the way network services are provided. High data rates and low latency demands can be met thanks to improved network flexibility and accessibility. For their implementation, some issues must be sorted out regarding the migration from the current infrastructure, management, automation and security schemes, as well as the coexistence of NFV, SDN and cloud-based networking.

B) PHY layer

This section summarizes key enabling technologies related to the physical layer of the 5G mobile network. They focus on the characterization of the mm-Waves channel and the RF technology. The mm-waves channel measurement and models, the antenna design and full-duplex radio technology are explored in this section.

Mm-Waves channel measurements and models

The new propagation properties of the channels used by 5G communication technologies have been studied through a manifold of measurement campaigns summarized in [48]. Most of them focused on four different topics, characterizing MIMO channels, studying mm-Waves propagation properties and measuring the channel in Vehicle-to-Vehicle (V2V) and High-Speed Trains (HST) communications (see Table 1.7).

It can be noticed that most of massive MIMO, V2V and HST measurement campaigns were realized at sub 6 GHz bands. Only a few of them (e.g. mm-Waves massive MIMO and HST mm-Waves) combined multiple technologies [48], [49]. Similar campaigns employing multiple technologies and in a further variety of scenarios still need to be realized. Many of the proposed 5G channel models (e.g. the 3GPP model) are based on some of these measurement campaigns. According to [48], 5G channel modeling is driven by a new set of requirements, including:

- Wide frequency range.
- Broad bandwidth.
- Wide range of scenarios.
- Three-dimensional modeling.
- Smooth time evolution.
- Spatial consistency.
- Frequency dependency and frequency consistency.
- Massive MIMO.

Table 1.7 – 5G channel measurements, inspired from [48]

Category	Scenario	Carrier Frequency (GHz)
massive MIMO	court yard	2.6
massive MIMO	top of building	15
massive MIMO, mm-Waves	Indoor office	11, 16, 28, 38
massive MIMO	campus	2.6
massive MIMO	Indoor canteen	5.8
V2V	Urban, open highway	5.12
V2V	suburban	5.9
V2V	Campus, urban	5.8
V2V	crossroad	5.3
V2V	Urban, highway	5.12
V2V	Campus, highway, urban, suburban	5.3
HST	viaduct	2
HST	Viaduct, cutting	0.930
HST	Hilly terrain	2.4
HST	Open space	5.25
HST	viaduct	2.35
HST	cutting	2.35
HST mm-Waves	rural	28
mm-Waves	urban, suburban	28, 38, 60, 73
mm-Waves	urban	35, 103
mm-Waves	urban	29.5
mm-Waves	Indoor restaurant	26, 39.5
mm-Waves	In and around building	28
mm-Waves	Indoor office	57.5
mm-Waves	Indoor, parking garage	28, 40
mm-Waves	Indoor office	60
mm-Waves	Street canyon, roof-to street	83,5
mm-Waves	urban	59
mm-Waves	Indoor, urban, O2I	15, 17, 28, 60, 86
mm-Waves	Indoor office	60

- Direct D2D/V2V.
- High mobility.

A group of 5G channel models has been proposed to meet such requirements. They are COST 2100 channel model, MiWEBA channel model, QuaDRiGa, mmMAGIC channel model, METIS channel model, 5GCMSIG, 3GPP channel model, IMT-2020 channel model, IEEE 802.11ay, and 5G channel model (MG5GCM) (see Table 1.8). They are based on stochastic, deterministic or combine both methods, such as hybrid and quasi deterministic (Q-D) modeling approaches. Most of them have been developed on a wide frequency range, e.g., from 0.45–100 GHz, except for MiWEBA and IEEE 802.11ay channel models which only support the 60 GHz band.

Blockage and gaseous absorption effects are considered in the MiWEBA, IEEE 802.11ay, 3GPP TR38.901, mmMAGIC, IMT-2020. Additionally, only the MG5GCM can support the four most

Table 1.8 – Comparison of General 5G models, inspired from [48]

Feature	COST 2100	MiWEBA	QuaDRiGa	METIS		5GCMSIG	3GPP	mmMAGIC	IMET-2020	IEEE 802.11ay	MG5GCM
Modeling approach	Stochastic (GBSM)	Q-D based model	Stochastic (GBSM)	Stochastic	Deterministic (map-based)	Stochastic (GBSM)	Stochastic (GBSM), Deterministic (map-based), hybrid model	Stochastic (GBSM)	Stochastic (GBSM), Deterministic (map-based), hybrid model	Q-D based model	Stochastic (GBSM)
Frequency range (GHz)	< 6	57-66	0.45-100	< 70	< 100	0.5-100	0.5-100	6-100	0.5-100	57-68	-
Bandwidth (GHz)	-	2.16	1	0.1 (< 6 GHz) 1 (> 6 GHz)	10% of f_0	0.1 (< 6 GHz) 2 (> 6 GHz)	10% of f_0	2	0.1 (< 6 GHz) 10% of f_0 (> 6 GHz)	2.64	-
Support large array	-	yes	yes	no	yes	limited	yes	yes	yes	no	yes
Support 3D	yes	yes	yes	yes	yes	yes	yes	yes	yes	yes	yes
Support mm-Waves	no	yes	yes	partly	yes	yes	yes	yes	yes	yes	yes
Spatial consistency	yes	yes	yes	Shadow fading only	yes	yes	yes	yes	yes	no	no
High mobility	yes	no	yes	limited	no	yes	limited	yes	limited	no	yes
Blockage modeling	no	yes	no	no	yes	yes	yes	yes	yes	yes	no
Gaseous absorption	no	yes	no	no	yes	no	yes	yes	yes	yes	no

-: There is not information in the related documents

challenging scenarios of 5G systems, i.e., massive MIMO communications, V2V, HST communications, and mm-Waves communications. Despite the numerous channel measurement and models proposed for 5G, there is still room for improvement. It is recommended to combine multiple modeling approaches, such as stochastic and deterministic models so that a trade-off between accuracy and computational complexity is achieved. The combination of these methods, the use of multiple technologies and the increase in the variety of scenarios are some of the future research directions in this field.

Antenna design. Multibeam forming

Antenna design is a key technology in the successful deployment of 5G networks. Given the high absorption due to environmental conditions and high path loss characteristic to mm-Waves, the use of directive antenna systems is recommended in order to mitigate such effects. Omnidirectional coverage can be provided using multibeam antennas (MBAs) where directional beams are simultaneously steered towards different UEs or angular sectors. Such antenna systems are crucial for enabling massive MIMO techniques in 5G. According to [50], MBAs can be classified as passive MBAs, multibeam phased arrays antennas and active digital MBAs. They are summarized in Table 1.9.

Full digital MBAs (DMBAs) can enable fully adaptive beamforming with highly flexible beam-steering and beamforming. They are a promising technique in the implementation of massive MIMO. However, their application to the coming mobile generation is limited by a group of challenges regarding, the current state of their beamforming algorithms, digital processing hardware and cost, power, and thermal efficiency issues [16], [18], [50]. At present, the main cost-effective candidates considered for enabling multibeam forming in 5G are based on passive MBAs, phased array antennas and hybrid MBAs, their selection depends on the application and hardware constraints. Given their relevance to this thesis, the state of the art on antennas for 5G is covered in Section 2.

Table 1.9 – Review of MBA architectures

MBA architectures	Concept	Beam-forming	Implementation	Pros/Cons
Passive MBAs	Beamforming is performed in RF domain without using active components. Prefixed beams and pointing (except for Blass and Nolen matrices)	Analog	Reflector fed by multiple antennas	+ Designs with simple and non-expensive fabrication can be realized - Beams have fixed directions - Adaptive beamforming is not possible - Difficult scalability leading to bulky and lossy systems
			Lens fed by multiple antennas	
			Beamforming circuits (e.g. Butler, Blass and Nolen matrices)	
Phased arrays antennas	Beamforming is performed in RF domain. Multiple beams are obtained via phased array		Passive	- Difficult scalability leading to lossy, bulky and expensive system Compared to passive MBAs: + Improved flexibility in beam shaping and steering
			Active (Each antenna element has its own amplifying module)	
Digital MBAs	Beamforming is performed in digital domain at base band.	Digital	Full Digital MBA (DMBAs)	+ Fully flexible adaptive beamforming + High spatial resolution in a given angular range + Key for fully enabling Massive MIMO - Complex beamforming algorithms - High power consumption and cost
		Hybrid	Fixed subarray Phased subarray	Compared to full DMBAs: + Number of transceivers is reduced + The required beamforming processing is relaxed - Narrower angular coverage - Additional multiplexing technique might be required Compared to Passive MBAs: + Better system scalability + Less bulky- higher cost

Full duplex radio technology

Half-duplex Frequency Division Duplexing (FDD) and Time Division Duplexing (TDD) are widely used in 4G [51]. As shown in Figure 1.8 b) and c), in half-duplex FDD the uplink and downlink signals are separated by orthogonal frequency bands, while in its TDD counterpart orthogonality is achieved via time-slots [52]. These duplexing techniques have been compared in order to identify their advantages and drawbacks regarding their coverage capacity, hardware cost, and their ability to support asymmetric links, unpaired spectrum and beamforming techniques. [53].

While in half-duplex, a single radio access technology is supported at a time, in full-duplex more than one UE can be served per frequency/time unity. This depends on the nodes and users being half or full-duplex. Full duplex (FD) offers to double the spectral efficiency of a point-to-point radio link. Other FD advantages summarized in [54] include:

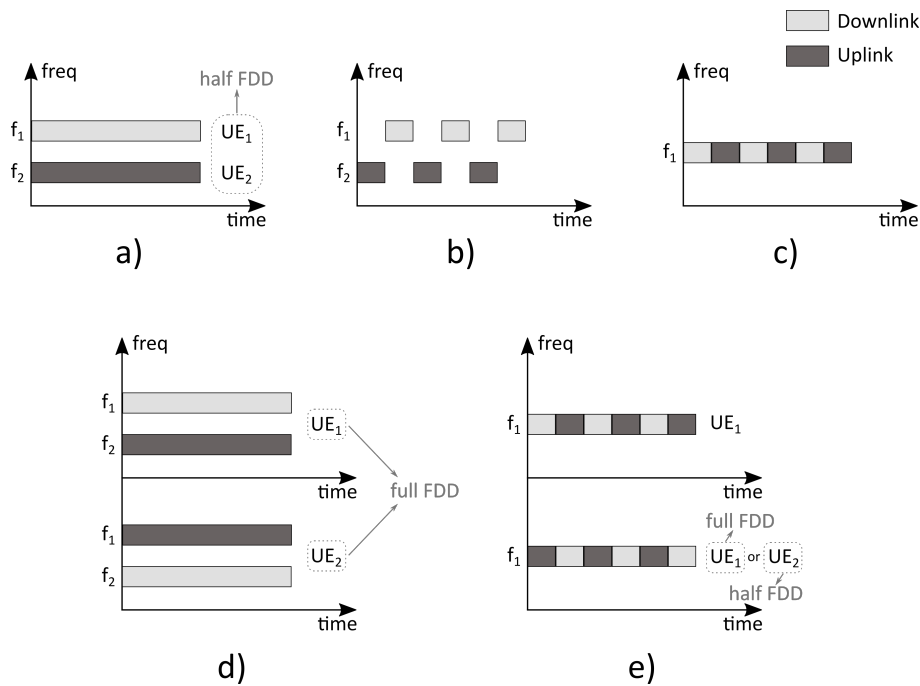


Figure 1.8 – a) Full duplex FDD node with half duplex UEs b) half duplex FDD c) half duplex TDD d) Full duplex FDD node with full duplex FDD UEs and e) Full duplex TDD node with full or half duplex FDD UEs.

- Latency reduction (Reduction of feedback and end-to-end delays).
- Improvement of network secrecy.
- Efficiency improvement of ad-hoc network protocols.
- Increment of spectrum usage flexibility.

Although FD has been considered in LTE-A in relay transmission for wireless networks, its drawbacks regarding self-interference (SI), imperfect interference cancellation, inter-user interference and increase power consumption and complexity have limited its extension to point-to-point transmissions [51]. Due to the current advances in RF and beamforming antenna design technologies, FD can be implemented at a reasonable cost and complex radio hardware. Namely, beamforming, massive MIMO, centralized architecture and small cell deployment have shown to be key in the FD realization [55]–[57]. Future research on the implementation of FD should tackle the miniaturization of the RF technology in charge of the SI cancellation modules such that they can be integrated into cell phones and other portable devices. The efficient coexistence between HD and FD modes needs to be further investigated where dynamic switching between the HD and FD modes is considered. Other open issues in the FD implementation are related to power efficiency, the FD-based MAC protocol design and backhauling [58].

B) MAC layer

This section includes the enabling technologies associated to the MAC layer. They include the Novel multiple access techniques and the antenna training protocols necessary to overlay the PHY layer. References to some other MAC enabling techniques such as directional MAC protocols, Random Access Channel and Cognitive Radio are provided.

Novel Multiple Access

OFDMA

Orthogonal Frequency Division Multiple Access (OFDMA) consists on assigning frequency carriers to each user while the system bandwidth is divided into a set of orthogonal carriers with narrower bandwidth than the coherence bandwidth of the fading channel. Consequently, intersymbol and intercarrier interferences are reduced and high data performance is enabled [32]. Its main drawbacks are a need for synchronous multiplexing and link budget loss for a large number of simultaneous users [29]. The concept of OFDMA is illustrated in Figure 1.9, where different users are marked in different colors.

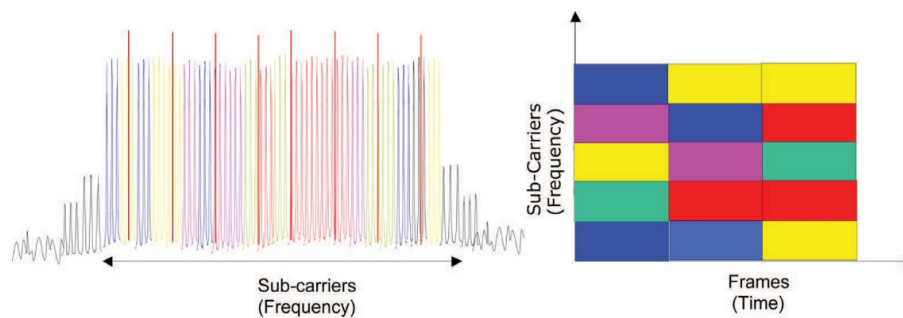


Figure 1.9 – OFDMA concept [32]

SDMA

Space-division multiple access (SDMA) holds a central part in the design of smart antennas. The SDMA concept consists of the spatial filtering of spectrally and temporally overlapping signals from multiple users. SDMA is used jointly with other multiple access techniques: FDMA, TDMA or CDMA.

Users in a cell are differentiated based on a time delay of signals arriving from different sources that are located at different distances from a receiver. SDMA base stations are equipped with independent beamformers that can target a certain user based on adaptive beamforming algorithms. Accordingly, beams can be pointed at the desired user, while undesired users are attenuated or nulled. This enables multiple users to simultaneously transmit/receive signals in the same radio cell and in the same frequency band without interfering with the neighboring cells [59], [60].

Since directional beams and localization of users are interesting to 5G communications, the suitability of SDMA for mm-Waves antenna systems has been investigated [61], [62]. In [61] SDMA for 60 GHz has been addressed by developing an iterative antenna training protocol

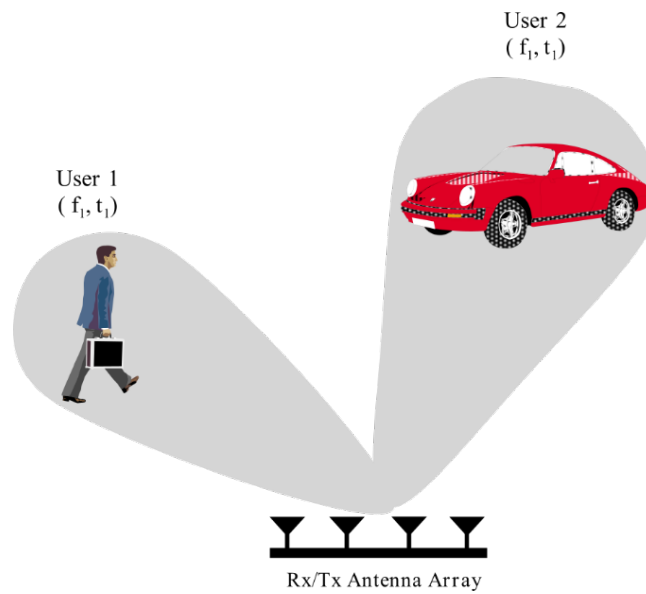


Figure 1.10 – SDMA concept [59]

that computes the optimal transmit/receive beamforming vectors without explicit knowledge of the actual wireless channels. It has been shown that the proposed training method is efficient for a systems with a significantly smaller number of RF chains than antennas, which is typically the case for 60 GHz beamforming networks (see Figure 1.11).

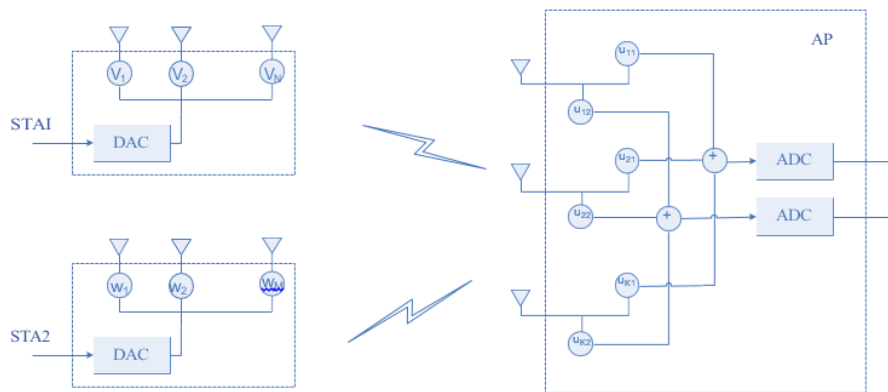


Figure 1.11 – Spatial division multiple access based on 60 GHz transceiver beamforming [61]

Moreover, a joint SDMA-TDMA approach has been considered as a solution to overcome the hardware constraints and operation loads of fully digital systems at mm-Waves. Results illustrate that SDMA-TDMA can enable a high data rate per user with low complexity and overhead [62]. In addition, SDMA can coexist with OFDM and has been already used in MIMO systems [63], [64].

Non-Orthogonal Multiple Access Concepts

Novel concepts of non-orthogonal multiple access schemes for 5G mobile communications

have been extensively studied. Various non-orthogonal multiple access techniques are Non-Orthogonal Multiple Access (NOMA), Sparse Code Multiple Access (SCMA), Multi-User Shared Access (MUSA), Pattern Division Multiple Access (PDMA) and Resource Spread Multiple Access (RSMA) [29], [31]. Given its relevance, NOMA is further detailed in this section.

NOMA

A Non-Orthogonal Multiple Access (NOMA) scheme has been proposed by NTT DOCOMO in [31]. To increase the spectrum efficiency, NOMA separates multi-user signals by applying successive interference cancellation (SIC) on the receiver side while non-orthogonal transmitter's transmission intentionally introduces intra-cell and/or inter-cell interference (Figure 1.12). SIC represents a physical layer technique that enables the receiver to decode simultaneous signals, at the expense of increasing its hardware complexity. As a result, a receiver is capable of decoding the strongest signal and determining the weakest signal from the residue of the combined signal. In [65] OFDMA and NOMA concepts are compared by evaluating an example of two UEs with different channel gains. As it can be seen in Figure 1.13 NOMA offers a higher sum-rate (increased more than a 32%) when the path loss between users is large. In 2010 NTT DOCOMO proposed NOMA for macrocells operating at 800 MHz and 2 GHz bands with a throughput increased by a 50%. However, its hardware complexity and signal processing constraints stills prevent NOMA from being deployed at mm-Waves [24].

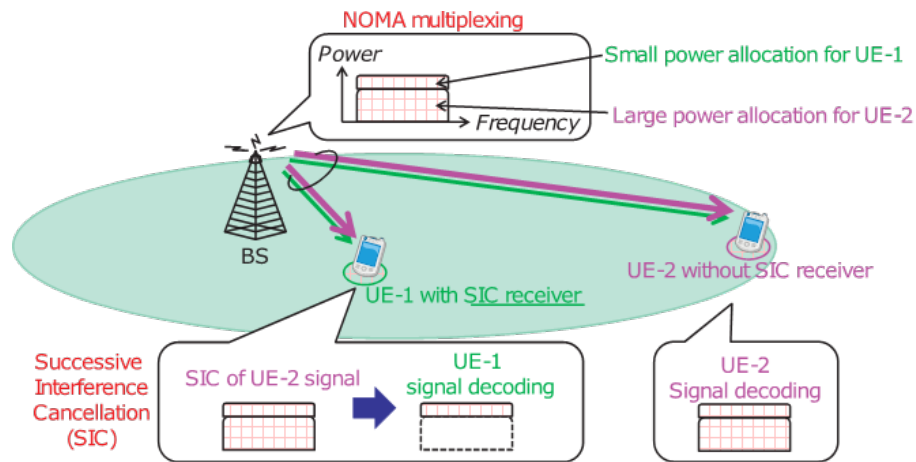


Figure 1.12 – NOMA when SIC is used at UE [65]

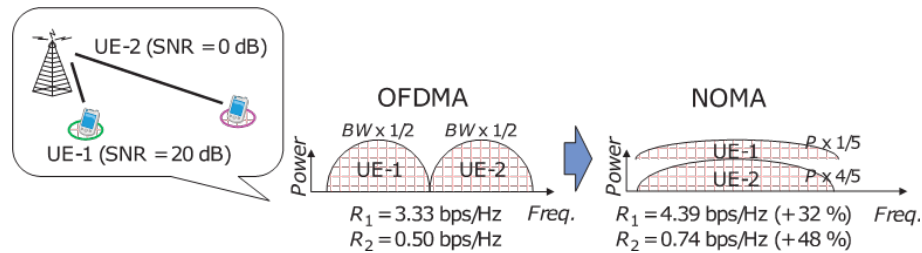


Figure 1.13 – Comparison of NOMA and OFDMA for downlink [65]

Antenna training protocols. Angle of Arrival distributions

As described, multibeam antennas can enable omnidirectional coverage in an antenna system based on directive antennas. Given that the BS-UE link might be aligned, attenuated or blocked (see Figure 1.14), a variety of scenarios need to be taken into account leading to increasing the complexity of the communication protocol design.

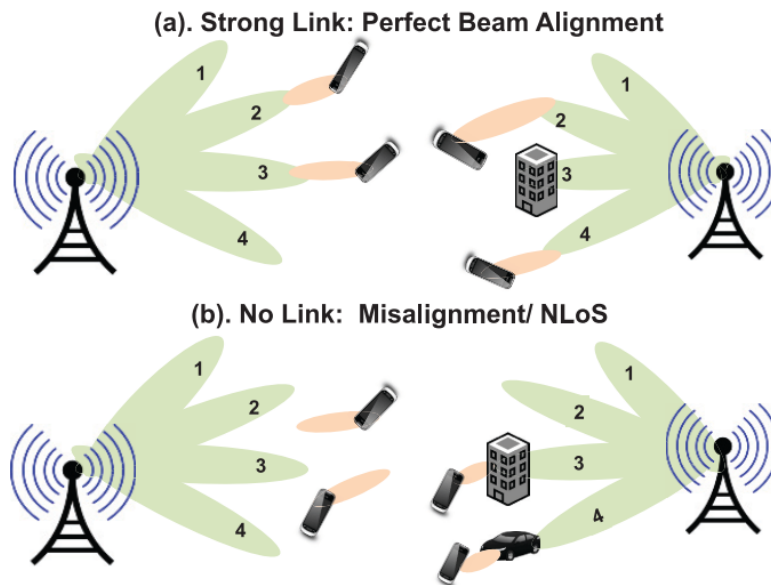


Figure 1.14 – Antenna Training: Beam Steering for Link Alignment [9]

Beamforming training protocols for identifying the best beam direction pair have been investigated in [66]–[68]. They propose:

- Using pseudo-noise sequences.
- Using narrowband pilot signals.
- Employing Singular Value Decomposition of a series of independent beamforming vectors.

Due to the high multipath in mm-Waves communications, a direct beam between BS and UE might not always be optimal. In [66] the AoA was measured at the transmitter to obtain the angles with the highest received power in LOS, partially obstructed LOS, and NLOS conditions. In the NLOS case, it was demonstrated that a link could be created by illuminating surrounding objects. Thus, in such scenario, having knowledge of the time-varying Angle of Arrival (AoA) can be useful. In addition, in [67] acquiring the AoA is proposed as a tool to identify the second-best path when the LOS link is blocked by human movement. The use of AoA information in

Directional Self pursuing Protocol (DSP) is proposed in [69] for discovering the shortest path in wireless broadcast.

Other key enabling technologies in this layer include Directional MAC protocols, Random access channel and cognitive radio [9].

In this chapter, a general introduction on the 5G mobile network generation is presented to contextualize the core of the work covered in this thesis. The rest of this chapter includes the motivation, the research problem definition and objectives, and the organization of the thesis.

1.4 Motivation

A manifold of technologies and emerging applications has been proposed to fulfill the 5G mobile network requirements. They represent a paradigm shift in the way mobile communications are designed and used, enabling higher data rates, lower latencies and enhanced quality of service. A field of application where these capabilities may bring significant advantages is emergency services. It is crucial that the communication systems of these service providers are up-to-date and capable of providing effective communication to users in case of emergency situations. This thesis aims at exploring the applicability of mm-Waves 5G enabling technologies to improve deployable terrestrial emergency communication systems (e.g. Mobile Master Node and Emergency Vehicle in Figure 1.15). These systems are to be applied as portable stations to support the coordination of rescue services with high-performance communications in areas where these are not available or have been damaged. This project focuses on the investigation of mm-Waves 5G picocell stations as the core element of such portable systems for the described application.

Picocells (or mm-waves stations) can be defined as the outdoor 5G small-cell stations to be deployed in urban or rural scenarios. Working mostly in mm-Waves bands, they will cover an area of a few hundred meters. Picocells, together with microcells will be the core of small cell deployment in the 5G mobile network architecture. Picocell antennas combine some of the most challenging techniques in antenna design like mm-Waves antennas, multiple beamforming and massive MIMO. Therefore, yielding the design of complex and efficient devices that work according to the mobile quality and capacity demands.

1.5 Research problem definition and objectives

This project has been driven by the following research problems:

- Immature state of the art about 5G due to the underdeveloped mm-Waves mobile communications and the still in progress 5G standard definition.
- Necessity of having an up-to-date antenna system capable of establishing communication with users in case of security situations.

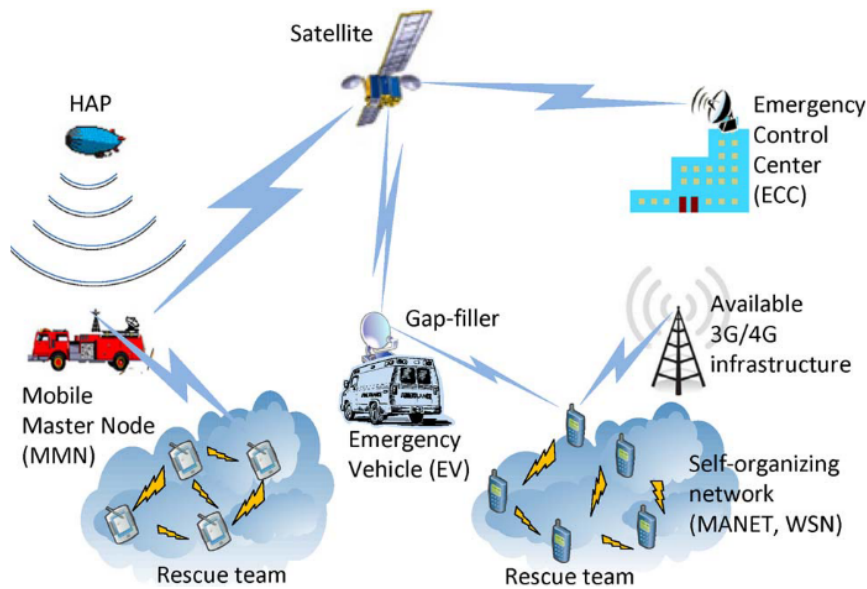


Figure 1.15 – Emergency communication scenario [70]

Our objective with this project is to obtain a demonstrator of a portable picocell antenna for security applications, based on mm-Waves 5G standards. The antenna should be thus compatible with the 5G principles. Furthermore, special attention will be put on the antenna portability, enabling the possibility of bringing service to a region in case of rescue, disaster or other security situations.

A scheme of potential picocell links can be seen in Figure 1.16. Instead of a fixed picocell base station, a portable picocell node (vehicle) has been considered. This picocell vehicle, once located in the strategically chosen position, is not supposed to move. Therefore, the portable characteristic does not require including dynamic analysis of the system.

1.6 Organization of the thesis

This thesis is organized into six chapters addressing the design and implementation of a portable picocell antenna for 5G, with special interest in terrestrial emergency communications. The investigation carried out in this thesis is an integral work, covering all the stages of the design process, from the study of the scenario and the definition of the requirements to the final antenna design and implementation. Chapters are thus strongly interconnected and at the same time address independent problems. Each chapter thus opens with a short literature review specific to the topic tackled in it.

Chapter 2 presents a study of the picocell scenario for this application. The available standard information about 5G picocells and propagation properties of the considered band of operation are investigated. An analysis of the link budget is performed, yielding the definition of the

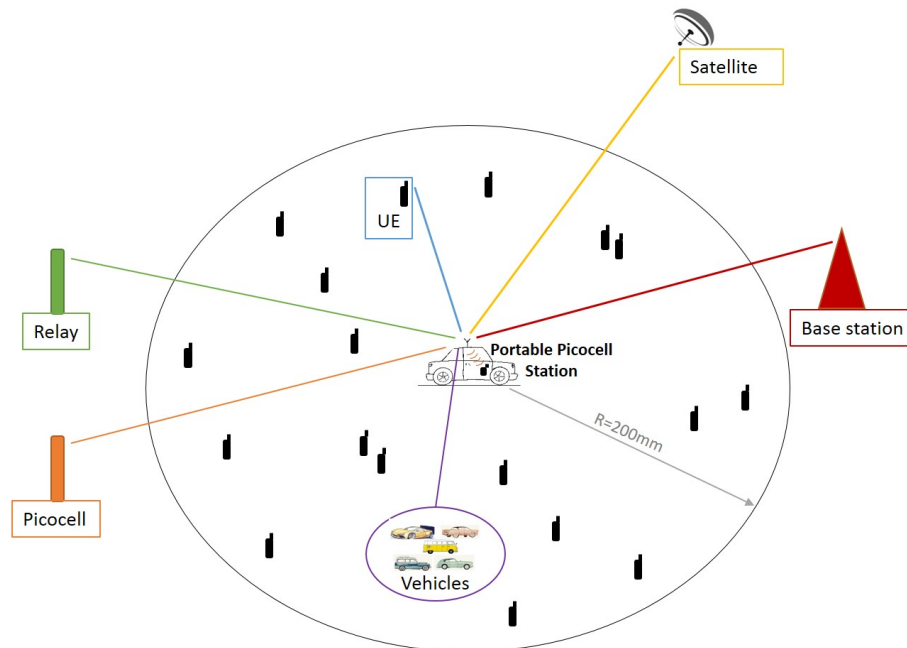


Figure 1.16 – Picocell scenario

antenna design requirements. In addition, the state of the art on antennas for 5G is reviewed and a general antenna architecture for the studied application is defined.

Chapter 3 provides an introduction to recently proposed hybrid beamforming networks and a summary of the main synthesis methods, focusing on the methods based on convex optimization. In addition, this chapter describes the synthesis of the hybrid beamforming network for the antenna architecture defined in Chapter 2. This synthesis is divided in two different problems tackling the design constraints of the analog beamforming network (ABFN) in elevation and the digital beamforming network (DBFN) in azimuth.

Chapter 4 addresses the design and implementation of a csc^2 pattern shaped antenna subarray. The scenario and design requirements are outlined and the transmission line and antenna element are described. In addition, the guidelines in the design of the subarray are given, including the solution of the synthesis problem in elevation, the selection of the feeding network topology and layout and the design of the feeding network components. This chapter additionally includes the subarray implementation and the description of the fabrication process. The required measurements in the validation of the subarray performance are presented and conclusions are drawn.

Chapter 5 presents the picocell multibeam antenna fed by a hybrid beamforming network (HBFN). The limitations of the subarray proposed in Chapter 4 considering the required multibeam forming capabilities in azimuth are investigated. Based on this, an optimized subarray is proposed. A section of the multibeam antenna array is implemented and measured. Comple-

mentary, details about the fabrication of this antenna are given. The adequate performance of this prototype is studied taking into account the constraints specified in elevation and azimuth. The results demonstrate that the proposed antenna is a promising solution for the considered application.

2 Scenario and design requirements

In this thesis, we aim at developing a portable picocell antenna, for enhancing the communication systems of terrestrial emergency services, according to the mm-Waves 5G specifications. Such antenna will be located on top of a vehicle and it should provide coverage to a small number of users in mostly LOS condition, located in a cell radius of a few hundred meters. Additionally, this picocell is mainly meant to be deployed in rural or light urban environments.

This chapter addresses the study of the picocell scenario and the link budget definition, considering the desired compatibility with 5G and the preliminary design constraints. Moreover, the state of the art on MBAs for mm-Waves applications are investigated. Finally, the antenna architecture and design specifications are defined.

2.1 Scenario and Link budget analysis

In this section, we summarize the parameters involved in the link budget definition according to the studied picocell scenario. Given that the available standard information about 5G picocells is not complete, we have additionally reviewed the experimental data (namely from realized measurement campaigns) aiming to identify the rest of the required parameters in the link budget calculation.

2.1.1 Link budget parameters

The deployment of pico-nodes (also referred to as low-power or local area nodes) under a macrocell tier has been proposed in 5G as a fundamental solution to increase the network capacity and the end-user service experience. In 5G HetNet networks, picocells will be most likely installed at indoor or outdoor hotspots, providing local-area access. In release 15 of 3GPP [11], picocells features have been specified, including BS-UE minimum distance along the ground, BS-UE minimum coupling loss and the base station output power and reference sensitivity level, as shown in Table 1.4.

Table 2.1 – Small base stations parameters given in 3GPP Release 15 [11]

BS-UE minimum distance from the ground	$\geq 2m$
BS-UE minimum coupling loss	45 dB
Base station output power	≤ 24 dBm
Reference sensitivity level	$-93.8 \text{ dBm} \leq P_{\text{REFSENS}} \leq -87.3 \text{ dBm}$

These values have been considered in the link budget calculation associated with our picocell scenario. Some other link parameters of interest, not yet specified due to the uncompleted standard, have been obtained from the available experimental data.

After the performed study in [71], considering the ***potential operating bands for 5G***, we selected the n258 band (24.25 GHz to 27.5 GHz) with central frequency at 26 GHz as the operating band for our picocell station, since it represents a good compromise between signal attenuation due to different environmental conditions and available bandwidth.

As shown in Figure 1.3, the 5G operating bands (n257 and n258) in the range 24.25 GHz to 29.5 GHz varies in different regions, for example, in Europe and China the bands of interest are located at the lower half of that range, while in USA, South Korea, and Japan the upper half has been considered. Such diversity has reduced the number of available measurement campaigns and channel models characterizing each specific frequency range. However, they can still be used as a reference since their propagation characteristics are similar [19]. Taking into account that most of the research has been carried out at 28 GHz [18], [72]–[74], the propagation characteristics of this band are summarized herein.

Attenuation due to oxygen and light rain is negligible at microwaves and mm-Waves bands, with the exception of frequencies around 60 GHz with 20 dB/km oxygen absorption and on a minor scale 24 GHz with 0.2 dB/km due to water vapor absorption. On the other hand, heavy rain may induce higher attenuation at mm-Waves [19], [75]. Table 2.2 includes atmospheric, intensive rainfall, heavy fog, and heavy snow absorption at 28 GHz. Compared to higher bands in the mm-Waves range considered for 5G (e.g. 60 GHz), the n257 and n258 range present low values of ***attenuation due to different environment conditions***.

Table 2.2 – 28 GHz losses due to different environment conditions at 200 m [1]

Atmospheric	Intensive rainfall	Heavy fog	Heavy snow
0.02 dB	4 dB	< 0.1 dB	< 0.1 dB

Foliage penetration losses, depending on the foliage depth, varies from 12 dB (foliage depth 5 m) to 40 dB (foliage depth 40 m) [76].

The shadowing factor S_{σ_s} , used to describe the received signal fading caused by obstructions and other random propagation effects, was also measured in 28 GHz campaigns. The slow fading margin (or shadow fading margin) was measured in LOS and NLOS links with values typically varying between 0.2 dB and 9.02 dB [77].

Material penetration losses were measured for different common building materials (clear and tinted glasses, brick, wall or concrete). Results show highly reflective characteristics of most of these surfaces with losses up to 40 dB. These results show that the signal building penetration at mm-Waves should be scarce, yielding considerable isolation between outdoor and indoor networks [4].

Human blockage for 28 GHz was modeled and measured in [21] using different human subjects located at a height such that the LOS path was blocked by the human torso. This measurement was repeated after rotating the subjects at different azimuth angles. Measured values reveal penetration losses around 17 dB.

With the objective of measuring the path loss at 28 GHz, different communication setups were deployed in light and dense urban environments at Suwon and Manhattan cities respectively [4], [78]. In order to obtain the **path loss exponents (PLEs)**, defined as n , the average measured received power was compared to its equivalent in a free space outdoor cellular channel at the same frequency (See Figure 2.1).

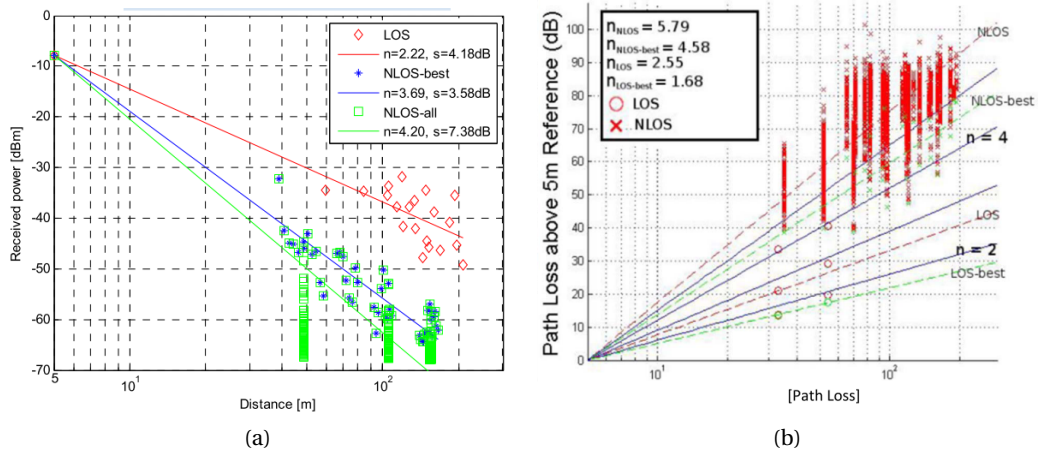


Figure 2.1 – Measured Path Loss Exponent (n) for 28 GHz outdoor cellular channels a) In Suwon, Korea [78] and b) New York, Manhattan [4]

In Figure 2.1, the average PLE for LOS links were $n_{LOS} = 2.22$ and $n_{LOS} = 2.55$, while $n_{NLOS} = 4.20$ and $n_{NLOS} = 5.79$ were the average PLE values for NLOS links, respectively.

The extent of cell coverage at 28 GHz was studied in various measurement campaigns [23], [78], [79]. A cell distance of a few hundred meters (typically 200 m) was recommended since satisfactory communication links were established in some cases even in NLOS conditions.

Another criterion used to examine the coverage area is the relationship between root mean square (RMS) delay spread and the distance. This term relates the difference between the time of arrival of the earliest significant multipath component (typically the line-of-sight component) and the time of arrival of the latest multipath components. Figure 2.2 shows the

RMS delay spread values for different distances. In NLOS links, RMS values were measured for longer distances (up to 200m) compared to the LOS measurements [4].

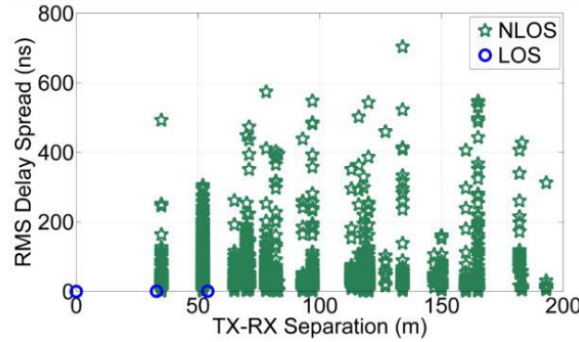


Figure 2.2 – RMS delay spread as a function of TX-RX separation for all links using all possible pointing angles at 28 GHz in New York City [4]

Considering propagation characteristics of the 28 GHz carrier, this band is considered as a very interesting option for small cells and wireless backhaul communications [26], [77], [80].

The aforementioned parameters used to characterize the propagation characteristics of 28 GHz will be used as a reference in the link budget calculation of our picocell scenario.

The estimation of the path loss (PL) is crucial in the calculation of the link budget. Different path loss models considered for mm-Waves have been summarized in [81]. In these models, attenuation due to different factors, such as absorption due to environment conditions, foliage and human blockage, diffuse reflection and shadowing obtained after extensive measurement campaigns have been included. The simplest and yet widely used model is called Reference PL model. In this model, path loss is estimated via the path loss exponent and shadowing effects (see Equation 2.1).

$$PL_{[dB]} = \left[PL_0 + 10n_p \log \left(\frac{R}{R_0} \right) \right] + S_{\sigma_s} \quad (2.1)$$

where R_0 (m) is the free-space reference distance, R is the cell radius and S_{σ_s} denotes a zero-mean Gaussian distribution with a standard deviation of σ_s . Furthermore, PL_0 indicates the reference free-space loss at distance R_0 and n_p is the PLE.

Other models have been proposed for either increasing the accuracy in the description of NLOS links, obtaining path loss in longer link distances via extrapolation from smaller links data or combining PL in indoor and outdoor scenarios [81].

The parameters described in this section have been considered in the link budget analysis associated with our picocell scenario.

2.1.2 Link budget analysis

In order to have a clearer picture of the different aspects that are considered in the link budget calculation, a graphic representation of our picocell scenario is shown in Figure 2.3, including some of the terms that will be further addressed such as the picocell radius (R), the transmitter and receiver power (P_t, P_r) and gain (G_t, G_r), and the elevation and azimuth planes.

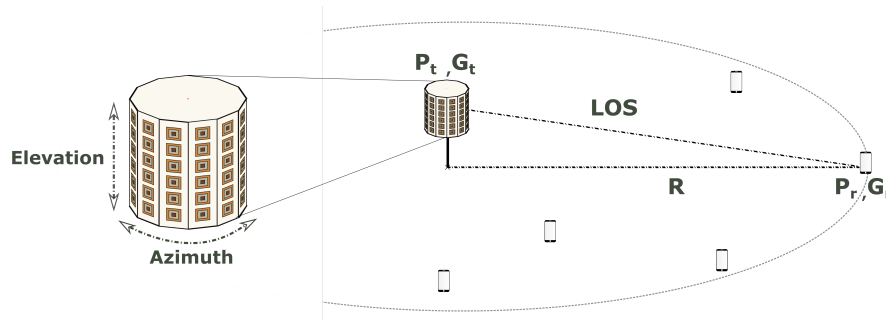


Figure 2.3 – Picocell scenario

Path loss in the picocell has been calculated using equation 2.1, since it is suitable for LOS links at mm-Waves. Substituting PL and the parameters in Table 1.4 in the Friis formula, the required gain at the picocell station was obtained.

$$G_t = P_r - P_t + G_r + PL \tag{2.2}$$

Table 2.3 summarizes the link budget parameters associated with the picocell scenario studied in this work.

Table 2.3 – Picocell requirements.

Parameters	Value
Carrier Frequency	26 GHz
Bandwidth*	BW > 7%
Coverage distance (R)	200 m
Path loss exponent (n_p)	$2.22 \leq n_p \leq 2.45$
Transmitter power	24 dBm
Transmitter gain	≥ 10 dBi
Receiver sensitivity level	-87.3 dBm
Receiver gain	5 dBi

*Referred to both, impedance and pattern shape bandwidths

The picocell operates at 26 GHz with bandwidth higher 7%. The picocell transmission power has been chosen to be 24 dBm and the receiver sensitivity -87.3 dBm complying with the parameters for picocell scenarios given in [11]. Considering a LOS urban scenario, a path loss exponent between $2.22 \leq n_p \leq 2.45$ has been assumed. The UE antenna gain has been chosen

to be 5 dBi [82]–[84]. Under the specified scenario, a transmitter with a gain higher than 10 dBi would ensure signal reception to a user located 200 m away from the picocell station.

In addition, the proposed antenna should enable omnidirectional coverage along the picocell. This, together with the link budget requirements in Table 2.3, will be considered in the definition of the antenna architecture and its design specifications.

2.2 Definition of the picocell antenna architecture

In this section, a study of the state of the art on antennas for 5G is included, followed by the definition of the picocell antenna configuration and its design requirements.

2.2.1 State of the art on antennas for 5G base stations

In the context of upcoming mobile network scenario with a standard to be born, a group of attractive and innovative solutions has been proposed for 5G base stations, however most of them lacking specific application regarding the type of cell (e.g. macrocell, microcell or picocell) or other link budget characteristics (e.g. coverage area, transmitter power, number of users per cell).

With a variety of architectures, principles of operation and technologies, various antenna arrays intended for 5G base stations have been proposed. We have classified them, according to MBAs in Table 1.9.

Passive antennas

Antennas proposed in [85]–[89] are passive MBAs based on Butler matrices [85]–[88] and a lens antennas in [89]. Butler matrices in [85], [87], [88] have been designed using substrate integrated waveguide (SIW) feeding lines, while in [86] a microstrip line has been used.

A wide radiation bandwidth was obtained in [87], [88] by using air gaps between antenna elements to diminish surface waves in [87], while the subarray in [88] is based on a multilayer structure of aperture coupled antenna elements. Considering that both subarrays are designed on SIW, they present a low profile, however, they occupy a relatively large area.

Regarding their architecture and principle of operation, antennas in [88], [89] generate multiple beams in two planes. This is achieved in [88] using two sets of beamforming networks based on SIW Butler matrices feeding a 4x4 antenna, where the antenna element (shown in Figure 2.4 b)), consists of a magnetolectric-dipole. Additionally, aperture coupling is used for both, interconnecting the feeding networks and feeding the antenna elements (see Figure 2.4 a)). The proposed antenna achieves beamforming of 16 beams covering approximately $\pm 40^\circ$ in elevation and $\pm 60^\circ$ in azimuth.

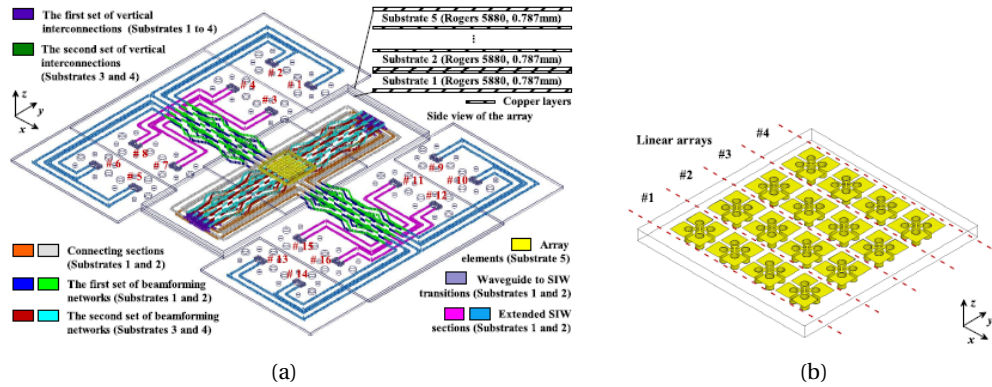


Figure 2.4 – a) perspective view of the multibeam antenna b) 4x4 magnetolectric-dipole antenna array [88].

In [89] flat lenses (with circular and cylindrical shapes) based on a low-temperature co-fired ceramics (LTCC) dielectric are tested by mechanically positioning a waveguide feed (WR-15) to provide 2D beamsteering (see Figure 2.5a). In the circular lens, beamsteering along $\pm 45^\circ$ in both planes with gains higher than 11 dBi is achieved. The cylindrical lens can cover $\pm 55^\circ$ with gain higher than 10 dBi. In addition, the cylindrical prototype fed by an antenna array is proposed for 5G mm-Waves applications (as shown in Figure 2.5b). The feeding array consists of a frequency-scanned slot antenna array, thus providing beam scanning by sweeping the frequency. Since the subarrays are fixed, the scanning is performed in one plane.

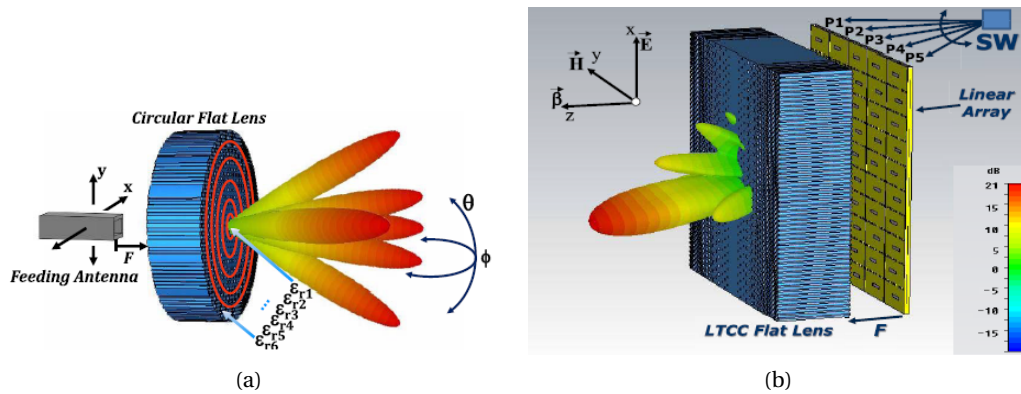


Figure 2.5 – a) Flat lens for 2D beamsteering b) Switched-beam antenna array [89].

On the other hand, prototypes in [85]–[87] achieve multibeam forming in one plane. In [85], a multilayer antenna consisting in 8 subarrays coupled via slots to the SIW Butler matrix is proposed (see Figure 2.6 a)). The antenna subarray is a 1x10 patch array series-fed by a microstrip line. The beam is scanned along $\pm 36^\circ$, with gain higher than 19.8 dBi. In [86] a 1x6 antenna array fed by a 4x6 microstrip Butler matrix is presented. A conventional 4x4 Butler matrix has been extended to a 4x6 configuration (as depicted in Figure 2.6 b)) with the objective of increasing the antenna gain and reduce the sidelobe level (SLL). The two added

output ports are located on a second layer coupled through two microstrip-slotline transitions. This antenna achieves multi-beamforming of 4 beams scanning the $\pm 45^\circ$ range, with gain higher than 9.2 dBi.

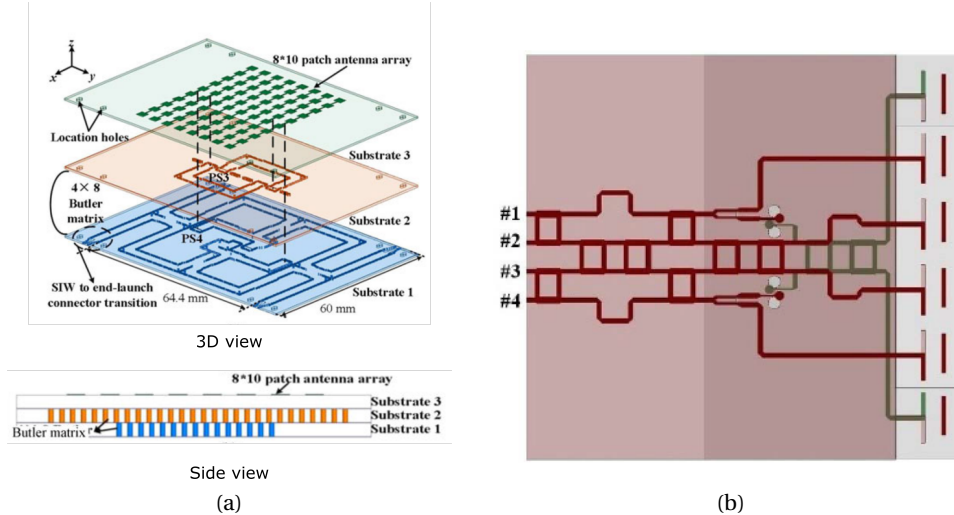


Figure 2.6 – a) 8x10 patch array with Butler matrix [85] b) 4x6 Butler matrix cascaded with the antenna array [86].

The prototype in [87] consists of a 4x4 Butler matrix with 8 possible feeding ports and 4 antenna elements (see Figure 2.7 a)). This antenna can adopt two configurations: when ports 1-4 are excited, the proposed array presents a Left-Handed Circular Polarization (LHCP) pattern, while ports 5-8 provide a Right-Handed Circular Polarization (RHCP) polarization. The antenna elements consist in dielectric-loaded stepped slots (see Figure 2.7 b)).

Phased array antennas

Various phased array antennas have been proposed for 5G mm-Waves applications. The prototype in [90] is a passive multibeam phased array, while the antennas presented in [91]–[93] are based on single-beam phased arrays. Although the prototypes [91]–[93] are not MBAs, they have been proposed for mm-Waves applications. Hence, their subarrays design can be used for comparison in this section.

The antenna in [90] consists of two identical waveguide-based radiating reconfigurable structures (RRSs) (see Figure 2.8a). As depicted in Figure 2.8b, each RRS is formed by 1x15 slots with embedded S-PIN diodes that can be reconfigured to form beams pointing at (a) 45° , (b) 30° or (c) 0° . A commercial electromechanical radio frequency switch (ERFS) has been located between the two RRSs. This switch activates one of the RRSs to guarantee beamforming on both sides of the axis, achieving five beams pointing at 0° , $\pm 30^\circ$, and $\pm 45^\circ$.

In [91], a single-beam phased antenna, consisting in a 6×5 planar array has been proposed. A 6-way series-parallel power divider feeds the subarrays (see Figure 2.9a). This divider was

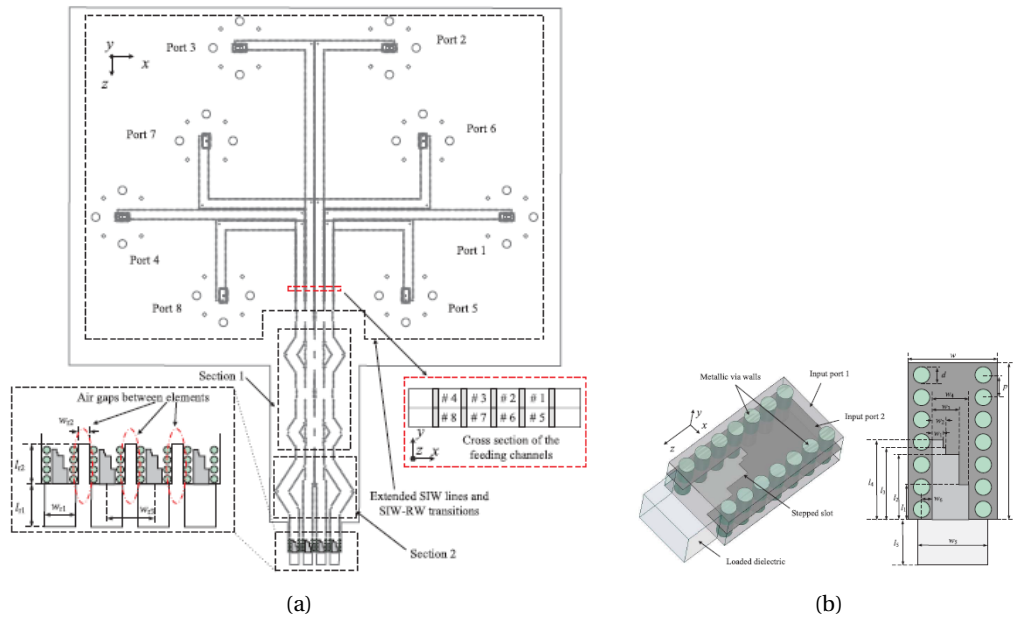


Figure 2.7 – a) 4x4 Butler matrix b) Geometry of the dielectric-loaded stepped slot antenna [87].

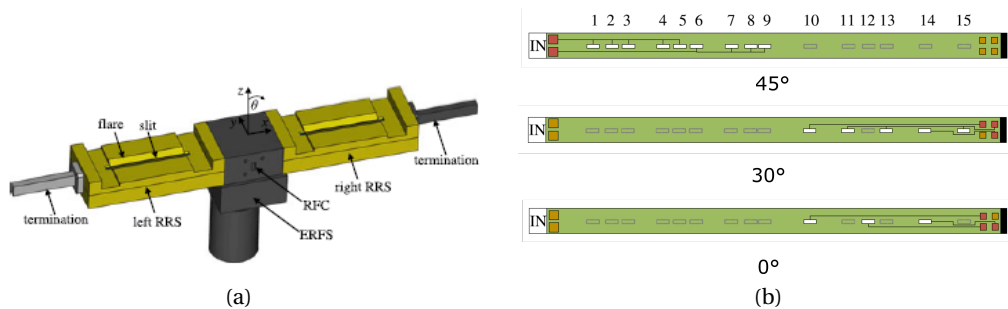


Figure 2.8 – a) Model of the switched-beam antenna b) RRS with highlighted group of slots forming a beam in different directions [90].

chosen for achieving a more compact antenna size compared to regular corporate feeding networks. Additionally, via holes surrounding the lines were added in order to minimize spurious radiation. The antenna subarray (shown in Figure 2.9b)) consists of 1x5 antenna elements proximity-coupled in a series configuration. The antenna elements width was tuned according to a Dolph-Chebyshev amplitude-tapering for minimizing SLL and slits were placed along the feeding line for reducing reflections. This antenna achieves a fixed pencil beam along a 3.6% radiation bandwidth.

Two single-beam phased arrays for LHCP and RHCP radiation are proposed in [92]. Both antennas consist of aperture coupled patches (1x8 patches) fed by a SIW corporate feeding network (see Figure 2.10a). Having identical feeding networks, the antenna elements design

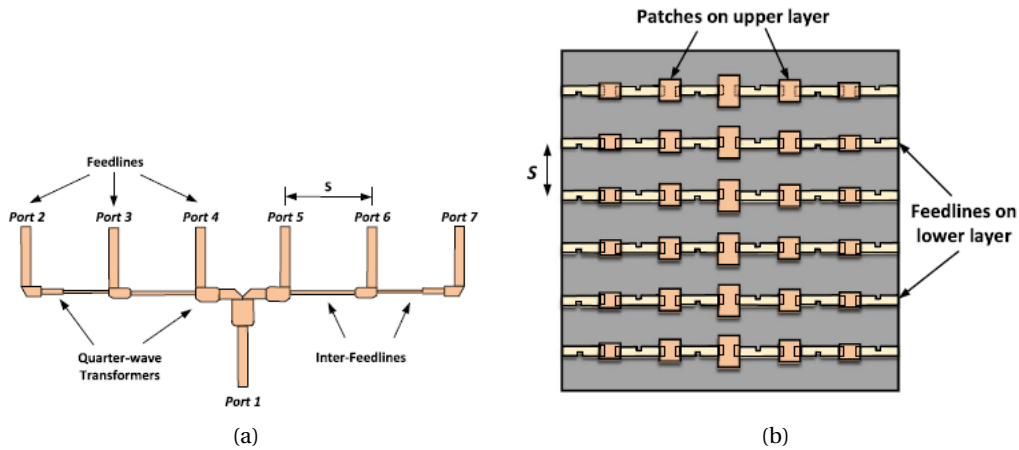


Figure 2.9 – a) 6-way series parallel power divider b) 6×5 proximity-coupled planar array 2.9.

(depicted in Figure 2.10b) is different in dimension and rotation to achieve the desired Circular Polarization (CP). The second slot in the antenna element was added for increasing the bandwidth. These antennas present a fixed pencil beam over a 3.9% radiation bandwidth.

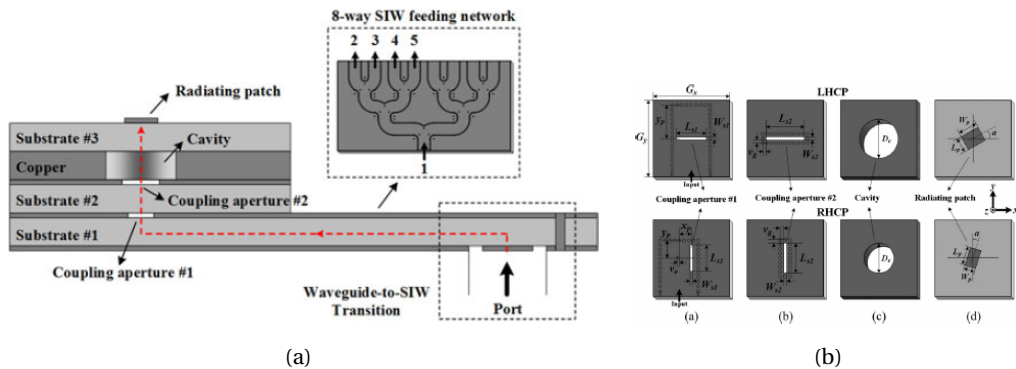


Figure 2.10 – a) Side view of the proposed CP antenna array b) Geometry of the two types of CP antenna elements [92].

The prototype proposed in [93] is a single beam phased array with dual polarization. Two antennas (colored in red and blue) with orthogonal polarization have been located in an interdigital shape as shown in Figure 2.11. Each antenna consists of a 4-way power divider and four series-fed subarrays of 1×6 antenna elements, yielding an array of 4×6 antenna elements. The antenna element consists of an aperture coupled patch and the feeding network is based on T-type folded substrate integrated waveguide (TFSIW) which is narrower compared to typical SIWs. In addition, this antenna has been designed to provide a beam pointing at 30° .

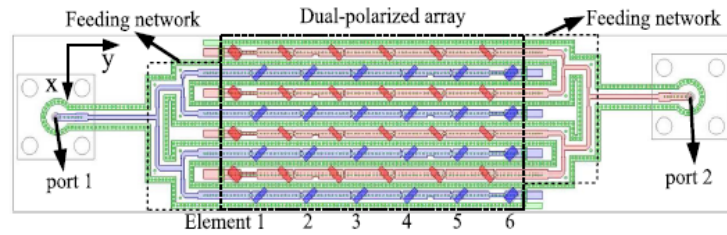
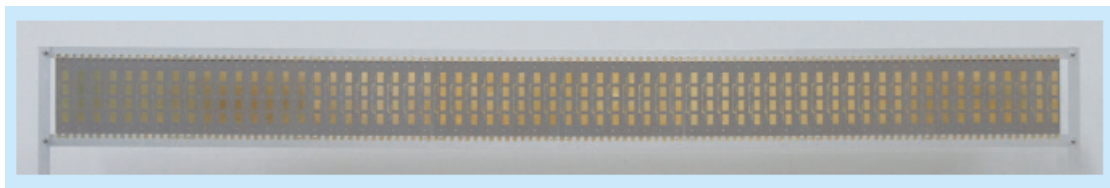


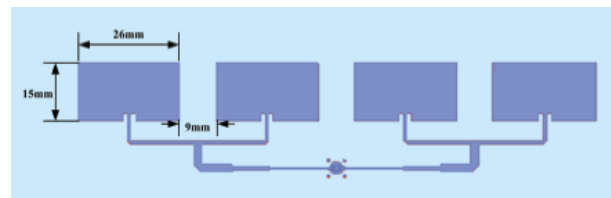
Figure 2.11 – Front view of the TFSIW-excited dual-polarized antenna [93].

DMBA antennas and Transceivers

Antennas presented in [94] and [95] are DMBA based on fixed subarrays for 5.8 GHz and 28 GHz, respectively. The prototype in [94] consists of an array of 64x4 antennas (Figure 2.12a) with 64 RF transceiver channels that control the same number of subarrays. Each subarray is formed by 1x4 patches fed by a parallel microstrip feeding network (Figure 2.12b). Since the fixed subarrays are vertically arranged, multiple beams are generated in the horizontal direction, covering $\pm 30^\circ$.



(a)



(b)

Figure 2.12 – a) 64x4 Antenna array b) 1x4 antenna subarray [94].

In [95], a 4x8 planar antenna array consisting in four horizontal 8-element subarrays is presented (as depicted in Figure 2.13). While the antenna design is not described in detail, the authors report achieving a horizontal scanning of $\pm 30^\circ$.

Given their relevance in the definition of DBMAs, the transceivers presented in [94] and [95] are summarized next. The transceiver used in [94] operates at 5.8 GHz (see Figure 2.14) and it consists of three main blocks:

- Digital Baseband Processing Unit, in charge of the baseband signal processing in the digital domain

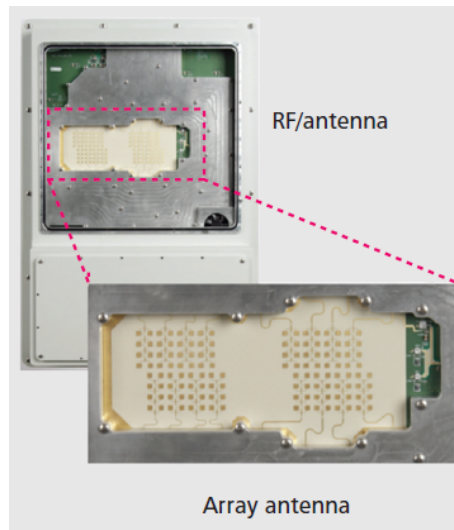


Figure 2.13 – 4x8 planar antenna array [95].

- High-Speed Interface Board, that contains the 64 RF-channels, including ADCs and DACs
- RF-front ends, where In-Phase/Quadrature (I/Q) baseband signals are modulated/de-modulated into analog signals by two orthogonal Local Oscillator (LO) signals (i.e., quadrature modulation/demodulation). Additionally, each RF front contains amplifiers and filters associated with each antenna element.

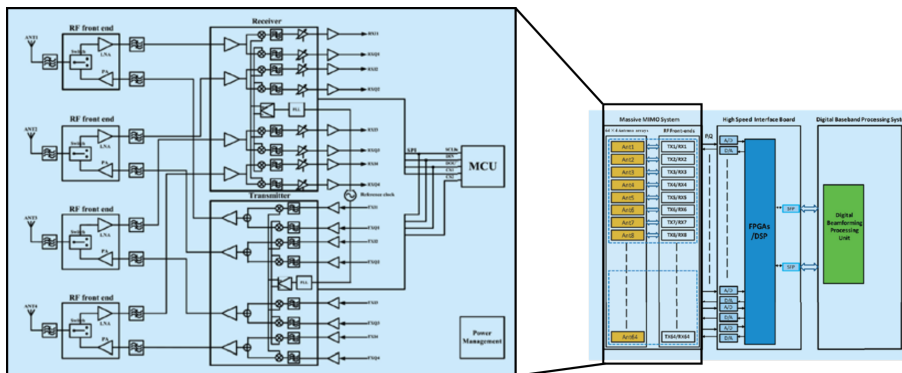


Figure 2.14 – Transceiver architecture proposed in [94].

The transceiver used in [95] consists of a modem operating in real-time at mm-Waves, which contains integrated commercial off-the-shelf units including, Field-Programmable Gate Arrays (FPGAs) and ADC and DAC with 1 GS/s conversion rate (see Figure 2.15).

In the described DMBAs antennas, details about the specific signal processing units and their power consumption figures are not given. The small number of proposed DMBAs in the literature show that the design of mm-Waves transceivers is currently an open issue. The main

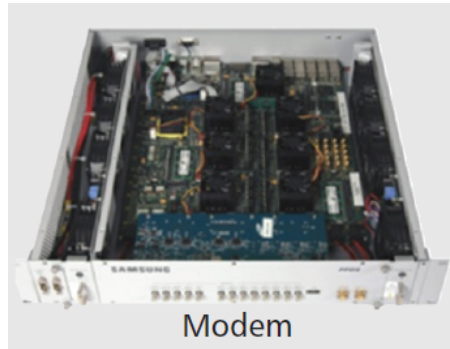


Figure 2.15 – Modem used in the DMBA antenna proposed in [95]

challenges are linked to:

- Space limitation in the RF front-end stage, due to the densely packed antenna arrays and the small available space to locate one RF chain per antenna element
- Heating issues due to the significant power dissipation of mm-Waves devices. The small available space in mm-Waves antennas hinders the integration of cooling systems [96]
- Power consumption due to power-hungry mm-Waves front-end devices and highly demanded signal processing in the digital domain. Table 2.4 summarizes the state of the art on consumed power by a group of mm-Waves front-end devices [97].

Table 2.4 – Consumed power by various mm-Waves front-end devices [97]

Device	Power [mW]
PA	40-250
LNA	4-86
Phase shifter	15-110
ADC	15-795
VCO	4-25

In order to mitigate the power consumption in mm-Waves communications, the implementation of hybrid beamforming architectures has been proposed. The analog stage in this architecture reduces the amount of required mm-Waves devices. Other techniques suggest that instead of high-resolution ADCs/DACs with sampling rates in the GS/s range, lower resolution converters (i.e. few to 1-bit ADCs and DACs) are used. This is at the expense of a more challenging channel state information acquisition, yielding more complex channel sensing estimation algorithms [97]. Regarding heating issues of densely packed mm-Waves antennas, the authors of [96] propose including thermal management considerations in the antenna synthesis by varying the array layout and the element position. These approaches provide practical solutions to overcome the present development gap on mm-Waves communications until fully DMBA are cost-effective. Analyzing this in more detail is out of the scope of this work.

Tables 2.5 and 2.6 summarize the presented state of the art on antennas for 5G base stations regarding their MBA architecture, antenna geometry and subarray design. In addition, other parameters such as the antenna band of operation, bandwidth, gain and efficiency are depicted.

Table 2.5 – Comparison among the up-to-date passive MBAs for mm-Waves applications (*Referred to both, impedance and pattern shape bandwidths)

Parameter	[85]	[86]	[87]	[88]	[89]
MBA type	Passive (Butler matrix)	Passive (Butler matrix)	Passive (Butler matrix)	Passive (Butler matrix)	Passive (lens)
Antenna geometry	Planar multilayer	Planar	Planar	3D	Planar
Number of elements	8x10	1x6	1x4	4x4	5x10
(Subarray) Feeding line configuration	(1x10) Microstrip in series	(1x6) Microstrip Butler matrix	(1x4) Microstrip Butler matrix	(1x4) Butler matrix	(1x10) Stripline in series (frequency scanned)
Antenna element	Patch	Dipole	Dielectric loaded stepped slot antenna	Dipole Aperture-coupled	Slot
Frequency, bandwidth*, gain, efficiency	38 GHz, 3.6%, 19.8 dB, —	28 GHz, 3.6%, 9.2 dBi, 48.3%	37.5 GHz, 13.3%, 10.4 dBi, 54.4 %	60 GHz, 11.6%, 10 dBi, 35%	60 GHz, 15%, 17.79 dBi, 70%

Table 2.6 – Comparison among the up-to-date phased arrays MBAs and DMBA for mm-Waves applications (*Referred to both, impedance and pattern shape bandwidths)

Parameter	[90]	[91]	[92]	[93]	[94]	[95]
MBA type	Phased array (active)	Phased array (single-beam)	Phased array (single-beam)	Phased array (single-beam)	DMBA Fixed subarray	DMBA Fixed subarray
Antenna geometry	Linear	Planar	Planar	Planar	Planar	Planar
Number of elements	1x15	6x5	1x8	8x6	64x4	4x8
(Subarray) Feeding line configuration	Not specified	(1x5) / Microstrip in Series	(1x8) / SIW in parallel	(1x6) T- type folded SIW in series	(1x4) / Microstrip in parallel	(1x8) / Not specified
Antenna element	Slots with embedded S-PIN diodes	Patch Proximity- coupled	Patch Aperture- coupled	Patch Aperture- coupled	patch	patch
Frequency, bandwidth*, gain, efficiency	28 GHz, 1.8%, 18 dBi,—	28 GHz, 3.6%, 21 dBi, —	28 GHz, 3.9%, 19.09 dBi, 59%	28 GHz, 3.6%, 13 dBi, “low”	5.8 GHz, 3.4%, 18 dBi	28 GHz, 1.8%, 18 dBi

The analysis performed hitherto has lead us to select a hybrid DMBA as the multibeam forming architecture for the studied picocell, given their suitability for providing omnidirectional coverage in mm-Waves communications and enabling massive MIMO. Additionally, the stringent challenges linked to mm-Waves transceivers suggest that the design requirements should be met with a minimum number of transceivers. Further details related to state-of-the-art antennas presented in this section will be taken as reference across the rest of the document.

A description of the proposed antenna architecture in the frame of this project, together with the design requirements derived from the link budget analysis, are summarized next.

2.2.2 Antenna architecture

Among the most commonly used antenna configurations, we have selected the sectorized (or segmented) geometry since it presents a good compromise between the features offered by circular and planar arrays [9]. A circular geometry allows wider scan angles than a planar one, however at the expense of a more complex fabrication. On the other hand, a planar configuration can provide a higher directivity leading to a longer coverage extent (see Figure 2.16).

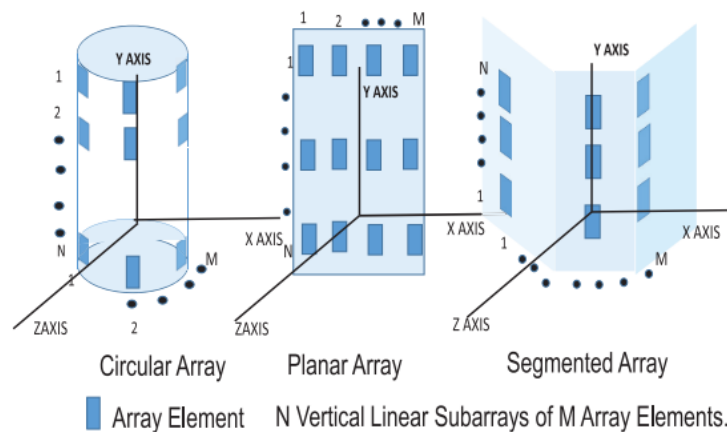


Figure 2.16 – Typical array configurations for antennas for mobile network communications [9]

The proposed picocell antenna in this work consists of a sectorial (or segmented) architecture, as depicted in Figure 2.17. In each sector, antenna elements have been grouped in vertical subarrays. Thus, the picocell antenna configuration consists of M subarrays, each containing N antenna elements.

In order to enable omnidirectional coverage, this antenna is fed by a hybrid beamforming network (HBFN), as shown in Figure 2.18. This network consists of a DBFN controlling M subarrays for providing multibeam forming in azimuth, while each subarray is fed by an ABFN guaranteeing uniform power distribution in elevation. This architecture provides a relatively flexible beamsteering performance at lesser cost and power consumption expenses considering currently existing full DMBAs.

As summarized in Table 1.9, the ABFN feeding the subarray can be phased (with variable phase shifters) or fixed. Given the relatively small number of users in the studied picocell scenario, a fixed subarray has been chosen.

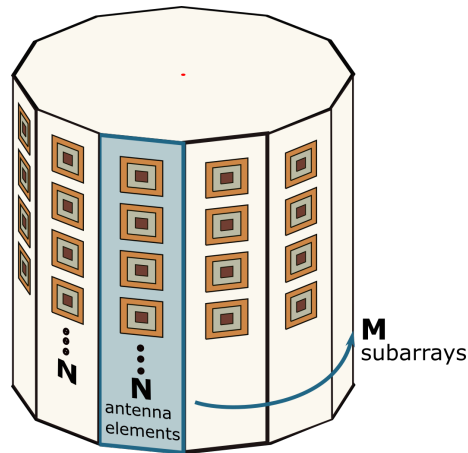


Figure 2.17 – MxN antenna array in a segmented configuration

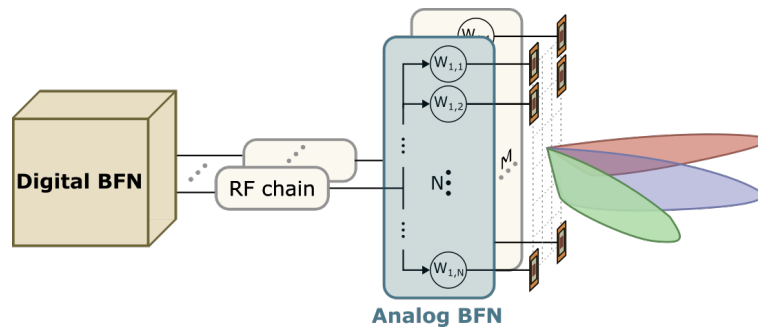


Figure 2.18 – Sketch of an antenna array fed by hybrid beamforming network

2.2.3 Subarray antenna and ABFN requirements

A fixed vertical subarray implies having a fixed radiation pattern in elevation. If a simple Uniform Linear Array (ULA) subarray is designed, their pencil beams would create blind spots in the picocell coverage area, leading to the non-fulfillment of the omnidirectional coverage requirement in our design. Instead, a csc^2 subarray has been proposed, i.e. the subarray radiation pattern in elevation should approximate a csc^2 function (see Figure 2.19). This radiation pattern is an established solution, widely used in radar and mobile wireless communications [98], [99] for guaranteeing a uniformly distributed power from the cell edge (R_{max} at θ_{max}) to the mast shadow (R_{blind} at θ_{blind}).

Taking into account the link budget calculated in Section 2.1.1 and the desired radiation pattern shape in elevation, the main subarray requirements have been summarized in Table 2.7.

The investigated subarray should work at 26 GHz with a bandwidth larger than 7%. The subarray gain should be higher than 10 dB to guarantee coverage in a cell radius of 200m approximately. On the other hand, the feeding network (or ABFN) should provide an adequate weighting vector to guarantee a csc^2 pattern in elevation.

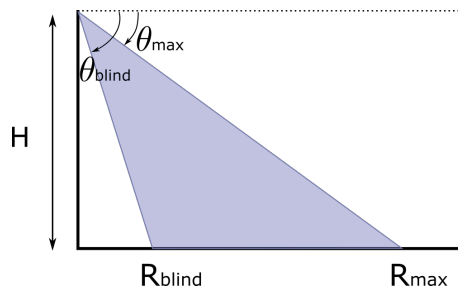


Figure 2.19 – Diagram of parameters defining coverage in vertical plane

Table 2.7 – Subarray requirements.

Parameters	Value
Carrier Frequency	26 GHz
Bandwidth*	BW > 7%
Coverage distance (R)	200 m
Subarray gain	≥ 10 dBi
Feeding network	fixed ABFN (for N antenna elements)

*Referred to both, impedance and pattern shape bandwidths

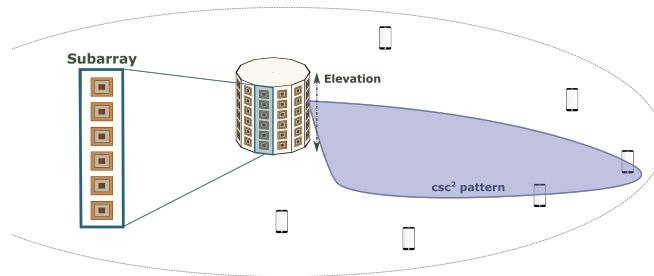


Figure 2.20 – Subarray with required csc^2 pattern in elevation

2.2.4 Multibeam antenna and DBFN requirements

In the proposed antenna architecture, the digital beamforming network (DBFN) should consist of M transceivers, controlling an equal number of subarrays for enabling beamsteering along 360° in azimuth. Hence, the DBFN operates in the azimuth plane (see Figure 2.21) and it should allow beamforming towards the desired direction, with a specified beamwidth. Additionally, in order to achieve spatially orthogonal beams with a relatively small interference among them, their sidelobe level (SLL) should be minimum. The antenna requirements in azimuth are organized in Table 2.8.

This, together with the uniformly distributed power in elevation should provide omnidirectional coverage along the cell radius. Besides, the proposed MBA architecture provides suitable hardware to enable MIMO techniques.

Based on the antenna configuration and the design requirements obtained in this chapter, the

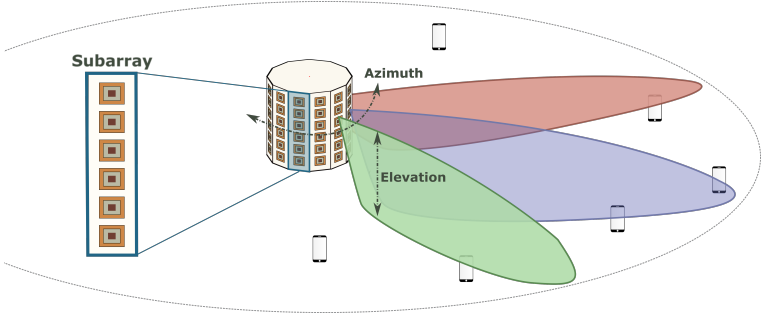


Figure 2.21 – Antenna array with multibeam forming capabilities in azimuth

Table 2.8 – Multibeam antenna requirements

Parameters	Value
Carrier Frequency	26 GHz
Bandwidth*	BW > 7%
Coverage distance (<i>R</i>)	200 m
Transmitter gain	≥ 10 dBi
Feeding network	DBFN (for <i>M</i> subarrays)
Radiation pattern in azimuth	Steerable in azimuth (for a desired target, beamwidth and SLL)

*Referred to both, impedance and pattern shape bandwidths

synthesis, design and implementation of the proposed antenna are covered in Chapters 3-5

3 Synthesis of the hybrid beamforming network

This chapter presents the synthesis of the proposed hybrid beamforming network (HBFN) according to a set of required constraints in both planes, elevation and azimuth. The proposed algorithms in both cases are tested using analytical antenna arrays based on the radiation pattern of a conventional patch antenna. Key parameters influencing the HBFN performance, given the defined set of constraints, are investigated. This is preceded by an introduction to the recently considered hybrid beamforming architectures for mm-Waves communications and an overview of the different antenna synthesis methods of interest in the studied scenario.

3.1 Introduction to hybrid beamforming architectures

As mentioned in Chapter 2, hybrid beamforming architectures have been proposed as a compromise to enable mm-Waves communications with the currently power-affordable and available RF technology. Hybrid beamforming architectures are mainly divided into two types: fully connected and partially connected [100]. In the fully connected architecture, all the RF chains are connected to all the antennas, while in the partially connected case, each RF chain is connected to a group of antennas (see Figure 3.1).

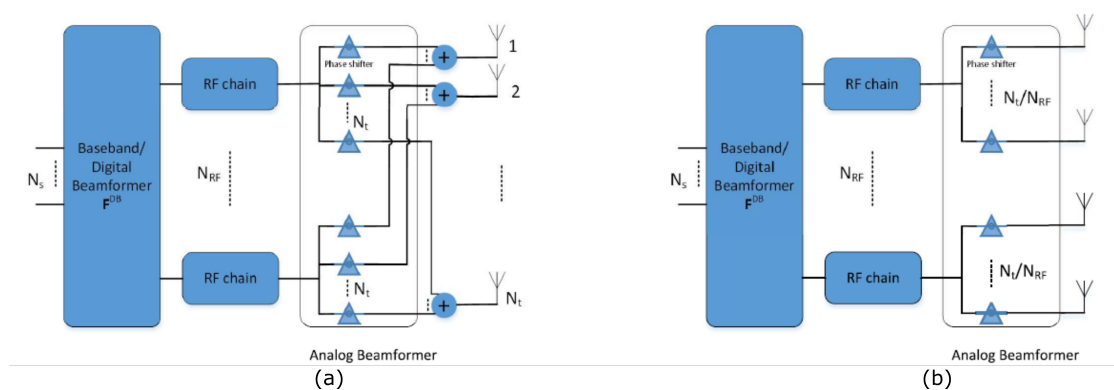


Figure 3.1 – HBFN architecture in mm-Waves systems a) fully connected b) partially connected [100]

Under the same conditions, fully connected architectures contain $N_T \times N_{\text{RF}}^2$ signal processing paths, while in partially connected architectures $N_T \times N_{\text{RF}}$ paths are possible (with N_T being the number of transmit antennas and N_{RF} the number of RF chains). On the other hand, neglecting transmission line losses, the fully connected architecture presents a beamforming gain N_{RF} times higher than the partially connected one. The study of hybrid beamforming architectures has been based on evaluating this complexity-gain trade-off with the objective of enabling an adequate performance (close to fully-digital architectures) with the smallest possible hardware and signal processing complexities.

An exhaustive description of the recently proposed hybrid architectures is given in [57], [100]–[102]. Their main conclusions are summarized herein:

- In partially-connected architectures, increasing the number of antennas per RF chains is a recommended technique to overcome their performance loss with respect to fully-connected architectures.
- Fully-connected architectures can only approach a near-optimal performance if the number of RF-chains is slightly larger than the number of data streams. It is suggested that for a performance similar to fully digital schemes, the number of RF chains should be twice the number of data streams.
- In ideal scenarios (ideal transceivers), fully connected schemes present higher Spectral Efficiency (SE) than sub-connected architectures given the higher degrees of freedom in the RF domain. However, sub-connected schemes show to be more energy efficient due to its simplified architecture. However, these results are inconclusive since more realistic scenarios need to be tested. The authors of [102] noted that the lack of knowledge about the mm-Waves transceivers imperfections prevents the proper estimation of its effect in the SE degradation in the studied beamforming architectures. Taking that into account, the estimation of the Energy Efficiency (EE)-Spectral Efficiency (SE) trade-off has been suggested as a good way to investigate the optimal number of RF chains achieving the maximal EE for any given SE constraints.
- In order to alleviate signalling overhead and processing complexity characteristic to fully-connected architectures, a new beamforming scheme has been proposed in [103] (shown in Figure 3.2 a)) where virtual sectors are created for independently precoding/-combining different groups of users.
- In [104], [105], the use of hybrid beamforming architectures based on switches instead of phase shifters is proposed (see Figure 3.2 b)), presenting a considerable reduction of consumed power when both schemes are compared with equal number of transceivers.
- The optimal number of transceivers and antennas in a hybrid beamforming scheme can be obtained considering the required multi-user channel capacity. With that aim, using the Singular Value Decomposition (SVD) of the matrix containing beamforming weights and channel information has been suggested in [106], [107].

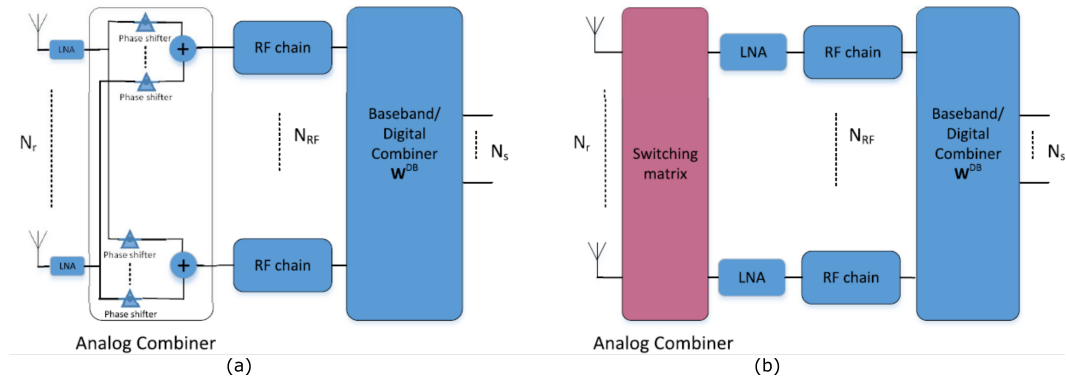


Figure 3.2 – Fully connected HBFN a) with phase shifters b) with switches[100]

Substantial research has been devoted to the design of hybrid beamforming architectures, but the majority of the reviewed literature is still not targeting realistic environments. Various significant open questions thus require further investigation.

3.2 Antenna pattern synthesis

3.2.1 Analytical methods

Analytical antenna pattern synthesis methods can be classified into three main categories:

- Nulling theory, where patterns with nulls in the desired direction are required. This can be accomplished via *Schelkunoff* method.
- Beam shaping, where a desired distribution in the main pattern beam is desired. This can be obtained using *Fourier transform* and *Woodward-Lawson* methods.
- Sharp pencil beams with low SLL. Usually, binomial method, *Dolph-Tschebyscheff* method and *Taylor line-source* are used to produce narrow beams with low SLL.

A detailed description of these methods can be found in antenna textbooks, see for instance [60], [108].

3.2.2 Numerical methods

Most of the analytical methods are limited to uniformly spaced arrays of isotropic antenna elements, preventing the inclusion of mutual coupling in the optimization process. Compared to them, numerical methods can consider a higher variety of problems such as antenna elements with different patterns, with arbitrary array grid and beam shape constraints. Some of the most typically mentioned numerical techniques in recent antenna pattern synthesis literature are *Iterative Fast Fourier*, *Iterative Sampling* and *Alternative Projection* [109]–[117].

In the majority of these techniques, obtaining an optimum solution is not ensured. For instance, the methods based on *Alternative Projections* [117] may reach a local minimum if a good reference or starting point is not used. Some other deterministic synthesis techniques inspired on the *Density Taper Procedures* have been proposed in [118]–[120]. Although they require a priori knowledge of an optimal reference point, these techniques have been used for effectively solving optimization problems with a high number of unknowns.

3.2.3 Global optimization methods

Optimization methods based on *Genetic Algorithms*, *Particle Swarm*, *Simulated Annealing*, *Differential Evolution* and *Branch-and-Bound* have been used to find a global optimum in various antenna array pattern synthesis problems [121]–[123]. Apart from the benefits of reaching good results, these methods have shown to be flexible and effective when little is known about the optimization scenario. However, it has been suggested that they are used when the problem size is relatively small since their computational and time burden increases rapidly with the number of unknowns and reaching a global solution may not be longer guaranteed.

3.2.4 Methods based in convex optimization

Using convex optimization to solve an antenna pattern synthesis problem can ensure reaching the global solution as demonstrated in [124]. Until recently this technique was considered computationally demanding, but the increased computer power, the development of powerful algorithms and optimization tools have enabled solving not only larger problems but also at a higher speed. This has made possible the use of real-time convex optimization in antenna pattern synthesis problems [125]. Additional benefits of using this optimization technique include the possibility of using arbitrary array configurations, different antenna elements, including mutual coupling and polarization in the optimization algorithm [126], [127].

A convex optimization problem has the form

$$\begin{aligned} & \text{minimize } f_0(x) \\ & \text{subject to } f_i(x) \leq b_i \quad i = 1, \dots, m, \end{aligned} \tag{3.1}$$

where the functions $f_0, \dots, f_m : \mathbb{R}^n \rightarrow \mathbb{R}$ are convex, i.e., satisfy

$$f_i(\alpha x + \beta y) \leq \alpha f_i(x) + \beta f_i(y) \tag{3.2}$$

for all $x, y \in \mathbb{R}^n$ and all $\alpha, \beta \in \mathbb{R}$ with $\alpha + \beta = 1$, $\alpha \geq 0$, $\beta \geq 0$.

The inequality in Equation 3.2 is graphically represented in Figure 3.3.

A typical antenna pattern synthesis problem with constraints specifying the beam target and

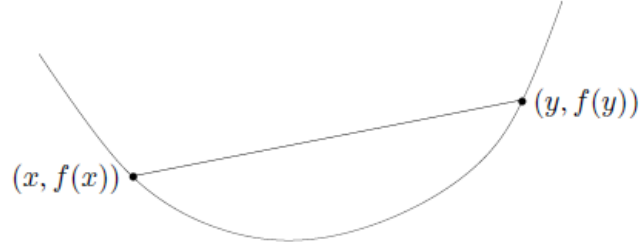


Figure 3.3 – Convex function [128]

SLL limit can be written in a convex formulation. Considering the weighted output signal

$$y_s = w^T A \quad (3.3)$$

where w is the complex weighting vector applied to the array response A , the optimization problem can be expressed as the minimization of the output signal at all directions, except from the target. Accordingly, the problem's objective function consists of minimizing the expected value of the power of y_s , that is $\min E \{|y_s|^2\}$, which can be written as

$$\min E \{|y_s|^2\} = \min E \{|w^T A|^2\} = \min E \{w^T R_{AA} w\}, \quad (3.4)$$

where R_{AA} is the correlation matrix of the array response A .

In addition, the desired beam target and SLL threshold are included in the problem constraints as described in Equations 3.5:

$$\begin{aligned} C_{\text{tar}} : |A_{\text{tar}} w| &= 1 \\ C_{\text{SLL}} : |A_{\text{SLL}} w| &\leq \varepsilon \end{aligned} \quad (3.5)$$

with ε being the SLL threshold (for instance -20 dB under the main lobe), and A_{tar} and A_{SLL} the array response at the target and SLL regions, respectively (see Figure 3.4).

Taking into account that the objective function in Equation 3.4 is convex and the constraints are affine (equality constraint) and convex (inequality constraint), we can affirm that the optimization problem is convex. Convex optimization problems expressed in a convex programming manner can be solved using the CVX toolbox, which is a Matlab-based modeling system for solving this type of problem via interior point optimization [128], [129]. However, most of the pattern synthesis problems are not intrinsically convex. For example, if the problem of Equations 3.4 and 3.5 is additionally constrained adding a low bound for limiting the pattern beamwidth, as described in Equation 3.6 and represented in Figure 3.4.

$$C_{\text{HPBW}} : \rho_1 \leq |A_{\text{HPBW}} w| \leq \rho_2 \quad (3.6)$$

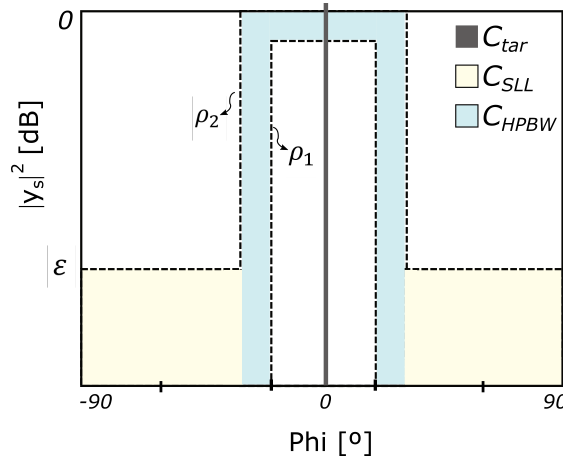


Figure 3.4 – Lower and upper bounded constraint mask

Different techniques for transforming this kind of non-convex problem into a convex formulation have been presented in [130], [131]. Other authors have proposed introducing approximations/relaxations [132]–[134] or solving iterations of a convex optimization problem [135], [136] In [137] and [138] non-convex optimization problems have been iteratively solved as a sequence of convex optimization problems. After comparing this approach to solutions obtained through global and deterministic algorithms, the iterative method was shown to be an effective solution to this kind of problem. Another technique for avoiding the non-convexity of antenna pattern synthesis problems was proposed in [139]–[141], where conjugate beamforming symmetric weights were used with the objective of expressing the array factor formula as a real function. This transforms the lower bound constraint into an affine function which allows the problem to be solved via convex optimization. Given the imposed symmetric weights constraint, a global solution may not be found, but this solution represents a good compromise between performance and algorithm costs.

On the other hand, the aforementioned synthesis methods have been commonly developed using analytical or isotropic antenna elements, thus neglecting real optimization scenarios. Including real antenna patterns and mutual coupling is crucial in antenna synthesis problems for ensuring appropriated results. With this aim, a technique proposed in [126] uses 3D-FEM to describe the antenna element used in the array synthesis. In addition, the antenna array is characterized based on Floquet modal and general scattering matrix analysis for working with finite arrays in infinite array environments. This allows to inherently include mutual coupling in the optimization problem formulation.

Considering the studied antenna pattern synthesis literature, we can say that there still exists a gap between proposed convex optimization methods and their effective implementation in realistic antenna scenarios, with only a small number of proposals combining in some manner electromagnetic analysis with the proposed optimization algorithms. However, convex optimization has demonstrated to be a suitable technique to solve antenna pattern synthesis

problems, given their effectiveness in addressing such problems at low computational costs, together with the readily programming optimization tool and the vast available literature.

In this work, iterative convex optimization is used to obtain the synthesized weighting vectors in both, the csc^2 subarray pattern in elevation and the multibeam forming in azimuth. The next sections describe the description of both problems, together with some exemplification that analytically validates the proposed techniques.

3.3 Synthesis of the proposed Hybrid BFN

As specified in Chapter 2 the proposed antenna architecture consists of $M \times N$ antennas fed by a HBFN. M subarrays (each of them containing N antenna elements) are concentrically arranged as shown in Figure 2.17. The proposed HBFN consists of a DBFN controlling M RF chains and subarrays for generating multiple beams in azimuth. In addition, the ABFN feeding each subarray should guarantee a csc^2 pattern shape in elevation. The diagram of the proposed HBFN is shown in Figure 3.5. A subarray fed by an ABFN is represented by a dashed line box. Additionally, each subarray is connected to a dedicated RF chain and controlled by the DBFN.

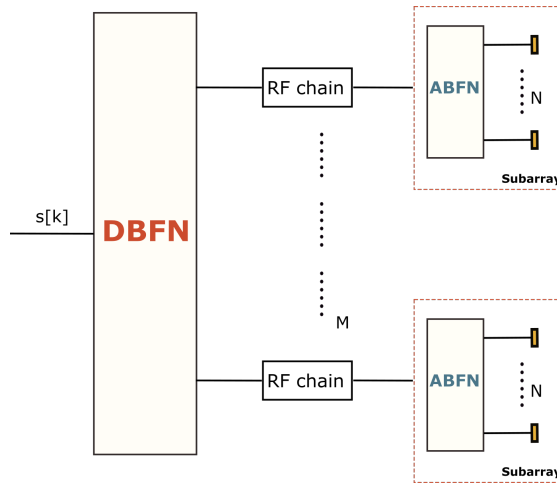


Figure 3.5 – Diagram of the proposed HBFN

3.3.1 Optimization problem in elevation. csc^2 subarray

In order to obtain a uniformly distributed received power between the cell edge and the mast shadow, the subarray pattern in elevation should approximate a csc^2 shape (as shown in Figure 2.19). The excitation weights of each element enabling such a pattern were obtained using a least-squares optimization scheme.

The weighting vector w_0 that minimizes the difference between the subarray pattern in elevation $AP_{sub} = A_{sub} \cdot w$ and the desired pattern mask Δ_{sub} , can be obtained by solving the

least squares problem

$$w_0 = \arg \min_w \|\Delta_{sub} - A_{sub} \cdot w\|^2$$

such that $\Delta_{sub} = \begin{cases} M_{csc^2} & \text{for } \theta \in \theta_{csc^2} \\ M_{SLL} & \text{for } \theta \in \theta_{SLL} \end{cases}$ (3.7)

The mask Δ_{sub} includes two main constraints as shown in Figure 3.6: i) the main beam shape, which is a csc^2 function (M_{csc^2}) over the angular region θ_{csc^2} , and ii) the maximum SLL that is represented by an upper bounded function M_{SLL} over the θ_{SLL} region (Figure 3.6).

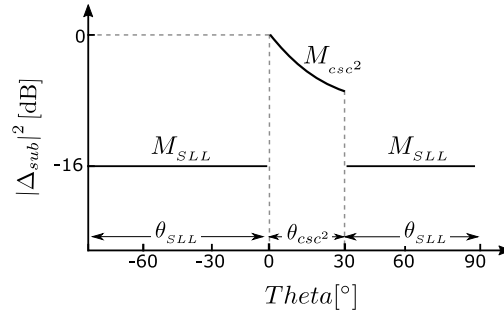


Figure 3.6 – csc^2 mask

The matrix A_{sub} in Equation 3.8 represents the radiated field $E_n(\theta, \phi)$ of each subarray antenna element, i.e.

$$A_{sub_{[n,\theta\phi]}} = \begin{bmatrix} E_{1j} e^{1j\psi(\theta,\phi=-90,-180)} & \dots & E_{1j} e^{1j\psi(\theta,\phi=-90,180)} \\ \vdots & \ddots & \vdots \\ E_{Nj} e^{Nj\psi(\theta,\phi=90,-180)} & \dots & E_{Nj} e^{Nj\psi(\theta,\phi=90,180)} \end{bmatrix}_{n=1:N}$$
 (3.8)

where n refers to the n_{th} antenna element with $n = [1, \dots, N]$, θ and ϕ represent the considered directions in elevation and azimuth planes respectively, with $\theta \in [-90^\circ, 90^\circ]$ and $\phi \in [-180^\circ, 180^\circ]$, and ψ is the relative progressive phase between elements.

ABFN performance analysis

The ABFN performance is evaluated in this section using analytical subarrays based on a conventional patch antenna, as depicted in Figure 3.7. The effect of varying the number of antenna elements (N) in the subarray, the distance (d) between them and the antenna element beamwidth (HPBW) is investigated.

Impact of the number of elements

In order to evaluate the ABFN performance when varying the number of elements N , various subarrays of 5, 6 and 7 antenna elements were analytically built. The influence of the number

of elements in the subarray and the antenna element beamwidth was studied regarding the csc^2 mask constraint (see Figure 3.6).

For this evaluation, all elements are considered identical and the matrix A_{sub} is simply obtained as

$$A_{sub_{[n,\theta\phi]}} = E_0 \begin{bmatrix} e^{1j\psi_{(\theta,\phi=-90,-180)}} & \dots & e^{1j\psi_{(\theta,\phi=-90,180)}} \\ \vdots & \ddots & \vdots \\ e^{Nj\psi_{(\theta,\phi=90,-180)}} & \dots & e^{Nj\psi_{(\theta,\phi=90,180)}} \end{bmatrix}_{n=1:N} \quad (3.9)$$

where E_0 is the pattern of an element.

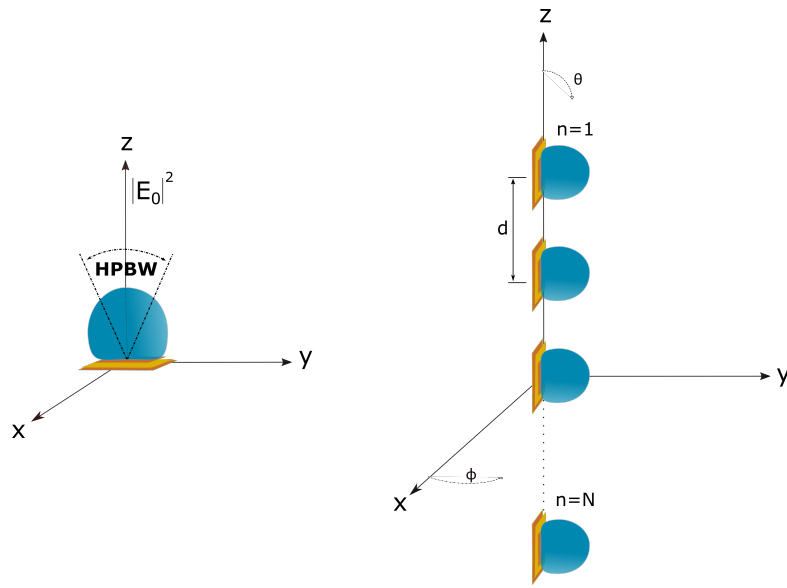


Figure 3.7 – Diagram of a generic analytical linear array illustrating the subarray in elevation

The first evaluated set up consists of a patch antenna of half power beamwidth (HPBW) = 50° replicated in a linear array of $N = [5, 6, \text{ and } 7]$ elements separated at a distance $d = 0.5\lambda$. The csc^2 pattern mask (represented in gray in Figure 3.8) is defined to present maximum radiation at broadside and a main beam with csc^2 pattern shape along 50° approximately. The mask SLL limit has been defined at -16 dB. Figure 3.8 shows the synthesized pattern AP_{sub} .

Figure 3.8 shows that the ABFN synthesis for a linear array with a higher number of elements presents lower grating lobes. Additionally, the main beam constraint is similarly fulfilled in the three studied linear arrays. Given that a higher number of elements requires a larger feeding network, the selection of the number of elements should be driven by a compromise between the ABFN performance, and reasonable antenna complexity and feeding network losses.

Impact of the distance between antenna elements

The influence of the distance (d) between antenna elements in the ABFN synthesis was studied.

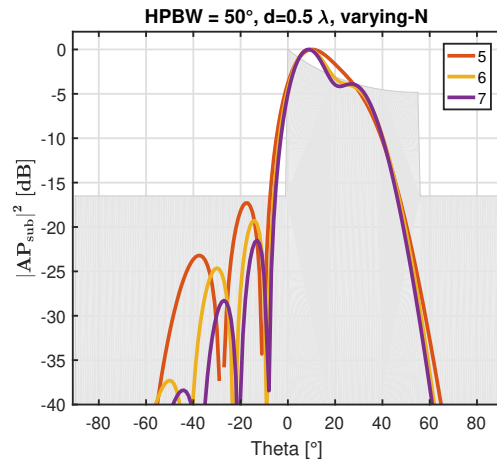


Figure 3.8 – Synthesized pattern for arrays with different number of elements N . Legend refers to N

Three linear antenna arrays formed by 6 antenna elements separated at $d = [0.5\lambda, 0.6\lambda$ and $0.7\lambda]$ and each having a 60° beamwidth were investigated (see Figure 3.9).

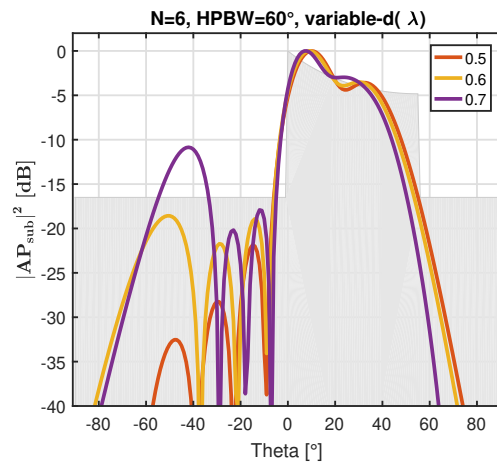


Figure 3.9 – Synthesized pattern for arrays with different distances between elements $d(\lambda)$. Legend refers to $d(\lambda)$

As expected, a smaller distance between elements provides a more adequate synthesized pattern when compared to the csc^2 pattern mask.

Impact of the antenna element beamwidth

The third evaluated parameter in the ABFN performance is the antenna element beamwidth (HPBW). In this case, linear arrays of 6 elements at a distance $d = 0.5\lambda$ with antenna elements presenting HPBW = $[40^\circ, 50^\circ$ and $60^\circ]$ were analyzed.

As shown in Figure 3.10, an antenna element with wider beamwidth may provide a synthesized

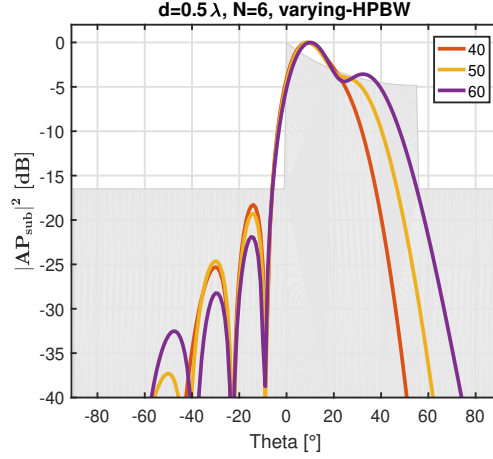


Figure 3.10 – Synthesized patterns for arrays with different beamwidths (HPBW). Legend refers to HPBW in degrees

pattern AP_{sub} that exhibits better agreement with the required mask. Hence, a linear array with a relatively small number of elements, each presenting broad beamwidth may be sufficient for fulfilling the ABFN synthesis constraints. These parameters are taken into account in the subarray implementation in Chapter 4.

3.3.2 Optimization problem in azimuth. Sectorial antenna

In this sub-section, we aim at synthesizing the digital beamforming network, such that it generates a matrix $U_{M \times I}(\theta_i, \phi_j)$ with column-wise distributed weighting vectors $u_{M \times 1}(\theta_i, \phi_j)$ that fulfill a set of constraints associated to the multibeam forming antenna capacities.

For the sake of simplification, the synthesized weighing vector $u_{M \times 1}(\theta_i, \phi_j)$ for each set of constraints is denominated u_0 . Accordingly, the synthesized radiation pattern is $AP_{MBA} = A_{MBA} \cdot u_0$, where A_{MBA} is the radiated field $A_{sub}(\theta, \phi)$ of each subarray (Equation 3.10).

$$A_{MBA[n, \theta \phi]} = \begin{bmatrix} A_{sub1j} e^{1j\psi(\theta, \phi = -90, -180)} & \dots & A_{sub1j} e^{1j\psi(\theta, \phi = -90, 180)} \\ \vdots & \ddots & \vdots \\ A_{subMj} e^{Mj\psi(\theta, \phi = 90, -180)} & \dots & A_{subMj} e^{Mj\psi(\theta, \phi = 90, 180)} \end{bmatrix}_{m=1:M} \quad (3.10)$$

In the DBFN synthesis problem formulation, four constraints have been primarily considered. The first constraint C_1 consists of targeting the radiation pattern maximum at a certain direction θ_i, ϕ_j . In addition, the beam should cover a certain area specified by the radiation pattern beamwidth. This is represented by constraint C_2 . Finally, in order to minimize interference, beams should be spatially orthogonal. That is, beams could be simultaneously active but the maximum of the beam pointing at θ_i, ϕ_j should overlap with the minimum of the rest of the

beams. This is represented by the third constraint C_3 , and it will be addressed as the beam on θ_i, ϕ_j having a SLL below a specified threshold. The three regions defined by constraints C_1 (A_{tar}), C_2 (A_{HPBW}) and C_3 (A_{SLL}) are used to build the desired mask function (shown in Figure 3.11).

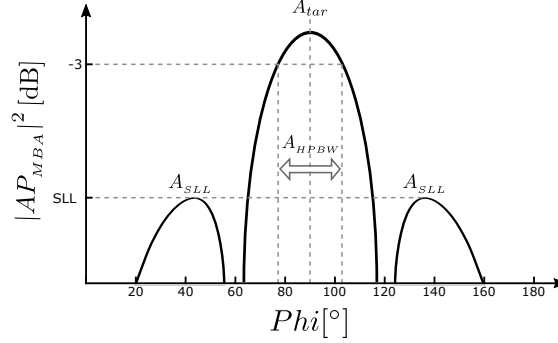


Figure 3.11 – Diagram of the regions defined by A_{tar} , A_{HPBW} and A_{SLL}

A fourth constraint C_4 was added in order to limit the network power distribution and thus avoid the use of active components in the antenna array ($C_4: \|u\|_1 < 1$).

The DBFN synthesis problem can be initially formulated as

$$\begin{aligned} & \text{find } \mathbf{u}_0 \\ & \text{such that } \begin{cases} C_1: & A_{tar} \mathbf{u} = 1 \\ C_2: & \text{abs}(A_{HPBW} \mathbf{u}) \geq \frac{1}{2} \\ C_3: & \text{abs}(A_{SLL} \mathbf{u}) < \epsilon \\ C_4: & \|\mathbf{u}\|_1 < 1 \end{cases} \end{aligned} \quad (3.11)$$

With the objective of transforming the problem described in Equation 3.11 into a convex formulation, constraints C_1 - C_3 have been integrated into a mask Δ_{MBA} (as shown in Figure 3.12) where the synthesized radiation pattern is:

- Upper and lower bounded over the main beam region, considering C_1 and C_2 .
- Upper bounded over the SLL region, considering C_3 .

That is,

$$\Delta_{MBA} = \begin{cases} |AP_{MBA}(u)| \leq M_{up} \\ |AP_{MBA}(u)| \geq M_{dw} \end{cases} \quad (3.12)$$

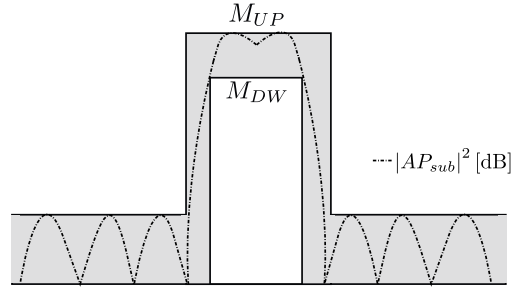


Figure 3.12 – Multibeam antenna mask integrating constraints C_1 , C_2 and C_3

The problem defined in Equation 3.11 has been thus re-formulated as

$$\begin{aligned} \min_u \quad & \|A_{MBA} u - \Delta_{MBA}\|_2 \\ \text{subject to} \quad & \|u\|_1 < 1 \end{aligned} \quad (3.13)$$

The proposed optimization problem is solved using iterative convex optimization based on the CVX toolbox. Two steps were added to the proposed algorithm since they demonstrated to be crucial for attaining a good local optimum:

- The initialization pattern $AP_{MBA}^{i=0}$ consists of a beam with a relatively narrow beamwidth.
- The phase of $AP_{MBA}^{i=0}$ was applied to the mask, i.e. $\Delta_{MBA} e^{j\angle AP_{MBA}^{i=0}}$.

After each iteration, the phase of the locally optimal pattern is applied to the mask. This last step consists of a projection derived from *Alternating Projection* algorithms in order to facilitate an effective convergence [142]. This process is repeated for a certain number of iterations or until a threshold condition is fulfilled. A generalization of the algorithms is summarized in the flow diagram in Figure 3.13.

DBFN performance analysis

The DBFN operating on the sectorial antenna in azimuth was studied in different analytical scenarios. In this analysis, each subarray has been represented by the radiation pattern of a conventional patch antenna (as depicted in Figure 3.14). The goal was to identify how the desired multibeam antenna performance is influenced by the antenna architecture, namely by the variation of the number of sectors (M) and the sector width (sub_a). While the selection of these parameters has an impact on the coupling between subarrays—crucial to meet the desired multibeam forming antenna capabilities—their practical implementation is limited by the antenna technology, the fabrication complexity and cost, which should be taken into account in the definition of the antenna architecture. The studied parameters in this section are included in Figure 3.14.

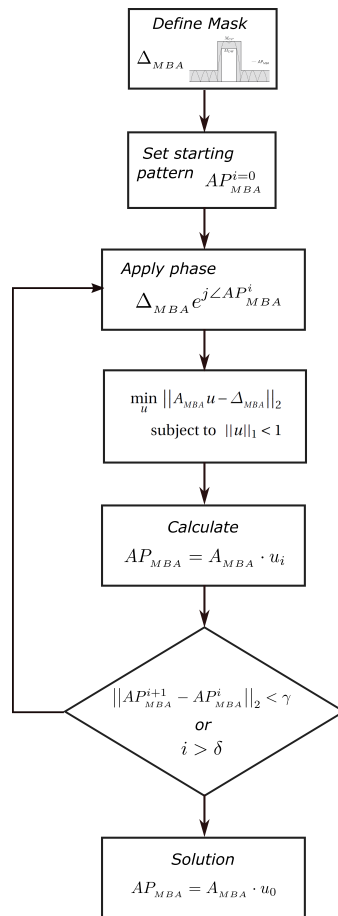


Figure 3.13 – Flow diagram of the DBFN synthesis algorithm

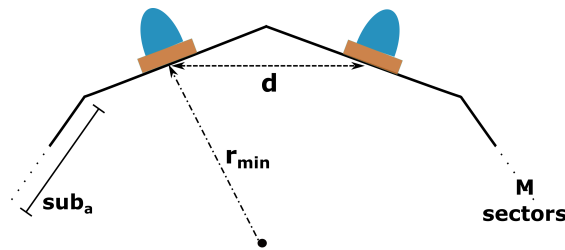


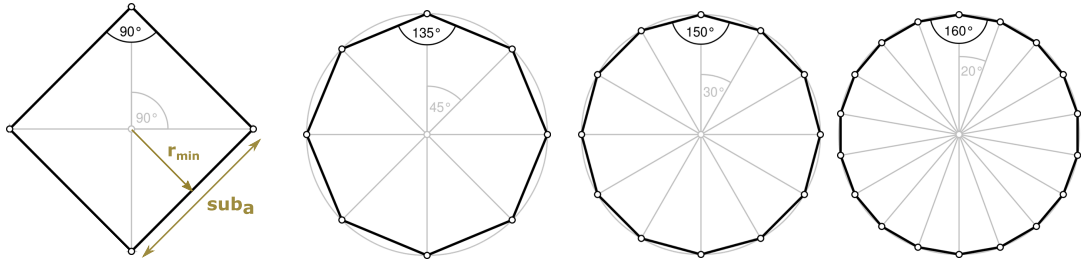
Figure 3.14 – Diagram of a generic sectorial antenna illustrating the MBA in azimuth

For a given subarray width (sub_a) and M number of sectors, r_{min} is the minimum radius of the sectorial antenna and d is the minimum distance between subarrays.

Number of sectors

In order to study the influence of the number of sectors (M) in the DBFN performance, four antenna arrays consisting of 4, 8, 12 and 18 sectors were analytically arranged (see Figure 3.15).

In general, the array response of the sectorial antenna can be built by both rotating and


 Figure 3.15 – Antenna architectures for different number of sectors M

translating the subarray matrix $AP_{sub}(\theta_i, \phi_j)$ obtained in the previous section. However, for the present evaluation it is sufficient to represent each sector by an analytical patch radiation pattern as depicted in Figure 3.16.

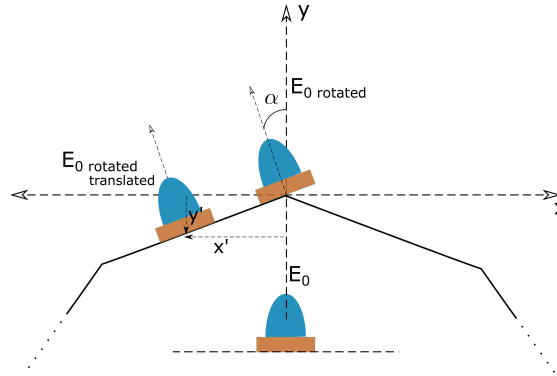


Figure 3.16 – Sketch illustrating the rotation and translation of the antenna elements forming a sectorial array

The sectorial antenna array response can be written as:

$$A_{MBA[m,\theta\phi]} = \begin{bmatrix} E_{01j} e^{1j\psi(\theta,\phi=-90,-180)} & \dots & E_{01j} e^{1j\psi(\theta,\phi=-90,180)} \\ \vdots & \ddots & \vdots \\ E_{0Mj} e^{Mj\psi(\theta,\phi=-90,-180)} & \dots & E_{0Mj} e^{Mj\psi(\theta,\phi=-90,180)} \end{bmatrix}_{m=1:M} \quad (3.14)$$

Table 3.1 summarizes the minimum radius (r_{min} defined in Figure 3.14) to geometrically arrange the specified number of sectors, considering that the subarray width is 8mm ($sub_a = 8$ mm). The distance d between subarrays for each configuration is also included.

Table 3.1 – Minimum radius and distance between subarrays for a given number of sectors

Number of sectors	4	8	12	18
r_{min} [mm]	4	9.66	14.93	22.69
$d(\lambda)$	0.49	0.64	0.67	0.68

In an antenna array, a distance between elements smaller than lambda ($d < \lambda$) is recommended if a radiation pattern with low grating lobes is desired [60]. This is one of our DBFN synthesis requirements, represented in constraint C_3 . Given the $d(\lambda)$ values in Table 3.1, an antenna of 4 sectors represents a more attractive solution than rest of the studied sectorial antennas. Nevertheless, the overall DBFN performance should be also evaluated considering the positive coupling between the antenna elements and including the rest of the constraints in the studied scenario. With that aim, the DBFN was computed for the antenna configurations in Figure 3.15 subject to the set of constraints S_1 .

$$S_1 = \begin{cases} C_1: & \varphi_{\text{tar}} = [90^\circ, 105^\circ, 120^\circ, 135^\circ] \\ C_2: & \varphi_{\text{HPBW}} = 40^\circ \\ C_3: & \varphi_{\text{SLL}} = -13 \text{ dB} \end{cases} \quad (3.15)$$

Figure 3.17 shows the synthesized pattern of the four studied antenna configurations when targeting 90° , 105° , 120° and 135° (Figure 3.17 a, b, c, d respectively).

For the studied set of constraints, the synthesized pattern is closer to the constraint mask when M increases. This is due to the fact that an antenna with a high number of sectors is comparative to the circular antenna geometry allowing wider scan angles. On the other side, a high M implies increasing the number of subarrays and RF chains, thus yielding a more costly antenna design. A cost-performance compromise should be made in the selection of this design parameter.

Sector width

The sector width (sub_a) is also linked to the distance between subarrays and hence it influences the DBFN synthesis. In order to study this, a 12-sector antenna was formed with subarrays of 6 mm, 18 mm and 30 mm width as depicted in Table 3.2. The set of constraints S_2 was implemented in this evaluation.

Table 3.2 – Minimum radius and distance between subarrays for a given subarray width

Sector width (sub_a) [mm]	6	18	30
r_{min} mm	11.2	33.59	55.98
$d(\lambda)$	0.5	1.51	2.51

$$S_2 = \begin{cases} C_1: & \varphi_{\text{tar}} = [90^\circ, 97^\circ, 105^\circ] \\ C_2: & \varphi_{\text{HPBW}} = 40^\circ \\ C_3: & \varphi_{\text{SLL}} = -13 \text{ dB} \end{cases} \quad (3.16)$$

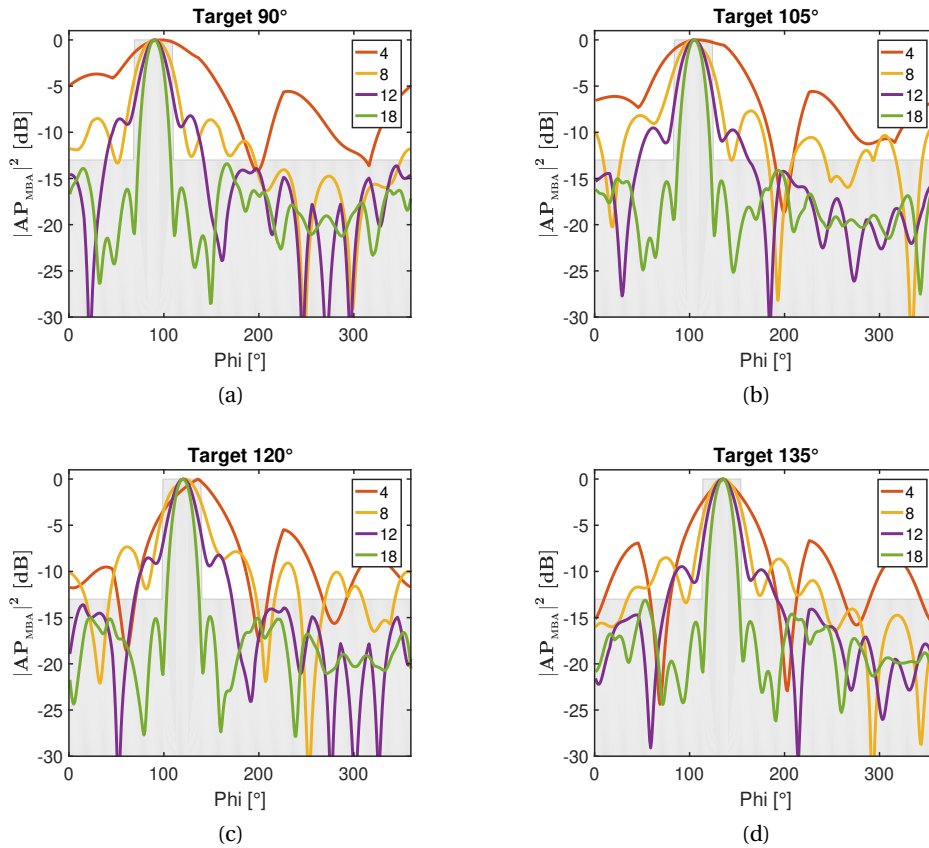


Figure 3.17 – Synthesized patterns for different antenna architectures, given by a variation of the number of elements, targeting a) 90°, b) 105°, c) 120° and d) 135°. Legend refers to number of sector (M)

The synthesized radiation pattern in a 12 sectors-antenna with 6 mm, 18 mm and 30 mm is shown in Figure 3.18 a), b) and c) respectively.

In the studied set of constraints S_2 , a narrower subarray ($sub_a = 0.6$ mm) provided a synthesized pattern closer to the desired mask. This result is expected since a smaller sub_a guarantees a smaller distance between subarrays. Although in the subarray implementation, this parameter is limited by the actual design technology, selecting a subarray architecture that enables a small sub_a should be taking into account for enhancing the DBFN flexibility.

In this chapter, the HBFN has been synthesized and its performance has been evaluated in various scenarios. These outcomes have been considered in the antenna design stage of this work:

- From the performed analysis in elevation, a wider antenna element beamwidth provided more flexible beamforming capabilities. This can be evaluated before increasing the number of elements, hence the antenna cost and complexity.

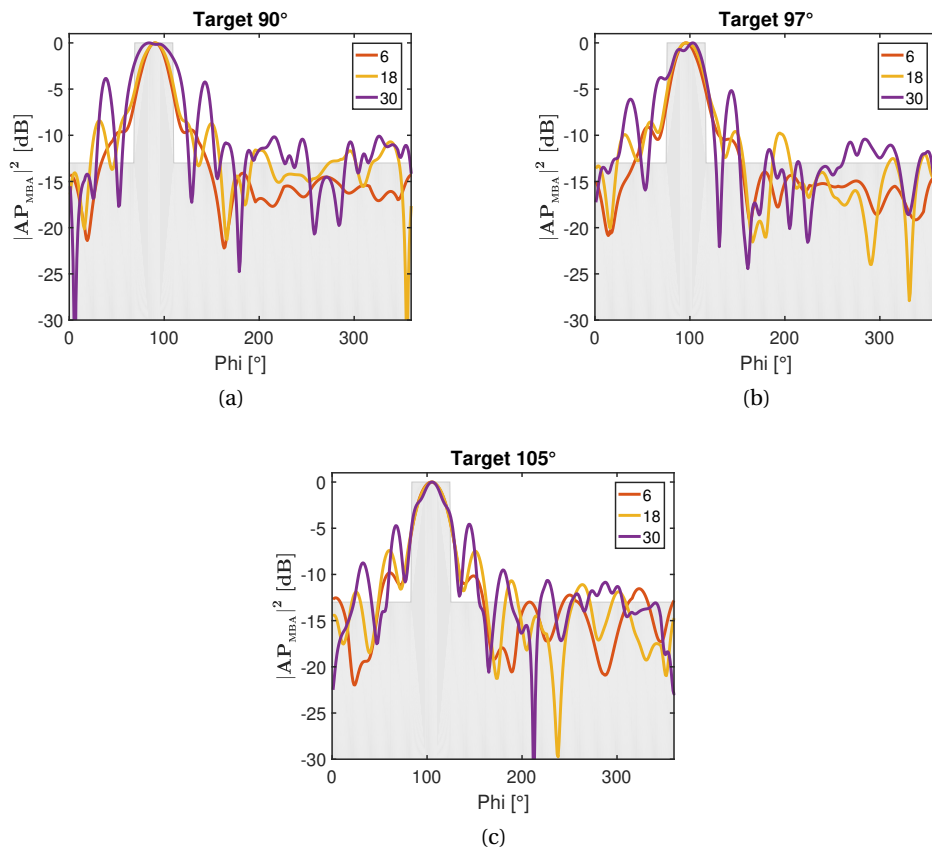


Figure 3.18 – Synthesized patterns for different antenna architectures, given by a variation of the subarray width, targeting a) 90° , b) 97° and c) 105° . Legend refers to subarray width (sub_a) in mm

- The distance between elements $d(\lambda)$ is a crucial parameter in the HBFN synthesis. In elevation, a smaller distance between elements in the subarray, and in azimuth, a smaller subarray width sub_a showed synthesized patterns that better fit the constraint mask.
- Although a smaller number of sectors implies a smaller distance $d(\lambda)$ between subarrays, the positive interference between array elements also needs to be taken into account. Increasing the number of sectors in the DBFN synthesis has shown a better correlation between the synthesized pattern and the constraint mask, but it involves increasing the antenna complexity and cost. A compromise between the number of sectors and the beamsteering capabilities should be considered.

4 Cosecant-squared pattern shaped subarray

In this chapter, a subarray with csc^2 pattern shape in elevation is designed and implemented. The subarray specifications considered in Chapters 2 and 3 are primarily summarized and the state of the art on csc^2 antennas is briefly described to establish the starting point in our design. The subarray design is addressed including the description of the transmission line, the antenna element design, and the synthesis of the feeding network associated with the desired csc^2 pattern shape. The selection of the feeding network layout is explained and the design of the required feeding network components is described. The proposed subarray is finally implemented and its performance is validated through the comparison of simulation and measurement results. The fabrication process of this subarray is specified. Complementary, the dimensions of the proposed models are detailed in technical drawings provided in Appendix A.

4.1 Subarray specifications

Various design requirements associated with the subarray design have been specified in previous chapters. Given the tackled frequency band, high antenna efficiency is desired in order to mitigate the intrinsically high material losses (conductor and dielectric) at mm-Waves. This has an impact on the design of both, the subarray feeding network and the antenna element. On the other hand, the HBFN synthesis study realized in Chapter 3 showed that using a subarray antenna element with wide beamwidth and a small subarray width is suitable to attain a wider beamsteering range. These remarks, together with the calculated link budget in Chapter 2, have driven the subarray design in this work. A summary of the subarray design specifications is depicted in Figure 4.1 and Table 4.1.

We can thus say that a csc^2 efficient broadband subarray operating at 5G mm-Waves with a relatively low profile and narrow width is attractive to the studied scenario. The relatively low profile and small size constraints are additionally adequate due to the portability characteristics of the considered application.

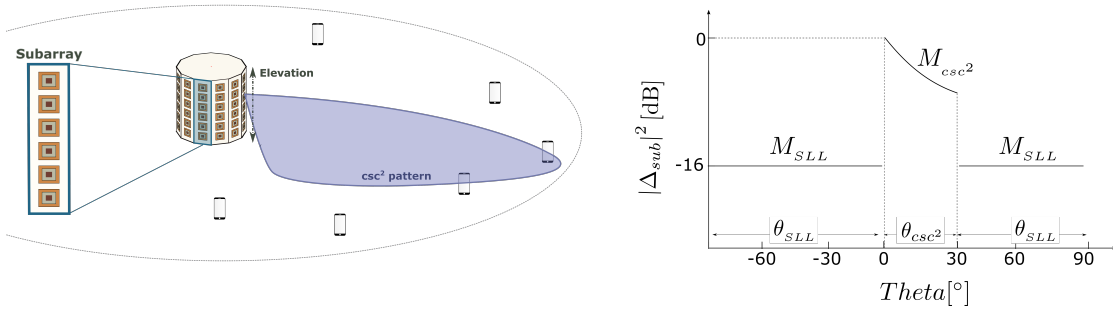


Figure 4.1 – Summary of the subarray synthesis specifications

Table 4.1 – Summary of the subarray design parameters

Parameter	Value
Carrier frequency	26 GHz
Bandwidth*	> 7%
Coverage distance (R)	200 m
Path loss exponent (n_p)	$2.22 \leq n_p \leq 2.45$
Shadowing factor (S_{σ_s})	9 dB
Transmitter power	24 dBm
Subarray gain	≥ 10 dBi
Receiver sensitivity level	-87.3 dBm
Receiver gain	5 dBi
Feeding network	fixed ABFN
Radiation pattern in elevation	csc^2

*Referred to both, impedance and pattern shape bandwidths

Recently, planar csc^2 antennas have been proposed for achieving a reduced profile, weight and fabrication cost, as well as enabling easy integration of the feeding network and the antenna elements [143]–[148]. Among them, the csc^2 planar antennas with feeding networks in a series configuration have been implemented with smaller sizes yielding smaller transmission losses, but also with intrinsically narrow bandwidth [146], [147]. On the other hand, the antennas fed by a parallel configuration usually can achieve a wider bandwidth but occupying a larger area. In that context, two subarray architectures with adequate features to be used as starting point in our design were considered: a slotted waveguide (WG) antenna and a multilayer printed structure, as shown in Figure 4.2.

A slotted WG (see Figure 4.2 a) can be designed to provide a csc^2 beam shape as presented by Gatti in [149]. By modifying the slot offset and length of a metallic WG the desired radiation pattern can be obtained. This is an interesting feature since both, the feeding network and antenna are the same structure. Nevertheless, slotted WGs are limited by a narrow bandwidth and a bulky, heavy and expensive footprint. A low-profile and low-cost subarray can be obtained using SIW technology instead, yet compromising the initial bandwidth constraint in the studied application. With this goal, the design of a slotted WG subarray for the present application was developed as part of a Master project carried out in our lab [150]. This work belongs to an ongoing investigation and thus will not be further discussed in this thesis.

The planar subarray for Ka-band space applications, shown in Figure 4.2 b), was proposed in

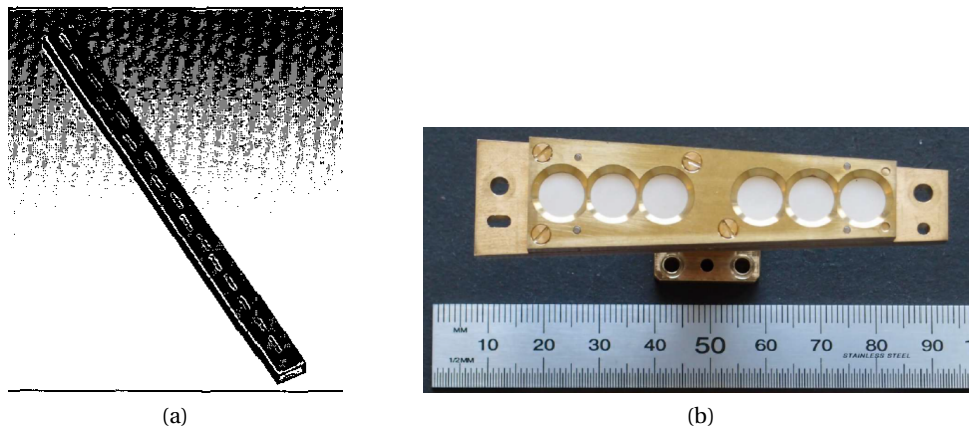


Figure 4.2 – Subarray architectures with adequate features to be used as starting point in the studied application, a) slotted WG antenna b) multilayer printed antenna

[151]. The proposed subarray is fed by a parallel feeding network with a compact design and a high antenna efficiency. These features make it a promising starting point for our project. We take some of the key principles of this solution and extend them to meet the pattern, gain, bandwidth and space requirements of the present application.

4.2 Transmission line

Microstrip or striplines are potential candidates for placing a corporate feeding network in a relatively small space, but they can become quite lossy at mm-Waves [152]–[154]. We have chosen to base the subarray feeding network on suspended stripline (SSL) technology. This transmission line consists of a stripline suspended on a substrate and shielded in an air-filled-cavity (see Figure 4.3) [155].

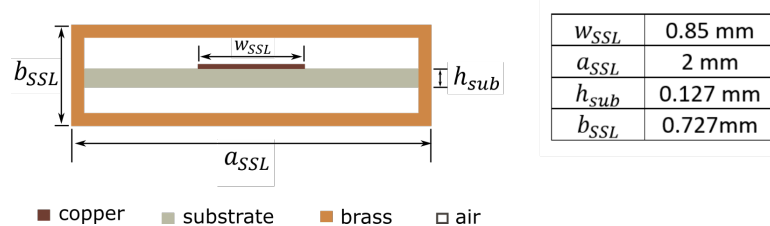


Figure 4.3 – Suspended strip line geometry

By selecting an electrically thin-low permittivity substrate, the attenuation due to dielectric material is reduced. Another advantage of this line is that the use of a shielding cavity prevents spurious radiation. SSLs are bulkier and more costly than regular printed lines but represent a good compromise for our application. With an acceptable profile, this transmission line can be confined in a relatively small area while enabling very attractive features such as low losses, low dispersion and broad bandwidth operation [156]. The SSL stripline was calculated for

enabling a 50Ω characteristic impedance, yielding a width w_{SSL} of 0.85 mm [157]. The line is mounted on Rogers Duroid (RT 6002) substrate with 0.127 mm height and permittivity of 2.94. For enabling TEM-mode only operation, the SSL width a_{SSL} is limited by the first WG TE_{10} mode, such that

$$a_{SSL} < \frac{c}{2f_c} \sqrt{1 - \frac{h_{sub}}{a_{SSL}} \left(\frac{\epsilon - 1}{\epsilon} \right)} \quad (4.1)$$

where f_c is the upper frequency limit of the studied operational bandwidth and ϵ is the substrate permittivity.

Moreover, the SSL cavity height is constrained by the structure power handling capabilities and its mechanical realization as described in [151], [155]. Considering the aforementioned designed specifications, the designed SLL cavity consists of hollow brass of 2 mm x 0.727 mm. The simulated SSL shows an effective permittivity of 2.3 and an attenuation of 0.07 dB/cm which is low compared to other printed lines as presented in [156].

4.3 Antenna element

To attain a broadband-efficient planar antenna design, the antenna consists of stacked patches [158]. The advantage of using stacked patches compared to an aperture coupled simple patch is that in the latter the aperture is resonant, which generates non-negligible back radiation. In the stacked patches structure, the required slot length is reduced due to the strong interaction between the aperture structure and the patches. The two main resonances in this structure stem from the coupling between the aperture and the bottom patch and the coupling between the patches. Accordingly, the width of both squared patches, the aperture length and the thickness of the two substrates supporting the patches are essential parameters in obtaining the adequate resonance system [159]. Additionally, in this antenna the stub and aperture lengths are adjusted to obtain an adequate antenna impedance coupling, where the stub variation modifies the reactance within an approximately constant resistance contour and the slot is inversely linked to the resistance [160].

As shown in Figure 4.4 a), both patches are suspended on thin and low-permittivity dielectric separated by layers of air. This thick and low permittivity effective substrate enables a broadband antenna operation. In addition, this technique guarantees the low losses requested in our design [161].

The slot, depicted in Figure 4.4 b), consists in a dogbone aperture. Compared to a regular rectangular slot, a dogbone slot of a smaller aperture can provide reduced back radiation, hence mitigating the field intensity within the antenna cavity. This is achieved preserving the adequate slot coupling capacities and polarization purity [162], [163].

Finally, the antenna element was shielded in a square cavity to minimize undesired mutual

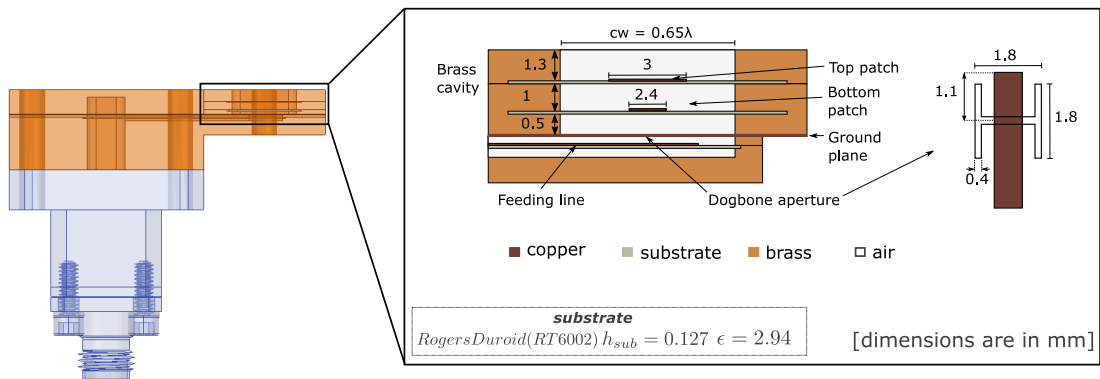


Figure 4.4 – Antenna element geometry

coupling between the subarray elements. The cavity size was chosen considering both, the minimum width to enable propagation along the operational bandwidth $cw > 0.6\lambda$ and the recommended distance ($d < \lambda$) among array elements to avoid grating lobes, yielding $cw < \lambda$. Hence, the selected square cavity is $(0.65\lambda)^2$ [60].

The described antenna element is fed by a 50Ω SSL which is accessed via a WG-to-SSL transition in order to minimize loss mismatches in the fabrication process while enabling a mechanically robust structure. In this transition, the quasi TEM mode of the SSL is obtained from the waveguide dominant mode TE_{10} and the resonating patch with dominant mode TM_{10} , as described in [164]. In addition, a waveguide short is located at around $\lambda/4$ from the matching patch to increase the power coupled to the latter. A set of equations for designing this kind of structure is proposed in [151]. Figure 4.5 shows an exploded view of the antenna element. In addition to the described components, the antenna connector is included consisting of a coax-to-WR-34 adapter, which is a practical solution to carry out the antenna measurements.

The results from the simulated antenna element at 26 GHz are depicted in Figure 4.6, with an S_{11} below -10 dB over a 16.5% bandwidth and a realized gain higher than 8.5 dB for the considered frequency bandwidth. The most critical dimensions in tuning the antenna to the design requirements were the air gap thickness, the slot and stub lengths, and the patches dimensions.

The antenna presents a high radiation efficiency of 97% and, as exhibited in Figure 4.6 b), the antenna radiation pattern at 26 GHz presents a wide beamwidth of 66° , as targeted in the subarray specifications.

4.4 Subarray synthesis

The minimum number of subarray elements to achieve a 10 dBi gain figure was calculated for a uniform linear array based on the simulated antenna pattern of Figure 4.6 b). Compared to

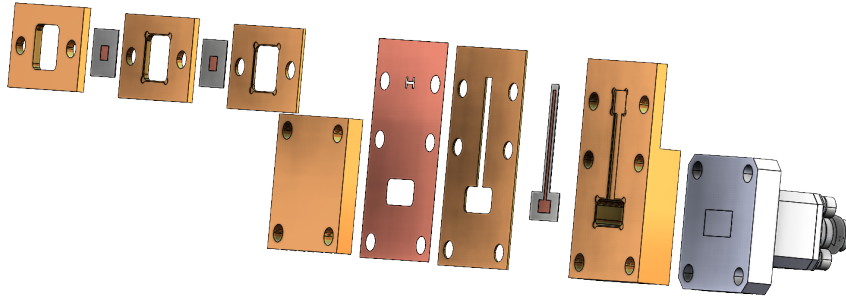
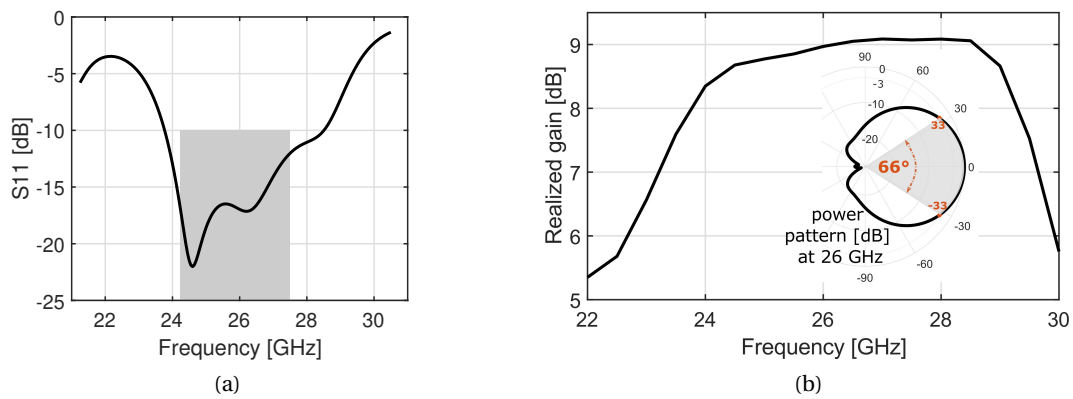


Figure 4.5 – Exploded view of the antenna element

Figure 4.6 – Radiating element results: a) S_{11} b) Realized gain and gain radiation pattern for 26 GHz

this, a 6-element subarray was analytically found as the simplest implementation meeting this specification with sufficient margin considering a csc^2 pattern [60]. Additionally, given the element cavity size $(0.65\lambda)^2$ and the required brass wall among them (1 mm thick), the distance between elements in the subarray is (0.75λ) . This, together with the transmission line geometry were considered in the definition of the feeding network layout.

The feeding network layout can be implemented in different architectures. We have selected a topology placing the feeding port close to the center to reduce transmission losses (Figure 4.7 a)). Additionally, considering that a relatively narrow subarray width is desired (given the performed analysis in Chapter 3), the possible layouts are shortlisted to three architectures as shown in Figure 4.7.

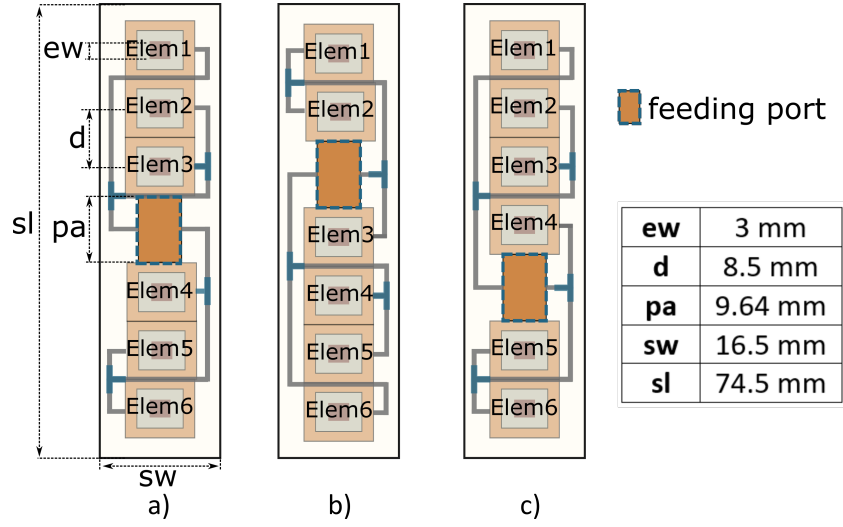


Figure 4.7 – Subarray layout with feeding port located after a) the third antenna element, b) the second antenna element, and c) the fourth antenna element

The final layout selection is determined by the requirement regarding the subarray radiation pattern in elevation.

4.4.1 Analog beamforming in elevation

As described in Chapter 2, a subarray having a csc^2 pattern shape in elevation is desired for guaranteeing uniformly distributed received power along the picocell. The weighting vector w_0 associated with the required csc^2 pattern mask (depicted in 4.1) can be synthesized using the optimization scheme proposed in Equation 3.7. The matrix A_{sub} in this equation represents the radiated field $E_n(\theta, \phi)$ of each subarray antenna element, i.e.

$$A_{sub[n,\theta\phi]} = \begin{bmatrix} E_{1j} e^{1j\psi(\theta,\phi=-90,-180)} & \dots & E_{1j} e^{1j\psi(\theta,\phi=-90,180)} \\ \vdots & \ddots & \vdots \\ E_{Nj} e^{Nj\psi(\theta,\phi=90,-180)} & \dots & E_{Nj} e^{Nj\psi(\theta,\phi=90,180)} \end{bmatrix}_{n=1:N} \quad (4.2)$$

where n refers to the n_{th} antenna element with $n = [1, \dots, N]$, with $\theta \in [-90^\circ, 90^\circ]$ and $\phi \in [-180^\circ, 180^\circ]$, and ψ is the relative progressive phase between elements.

If we would neglect the mutual coupling, all elements are identical and the matrix A_{sub} would be simply obtained from Equation (3.9) using the common element pattern E_0 . A better approach is to pre-compute the radiated field of each element by simulating the subarray with ideal ports at each element (see Figure 4.8), yielding $E_n(\theta, \phi)$ for each element, and then using Equation (4.2). This is the option followed in this work.

The three subarray layouts in Figure 4.7 were considered in the described least-squares optimization. The synthesized patterns $AP_{sub} = A_{sub} \cdot w_0$ are compared to the mask in Figure 4.9.

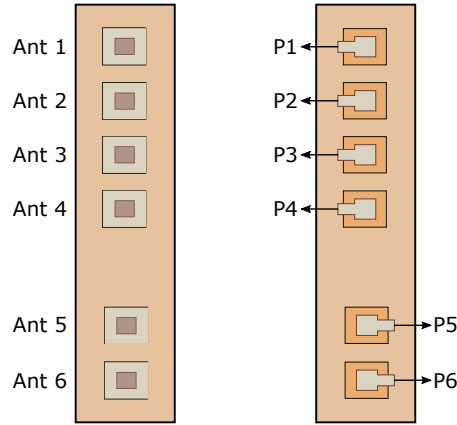


Figure 4.8 – Radiating elements of the subarray fed by ideal ports

The patterns AP_{sub} obtained with architectures a) and c) are the closest to the desired mask, and between them, layout c) achieves a better approximation to the main beam shape. We consider that this is due to the beam tilt of the mask pattern main beam.

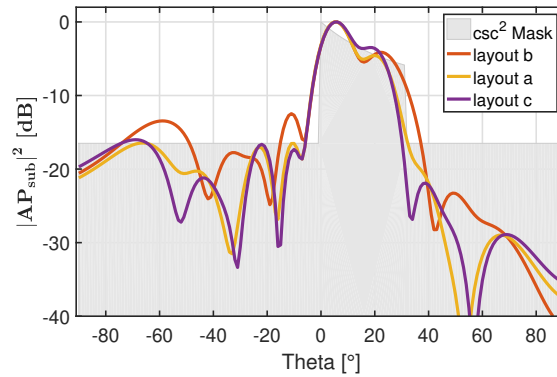


Figure 4.9 – Synthesized patterns for layouts a, b, and c

The synthesized pattern AP_{sub} of the subarray layout c) is compared to the ideal mask in Figure 4.10. Additionally, the synthesized weighting vector w_0 containing the amplitude and phase values for the six antenna elements can be seen in Table 4.2.

Table 4.2 – w_0 in amplitude and phase

	Elem #1	Elem #2	Elem #3	Elem #4	Elem #5	Elem #6
Amplitude [W]	0.1211	0.3163	0.3387	0.1597	0.0378	0.0263
Phase [deg]	136.42	92.56	45.09	0	-175.11	153.62

A subarray fed by a feeding line implementing the weighting vector in Table 4.2 should provide a radiation pattern AP_{sub} shown in Figure 4.10. The synthesized AP_{sub} guarantees a uniformly distributed power in elevation for more than 30° below the horizon, with SLL below -16 dB.

Various feeding line topologies that can be implemented in the selected layout architecture c)

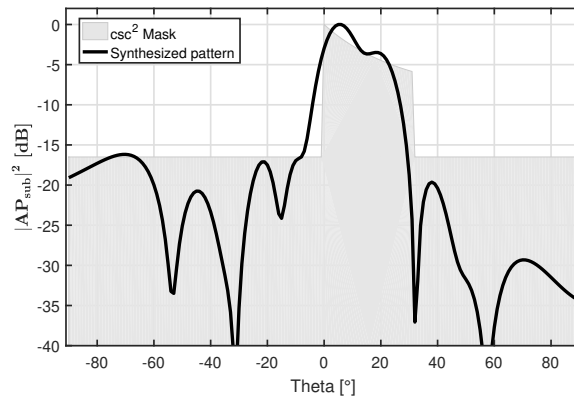


Figure 4.10 – Synthesized pattern for the selected subarray layout (layout c)

and are mechanically realizable, are exhibited in Figure 4.11, together with their respective set of power ratios, considering w_0 in Table 4.2.

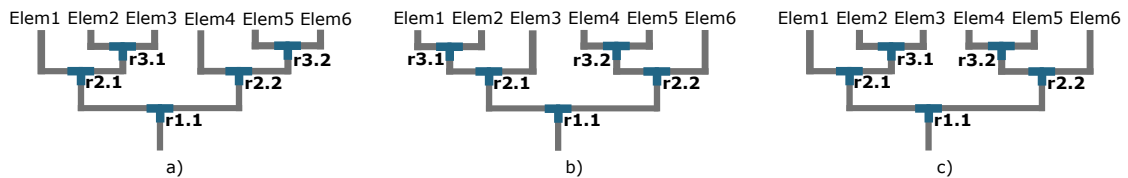


Figure 4.11 – considered feeding line topologies

Table 4.3 – Power ratio per node

	Node r1.1	Node r2.1	Node r3.1	Node r2.2	Node r3.2
Layout A	3.46	5.41	1.07	2.49	1.44
Layout B	3.46	1.29	2.61	7.51	4.22
Layout C	3.46	5.41	1.07	7.51	4.22

As summarized in Table 4.3, the topology a) exhibits the smallest power ratios among branches. This is convenient to assure the frequency stability of the used power dividers [165]. The selected feeding network layout and topology are depicted in Figure 4.12.

The design of the power dividers and phase shifters involved in the realization of this feeding network is described next.

Power dividers

Five power dividers were used in our design. The first power division was implemented in the feeding port containing the WG to SSL transition (See Figure 4.13) [164], [166], [167] .

The working principle of this transition is similar to the transition used in the antenna element, where the incident energy in the WG port is coupled to the SSL through a matching patch. In this case, the incident power is distributed among two SSL output ports which present

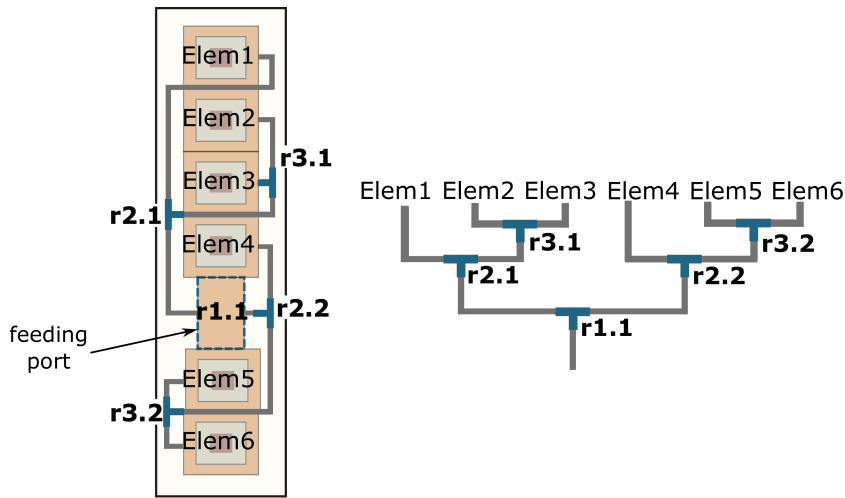


Figure 4.12 – Selected subarray layout and feeding line topology

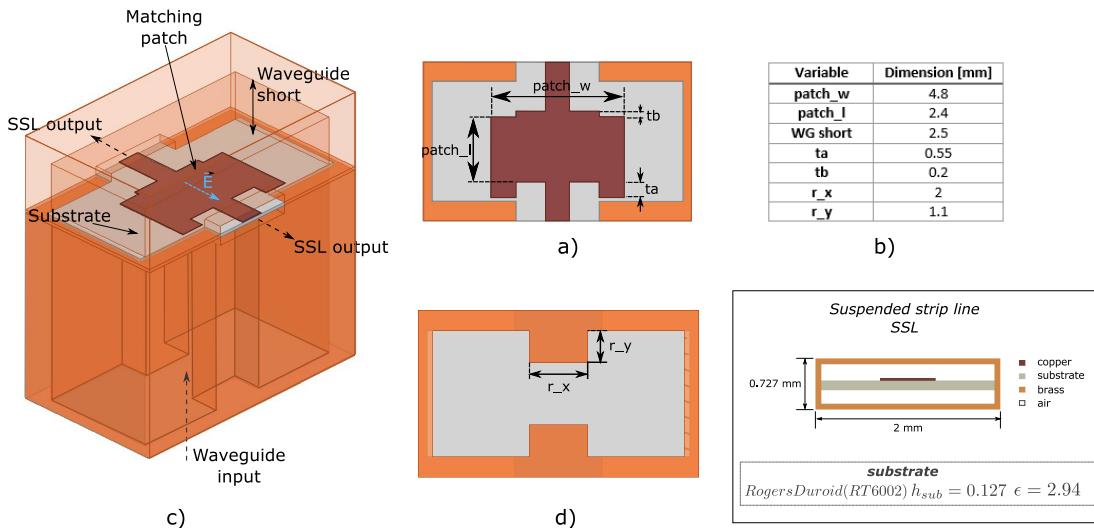


Figure 4.13 – WG-SSL transition a) top view b) dimensions c) geometry d) bottom view

opposite phases due to the transition geometry. In order to achieve the required power division between the two SSL ports the matching patch was placed off-center and its parameters, depicted in Figure 4.13 a), were modified. Since the WG-SSL transition is the first component in the feeding network, its performance is crucial to meet the specified bandwidth criteria. That is why instead of using a simple WG, a ridged WG was selected given its broadband characteristics [168]. As a result, the transition S_{11} parameter along the studied band is below -19 dB. Moreover, the WG-SSL transition power ratio is quite stable along the operation over the desired frequency band (see Figure 4.14).

The rest of the dividers were based on SSL technology. Two types of SSL power divider architectures were used, as depicted in Figures 4.15 and 4.16. They consist of a T structure where the power division is controlled by tuning gaps (g_1, g_2, g_3) in the superior side of the

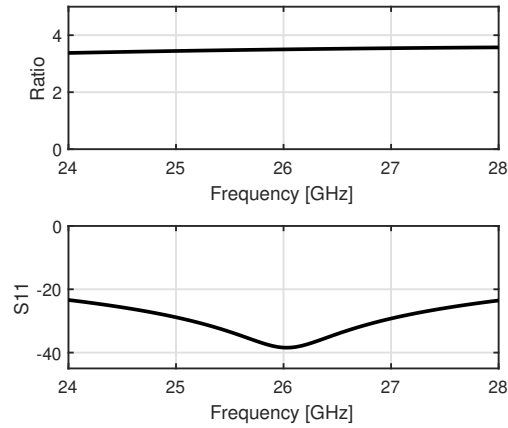


Figure 4.14 – WG-SSL transition power ratio and S11 parameters

substrate and T line lengths (p_1 , p_2 , p_3) on the opposite side of the substrate. Input and output lines present the same width and are located in the same plane avoiding the need for impedance transforming structures. These dividers were designed using the method described in Zürcher et. al. proposed in [165]. In this method, a typical T divider circuit equivalent model is used to calculate the impedances that, connected to each branch, provide the desired power ratio. Consequently, these impedances are associated with the tune gaps and line lengths. In this work, the divider equivalent circuit was implemented in the Ansoft Designer package from ANSYS EM and the final model was fine-tuned using HFSS.

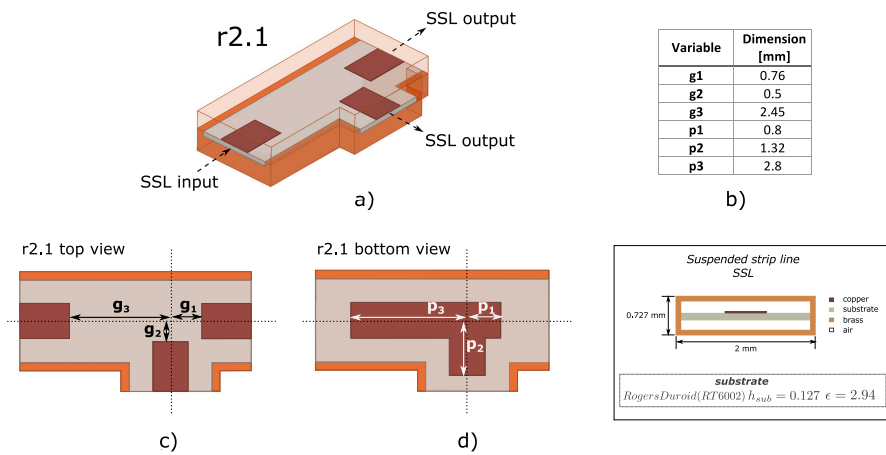


Figure 4.15 – Divider r2.1 a) geometry b) dimensions c) top view d) bottom view

The two structures present a good coupling, with S_{11} values below 10 dB and stable power ratios along the specified bandwidth. The power ratio is shifted by no more than ± 0.5 at the bandwidth edges.

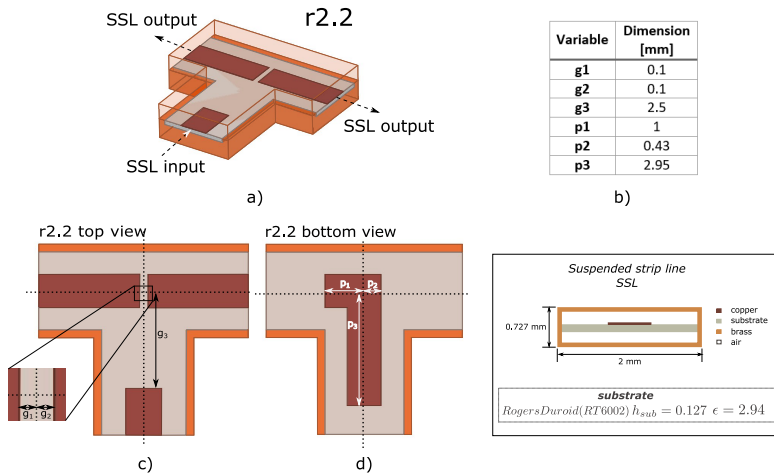


Figure 4.16 – Divider r22 a) geometry b) dimensions c) top view d) bottom view

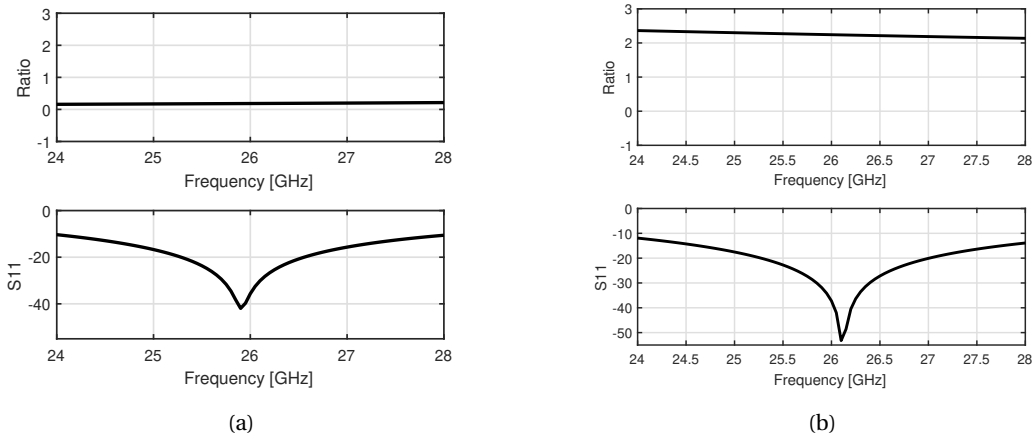


Figure 4.17 – Power ratio and S11 parameters of a) divider r21 b) divider r22

Phase shifters

Various U-shape shifters (see Figure 4.18) were used for phase shifts smaller than 45°. A 180° phase meander to compensate the out-of-phase SSL ports in the transition was also included in the feeding line.

With the objective of determining a suitable initial subarray, an equivalent model of the feeding network, based on the scattering matrix of the described subarray components, was designed in Ansoft Designer (see Figure 4.19). This model will be referred to as S-model in the rest of the document.

For increasing the model accuracy, the transmission line length and losses and the feeding line bends scattering matrices were included. In addition, each subarray antenna element was represented by a port and a load characterized by the input impedance of each antenna

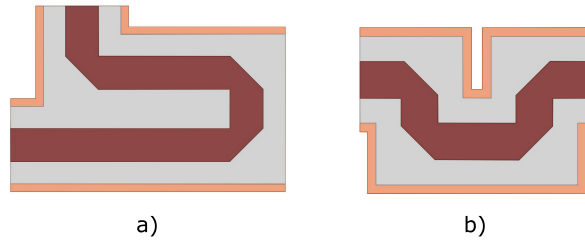


Figure 4.18 – Phase shifters configurations a) 180° phase meander b) U-shape shifter

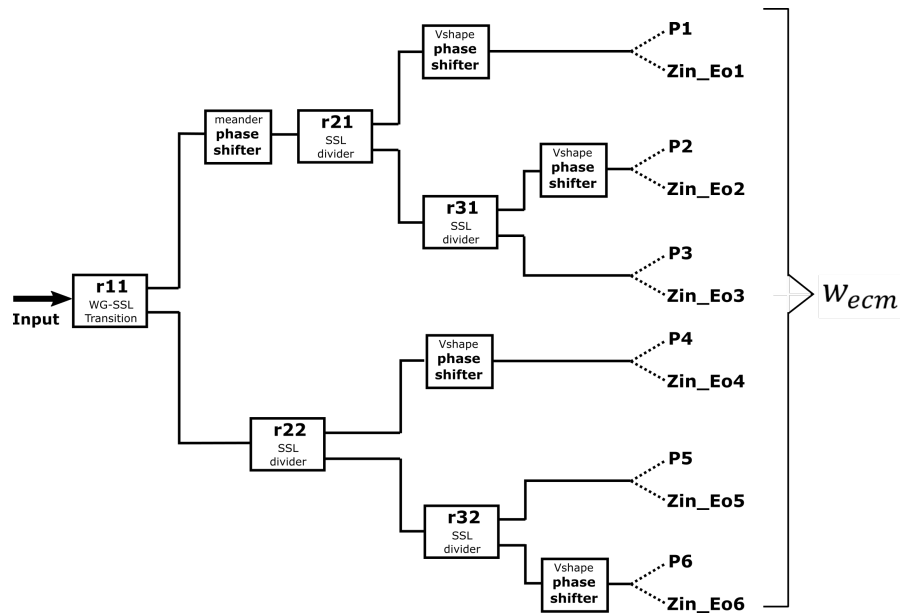


Figure 4.19 – Feeding network equivalent S-model

element in the subarray. The weighting vector generated using the equivalent S-model w_{ecm} , was compared to the synthesized vector w_0 . This was a crucial step for tuning each component before building the subarray in HFSS and thus reducing the overall optimization time. The optimized S-model was built in HFSS and each feeding line was ended with virtual ports, as shown in Figure 4.20. The weighting vectors generated in this full-wave model w_{fum} , was calculated and compared to its previous counterparts w_0 and w_{ecm} . The excitations associated with each computed weighting vector were introduced in the antenna array in Figure 4.8 to verify their agreement with the targeted csc^2 pattern shape.

The optimized feeding network and the antenna array depicted in Figures 4.8 and 4.20 were used to build the complete subarray in HFSS for the final fine-tuning of its components.

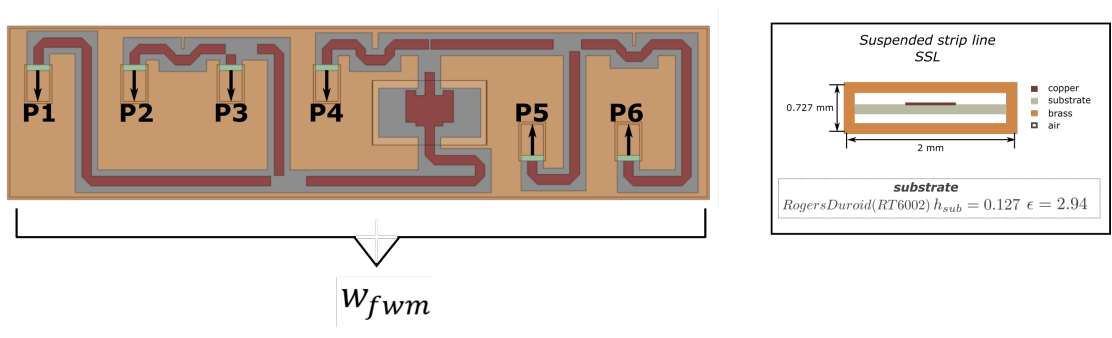


Figure 4.20 – Feeding network designed in HFSS

4.5 Subarray fabrication and results

The proposed subarray architecture is presented in Figure 4.21. The input power is fed into a ridged WG and through the transition to the shielded-SSL feeding network. This constitutes the ABFN designed according to the synthesized w_0 . Dogbone slots are used to couple the distributed power from the feeding line to the stacked patches. In addition, the brass layers between and above the stacked patches provide the desired shielded boundary between the subarray antennas. Technical drawings detailing each of the subarray parts are included in Appendix A.

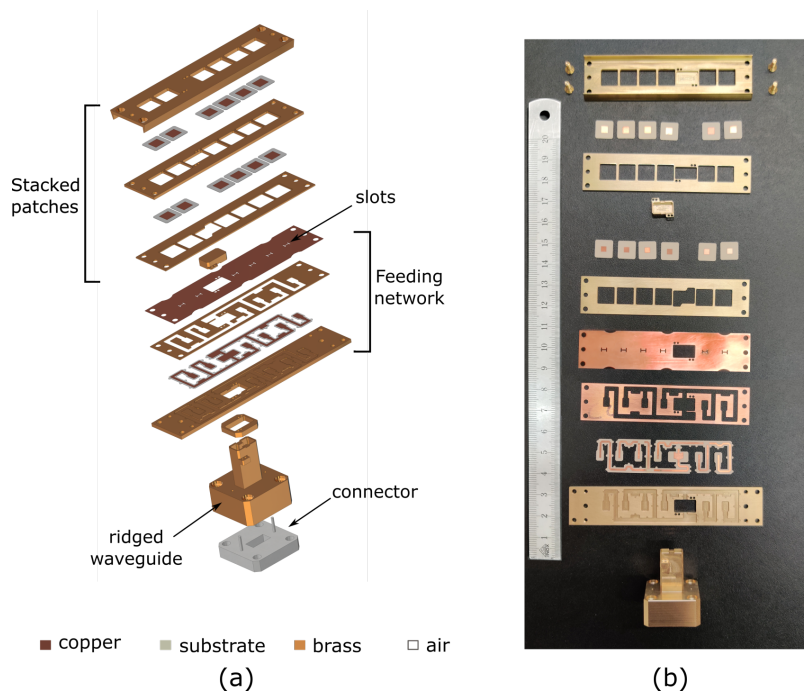


Figure 4.21 – Proposed subarray: a) exploded view of the subarray and b) fabricated subarray. Technical drawings detailing the subarray parts are included in the Appendix.

The techniques used in the subarray fabrication are:

- Photolithography on dielectric substrate Rogers Duroid (RT 6002).
- Laser cutting on both, brass and copper.
- Electro-erosion on brass.
- CNC milling of brass.

This fabrication was carried out in two different workshops at the EPFL campus, the Atelier de fabrication de Circuits Imprimés (ACI) and the Atelier de l'Institut de production et robotique (ATPR). The photolithography of the Printed Circuit Board (PCB) pieces was realized in ACI, while the rest of the techniques were carried out at ATPR. While the size of the subarray parts is too large for micromachining, their geometrical requirements are at the limit of classical fabrication methods. The fabrication process thus required extensive coordination to take into account the feasible technology tolerances and adapt the design accordingly. In addition, this process included preparing technical drawings, using a 3D modeling program (in this case Creo Parametric), with precise and complete information for each subarray part. Some key elements in the subarray fabrication process are detailed next.

The WG feeding port (depicted in Figure 4.22), is a monolithic part including a square structure adapted to the connector dimensions and the WG containing fixing elements to couple the rest of the parts. A transition 13.5 mm long from the standard WG to the ridged WG was designed to avoid high reflections.

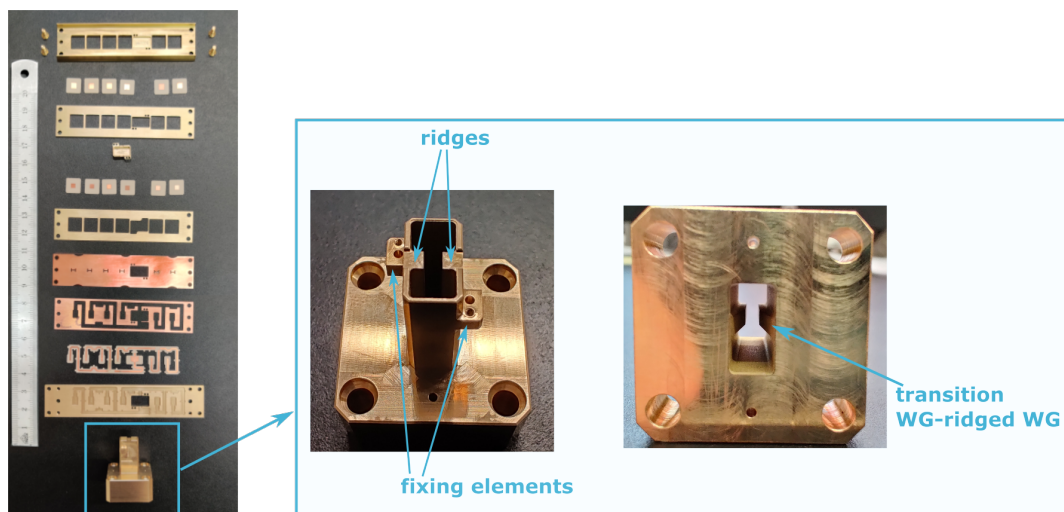


Figure 4.22 – Subarray WG feeding port

The feeding line holder is shown in Figure 4.23. This part contains the second set of fixing elements that are used to couple the rest of the parts from both subarray ends. In addition,

the feeding line area consists of a stepped structure holding the feeding line preceded by a 0.3 mm air-layer.

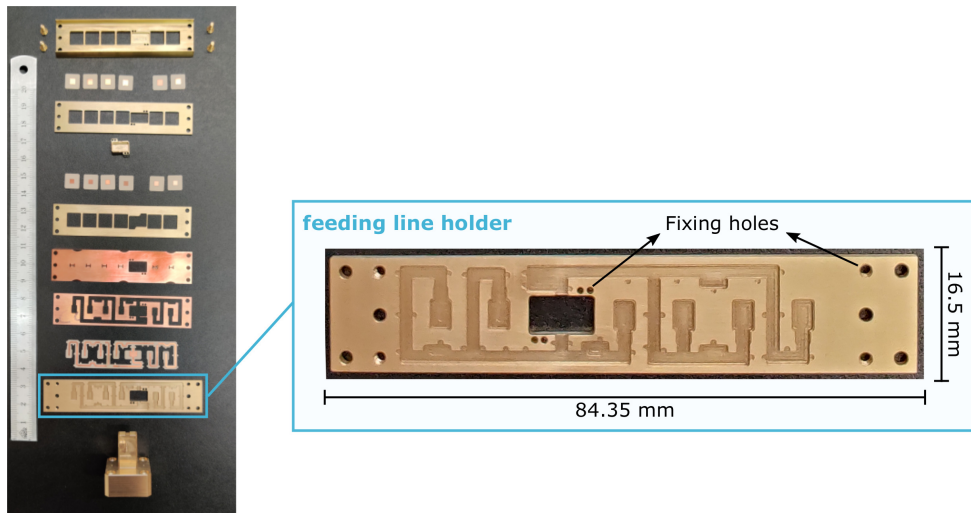


Figure 4.23 – Subarray feeding line holder

The parts highlighted in Figure 4.24 are the subarray thinnest metallic parts. They required more careful manipulation but were successfully obtained by laser cutting.

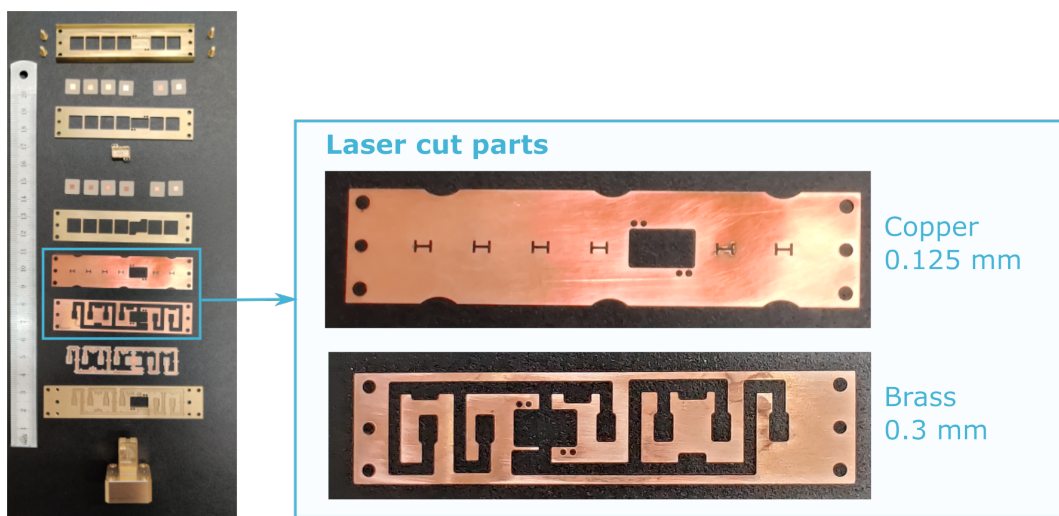


Figure 4.24 – Subarray metallic thin layers

An example of the PCB parts is included in Figure 4.25 containing the feeding line and one of the bottom patches. In the fabrication process of these pieces, the photolithography was performed in an ACI and the laser cutting in ATPR. For a correct implementation, defining an agreement between the reference planes used by both workshops was crucial.

The assembled subarray is shown in Figure 4.26. The dimensions of the complete assembly, including the connector, are 16.5 mm x 84.4 mm x 29.8 mm. It should be noted that the connector

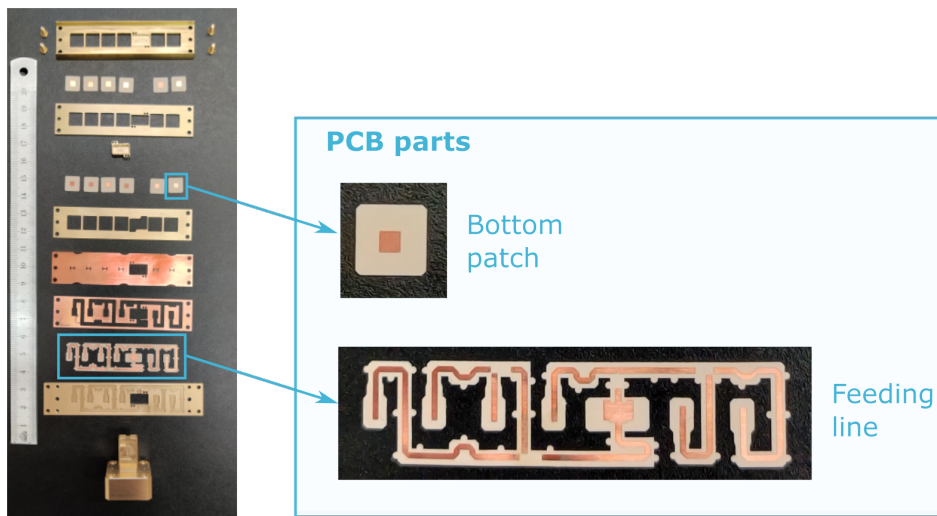


Figure 4.25 – Subarray pcb parts

is only necessary for the measurements and it is not part of the final antenna implementation. If the connector is not considered, the subarray dimensions are 16.5 mm x 84.4 mm x 5.7 mm, which shows its small size and low profile.

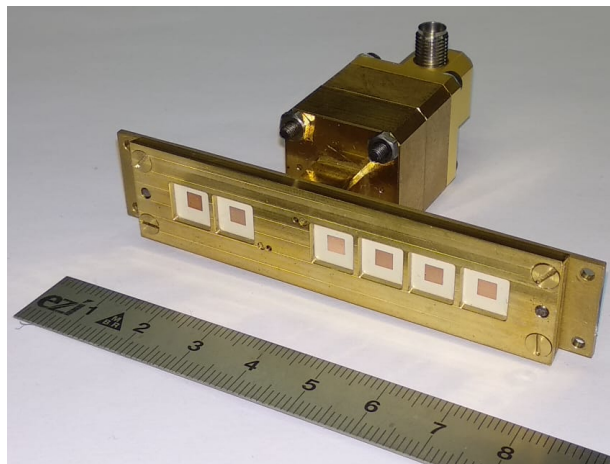


Figure 4.26 – Assembled subarray

For the adequate calibration of the vector network analyzer (VNA) used in the measurements, a Through-Reflect-Line (TRL) calibration set, consisting of a thru, short circuit and a line (as depicted in Figure 4.27) was designed [169] and fabricated.

Figure 4.28 shows the simulated and measured subarray S_{11} parameters. Although the overall tendency agrees well between both curves, minor variations can be seen in the upper half of the operational band. We consider that this is caused by assembly errors and expected fabrication tolerances. A broadband impedance bandwidth has been obtained covering more than the targeted 5G spectrum for Europe.

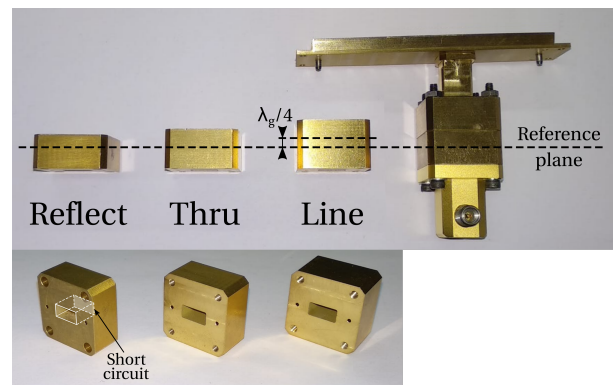


Figure 4.27 – Subarray TRL calibration set

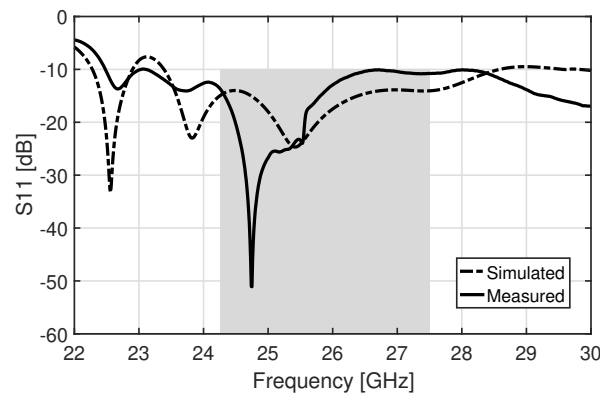


Figure 4.28 – Simulated and measured S_{11} of the subarray

The measured radiation pattern (depicted in Figure 4.29) is in good agreement with both, the simulated results and the ideal csc^2 mask. The cross-polarization level is better than -22.75 dB.

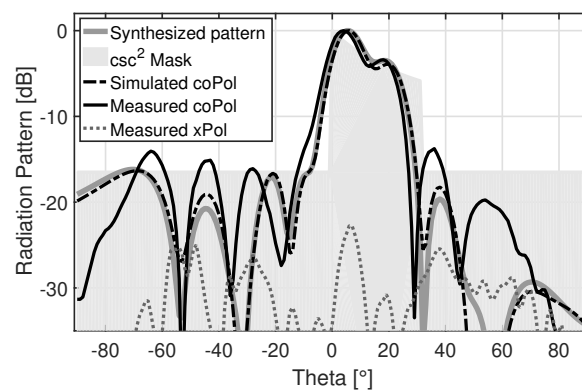


Figure 4.29 – Simulated and measured radiation pattern of the subarray at 26.5 GHz

Figure 4.30 shows the subarray simulated and measured realized gains as a function of the frequency for the considered frequency band. The measured curve is below the simulated one

due to uncertainties in the gain measurement. Larger deviations are noticeable at the upper half of the band, as expected given the discrepancies obtained for the S_{11} results. In addition, the measured gain is higher than 10 dBi from 24.5 GHz to 27.5 GHz, with a maximum value 12.94 dBi. In addition, the simulated subarray efficiency is 92.6%. Although we were not able to measure this parameter, we expect it to have a similar value, given the good agreement between measured and realized gains.

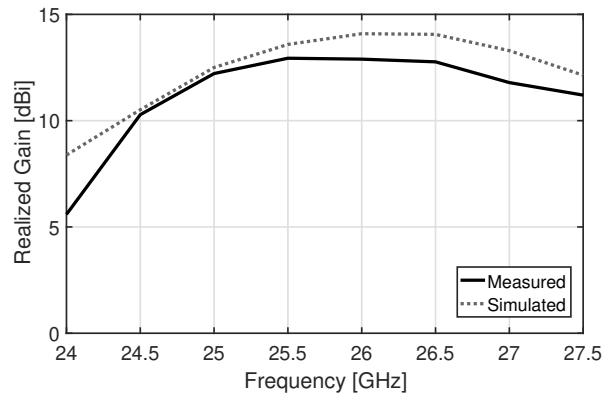


Figure 4.30 – Simulated and measured realized gain of the subarray as a function of frequency

In order to determine the subarray radiation bandwidth, the copolarized radiation pattern was measured for the studied frequency range. Figure 4.31 shows the results for five frequencies, located at the central region (25 GHz, 26 GHz and 26.5 GHz) and at the end of the foreseen frequency range for 5G (24.25 GHz and 27.5 GHz). Given the variability of these results over a wide bandwidth, an additional SLL threshold has been added at -10 dB for enabling a simplified visual comparison.

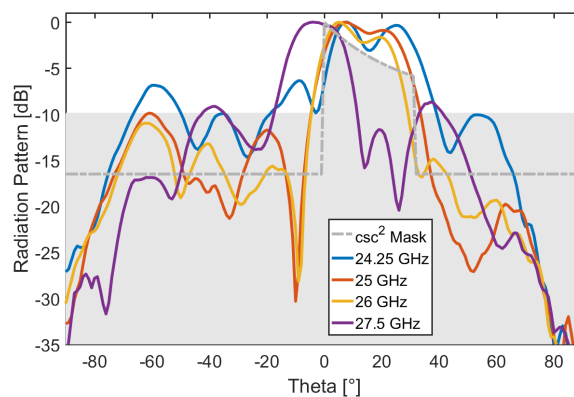


Figure 4.31 – Measure radiation pattern at 24.25 GHz, 25 GHz, 26 GHz and 26.5 GHz and 27.5 GHz

The measured radiation patterns at both ends strongly differ from the desired mask, considering both, the main beam shape and the SLL threshold. In order to evaluate the implications of these results in the coverage distribution requirement along the picocell, it is necessary to

calculate the received power versus distance considering the measured radiation pattern at each band, their gain figures, and the path loss with LOS conditions given by the PLE range $2.22 \leq n_p \leq 2.45$.

As an initial reference, these results are evaluated for a radiation pattern with good agreement to the constraint mask (depicted in Figure 4.1). Figure 4.32 shows the polar radiation pattern in dB for 26.5 GHz integrated in the picocell scenario. In addition, the pattern distribution over distance (Figure 4.33a) and the received power versus distance (Figure 4.33b) are depicted including red, yellow and blue dots for a clearer association with significant points in the pattern. An antenna height (h) of 2 m was used in the calculations with the objective of evaluating the worst-case scenario from the antenna height range considered for 5G picocells as depicted in Table 2.1.

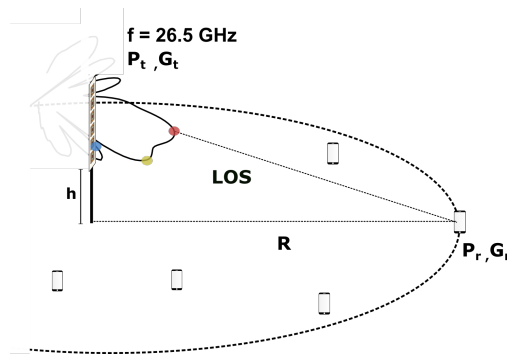


Figure 4.32 – Picocell scenario with a section of the measured radiation pattern in polar coordinates at 26.5 GHz. The antenna height h is 2 m

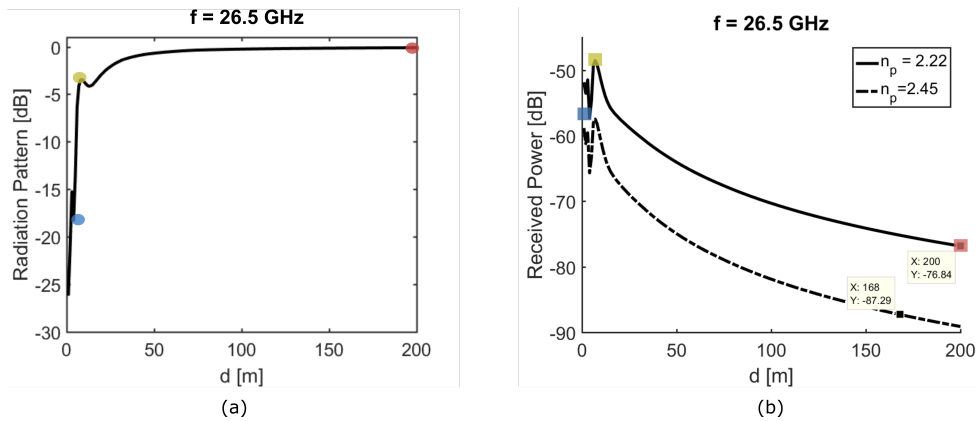


Figure 4.33 – a) Radiation pattern distribution versus distance at 26.5 GHz b) Received power versus distance at 26.5 GHz

The radiation pattern and received power as a function of distance are accordingly generated for the frequency band ends (see Figures 4.34 and 4.35).

Figures 4.33 b), 4.34 b) and 4.35 b) show that even for the frequency band ends, the received power is above the sensitivity limit along the picocell for radius higher than 200 m in LOS with

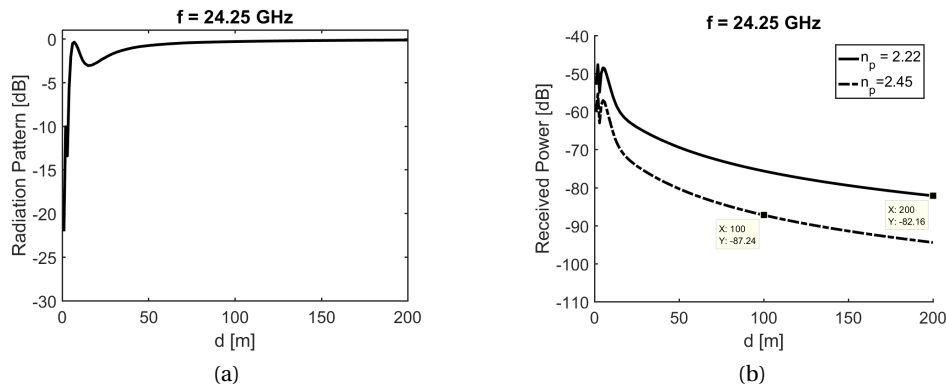


Figure 4.34 – a) Radiation pattern distribution versus distance at 24.25 GHz b) Received power versus distance at 24.25 GHz

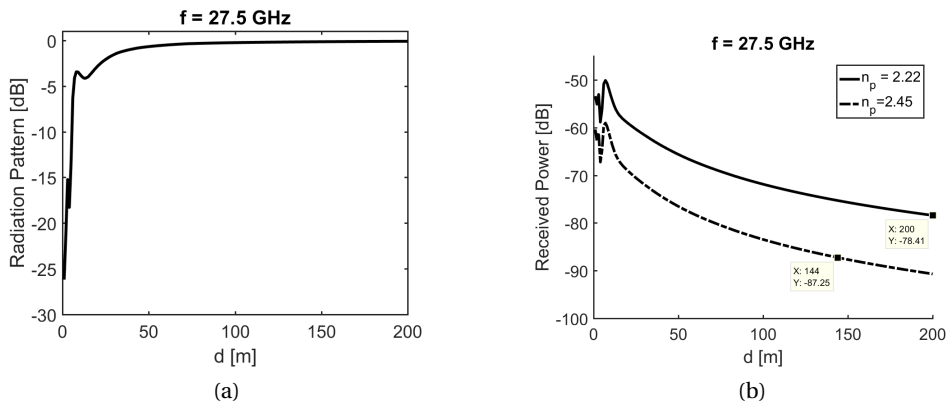


Figure 4.35 – a) Radiation pattern distribution versus distance at 27.5 GHz b) Received power versus distance at 27.5 GHz

$n_p = 2.22$. On the other hand, if the LOS is characterized by $n_p = 2.45$, then the picocell radius is limited by the result at $f = 24.25$ GHz where the signal can be detected in a radius smaller than 100 m.

Considering this, we can find the frequency range that fulfills the design requirements, taking into account both, the csc^2 pattern mask and the subarray coverage capabilities. A good correlation with the specified csc^2 mask was obtained for a frequency range from 24.75 GHz to 26.75 GHz as represented by the gray-shaded region in Figure 4.36. The mean copolarized and crosspolarized realized gains obtained for this frequency range are indicated using solid and dashed-dotted lines, respectively. While side lobes in the negative theta range do not have an impact from an interference point of view due to the antenna orientation, they should be bounded to reduce non-useful energy radiation. The subarray radiation pattern range has been defined so that the SLL is consistently below -10 dB.

Figure 4.37 depicts the received power over distance for a LOS $n_{p\min} = 2.22$ and $n_{p\max} = 2.45$.

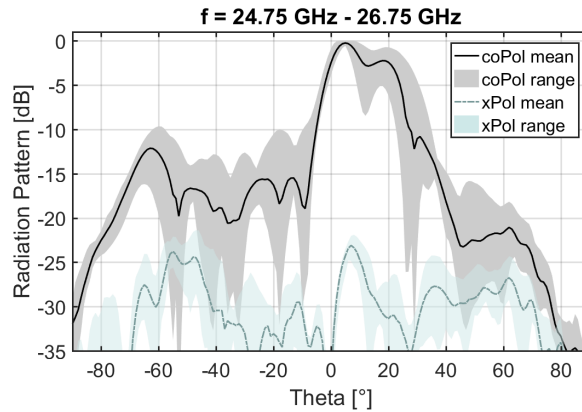


Figure 4.36 – Measured radiation pattern of the subarray: range (shaded) of the copolarized and cross polarized patterns at the band 24.75-26.75 GHz and mean (solid) of the copolarized and cross polarized patterns at the band 24.75-26.75 GHz

The shade region represents the frequency range from 24.75 GHz to 26.75 GHz and the solid and dashed lines the worst case of this range for n_{pmin} and n_{pmax} , respectively.

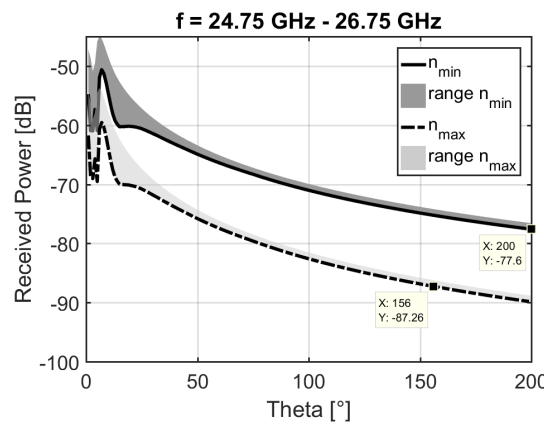


Figure 4.37 – Received power vs distance for LOS $n_{pmin} = 2.22$ and $n_{pmax} = 2.45$ at the band 24.75 GHz - 26.75 GHz (shaded) and worst case within this band (solid)

In the specified frequency bandwidth, a signal can be detected at a distance longer than 200 m for an n_{pmin} LOS link, while the picocell radius for n_{pmax} LOS conditions is 156 m.

With approximately 7.7% of radiation pattern bandwidth, the proposed subarray represents an attractive solution for the described picocell application to guarantee a uniform received power in elevation along the cell radius. The proposed subarray covers the bandwidth requirement specified in Table 4.1 for both, impedance and radiation pattern parameters.

In this chapter, a broadband subarray fed by an analog beamforming network for a portable picocell station has been proposed. The subarray design has been guided by a group of requirements considering the studied application. Both, the antenna element and the transmission

line have been designed on planar technology for enabling low profile and easy integration. They have been suspended on thin and low-permittivity dielectric for achieving low losses and broadband operation. Additionally, they have been enclosed in cavities to minimize spurious radiation from the transmission line and undesired mutual coupling among antenna elements. The subarray synthesis has been presented, solving an optimization problem to obtain the weighting vector associated with a csc^2 pattern in elevation. A realistic subarray design has been used to include mutual coupling in the problem solution. Furthermore, the feeding network components: WG-SSL transition, power dividers and phase shifters have been described. Results comparing simulated and measured S_{11} , radiation pattern, gain and pattern bandwidth results have been depicted. They validate the appropriate subarray performance achieving a bandwidth of 7.7% and a gain superior to 10 dBi along such range. The proposed subarray is usable with respect to the initial requirements. However, it will be additionally enhanced in Chapter 5 focusing on the antenna performance in azimuth.

5 Multibeam antenna fed by hybrid beamforming network

This chapter presents the design of the MBA fed by a HBFN. Compared to the HBFN synthesized in Chapter 3 for a fully analytical scenario, in this chapter a more realistic antenna array is considered, based on the subarray obtained in Chapter 4. This analysis is carried out taking into account the MBA design requirements in azimuth while maintaining the achieved performance in elevation. In order to improve the multibeam forming antenna capabilities, the relevant design parameters are investigated. Taking the outcome of this analysis, an optimized subarray is proposed and a section of the sectorial antenna array is fabricated for experimental validation. The initially proposed subarray and the optimized version are compared. Finally, results evaluating the antenna performance considering the design constraints in both elevation and azimuth are presented.

5.1 Overview of the MBA design requirements and limitations

In order to evaluate the DBFN performance of the antenna array in azimuth, the fabricated subarray in Chapter 4 (from here on referred to as Subarray₀) was used to design an antenna array of 12 sectors. The measured radiation pattern AP_{sub} at 26.5 GHz shown in Figure 4.30 was used to analytically build the array response matrix as depicted in Equation 5.1.

$$A_{MBA_{[m,\theta,\phi]}} = \begin{bmatrix} AP_{sub1j} e^{1j\psi(\theta,\phi=-90,-180)} & \dots & AP_{sub1j} e^{1j\psi(\theta,\phi=-90,180)} \\ \vdots & \ddots & \vdots \\ AP_{subMj} e^{Mj\psi(\theta,\phi=90,-180)} & \dots & AP_{subMj} e^{Mj\psi(\theta,\phi=90,180)} \end{bmatrix}_{m=1:M} \quad (5.1)$$

As presented in Chapter 3, the computed digital BFN in azimuth generates a matrix $U_{M \times 1}(\theta_i, \phi_j)$ with column wise distributed weighting vectors $u_{M \times 1}(\theta_i, \phi_j)$ that fulfill a set of constraints. These constraints are linked to the desired pattern direction (C_1), beamwidth (C_2) and SLL (C_3) and the weighting vector power bound (C_4). The solution of the DBFN synthesis problem in azimuth has been addressed by integrating $C_1 - C_3$ in a mask Δ_{MBA} (see Figure 5.1 c) used

to solve an iterative algorithm as depicted in Figure 3.13. Different masks can be defined considering different sets of constraints targeting a certain user position (C_1), desired coverage area (C_2) and beam interference tolerance (C_3) in azimuth.

The studied scenario, depicted in Figure 5.1, was used to evaluate the DBFN capabilities for a set of constraints (S_0) defined to generate beams targeting two directions (see Figure 5.1 d)). We selected the extreme angles, $C_1 = 105^\circ$ which is broadside for one sector and $C_1 = 90^\circ$ which lies exactly on between two sectors. In addition constraints C_2 and C_3 are relatively relaxed as a general testing scenario. The patterns AP_{MBA} synthesized according to S_0 are shown in

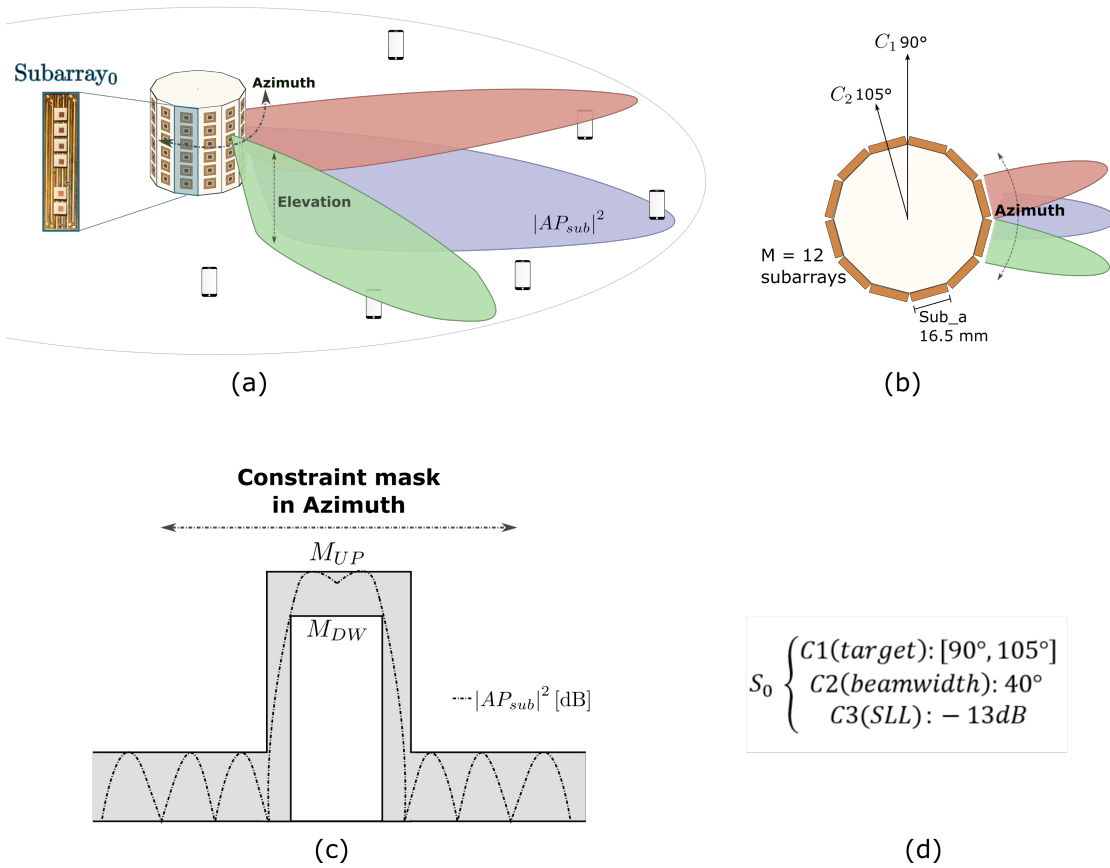


Figure 5.1 – Summary of the MBA synthesis specifications a) studied picocell scenario b) top view of the MBA antenna c) constraint mask in azimuth d) testing set of constraints S_0

Figure 5.2 for targets a) 90° and b) 105° . Although the target constraint is approximately met in both cases, the required beamwidth is not fully attained. In addition, results show relatively high SLL (SLL > -10 dB), which is an undesired parameter in this application, preventing multiple beams orthogonality. In order to improve these results, it is necessary to identify the key parameters limiting the desired MBA performance in azimuth. For that, we consider the

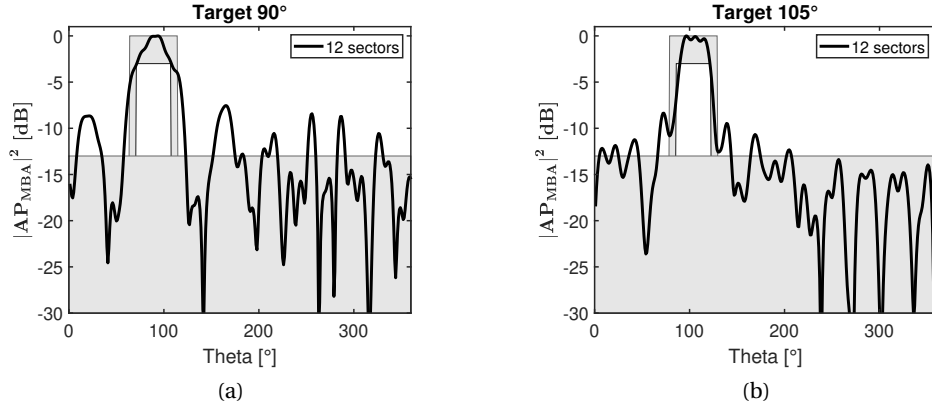


Figure 5.2 – Synthesized pattern of an array based on Subarray₀ for constraints S_0 targeting a) 90° b) 105°

antenna array equation

$$AP_{MBA} = AP_{sub} \sum_{m=1}^M u_m e^{j(m-1)\psi} \quad (5.2)$$

where AP_{sub} represents the embedded element pattern taking into account the mutual coupling (which is the same for each element due to the antenna symmetry). The sum term refers to the array factor, with M being the number of subarrays, u_m the weighting coefficient, and ψ the phase factor. Considering the main terms in Equation 5.2, the factors that potentially influence the MBA performance are linked to:

- The antenna architecture, specifically, the distance between subarrays and their orientation, linked to the number of sectors (M) and the subarray width (sub_a).
- The antenna element pattern in azimuth (AP_{sub}).

5.2 Relevant design parameters

In this section, the multibeam forming antenna capabilities are tested when modifying:

- The number of subarrays M (or sectors).
- The subarray width (sub_a).
- The subarray pattern in azimuth (AP_{sub}).

This analysis is based on the Subarray₀ radiation pattern, used to analytically build the examined antenna architectures. Since the DBFN acts only in the azimuth, we have narrowed our analysis to this plane, while taking care of preserving the csc^2 pattern obtained in elevation.

5.2.1 Impact of the number of subarrays

Aiming to consider the number of sectors used in our antenna array, the Subarray_0 pattern was rotated and replicated M times ($M = 4, 8, 12$ and 18) to form a sectorial antenna, as depicted in Figure 5.3).

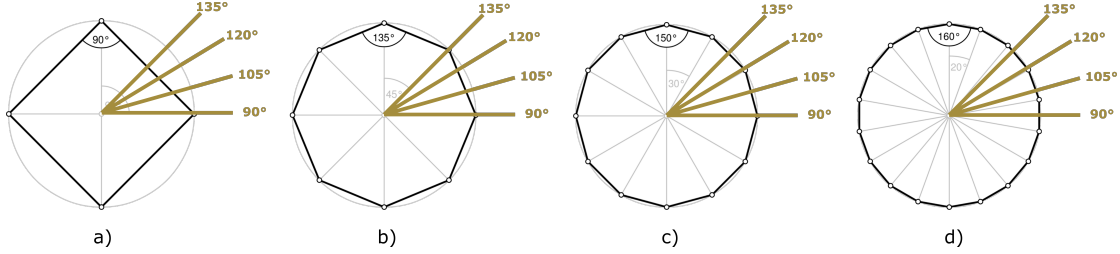


Figure 5.3 – Antenna architectures (based on Subarray_0) having a) 4 b) 8 c) 12 and d) 18 sectors. Targets defined in S'_0 are included

Given the Subarray_0 width ($\text{sub}_a = 16.5$ m), the minimum radius to geometrically arrange the four sectorial antennas is included in Table 5.1, together with the distance d between subarrays.

Table 5.1 – Minimum radius and distance between subarrays for a given number of sectors

Parameter	4 sectors	8 sectors	12 sectors	18 sectors
r_{\min} [mm]	8.25	19.92	30.79	46.79
$d(\lambda)$	1.01	1.32	1.38	1.41

A DBFN for each architecture is synthesized subject to a set of constraints S'_0 , defined to generate beams targeting a wide range of directions and relatively relaxed constraints C_2 and C_3 as a general testing scenario.

$$S'_0 = \begin{cases} C_1 \text{ (target)} : & [90^\circ, 105^\circ, 120^\circ, 135^\circ] \\ C_2 \text{ (beamwidth)} : & 40^\circ \\ C_3 \text{ (SLL)} : & -13 \text{ dB} \end{cases} \quad (5.3)$$

Figure 5.4 shows the synthesized pattern AP_{MBA} for the set of constraints S'_0 in the four studied antenna configurations when targeting 90° , 105° , 120° and 135° (Figure 5.4 a, b, c, d respectively). It can be noticed that, although constraint C_1 was mostly fulfilled with the four studied architectures, the radiation patterns that best fulfill constraints C_2 and C_3 were obtained with the 12-sector antenna. When targeting 90° and 135° , the 8-sector and 12-sector antennas present a similar performance; but in the rest of the targets the synthesized pattern with the 12-sector antenna yields lower SLL. Hence, a number of twelve subarrays ($M=12$) has been selected as a good cost-performance compromise for this application. The reduced number of

RF chains that would imply using a smaller number of sectors could compromise the antenna performance. On the other hand, increasing the number of sectors does not necessarily result in an improvement of the DBFN capacities, as depicted in the 18-sector antenna results. This can be given by the antenna pattern distribution in azimuth and the effect of having a distance between elements higher than λ (as depicted in Table 5.1).

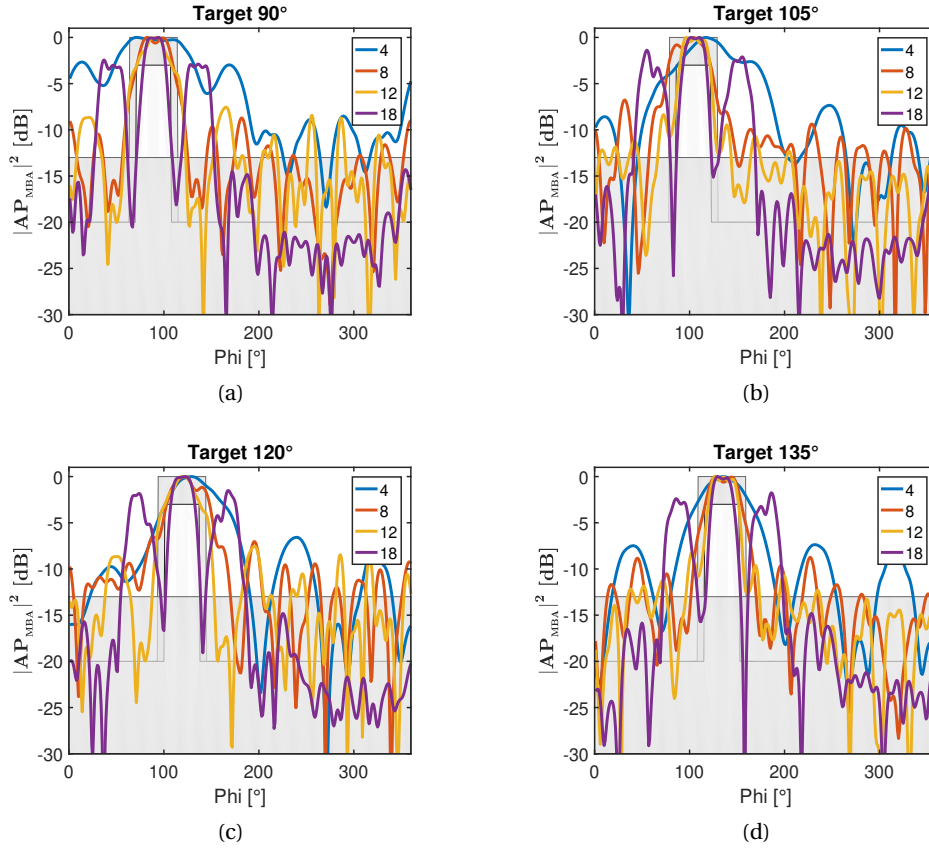


Figure 5.4 – Synthesized patterns, given the variation of the number of sectors, targeting a) 90° b) 105° c) 120° b) 135°. Legend refers to number of sectors M

5.2.2 Impact of the subarray width

As mentioned at the beginning of this section, the subarray width sub_a is a key parameter to take into account when investigating the MBA limitations. The $Subarray_0$ pattern was used to design three different antenna arrays of 12 sectors, based on a sub_a of 16.5 mm, 15.5 mm and 14.5 mm, as depicted in Figure 5.5 and Table 5.2. Smaller values of sub_a have been neglected given the subarray mechanical limitations in this plane. The DBFN weighting vectors were synthesized for the set of constraints S_0 (see Equation 5.4). Compared to S'_0 , S_0 only includes targets at 90° and 105°, given the 12-sector antenna symmetry.

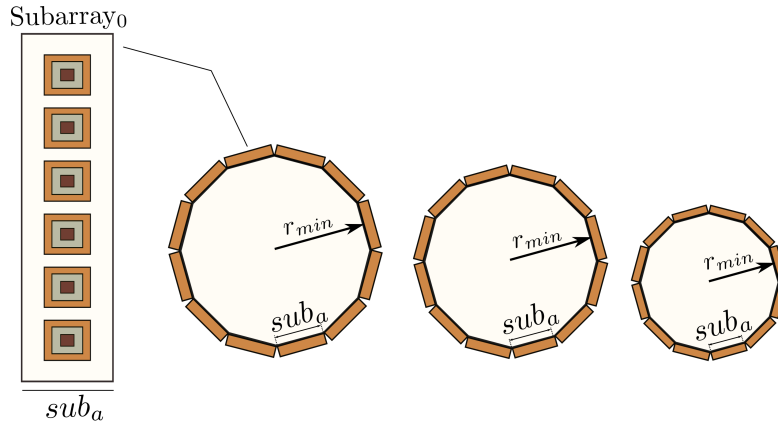


Figure 5.5 – 12-sector antenna architectures (based on Subarray₀) having different subarray width sub_a

Table 5.2 – Minimum radius and distance between subarrays for a given subarray width

Sector width (sub _a) [mm]	16.5	15.5	14.5
r _{min} [mm]	30.79	28.92	27.06
d(λ)	1.38	1.3	1.21

$$S_0 = \begin{cases} C_1 \text{ (target)} : & [90^\circ, 105^\circ] \\ C_2 \text{ (beamwidth)} : & 40^\circ \\ C_3 \text{ (SLL)} : & -13 \text{ dB} \end{cases} \quad (5.4)$$

The obtained patterns in the three antenna configurations are shown in Figure 5.6 targeting a) 90° and b) 105°. Although results are not significantly different, as expected by the relatively small variation of $d(\lambda)$, the synthesized pattern for the narrowest subarray showed a better approximation to the main beam mask. Regarding the SLL constraint, results are equivalent.

5.2.3 Impact of the subarray pattern in azimuth

In order to investigate the effect of the antenna element pattern in the DBFN performance, the subarray was substituted by an antenna element as shown in Figure 5.7. Four arrays were designed based on antenna elements with HPBW = [46°, 56°, 66°, 76°], defined around the actual beamwidth of the Subarray₀ pattern, which is 66°.

The DBFN given by the set S_0 was synthesized for the four array configurations. Results, depicted in Figure 5.8, show that a better approximation to the mask is achieved when reducing the antenna element beamwidth. Aiming to confirm this conclusion, a second test was

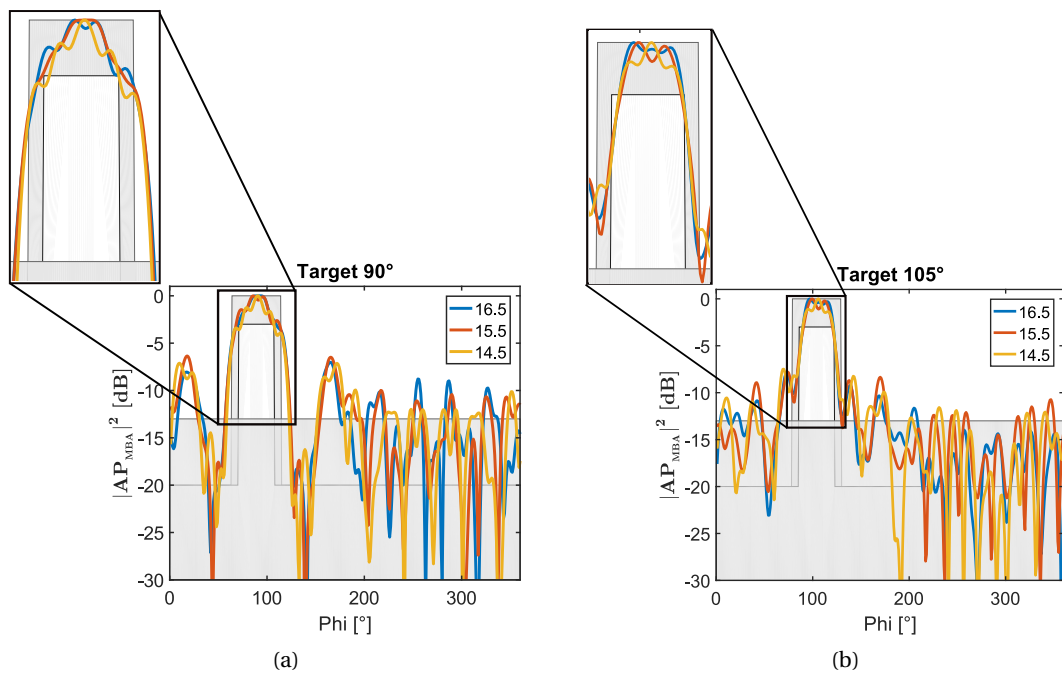


Figure 5.6 – Synthesized patterns, given the variation of the subarray width, targeting a) 90° b) 105° c) 120° b) 135°. Legend refers to subarray width sub_a in mm

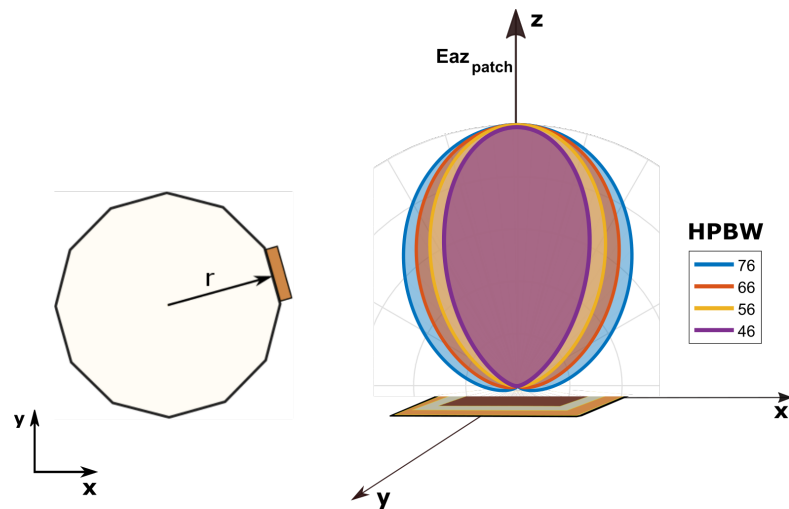


Figure 5.7 – 12-sector antenna architecture based on antenna elements with different beamwidths (HPBW = [46°, 56°, 66°, 76°])

performed for a constraint mask with C_2 (beamwidth) = 60°. Thus, S_0 is defined as

$$S_0 = \begin{cases} C_1 \text{ (target):} & [90^\circ, 105^\circ] \\ C_2 \text{ (beamwidth):} & [40^\circ, 60^\circ] \\ C_3 \text{ (SLL):} & -13 \text{ dB} \end{cases} \quad (5.5)$$

The obtained results in the second test (see Figure 5.9) additionally suggest that using an antenna element with narrower beamwidth can contribute to a better agreement to the mask, thus improving the MBA performance in azimuth. This can be obtained by either using an element with a larger aperture or an array of elements.

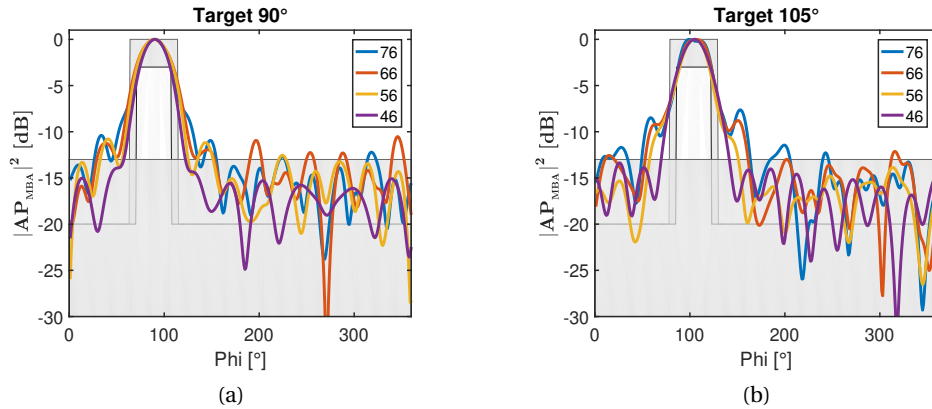


Figure 5.8 – Synthesized patterns for arrays based on antenna elements with different beamwidths, targeting a) 90° b) 105° with constraint $C_2 = 40^\circ$. Legend refers to the antenna element beamwidth HPBW in degrees

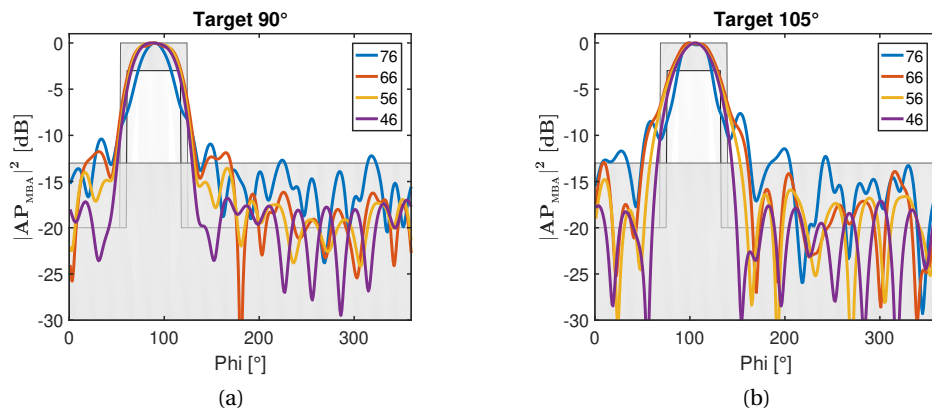


Figure 5.9 – Synthesized patterns for arrays based on antenna elements with different beamwidths, targeting a) 90° b) 105° with constraint $C_2 = 60^\circ$. Legend refers to the antenna element beamwidth HPBW in degrees

To sum up, the effect of the antenna number of sectors, the subarray width and the subarray pattern considering the antenna multibeam forming capabilities in azimuth was studied. The main outcomes of this analysis are:

- After considering different configurations (4, 8, 12 and 18 sectors), an antenna architecture of twelve subarrays ($M=12$) has been found to be a good cost-performance compromise.

- Reducing the subarray width sub_a showed to be beneficial for meeting the main beam synthesis constraints.
- Reducing the antenna element pattern beamwidth (HPBW) contributes to enhancing the desired array multibeam forming capabilities.

The two last outcomes seem contradictory, as having a narrower beam implies having a broader electrical width. However, a broader useful electrical width can be reached with a narrower physical width by reducing the lost space on the sides of the radiators. This lost space is imposed by the mechanical specifications of the feeding network layer.

5.2.4 Optimized subarray design

In this section, an optimized subarray is proposed taking into account the conclusions summarized above. Considering a 12-sector array configuration, the subarray pattern beamwidth in azimuth is reduced, and based on this prototype, the subarray width is also reduced.

Subarray beamwidth

A practical way of reducing the subarray element beamwidth in azimuth, only requiring minor modifications in the original design, is making the top patch antenna electrically larger. The optimized antenna is depicted in Figure 5.10, where the top antenna consists in a 1x3 patches separated at a distance of 0.3λ . Compared to the initial antenna element, the patches, the slot and the antenna cavity in azimuth were slightly modified. Note that in this new subarray (Subarray_{HPBW}) only the antenna element has been modified, whereas the feeding network has remained as in Subarray₀, with $sub_a = 16.5$ mm.

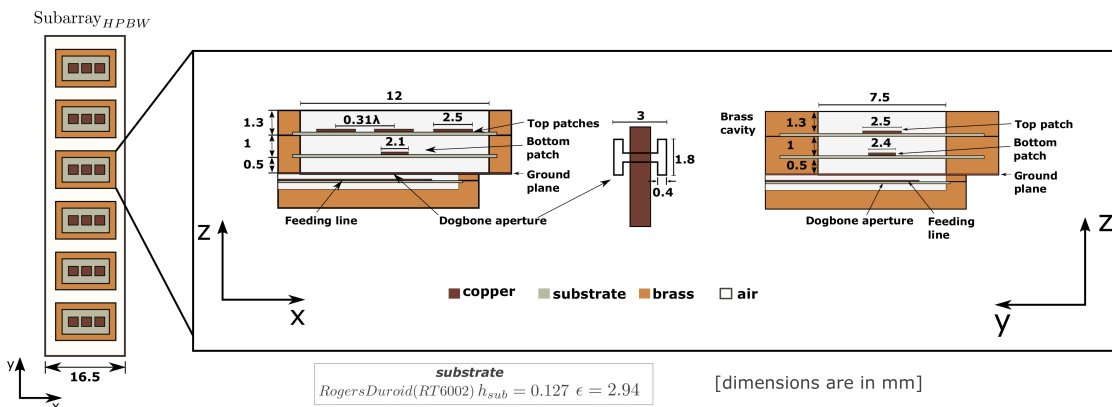


Figure 5.10 – Geometry of Subarray_{HPBW}

As shown in Figure 5.11, the optimized antenna element presents a radiation pattern with a narrower beamwidth than the initial element.

The subarray Subarray_{HPBW} was used to design a 12-sector antenna and the DBFN constrained

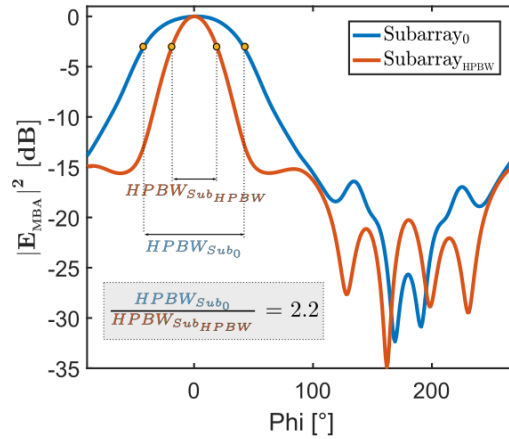


Figure 5.11 – Comparison between the radiation patterns in azimuth of Subarray_{HPBW} and Subarray₀

by S_0 was synthesized. Figure 5.12 shows this result compared to the initially proposed subarray Subarray₀.

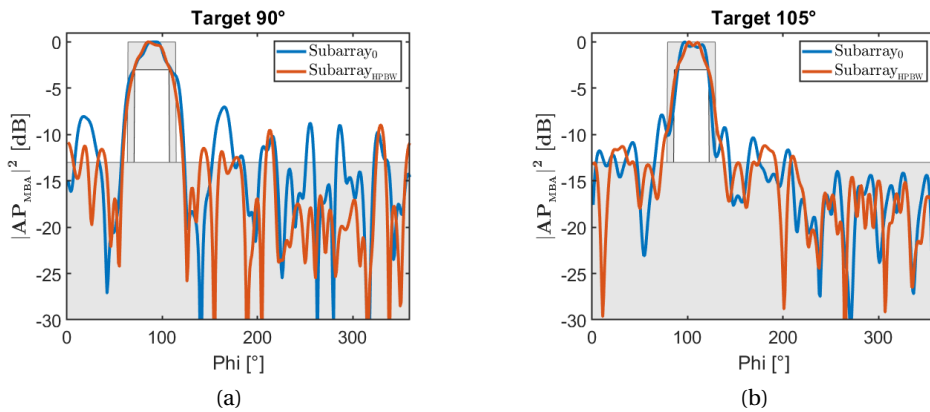


Figure 5.12 – Synthesized patterns of a 12-sector antenna based on Subarray₀ and Subarray_{HPBW} targeting a) 90° b) 105°

As depicted in Figure 5.12, the antenna based on Subarray_{HPBW} matches more adequately the defined constraint mask regarding both, the main beam shape and SLL threshold, which is reduced by approximately 2 dB.

Subarray width

Various 12-sector antennas (based on Subarray_{HPBW}) were analytically built having $sub_a = [16.5 \text{ mm}, 15.5 \text{ mm}, 14.5 \text{ mm}]$, as depicted in Figure 5.13.

Figure 5.14 shows the synthesized patterns AP_{MBA} considering S_0 when varying sub_a .

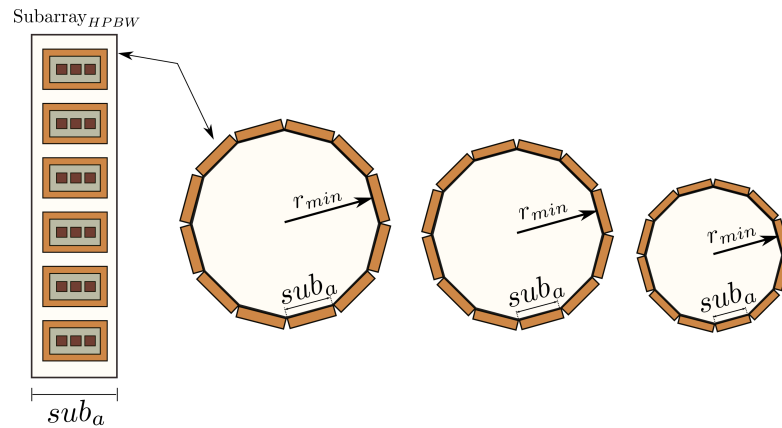


Figure 5.13 – 12-sector antenna architectures (based on Subarray_{HPBW}) having different subarray width sub_a

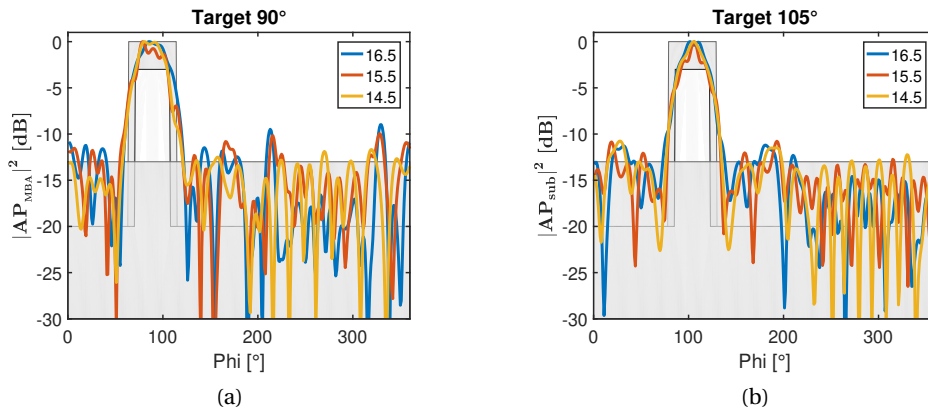


Figure 5.14 – Synthesized patterns, given the variation of the subarray width, targeting a) 90° b) 105° c) 120° b) 135°. Legend refers to subarray width sub_a in mm

Although the difference between the curves is less pronounced than in the previous analysis, the narrowest subarray presents an overall superior performance, with the main beam slightly closer to the constraint mask and the lowest SLL when targeting 90°. In the case of targeting 105° the three subarrays present similar SLL. Consequently, the goal is to find a practical layout that is as narrow as possible. The most critical layers in this regard are the ones forming the feeding line. This is due to the required space to fit the feeding network components and the transmission line being shielded in a 2-mm-wide cavity, which reduces its meandering flexibility. The subarray feeding line was spatially optimized by reducing the line length in the respective axis and adding a phase shifter if required. Figure 5.15 shows the evolution of the design process to reduce sub_a from Subarray₀ to Subarray_{opt}. In addition, Table 5.3 summarizes the variation of the sector antenna radius and the distance between subarrays.

A visual comparison of the first proposed subarray (Subarray₀) and the optimized subarray (Subarray_{opt}), including their corresponding dimensions, is shown in Figure 5.16. As depicted,

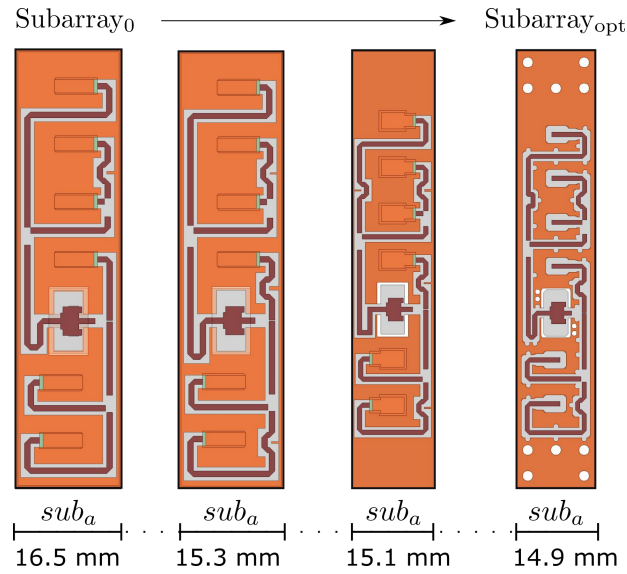


Figure 5.15 – Evolution of the design process to reduce the subarray width

Table 5.3 – Minimum radius and distance between subarrays for different subarray width

Sector width (Sub_a) [mm]	16.5	15.3	15.1	14.6
r_{min} [mm]	30.79	28.55	28.18	27.8
$d(\lambda)$	1.38	1.28	1.26	1.25

Subarray_{opt} is physically narrower, but electrically larger than Subarray₀ in the x axis. These modifications have been carried out as part of the optimization process to enhance the MBA performance in azimuth.

Figure 5.17 shows the synthesized pattern of 12-sector arrays based on Subarray₀ and Subarray_{opt}, both tested under the same set of constraints S_0 . Results show the performance superiority of the optimized subarray, where the main beam achieves a better agreement with the constraint mask and the SLL has been reduced to at least 2.7 dB, compared to Subarray₀.

Thus, this antenna provides an attractive solution for the studied application. The designed Subarray_{opt} in HFSS is depicted in Figure 5.18. The fabrication of the prototype and its performance evaluation through measurements are addressed in the following section. It is worth mentioning that, while the radiation pattern in azimuth was modified, the obtained csc^2 pattern in elevation was preserved, together with the minimum gain figure required in this application.

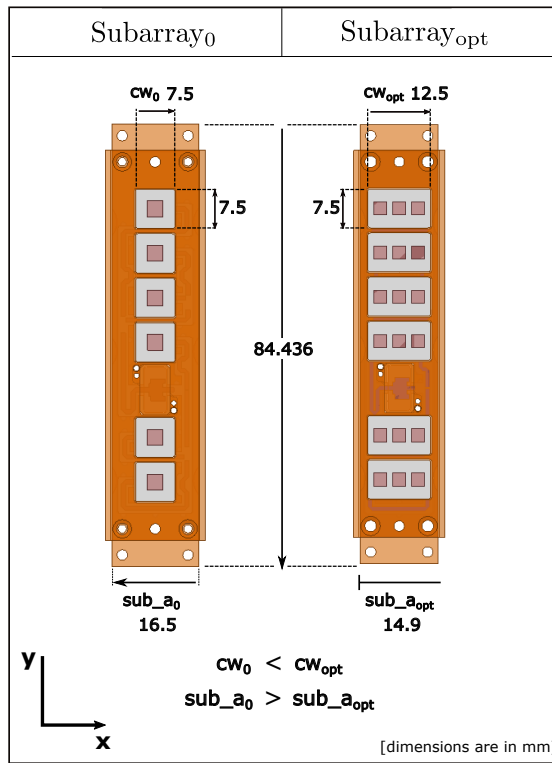


Figure 5.16 – Comparison of Subarray₀ and Subarray_{opt} geometries

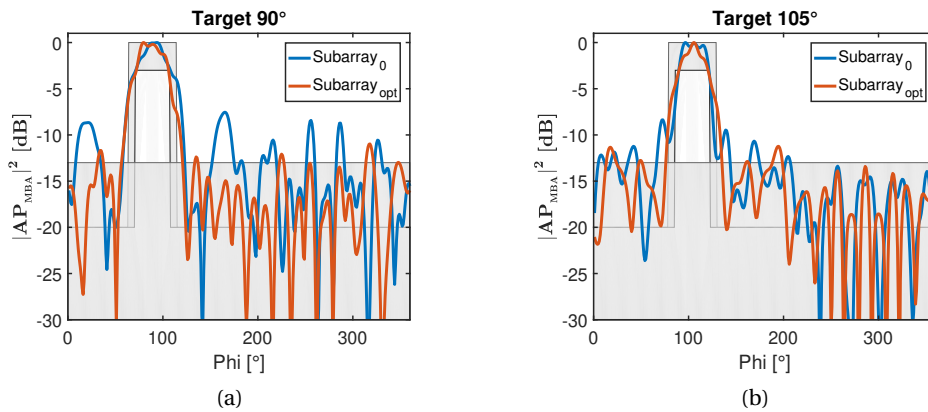


Figure 5.17 – Synthesized pattern of arrays based on Subarray₀ and Subarray_{opt} for constraints S_0 targeting a) 90° b) 105°

5.3 Multiple beam antenna implementation and results

The optimized subarray was used to build a section of the 12-sector multibeam antenna. With the purpose of experimentally validating the multibeam forming antenna capabilities in azimuth while taking into account the mutual coupling, three subarrays were implemented as shown in Figure 5.19.



Figure 5.18 – Optimized subarray $\text{Subarray}_{\text{opt}}$

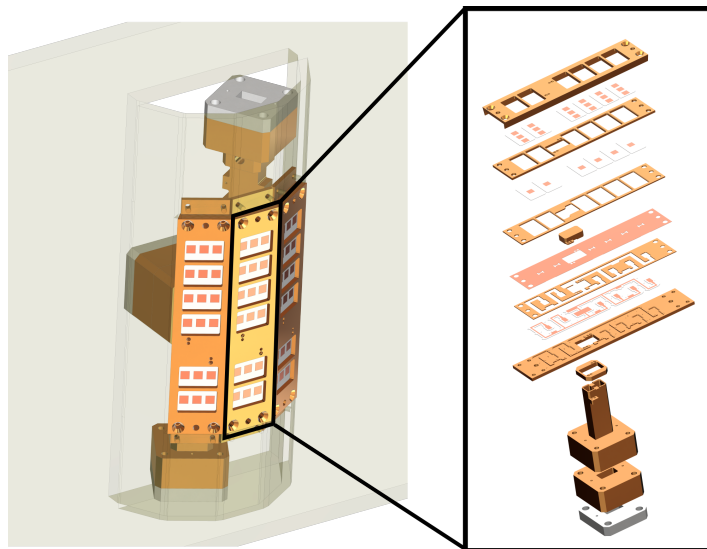


Figure 5.19 – Fabricated section of the proposed multibeam antenna. An exploded view of the subarray in central position is provided. Technical drawings detailing the subarray parts are included in the Appendix B.

Due to space limitations of the available connectors, the lateral subarrays are fed using a WG bend as depicted in Figure 5.20.

Although technical drawings detailing each of the subarray parts are included in Appendix B, some relevant parts of the implemented subarray are presented next.

The feeding port (see Figure 5.21) of the subarrays in lateral positions was realized in 4 parts:

- A square structure adapted to the connector size.
- A WG bend fabricated in two parts, each of them including a transition from a standard

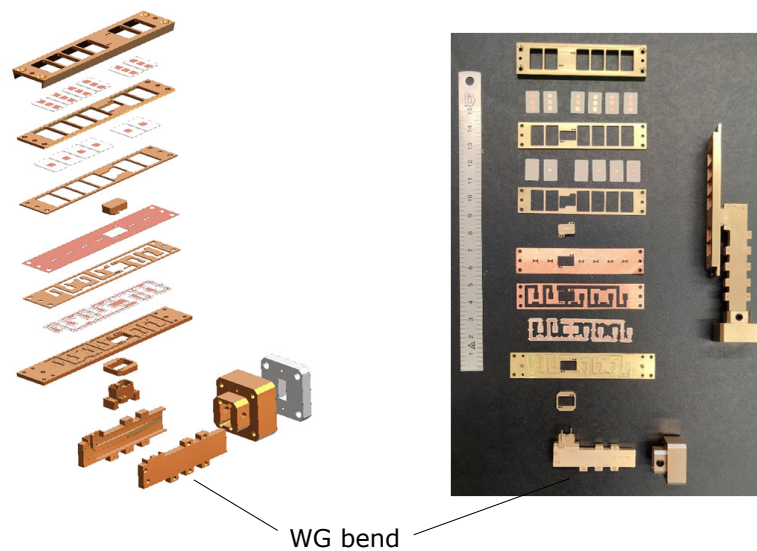


Figure 5.20 – lateral subarrays: (left) exploded view and (right) fabricated parts. Technical drawings detailing the subarray parts are included in the Appendix B.

WG to a ridged WG

- The ridged-WG-end structure containing fixing points to both, the WG bend and the rest of the subarray parts.

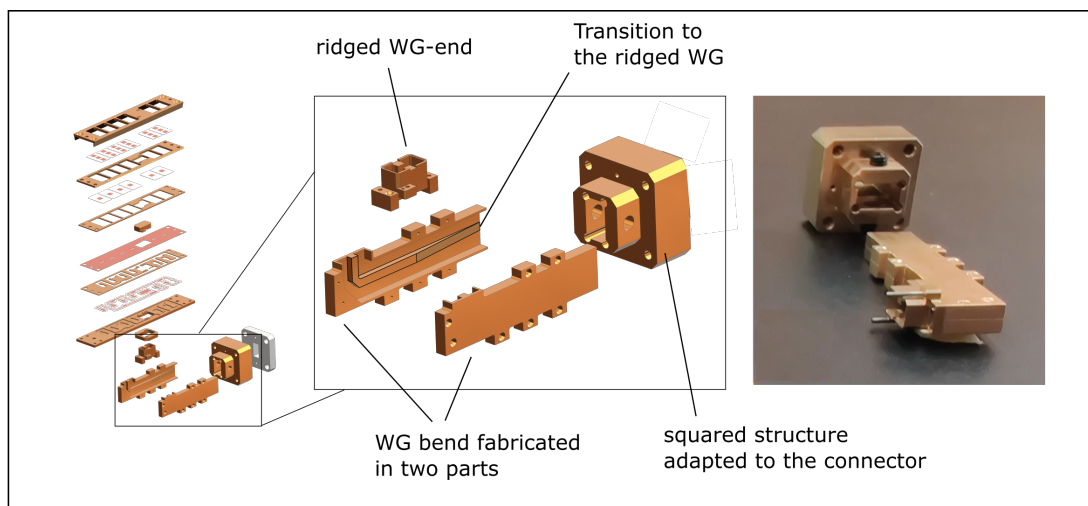


Figure 5.21 – Feeding port of the lateral subarrays

Various PCB parts are highlighted in Figure 5.22, including the feeding line and the antenna bottom and top layers, the latter containing the 1x3 patches.

The prototypes were assembled and mounted on a 3D printed structure that provides the appropriate array configuration (see Figure 5.23). In addition, Figure 5.24 shows the measure-

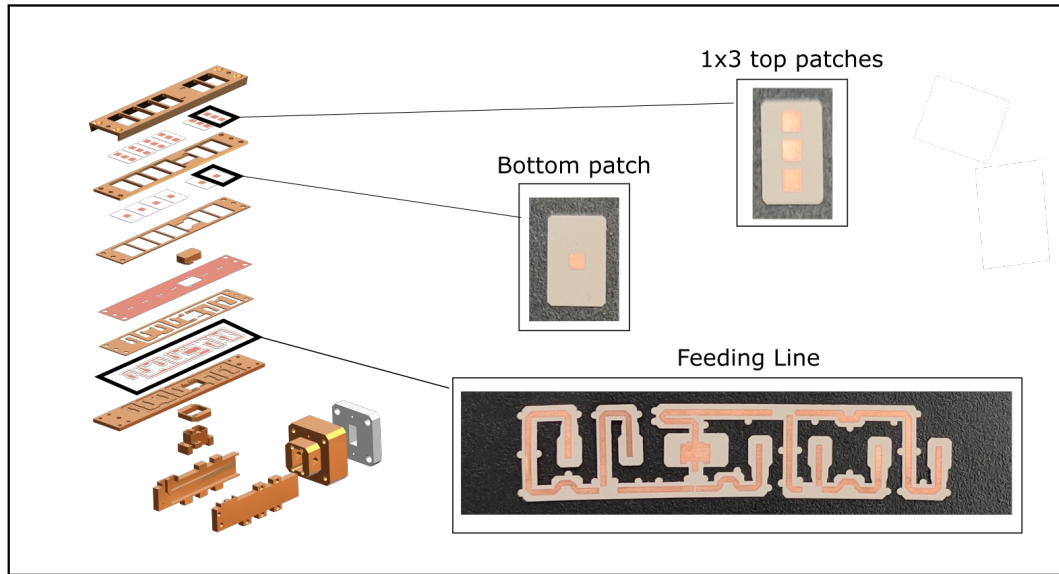


Figure 5.22 – Subarray PCB parts

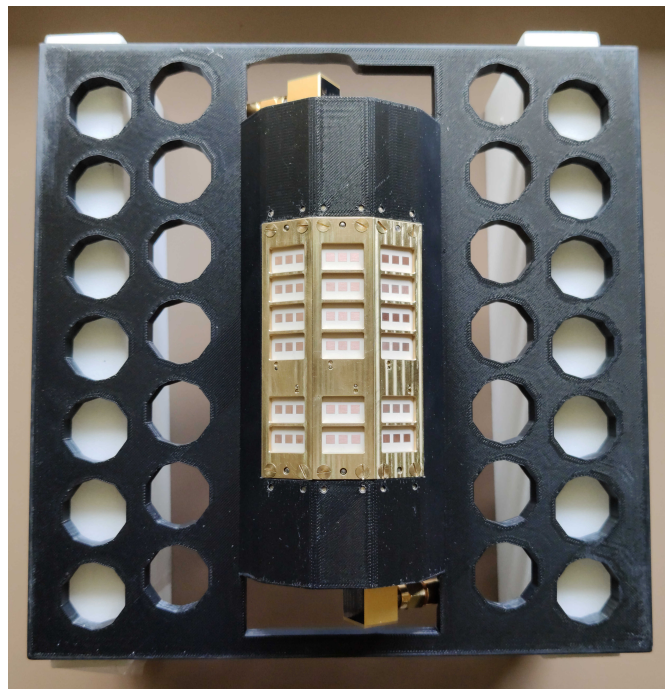
ment set-up for obtaining the antenna radiation pattern and gain results.

As depicted in Figure 5.25, there is a very good agreement between simulated and measured S_{11} curves. This confirms that the subarray impedance bandwidth covers the entire frequency band (12.5%) for the 5G mobile service in Europe in accordance with the first set of 5G standards.

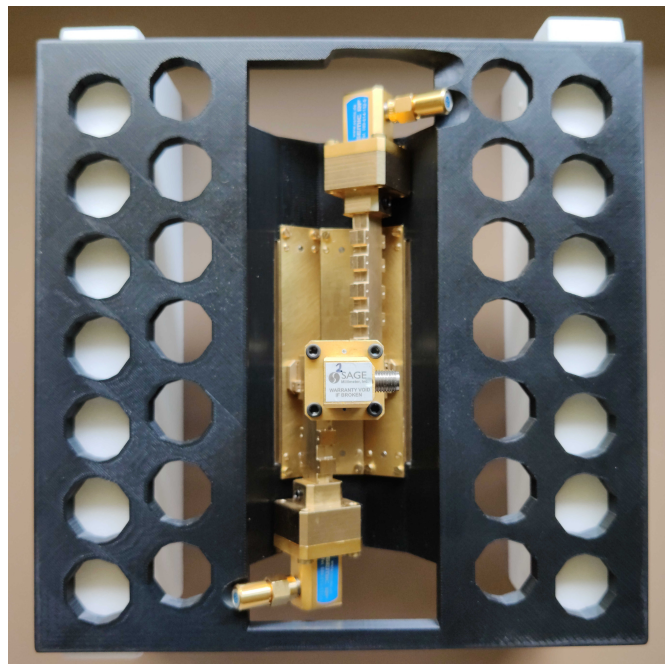
The subarray pattern in elevation was measured and compared to the csc^2 constraint mask. Figure 5.26 shows a good agreement between simulated and measured results, presenting a csc^2 pattern shape along the main beam (for 40° approximately) and SLL smaller than -14.91 dB, only 0.4 dB higher than the simulated SLL limit.

The measured realized gain (see Figure 5.27) is higher than 10 dBi along the operational bandwidth with a maximum value of 15 dBi. In the considered bandwidth, the measured gain is less than 1 dB different from the simulated parameter which indicates the reliability of the proposed solution.

Similar to the analysis carried out in Chapter 4, the subarray pattern bandwidth has been specified considering the frequency range that provides both, the desired pattern shape with $\text{SLL} < -10$ dB and the required picocell coverage capabilities. Figure 5.28 shows that the desired pattern shape is maintained, with $\text{SLL} < -10$ dB approximately, along the frequency range from 24.9 GHz to 26.8 GHz, covering a radiation pattern bandwidth of 7.3% . Regarding the coverage capabilities, the received power versus distance for a LOS path loss exponent $n_{p\min} = 2.22$ and $n_{p\max} = 2.45$ has been plotted in Figure 5.29. The shaded region represents the frequency range from 24.9 GHz to 26.8 GHz, and the solid and dashed lines, the worst-case within such range for $n_{p\min}$ and $n_{p\max}$, respectively. For the analyzed bandwidth (24.9 GHz -



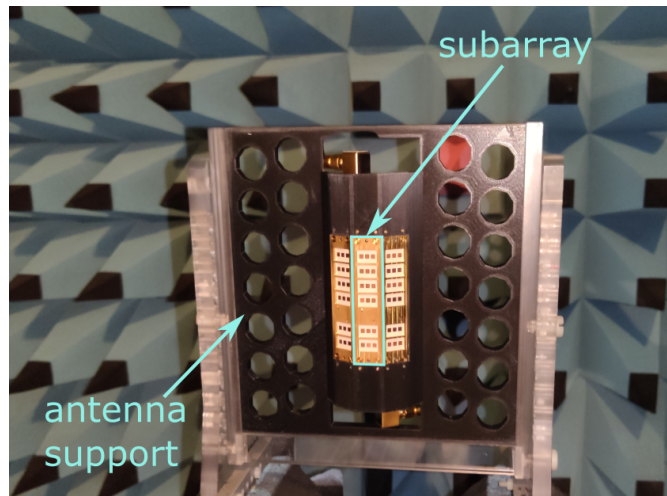
(a)



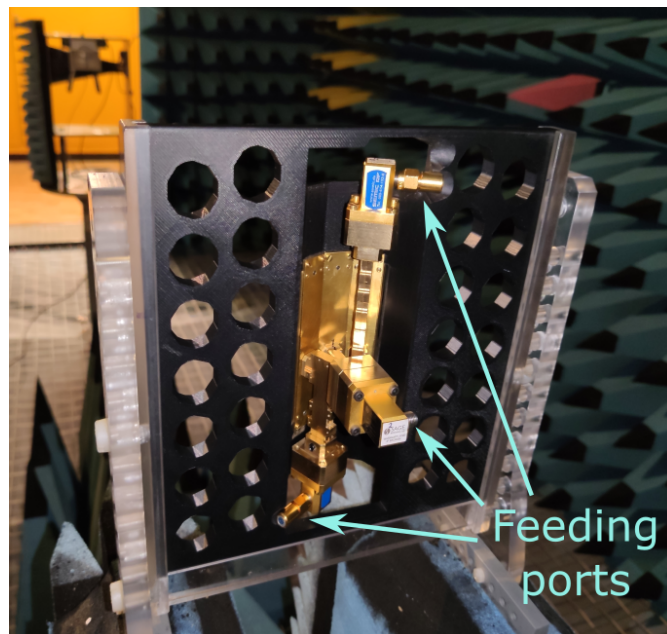
(b)

Figure 5.23 – Antenna array mounted on the 3D printed support a) front view b) back view

26.8 GHz), a signal can be detected at a radius longer than 200 m if $n_{pmin} = 2.22$. The coverage radius when $n_{pmax} = 2.45$ is only reduced to 183 m.



(a)



(b)

Figure 5.24 – Measurement set-up in the MAG anechoic chamber containing the multibeam antenna array mounted on 3D printed support a) front view b) back view

We can say that the subarray design requirements regarding, gain, pattern shape in elevation, and impedance and pattern bandwidths are fulfilled. The adequate performance of this prototype has been validated showing a very good agreement between simulated and measured results.

Table 5.4 summarizes the main features of both subarrays, Subarray₀ and Subarray_{opt}, compared to the specified design parameters. Both subarrays present attractive results regarding the S_{11} and radiation pattern bandwidths, and gain figures, fitting the design requirements.

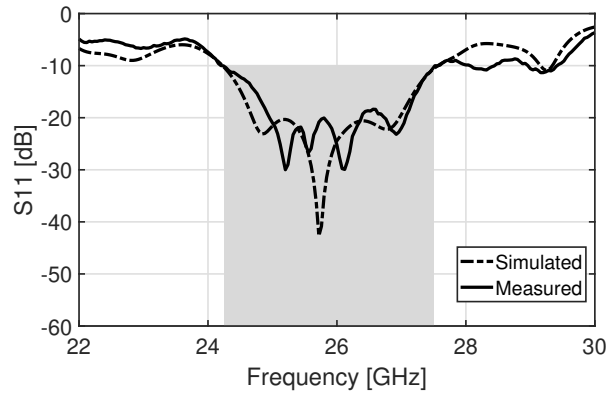


Figure 5.25 – Simulated and measured S_{11}

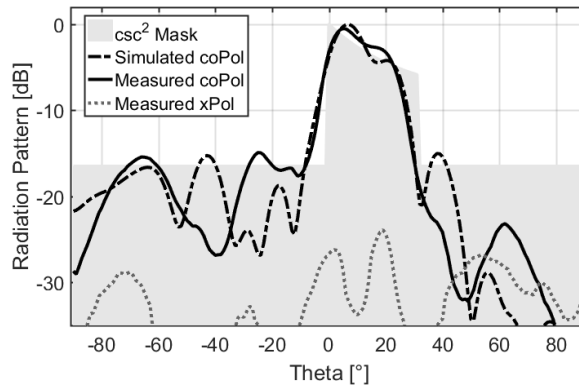


Figure 5.26 – Simulated and measured radiation pattern at 25.9 GHz

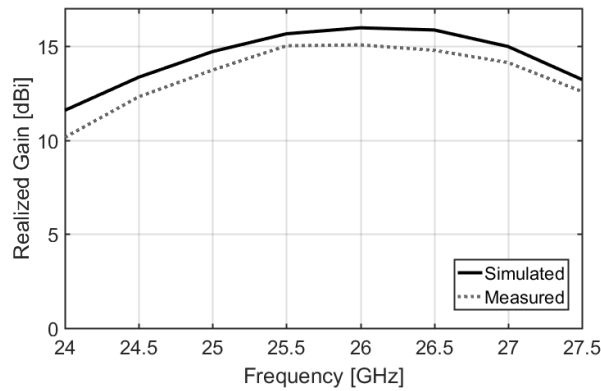


Figure 5.27 – Simulated and measured realized gain as a function of frequency

Compared to Subarray_0 , the subarray $\text{Subarray}_{\text{opt}}$ presents a smaller impedance bandwidth, yet wide and above the required value. In addition, with a higher gain, this prototype covers a longer picocell radius in the studied LOS n_p range. Furthermore, an antenna formed by $\text{Subarray}_{\text{opt}}$ has shown to be a more suitable architecture for generating multiple and

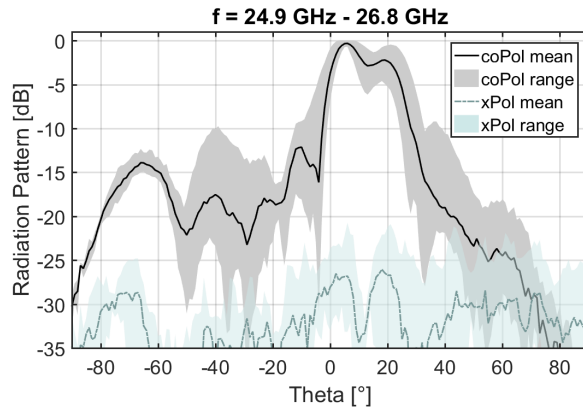


Figure 5.28 – Measured radiation pattern of the optimized subarray: range (shaded) of the copolarized and crosspolarized patterns at the band 24.9-26.8 GHz and mean (solid) of the copolarized and crosspolarized patterns at the band 24.9-26.8 GHz

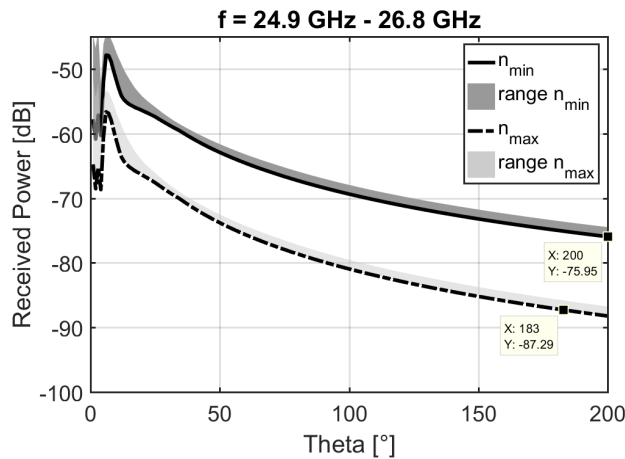


Figure 5.29 – Received power vs distance for LOS $n_{pmin} = 2.22$ and $n_{pmax} = 2.45$ at the band 24.75 GHz - 26.75 GHz (shaded) and worst case within this band (solid)

orthogonal beams in the studied application. This will be investigated next.

The multibeam forming antenna capabilities of a 12-sector antenna based on the fabricated prototype $Subarray_{opt}$ were examined, considering the design requirements of the DBFN in azimuth. With this aim, two sets of constraints S_1 and S_2 were defined. The set S_1 (defined in Equation (5.6)) aims at synthesizing orthogonal beams so that they are spaced approximately HPBW apart from each other and present little interference. This is successfully attained as shown in Figure 5.30 a). Given the antenna array symmetry, the synthesized pattern in Figure

Table 5.4 – Features of subarrays Subarray₀ and Subarray_{opt} compared to the required design parameters

	Requirements	Subarray ₀	Subarray _{opt}
S₁₁ bandwidth	7%	19.2%	12.5%
Radiation pattern bandwidth	7%	7.7%	7.3%
Gain	>10 dBi for 7% bandwidth	>10 dBi for 11.5% bandwidth	>10 dBi for 13.46% bandwidth
Maximum gain	-	12.94 dBi	15 dBi
Coverage	200 m	>200 m at LOS $n_p = 2.22$	>200 m at LOS $n_p = 2.22$
Picocell length		156 m at LOS $n_p = 2.45$	183 m at LOS $n_p = 2.45$

5.30 a) can be equivalently obtained in any other orientations.

$$S_1 = \begin{cases} C_1 \text{ (target):} & [35^\circ, 65^\circ, 90^\circ, 115^\circ] \\ C_2 \text{ (beamwidth):} & 20^\circ \\ C_3 \text{ (SLL):} & -13 \text{ dB} \end{cases} \quad (5.6)$$

As shown in Figure 5.30 b), the synthesized results obtained under the set of constraints S_2 (see Equation (5.7)) confirm that the proposed antenna can generate multiple orthogonal beams at arbitrary directions covering a wide variety of targets that imitates a possible service scenario.

$$S_2 = \begin{cases} C_1 \text{ (target):} & [35^\circ, 115^\circ, 240^\circ] \\ C_2 \text{ (beamwidth):} & 20^\circ \\ C_3 \text{ (SLL):} & -13 \text{ dB} \end{cases} \quad (5.7)$$

Next, the beamwidth range of the antenna in azimuth was analyzed. The studied set of

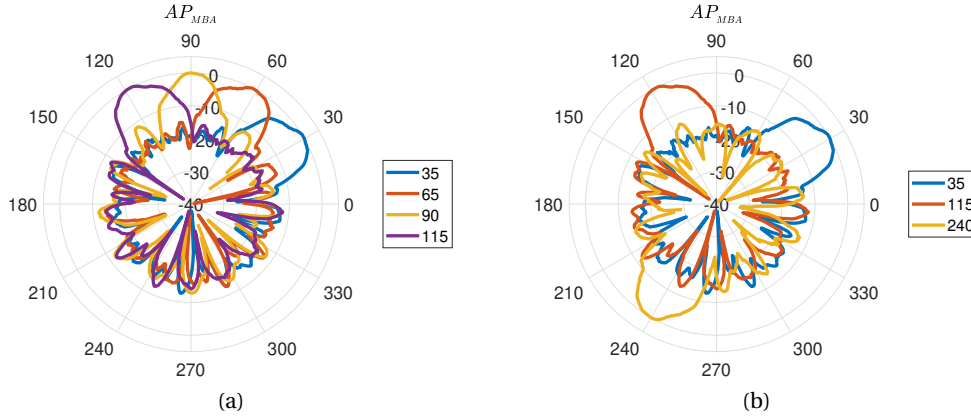


Figure 5.30 – Multiple beamforming a) in a continuous target range b) with arbitrary targets

constraints S_3 is summarized next.

$$S_3 = \begin{cases} C_1 \text{ (target)} : & 90^\circ \\ C_2 \text{ (beamwidth)} : & [20^\circ, 40^\circ, 60^\circ] \\ C_3 \text{ (SLL)} : & -13 \text{ dB} \end{cases} \quad (5.8)$$

The synthesized AP_{MBA} patterns correlate well to the constraint mask (defined by S_3), as depicted in Figure 5.31. This analysis was extended to a wider range of targets. Constraint C_1 was set at extreme angles, $C_1 = 75^\circ$, broadside for one sector, $C_1 = 90^\circ$, lying exactly on between two sectors and $C_1 = 82^\circ$, approximately in between the two previous values (see Figure 5.32).

The set of constraints in this case can be defined as

$$S_4 = \begin{cases} C_1 \text{ (target)} : & [75^\circ, 82^\circ, 90^\circ] \\ C_2 \text{ (beamwidth)} : & [20^\circ, 40^\circ, 60^\circ] \\ C_3 \text{ (SLL)} : & -13 \text{ dB} \end{cases} \quad (5.9)$$

Synthesized patterns targeting C_1 were centered at 0° for an adequate comparison. Figure 5.33 shows the mean synthesized pattern in solid line and its variation range (according to C_1) represented by the shaded region when C_2 is a) 20° , b) 40° and c) 60° .

In the three cases, synthesized patterns AP_{MBA} agree well with the constraint mask for the range of C_1 targets. Larger differences were obtained for beamwidths around 20° ($C_2 = 20^\circ$), defining a threshold in the proposed antenna performance.

The obtained results provide relevant insights into the DBFN beamsteering capabilities. Addi-

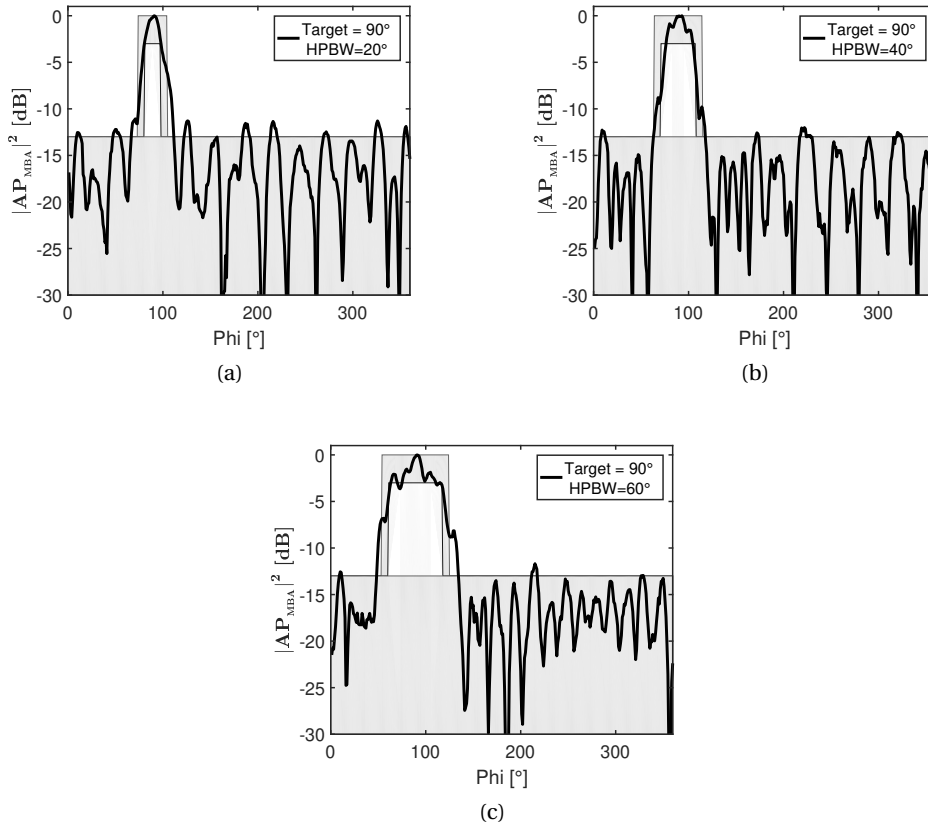


Figure 5.31 – Synthesized AP_{MBA} considering the set of constraints S_3 with a) $C_2 = 20^\circ$ b) $C_2 = 40^\circ$ c) $C_2 = 60^\circ$

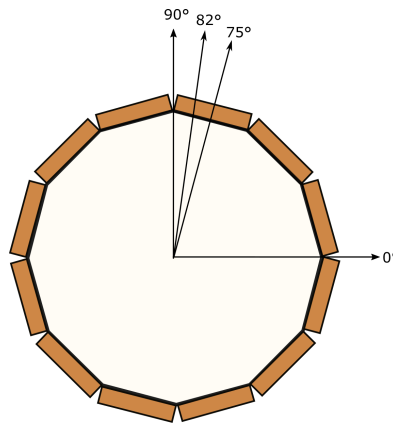


Figure 5.32 – Top view of the 12-sector antenna specifying targets C_1 considered in S_4

tionally, the synthesis of multiple orthogonal beams proving 360° coverage in azimuth has been validated in a wide variety of scenarios.

In this chapter, the subarray built in Chapter 4 was used as a building block to analytically

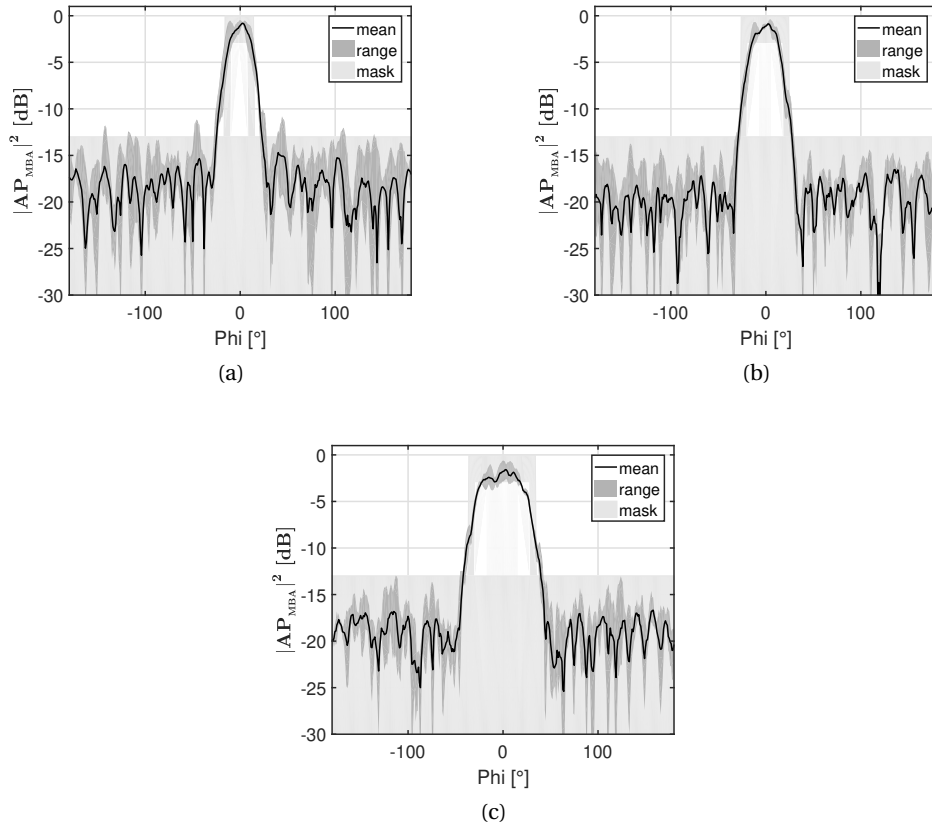


Figure 5.33 – Synthesized AP_{MBA} considering the set of constraints S_4 with a) $C_2 = 20^\circ$ b) $C_2 = 40^\circ$ c) $C_2 = 60^\circ$

build the sectorial MBA antenna. The DBFN for this antenna configuration was synthesized based on a set of constraints (S_0) according to the design requirements in azimuth. After obtaining results that do not reach the required performance, the main parameters influencing this outcome were investigated. Hence, the number of sectors, the subarray width and the antenna element pattern in azimuth were investigated regarding the aforementioned set of constraints. The performed analysis showed that reducing the subarray width and increasing the electrical size of the subarray in azimuth are adequate features to obtain a suitable MBA performance. As a result, the optimized subarray in this chapter (Subarray_{opt}) is physically narrower and electrically larger along the same axis than the initially considered subarray (Subarray₀). A section of the 12-sector antenna array (formed by three Subarray_{opt} subarrays) was built in order to measure the subarray pattern while accounting for the mutual coupling between subarrays. This is a reasonable approach thanks to the antenna symmetry. The DBFN operating in azimuth was synthesized in a wide variety of scenarios and multiple-orthogonal beams were generated, hence demonstrating the adequate antenna applicability. We can say that the proposed antenna represents an interesting solution for a portable picocell station.

6 Conclusions and future work

6.1 Summary

This thesis has addressed the design and fabrication of a portable 5G picocell antenna for emergency communication systems. In this work, enabling compatibility with 5G has been motivated by two main reasons: i) the necessity of having an up-to-date system that can effectively bring service to users in emergency situations, and ii) the possibility of profiting from the prospective 5G enhanced capabilities and reduced latency, compared to previous mobile network generations. In order to address the required traffic capacity and data rate figures in 5G, communications at mm-Waves have been widely recognized as a key enabling solution. Hence, our antenna design has been based on mm-Waves, namely within the range considered for mobile service in Europe (24.25 GHz - 27.5 GHz) in accordance with the first set of 5G standards.

Having defined the case study scenario, the link budget was calculated considering mm-Waves propagation properties, the experimental outcomes from recent measurement campaigns, and the available standard information. This led to the definition of the antenna design requirements. After investigating the state of the art on antennas for 5G, the picocell antenna architecture was proposed. An MxN antenna array fed by a HBFN was selected as a suitable configuration for enabling omnidirectional coverage while meeting the design requirements derived from the link budget. Choosing a HBFN for this antenna is a practical solution to overcome the current development gap on mm-Waves communications until fully-DBFNs are cost-effective. The proposed HBFN consists of a DBFN operating in azimuth and an ABFN providing the adequate excitations in elevation. With M subarrays controlled by the DBFN, multiple-orthogonal beams can be generated, covering 360° in azimuth. Complementary, each N-elements subarray fed by the ABFN can provide a csc^2 pattern shape in elevation, thus guaranteeing uniformly received power within the picocell. This HBFN was synthesized in order to identify key parameters influencing its performance in both elevation and azimuth. These parameters were taken into account in the design of the picocell antenna array. Given the studied application, the required picocell antenna posed challenging design constraints

that have been successfully overcome in this investigation.

The proposed 12x6 antenna array provides broadband efficient operation with relatively small size, adequate for the considered portable picocell station. A section of this antenna formed by three subarrays—sufficiently representative of the complete system in terms of mutual coupling effects—was fabricated and measured. The good agreement between simulated and measured results on the designed antenna validates its performance and the fulfillment of the initial requirements. The measurements demonstrate an impedance bandwidth higher than 12%, a gain higher than 10 dBi over the entire band (13.46%) and a csc^2 pattern shape (with SLL below -10 dB) preserved over a 7.3% of the bandwidth covering a cell radius of up to 183 m in the worst LOS PLE conditions. On the other hand, the DBFN operating in azimuth was synthesized for various sets of constraints. Results showed that multiple orthogonal beams can be obtained targeting any arbitrary direction in azimuth with beamwidths higher than 20° and SLL smaller than -13 dB. This thus demonstrated the antenna applicability for a wide range of service scenarios.

The uniform power distribution in elevation provided by the csc^2 pattern shaped subarray, together with the antenna multibeam forming capabilities in azimuth, guarantee omnidirectional coverage along the picocell. In addition, the fabricated prototype is mechanically robust at the expense of slightly relaxed fabrication costs compared to regular civil picocell stations—yet acceptable considering the smaller scale deployment of this kind of niche applications. The proposed multibeam system operating at mm-Waves bands thus constitutes an up-to-date solution for 5G-compatible terrestrial emergency communications.

The main contributions per thesis chapter are listed below:

- Chapter 1
 - An extensive state-of-the-art investigation was carried out to provide a global overview about 5G.
- Chapter 2
 - Given the immature state of 5G mm-Waves mobile communications and the still in progress 5G standard definition, this chapter presents a collection of the necessary information for calculating the link budget in the studied scenario. The mm-Waves propagation properties, recent measurement campaigns, and the latest available standard release were investigated.
 - Due to the novelty of 5G mobile communications, besides the state of the art on 5G antennas, a more specific literature investigation was carried out to identifying a proper picocell base station architecture for our case study scenario.
- Chapter 3
 - A summary on antenna pattern synthesis methods is provided.

- The HBFN is synthesized for an analytical array while considering the desired performance in elevation and azimuth. The ABFN synthesis algorithm, consisting of an iterative convex optimization algorithm, is proposed to obtain a csc^2 pattern shape in elevation. In addition, the DBFN is synthesized using iterative convex optimization and alternate projection for generating multiple-orthogonal beams in azimuth.
 - The main parameters influencing the HBFN performance are investigated considering the constraint masks in each plane.
- Chapter 4
 - This chapter provides the guidelines for designing the subarray feeding network, including the weighting vector synthesis, the selection of the adequate topology and layout, the preliminary optimization using the feeding network equivalent circuit model, and the fine optimization in a full-wave simulation tool.
 - In the feeding network synthesis, a practical way to reduce mutual coupling, which is usually neglected in antenna synthesis problems, is proposed. This approach helps to increase the results accuracy and to reduce the optimization time.
 - A novel broadband efficient csc^2 pattern shaped subarray architecture with a compact design and based on a SSL feeding network in parallel configuration is proposed.
 - The subarray components (ridged WG, WG-to-SSL transition, dividers, shifters, and antenna element) are strategically chosen to meet a group of challenging constraints typically found on mm-Wave antenna array design for 5G applications.
 - The implementation and fabrication of the proposed subarray, which did not follow established procedures, are described in detail, thus contributing to extend the fabrication alternatives in mm-Waves antenna design.
 - Chapter 5
 - In this chapter, the subarray is optimized considering the desired DBFN performance in azimuth.
 - The key parameters for improving such performance are identified and a study of such parameters yielding crucial conclusions for effectively optimizing the subarray design is carried out.
 - A section of the antenna array formed by three subarrays was fabricated and measured.
 - The proposed novel broadband efficient mm-Waves antenna capable of generating multiple orthogonal beams in azimuth and providing uniform power distribution in elevation with a relatively compact design is validated for the studied application.

6.2 Perspective and future work

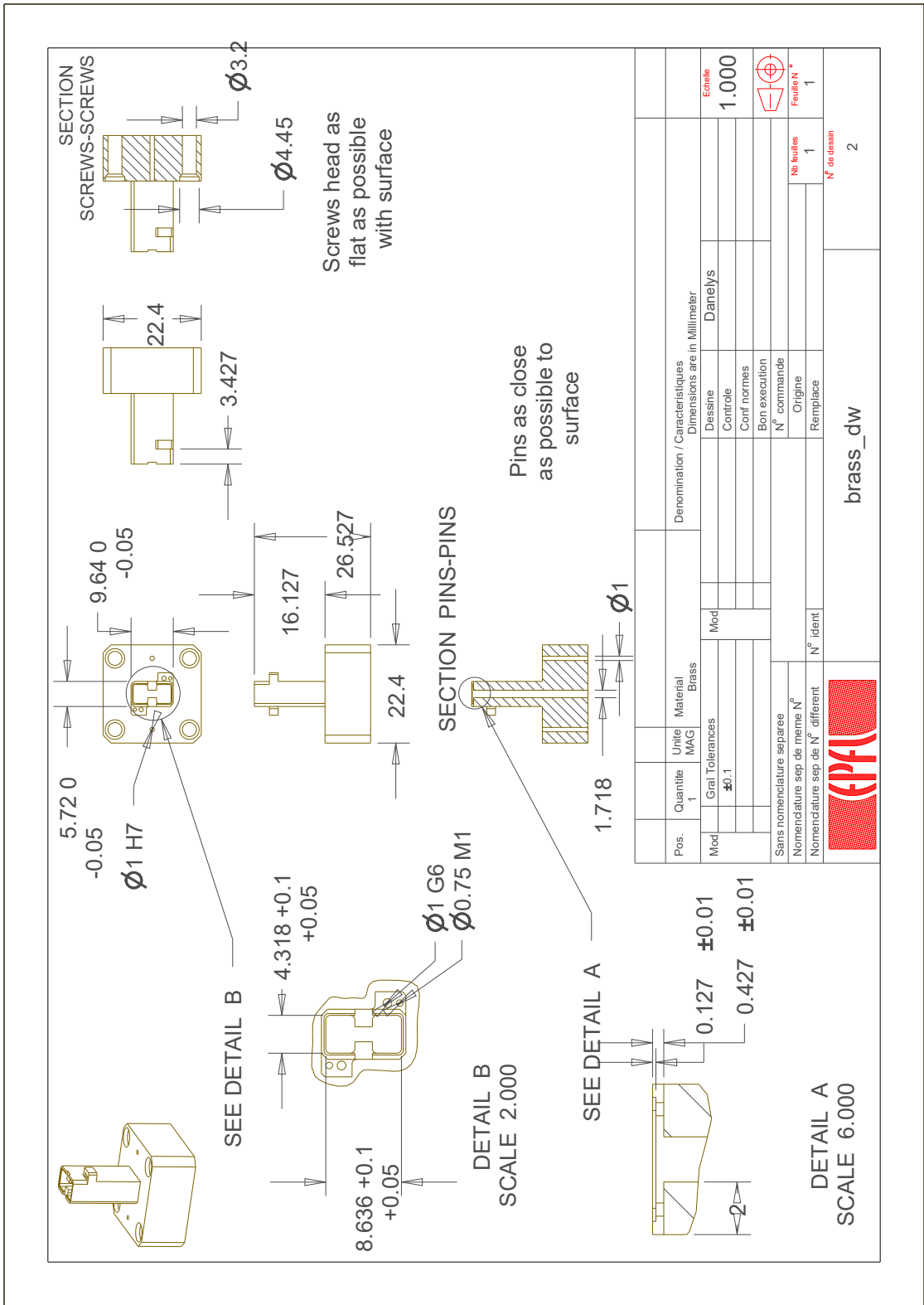
As mentioned in Chapter 2, state-of-the-art transceivers operating at mm-Waves are still power-hungry and costly. Once this technology gap is met and mm-Waves transceivers with compact design are available and affordable, the design and implementation of the DBFN required for the proposed multibeam antenna will be feasible. Additionally, the implementation of the 12-sector antenna would require a more compact connector adapted to the WG feeding port size. The prototype could be then comprehensively evaluated in a more realistic scenario by performing open-air measurements.

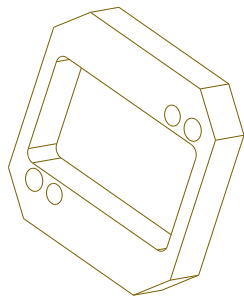
On the other hand, the overall antenna design can be solved using a System-by-Design paradigm [170]. In this approach, the design of a complex system is addressed as the combination of interconnected blocks with different functionalities, such as synthesis, analysis, configuration, and optimization. While its outcome would depend on the adequate definition of the overall optimization scheme, the flexibility provided by this method could enhance the antenna performance (further reducing the obtained bandwidth and SLL limits) given the evaluation of the system as a generality under a centralized optimizer. This approach could be implemented in the problem addressed in this work for integrating the optimization schemes used in elevation and azimuth.

Sparse array theory could be used to evaluate different antenna architectures to investigate the possibility of further reducing the SLL threshold of the synthesized patterns in azimuth. This would imply considering the mechanical limitations of the antenna technology. An approach proposed in [171] addresses this by defining an additional variable to the optimization scheme accounting for the minimal distance between array elements.

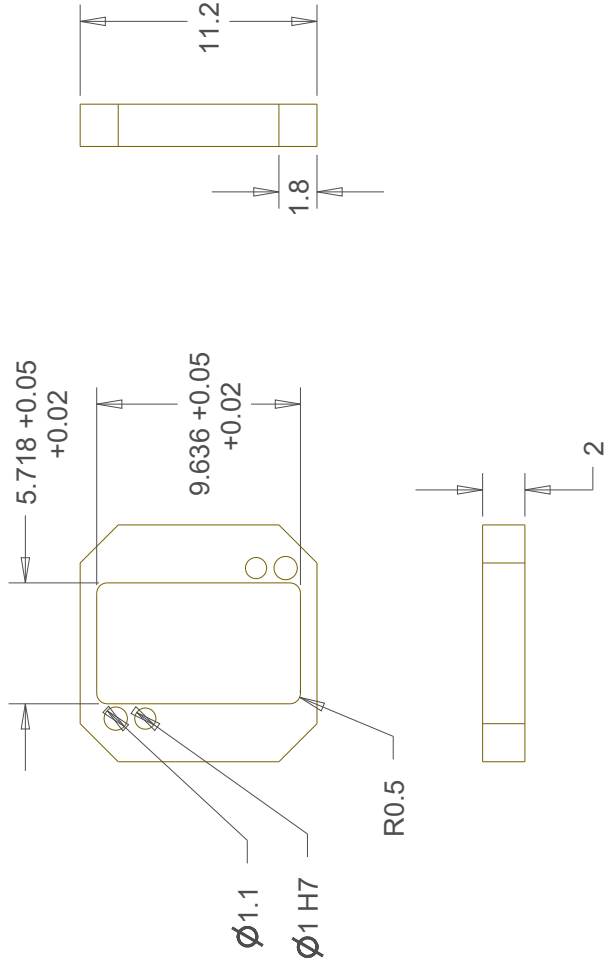
The investigation on slotted-SIW subarrays could be continued to obtain a simpler prototype with reduced cost, compared to the design proposed in this thesis. Considering that slotted-SIW antennas are intrinsically narrowband, a reduced bandwidth performance would be nevertheless expected. However, investigating its advantages and limitations and establishing comparisons with the SSL subarray proposed in this work could extend the available options for the studied application.

A Appendix A





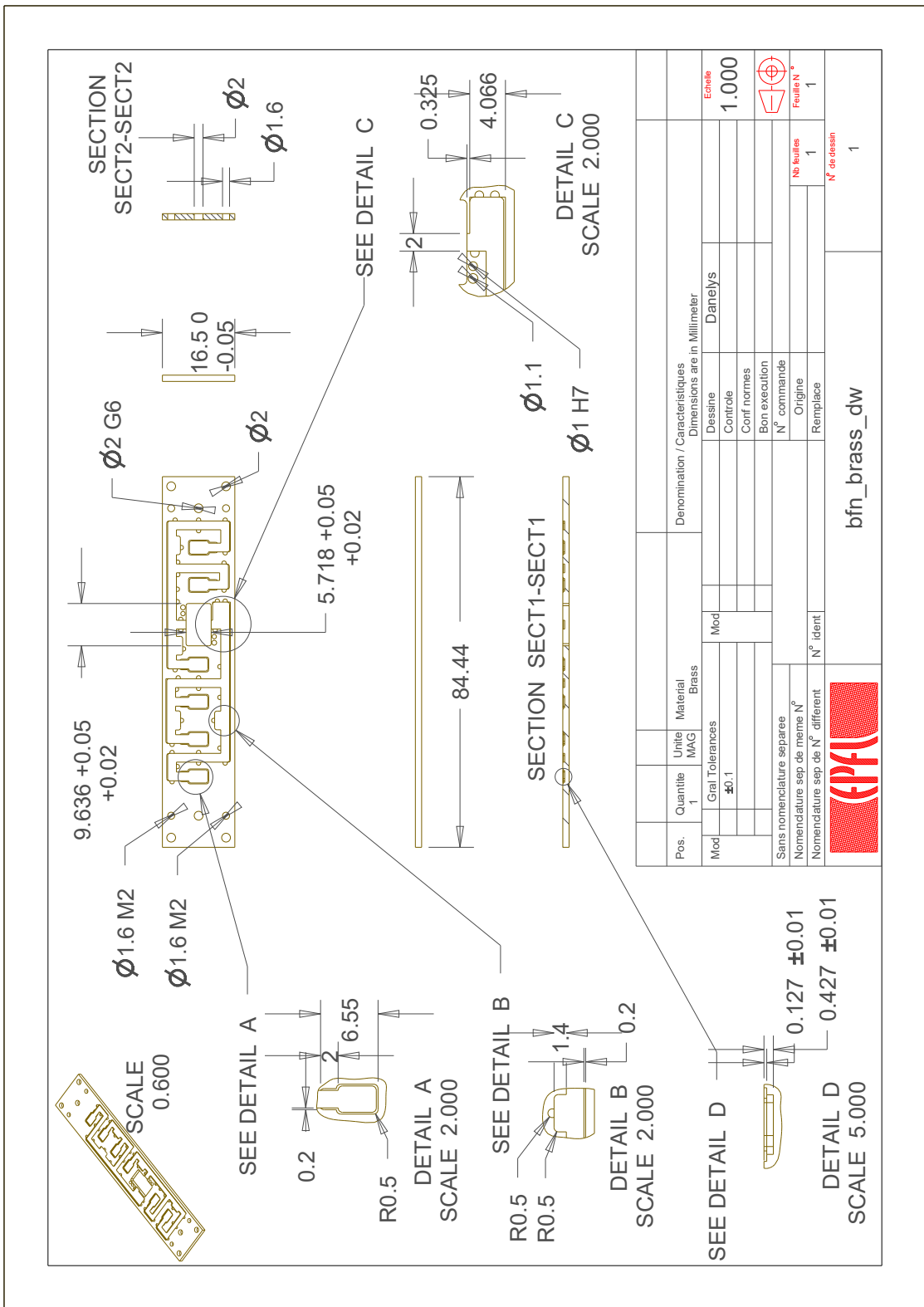
SCALE 4.000



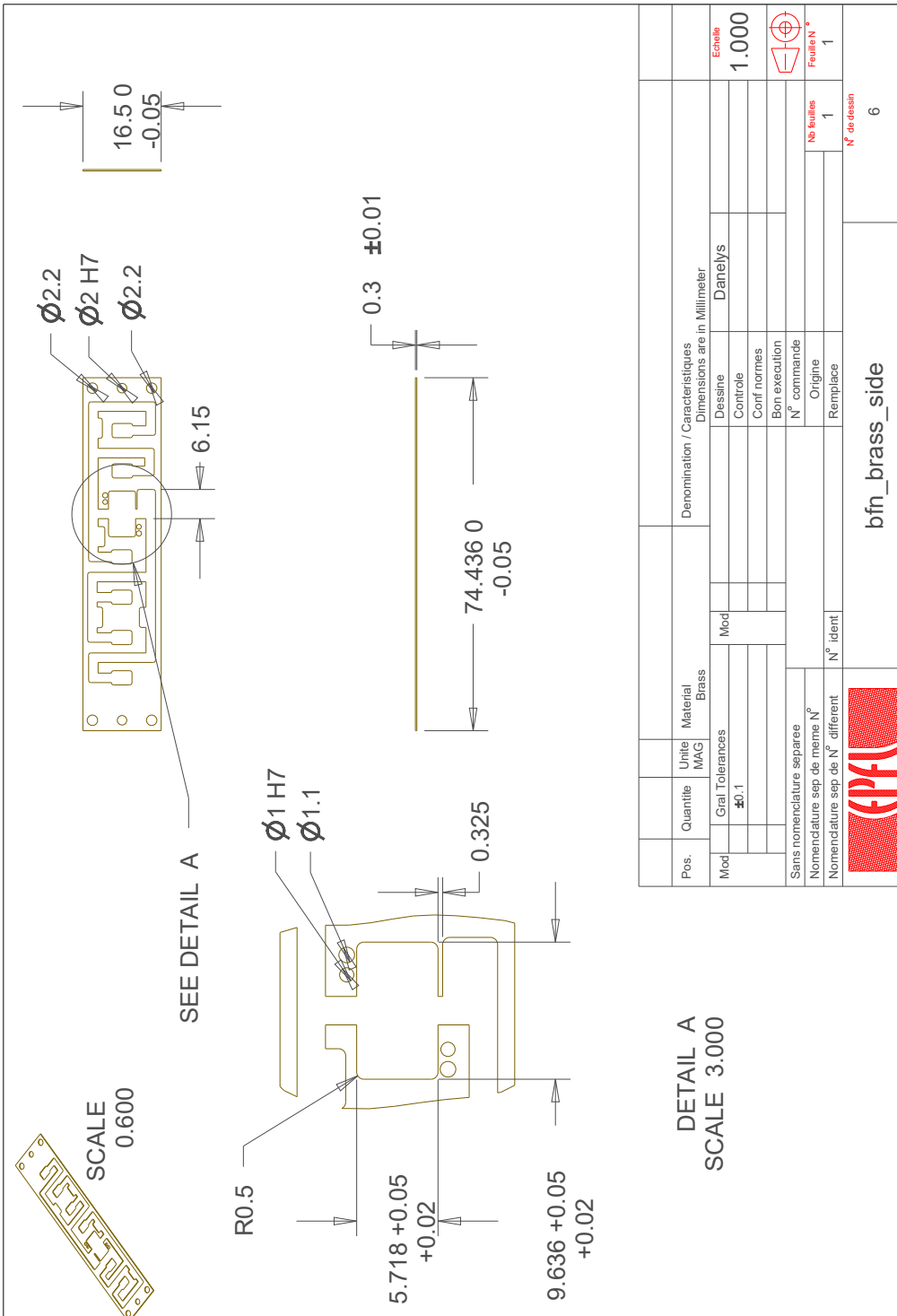
Pos.	Quantite	Unite	Material	Denomination / Caracteristiques	Dimensions are in Millimeter	Echelle
	1	MAG	Brass		Danelys	1.000
Mod	Grat	Tolerances	Mod	Dessine		
		± 0.1		Controle		
				Conf normes		
				Bon execution		
				N° commande		
				Origine		No feuilles
				Remplace		1
						N° de dessin
						5




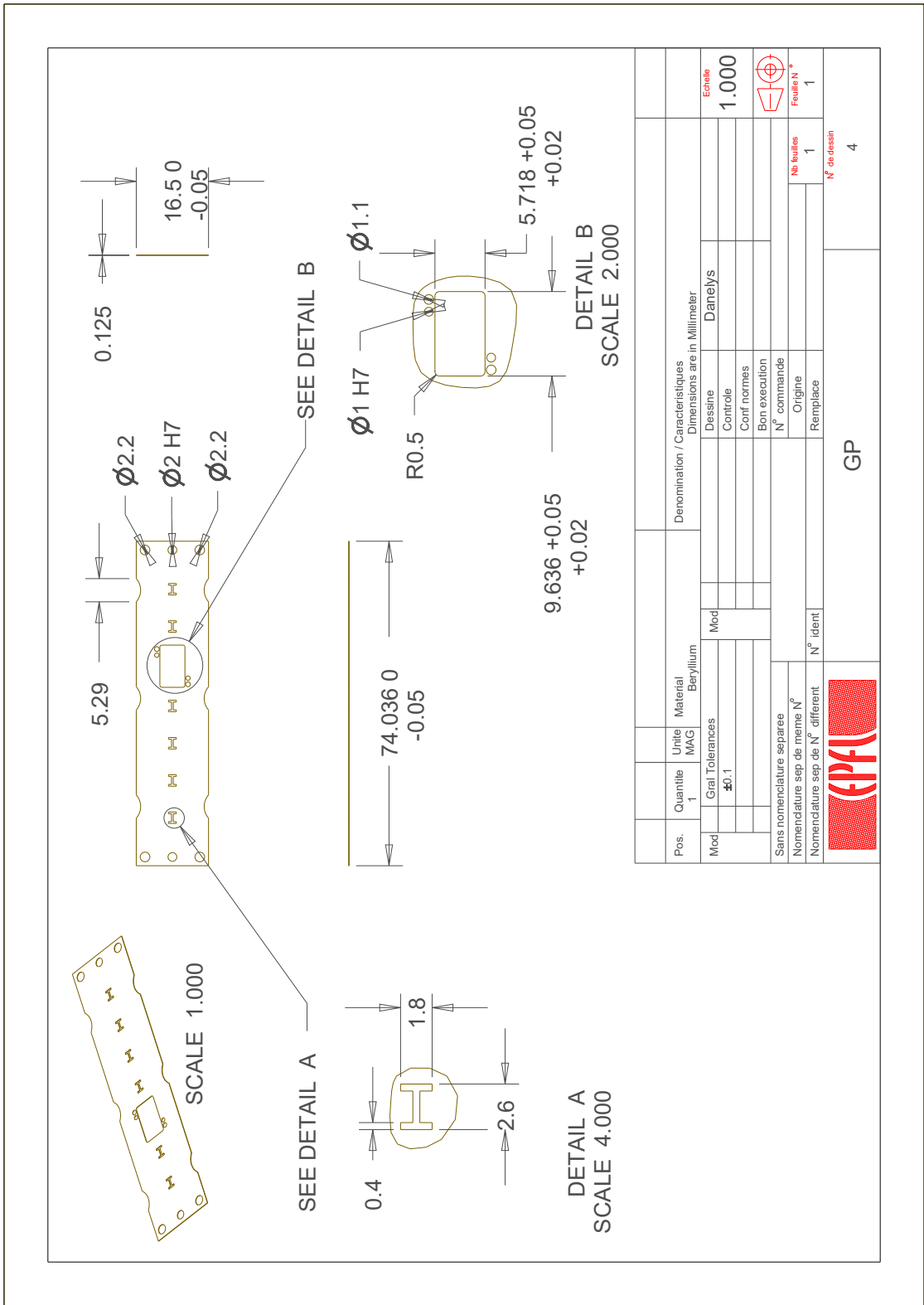
brass_dw_nut

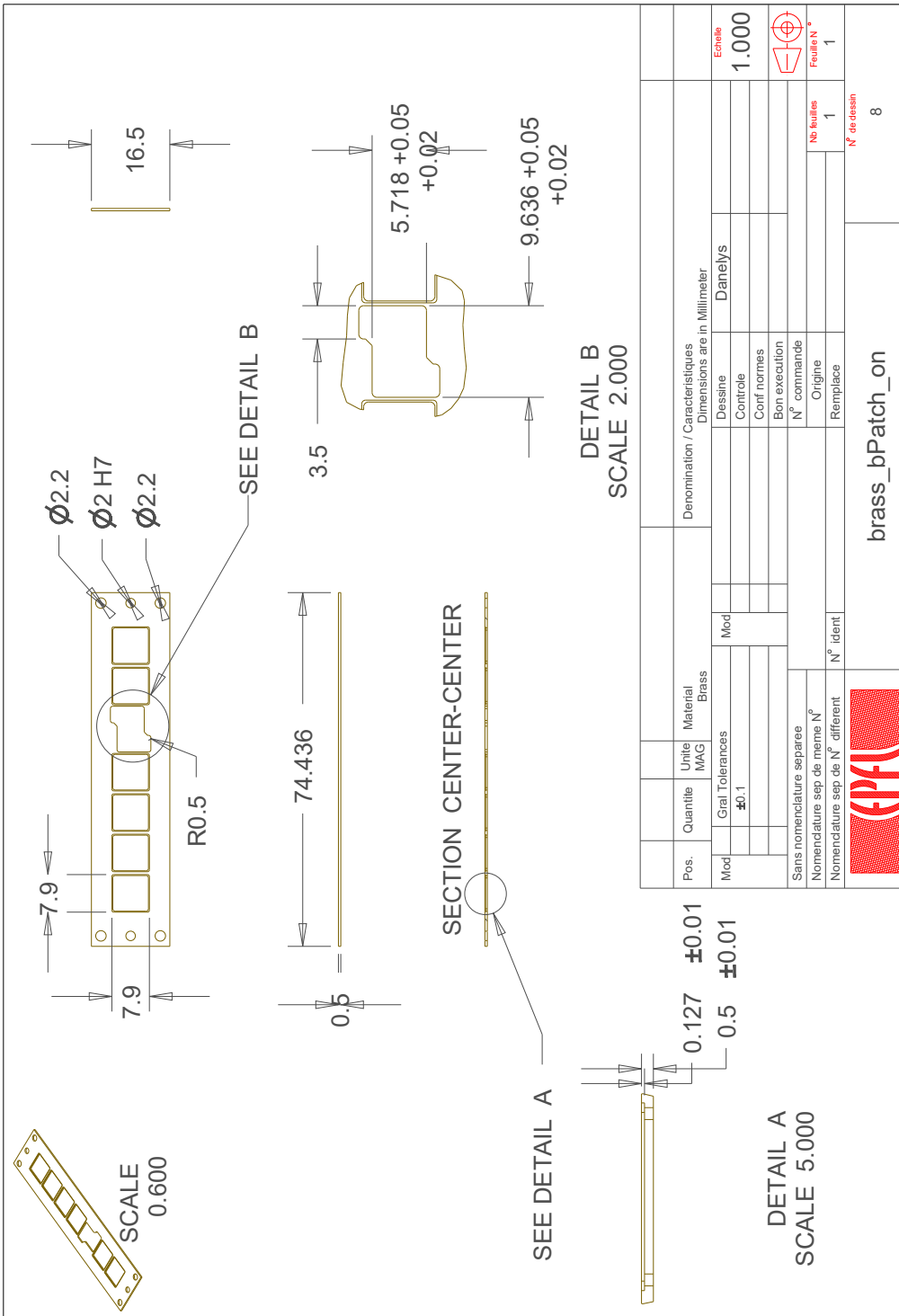


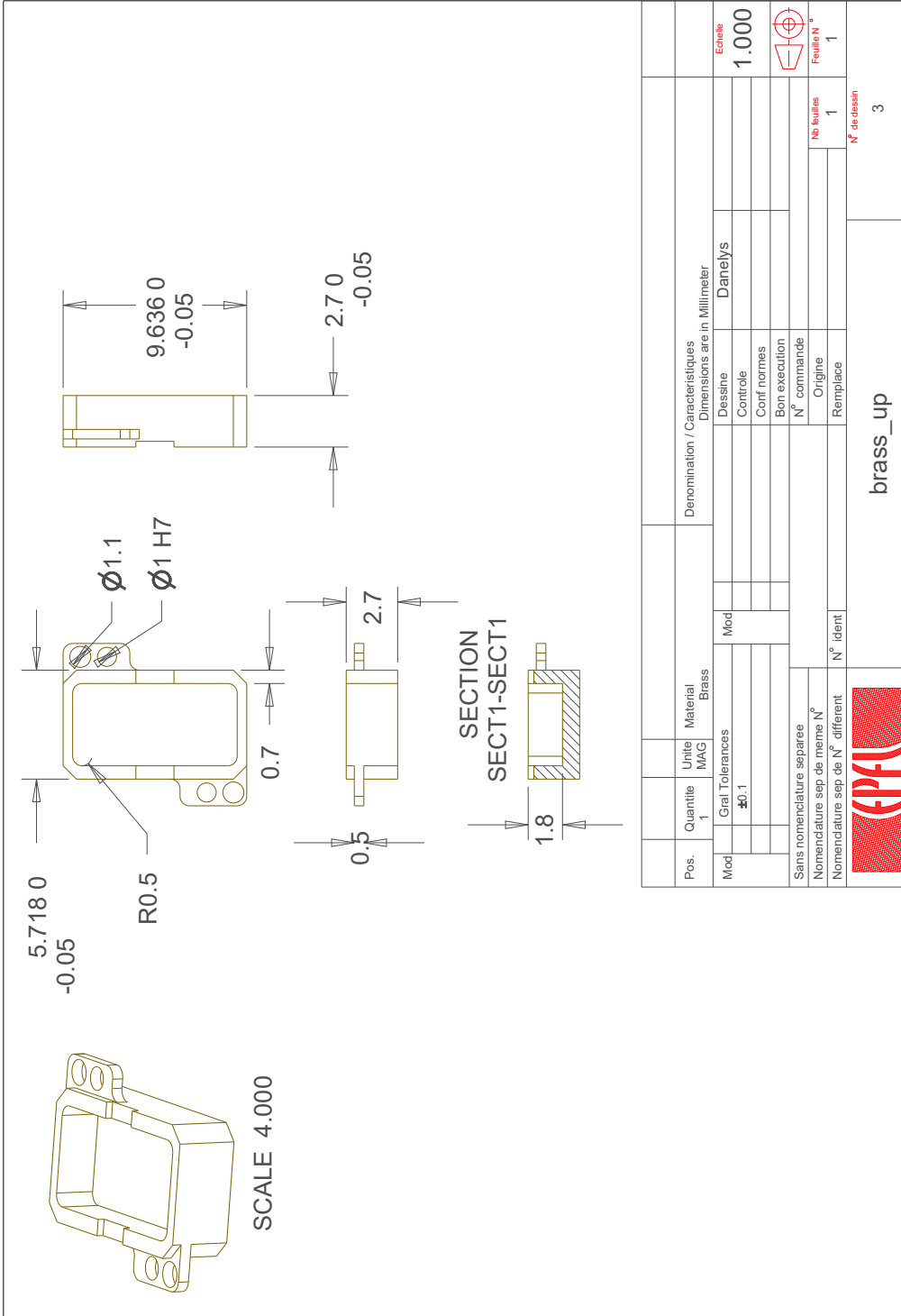
Pos.	Quantité	Unité	Material	Denomination / Caracteristiques	Dimensions are in Millimeter	Echelle
Mod	1	MAG	Brass	Dessine	Danelys	1.000
				Contrôle		
				Conf normes		
				Bon execution		
				N° commande		
				Origine		
				Remplace		
Sans nomenclature separee Nomenclature sep de meme N° Nomenclature sep de N° different				N° feuilles	1	1
				N° de dessin	1	
				bfm_brass_dw		



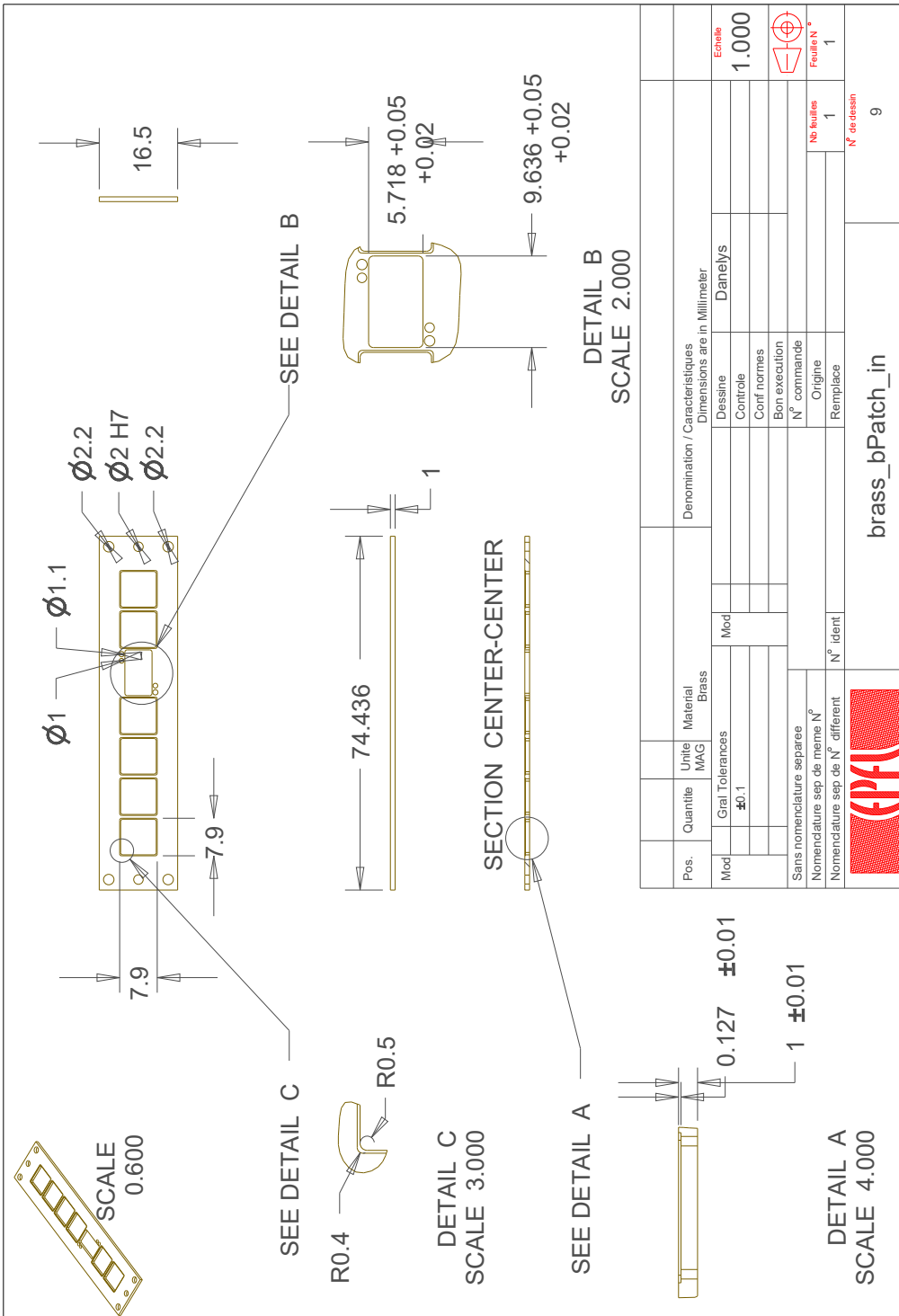
Pos.	Quantite	Unite	Material	Denomination / Caracteristiques	Dimensions are in	Echelle
Mod	Grat	Tolerances	Brass	Dessine	Millimeter	1.000
				Contrôle		
				Conf normes		
				Bon execution		
				N° commande		
				Origine		
				Remplace		
Sans nomenclature separee Nomenclature sep de meme N° Nomenclature sep de N° different				No feuilles 1		Feuilles N° 1
				N° de dessin bfn_brass_side 6		

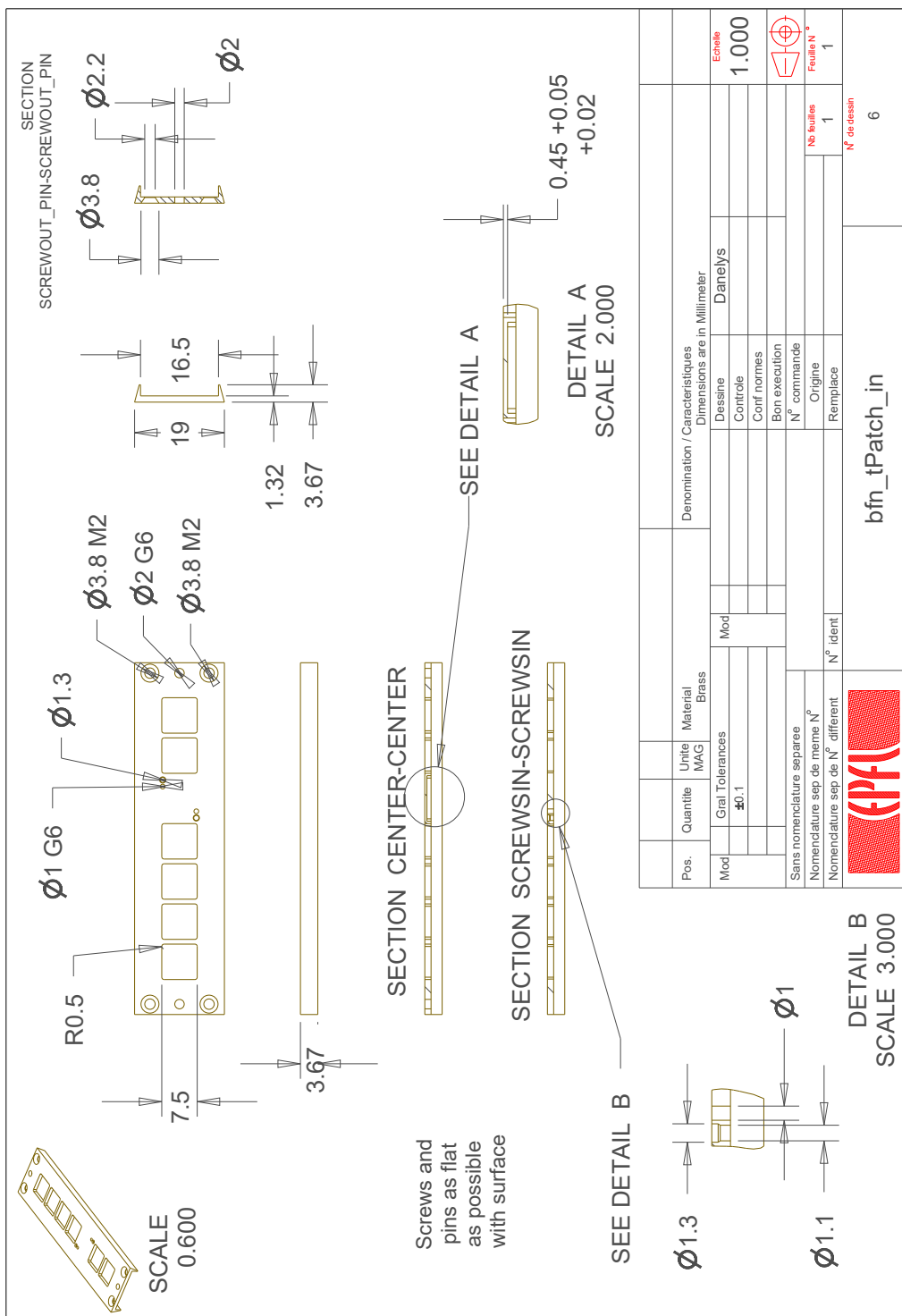






Pos.	Quantité 1	Unité MAG	Material Brass	Denomination / Caracteristiques Dimensions are in Millimeter	Echelle 1.000
Mod	Grat Tolerances ±0.1		Mod	Dessine Danehlys	
				Controle	
				Conf normes	
				Bon execution	
				N° commande	
				Origine	No feuilles 1
				Remplace	Feuille N° 1
					N° de dessin 3
				brass_up	

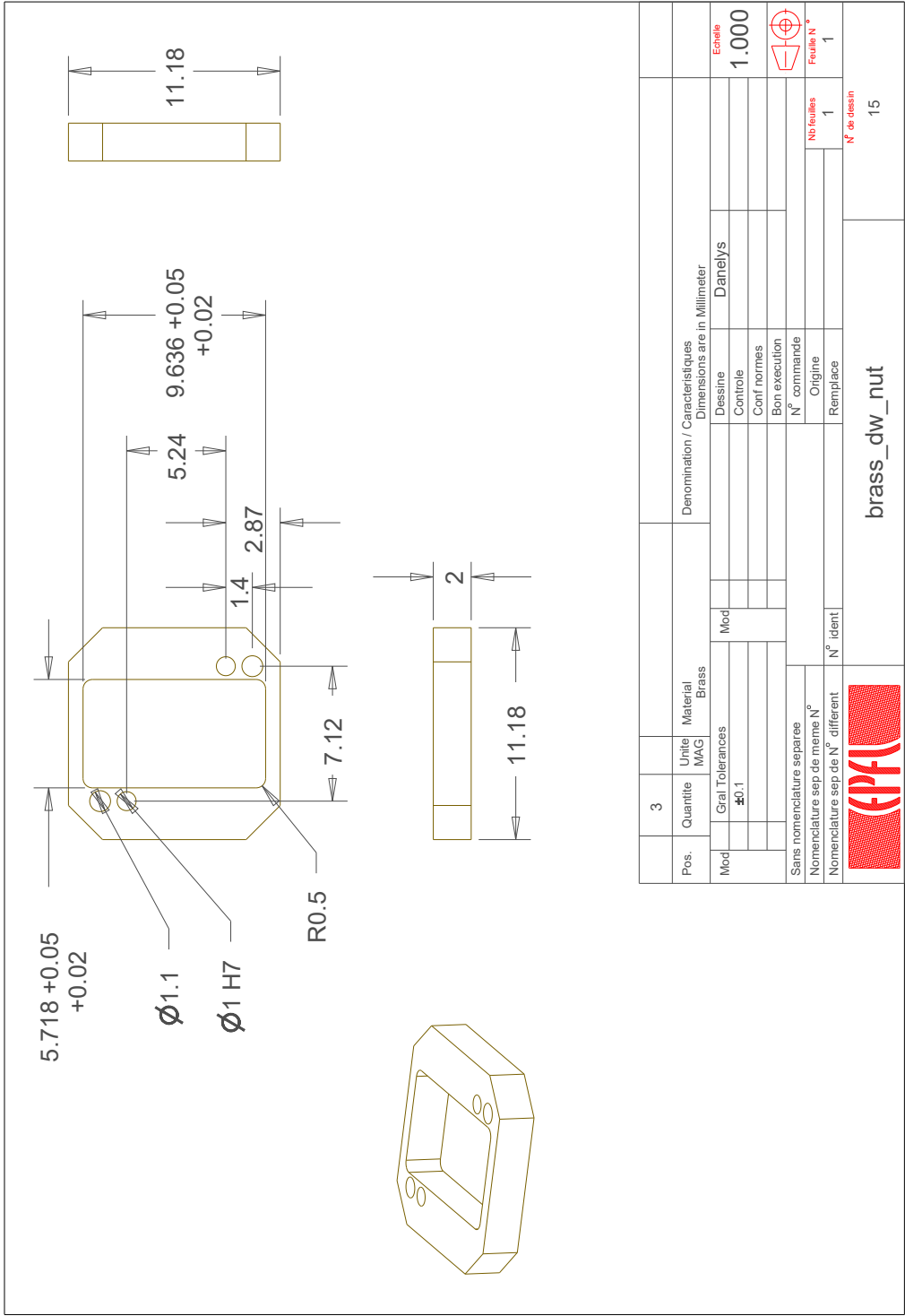


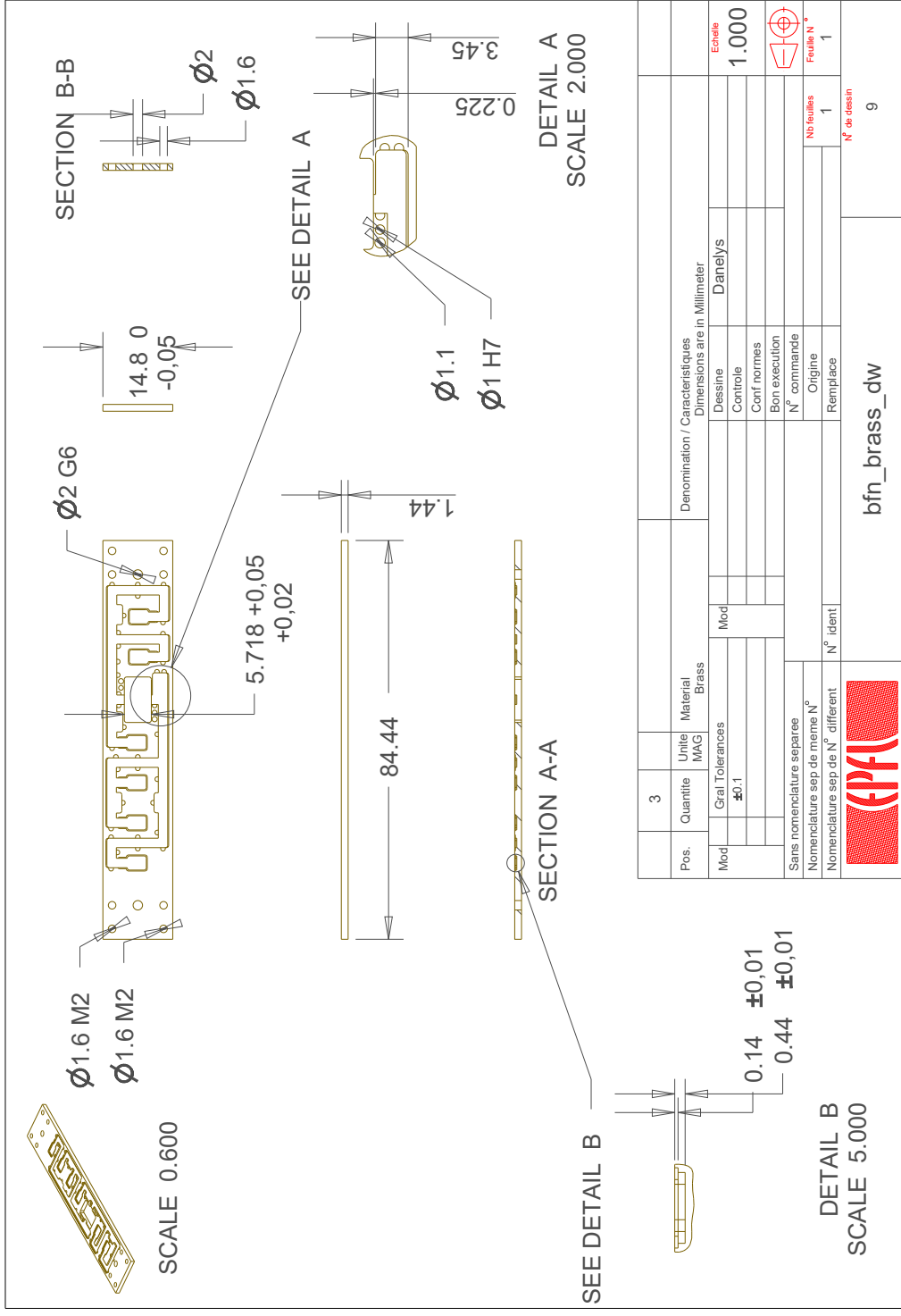


Pos.	Quantite	Unite	Material	Denomination / Caracteristiques
		MAG	Brass	Dimensions are in Millimeter
Mod	Grat Tolerances			Dessine
	± 0.1			Daneleys
				Contrôle
				Conf normes
				Bon execution
				N° commande
Sans nomenclature separee				Origine
Nomenclature sep de meme N°				Remplace
Nomenclature sep de N° different				
				No feuilles
				1
				Feuille N°
				1
				N° de dessin
				6

bfm_tPatch_in

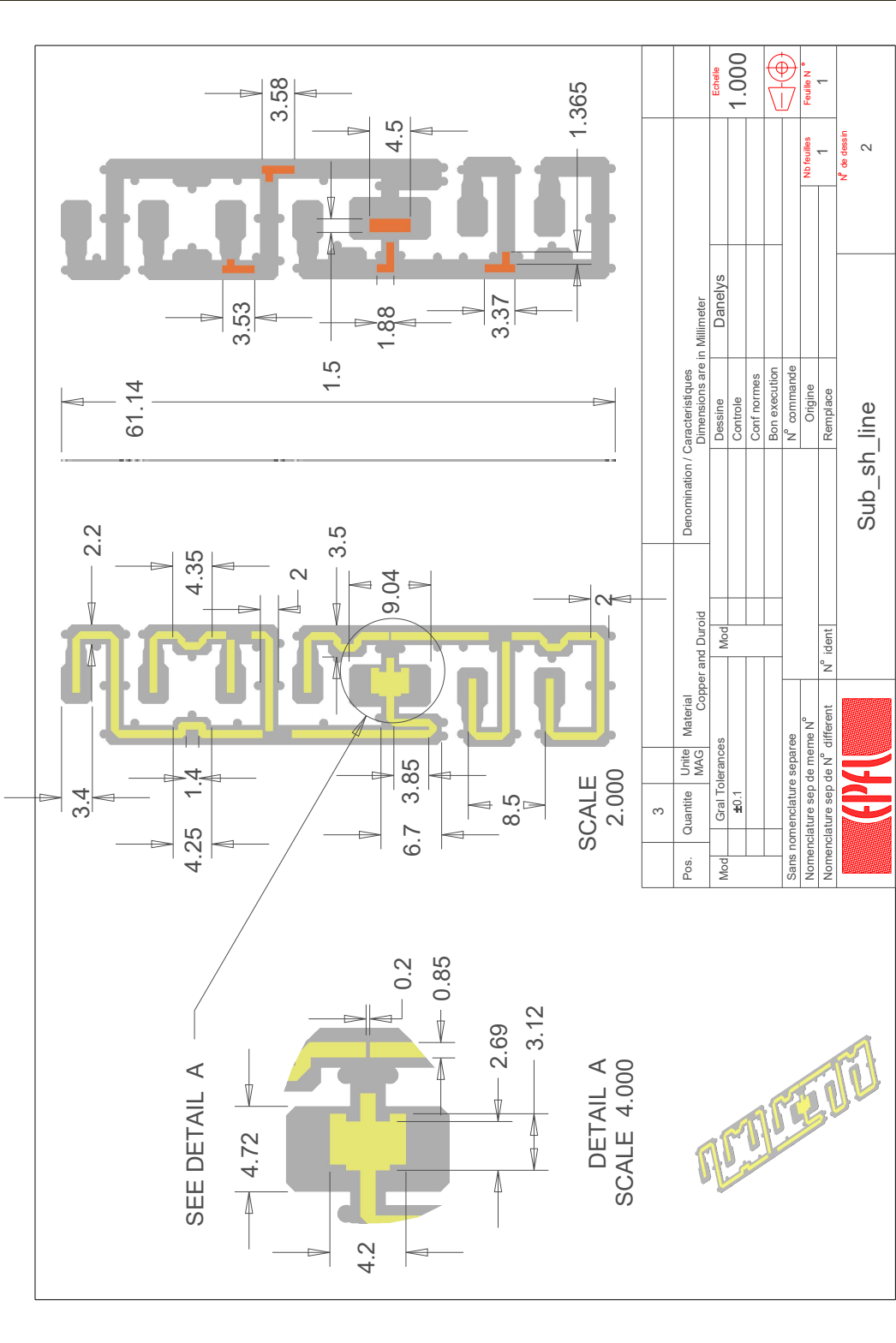
B Appendix B





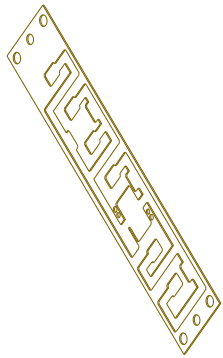
Pos.	3	Unité MAG	Material Brass	Denomination / Caracteristiques Dimensions are in Millimeter	
Mod		Grat Tolerances ±0.1	Mod	Dessine Danelys	Echelle 1.000
Sans nomenclature separee					
Nomenclature sep de meme N°					
Nomenclature sep de N° different		N° ident			
		N° feuilles		Feuille N°	
		1		1	
		N° de dessin		9	
		bfn_brass_dw			



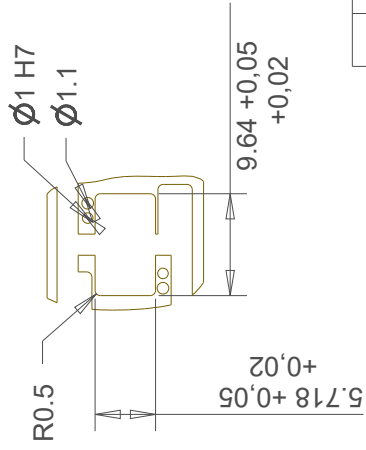
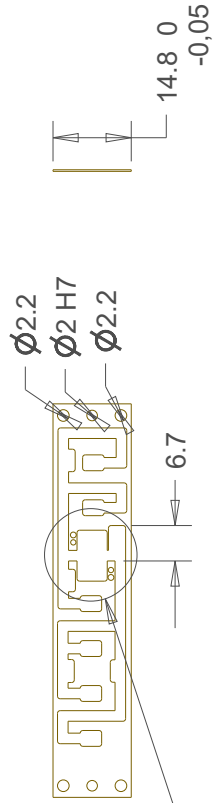


Pos.	Quantite	Unite	Material	Denomination / Caracteristiques	Dimensions are in Millimeter	Echelle
Mod	Grat Tolerances	IMAG	Copper and Duroid	Designe	Danelys	1.000
	Mod	40.1		Controle		
				Conf normes		
				Bon execution		
				N° commande		
				Origine		
				Remplace		
Sans nomenclature separee						
Nomenclature sep de meme N°						
Nomenclature sep de N° different						
				N° feuilles	1	1
				N° de dessin		2
				Sub_sh_line		



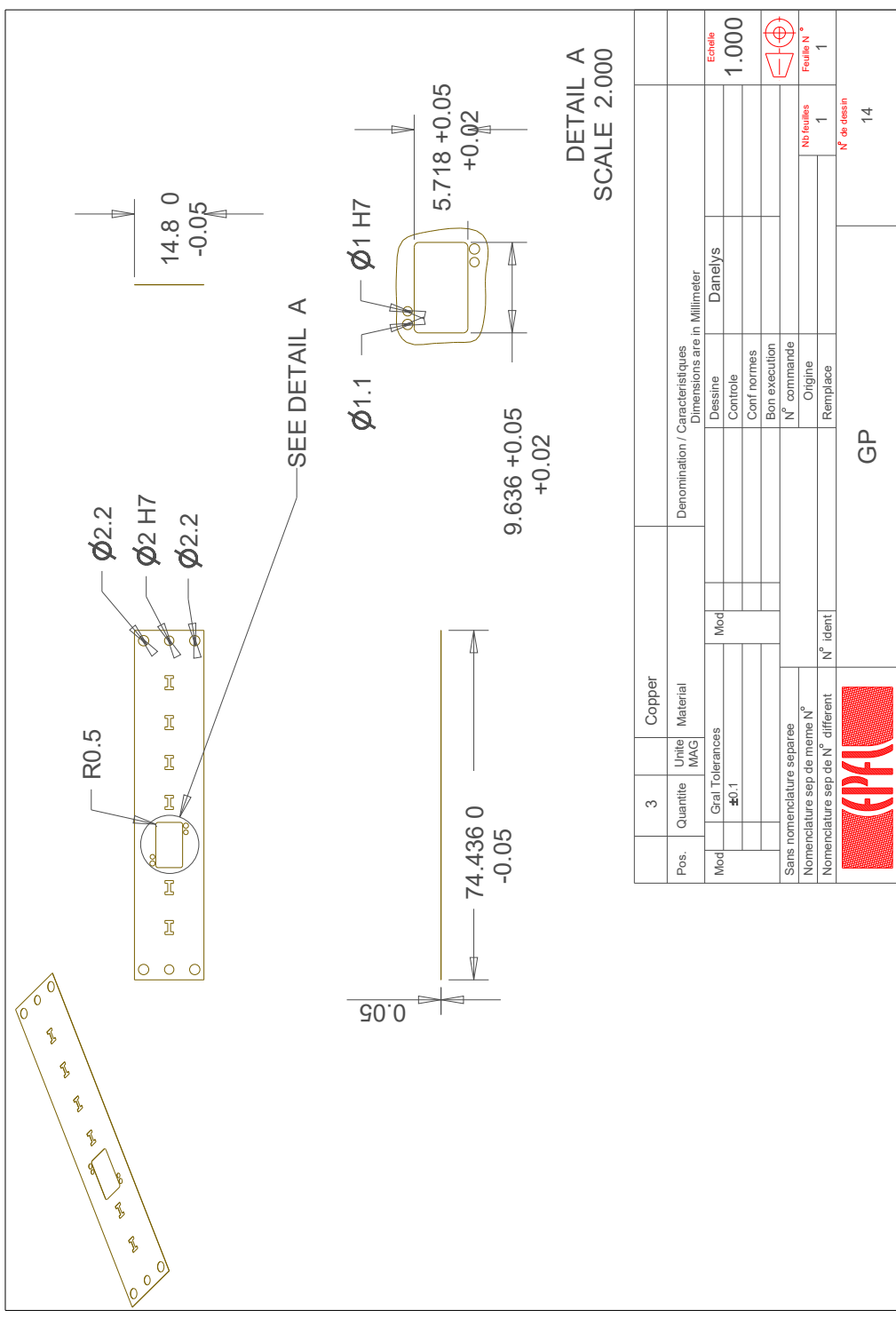


SEE DETAIL A



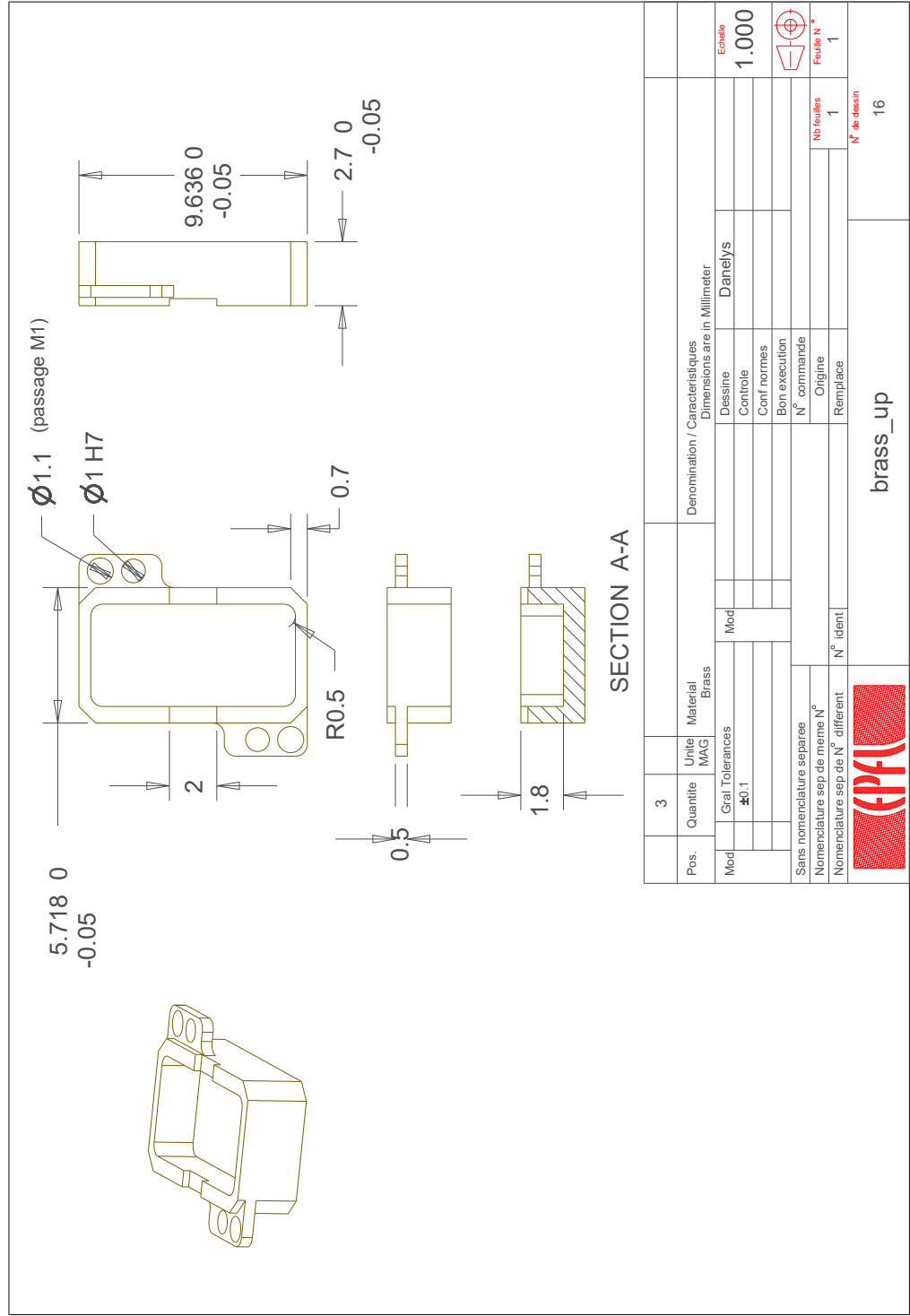
DETAIL A
SCALE 2.000

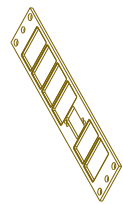
Pos.	3	Quantité	Unité	MAG	Material	Copper	Denomination / Caracteristiques	Dimensions are in Millimeter	
Mod		Grat Tolerances					Dessine	Danelys	
							Contrôle		
							Conf normes		
							Bon execution		
							N° commande		
							Origine		
							Remplace		
							N° feuilles	1	
							N° de dessin	10	
							bfn_brass_side		



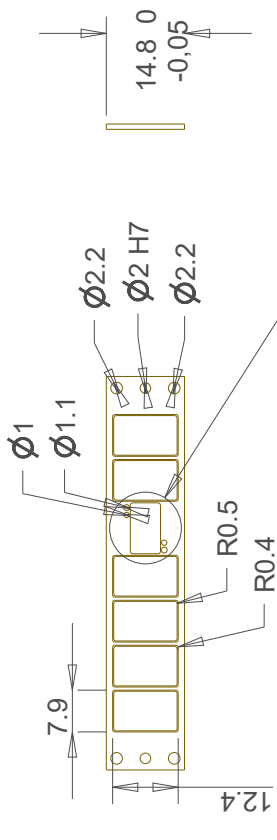
Pos.	3	Quantité	Unité	Material	Denomination / Caracteristiques	Dimensions are in Millimeter	
Mod		Grat Tolerances	MAG	Copper	Designe	Danelys	Echelle
		40.1			Controle		1.000
					Conf normes		
					Bon execution		
					N° commande		
					Origine		
					N° ident		N° feuilles
							1
							N° de dessin
							14



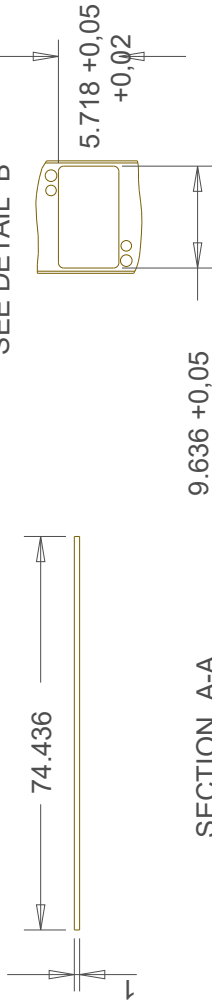




SCALE 0.600



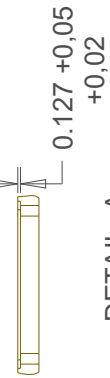
SEE DETAIL B



SECTION A-A

DETAIL B
SCALE 2.000

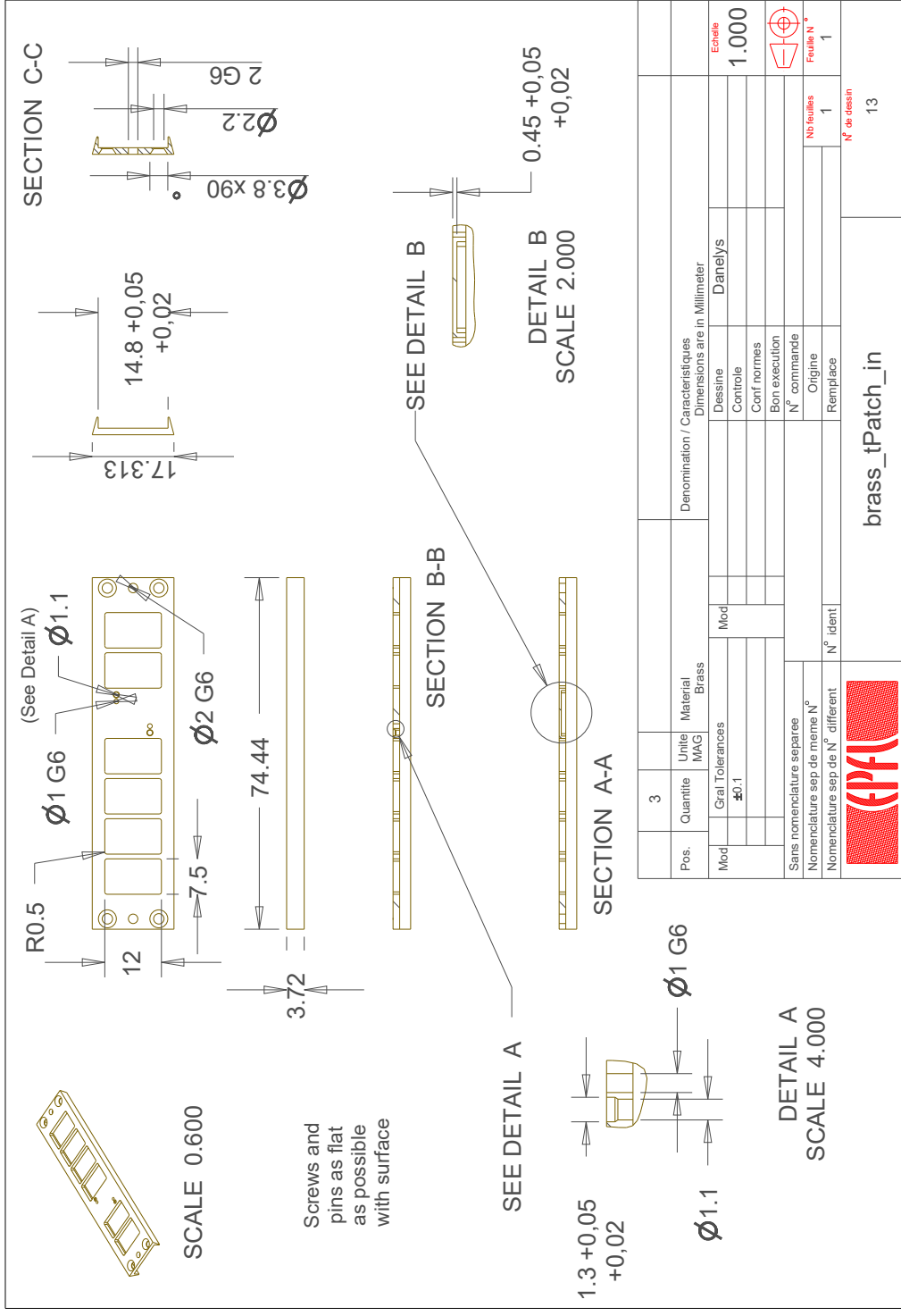
SEE DETAIL A



DETAIL A
SCALE 4.000

Pos.	3	Unité MAG	Material Brass	Denomination / Caracteristiques Dimensions are in Millimeter	
Mod		Grat Tolerances #0.1	Mod	Dessine Danelys	Echelle 1.000
Sans nomenclature separee					
Nomenclature sep de meme N°					
Nomenclature sep de N° different					
		N° ident	Origine	N° feuilles	Feuille N°
			Remplace	1	1
		brass_bPatch_in			N° de dessin 11

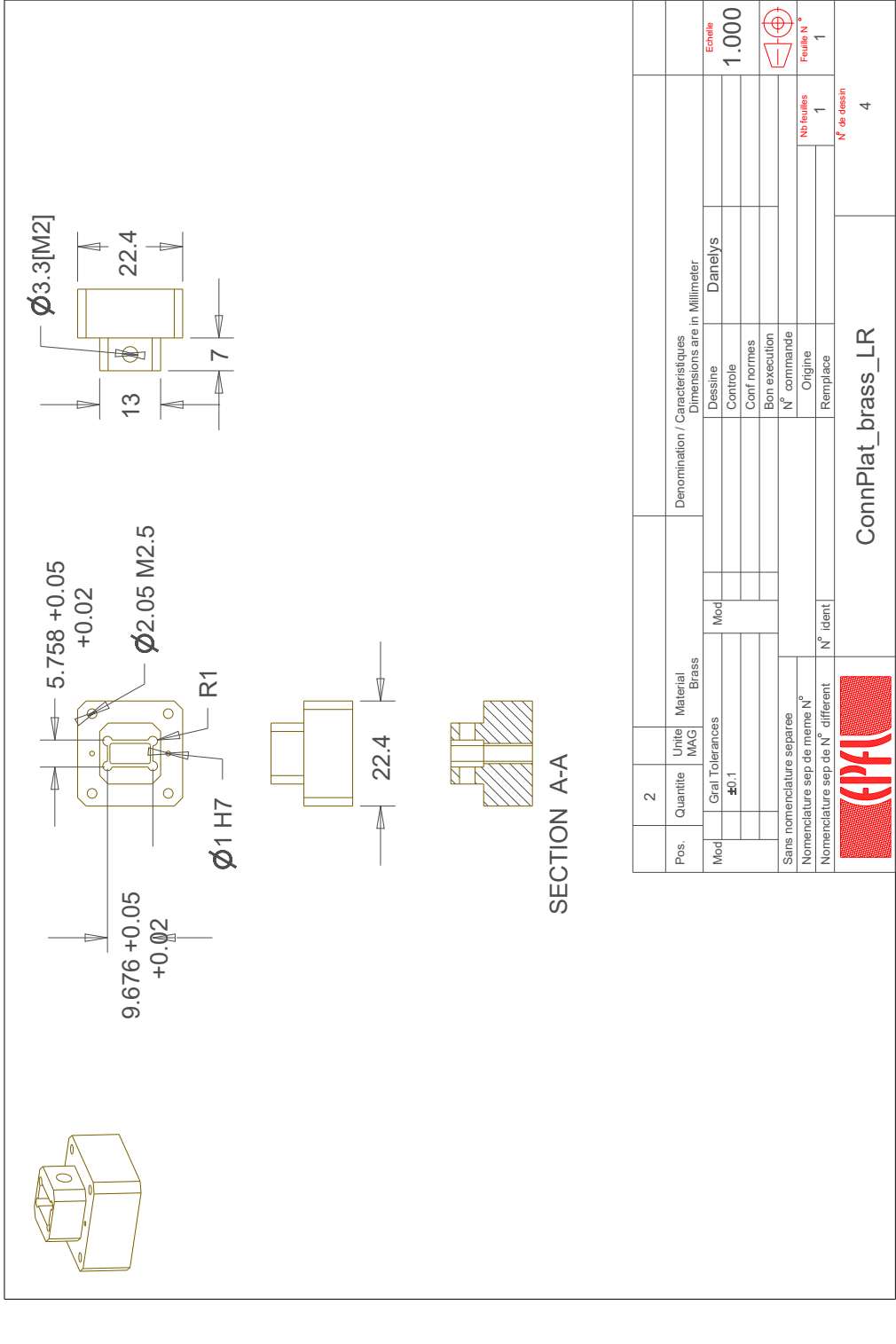


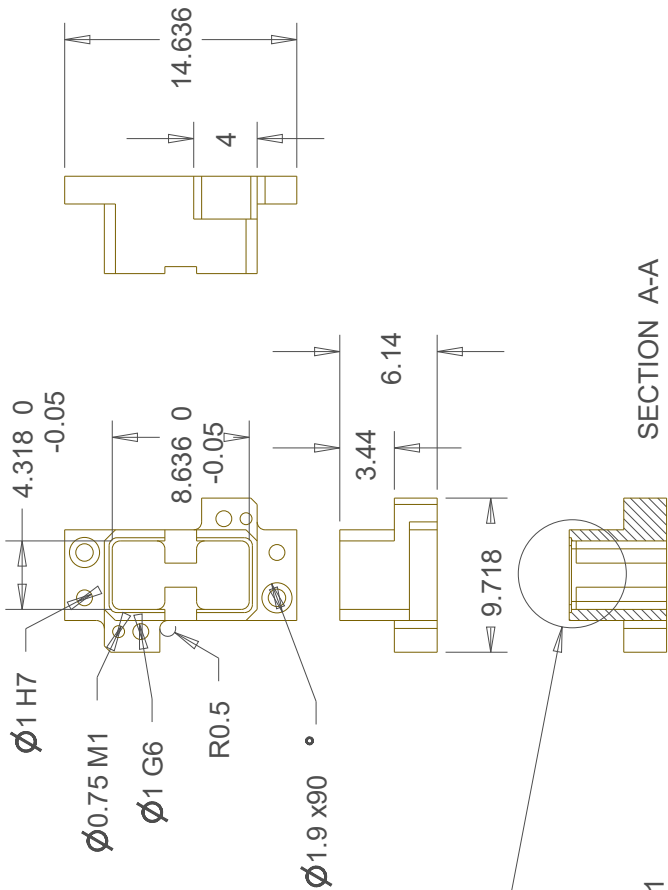
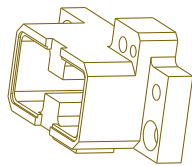


Pos.	3	Quantité	Unité	Material	Denomination / Caracteristiques
Mod		Grat Tolerances	IMAG	Brass	Dimensions are in Millimeter
		±0.1			Dessine
					Contrôle
					Conf normes
					Bon execution
					N° commande
					Origine
					Remplace
					N° feuilles
					1
					Feuille N°
					1
					N° de dessin
					13

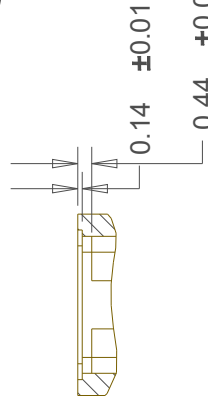


brass_tPatch_in





SEE DETAIL A



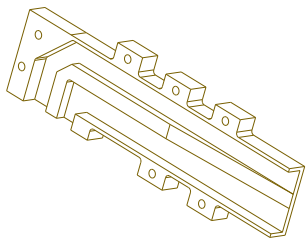
DETAIL A
SCALE 6.000

SECTION A-A

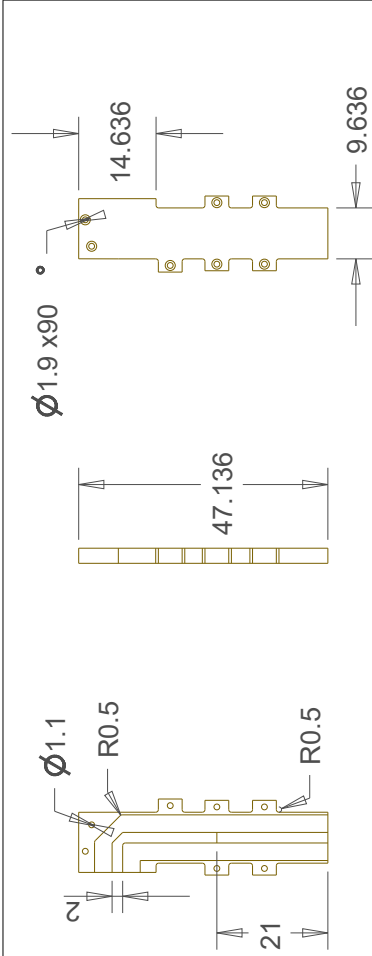
Pos.	2	Quantité	Unité	Material	Denomination / Caracteristiques	Dimensions are in Millimeter	
Mod		Grat Tolerances	MAG	Brass	Dessine	Danelys	Echelle
					Contrôle		1.000
					Conf normes		
					Bon exécution		
					N° commande		
					Origine		
					N° ident		N° feuilles
							1
							N° de dessin
							3



brass_dw_LR

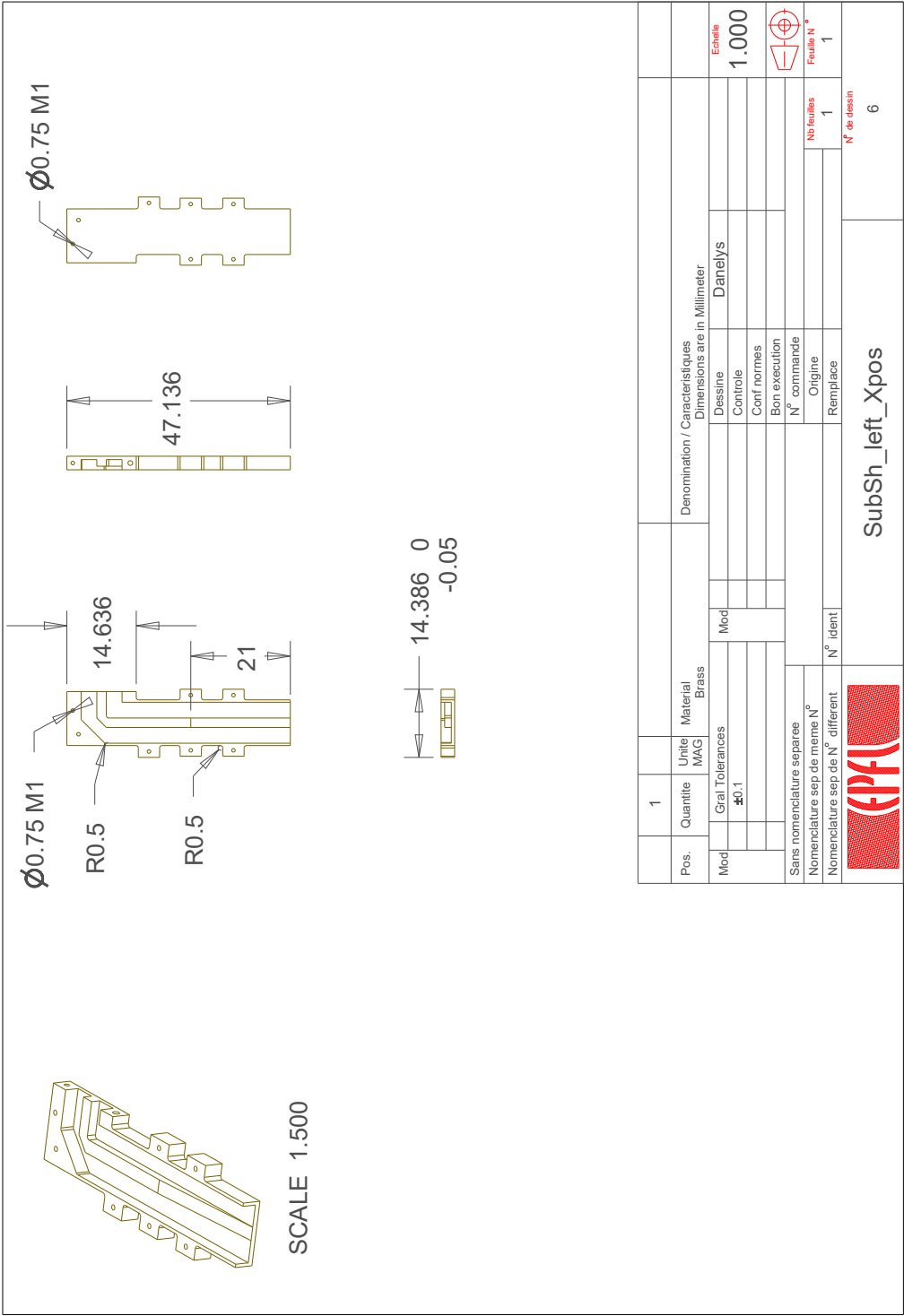


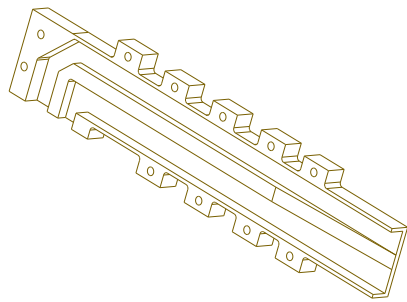
SCALE 1.500



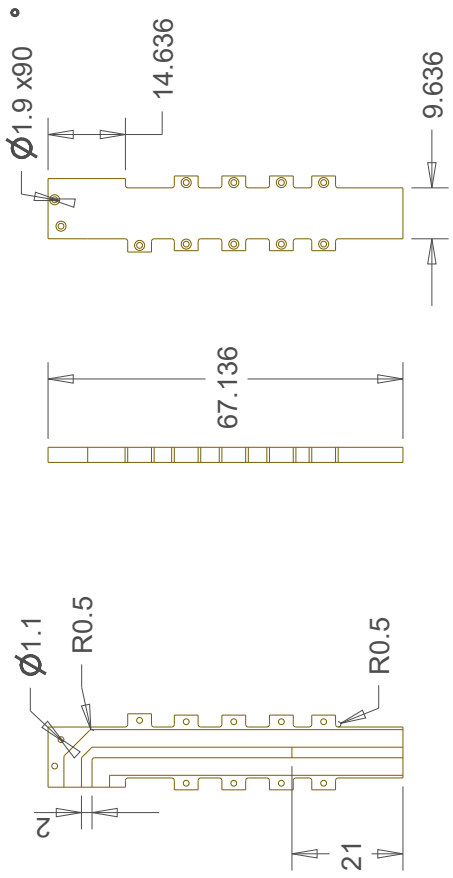
Pos.	1	Quantité	Unité	Material	Denomination / Caracteristiques
Mod		Grat Tolerances	MAG	Brass	Dimensions are in Millimeter
					Dessine
					Contrôle
					Conf normes
					Bon execution
					N° commande
					Origine
					Remplace
				Sans nomenclature separee	
				Nomenclature sep de meme N°	
				Nomenclature sep de N° different	
				N° feuilles	
				1	
				N° de dessin	
				5	
				SubSh_leftXneg	
				Echelle	
				1.000	
				Feuille N°	
				1	







SCALE 1.500



Pos.	1	Quantité	Unité	Material	Denomination / Caracteristiques
			MAG	Brass	Dimensions are in Millimeter
Mod		Grat Tolerances		Mod	Dessine
		±0.1			Controlé
					Conf normes
					Bon execution
					N° commande
					Origine
					Remplace
					N° feuilles
					1
					N° de dessin
					7



SubSh_rightXneg

Echelle
1.000

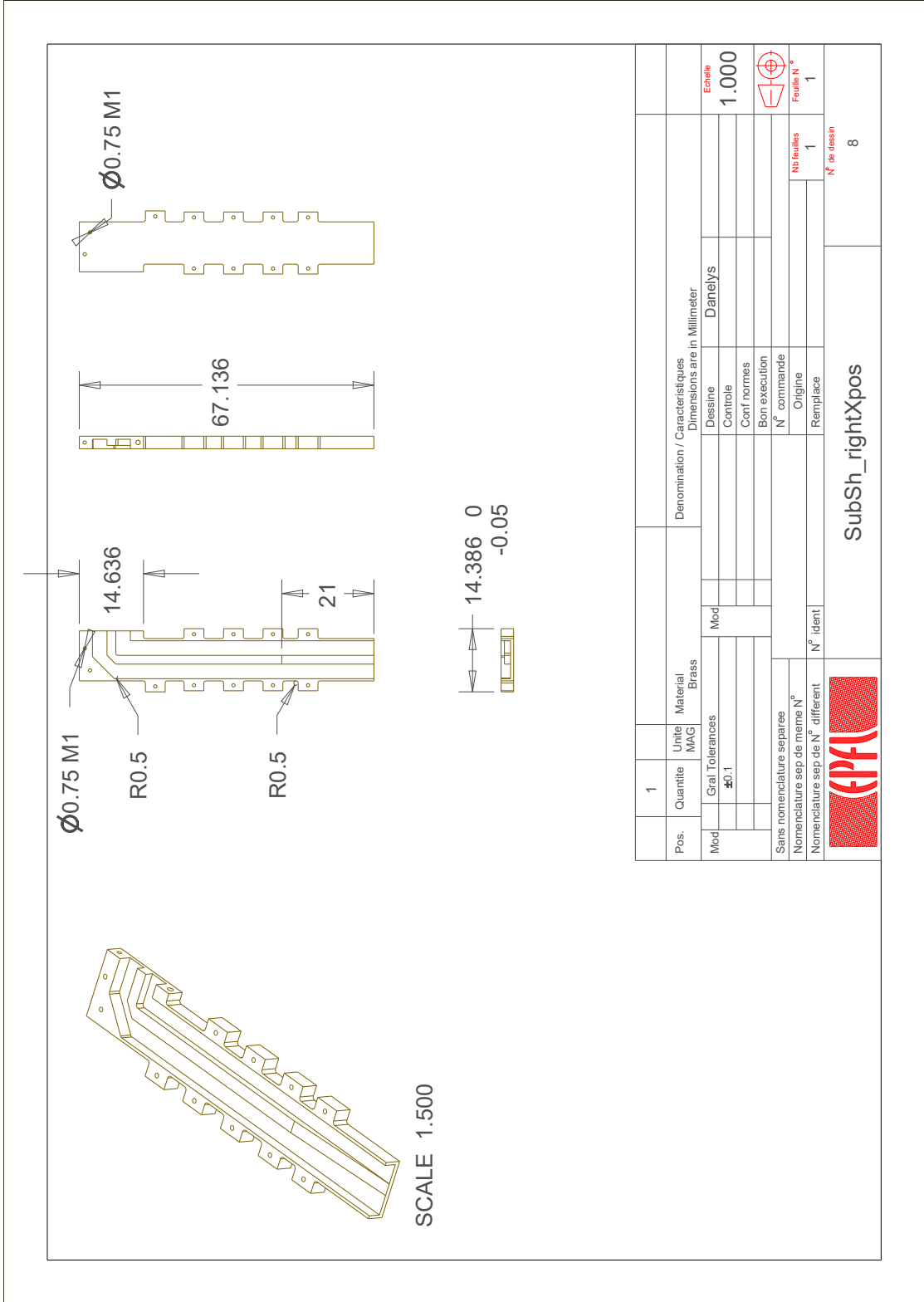


Feuille N°

1

N° de dessin

7



Pos.	1	Quantité	Unité	Material	Denomination / Caracteristiques
			MAG	Brass	Dimensions are in Millimeter
Mod		Grat Tolerances		Mod	Dessine
		± 0.1			Controlé
					Conf normes
					Bon execution
					N° commande
					Origine
					Remplace
					N° feuilles
					1
					N° de dessin
					8



SubSh_rightXpos

Bibliography

- [1] GSMA, G. Intelligence, GSMA, and G. Intelligence, “Understanding 5G: Perspectives on future technological advancements in mobile”, *GSMA Intelligence Understanding 5G*, no. December, pp. 3–15, 2014. [Online]. Available: <https://gsmaintelligence.com/research/?file=141208-5g.pdf%7B%5C%26%7Ddownload>.
- [2] A. Gupta and R. K. Jha, “A Survey of 5G Network: Architecture and Emerging Technologies”, *IEEE Access*, vol. 3, pp. 1206–1232, 2015, ISSN: 21693536. DOI: 10.1109/ACCESS.2015.2461602.
- [3] H. Viswanathan and M. Weldon, “The Past, Present and Future of Mobile communications”, *Bell Labs Technical Journal*, vol. 19, pp. 8–21, 2014.
- [4] T. S. Rappaport, S. Sun, R. Mayzus, H. Zhao, Y. Azar, K. Wang, G. N. Wong, J. K. Schulz, M. Samimi, and F. Gutierrez, “Millimeter wave mobile communications for 5G cellular: It will work!”, *IEEE Access*, vol. 1, pp. 335–349, 2013, ISSN: 21693536. DOI: 10.1109/ACCESS.2013.2260813.
- [5] Cisco, “Cisco Visual Networking Index: Global Mobile Data Traffic Forecast Update, 2017–2022”, Tech. Rep., 2019, pp. 1–36.
- [6] E. Z. Tragos, S. Zeadally, A. G. Fragkiadakis, and V. A. Siris, “Spectrum assignment in cognitive radio networks: A comprehensive survey”, *IEEE Communications Surveys and Tutorials*, vol. 15, no. 3, pp. 1108–1135, 2013, ISSN: 1553877X. DOI: 10.1109/SURV.2012.121112.00047.
- [7] N. Devroye, P. Mitran, and V. Tarokh, “Achievable rates in cognitive radio channels”, *IEEE Transactions on Information Theory*, vol. 52, no. 5, pp. 1813–1827, 2006, ISSN: 00189448. DOI: 10.1109/TIT.2006.872971.
- [8] NTT Docomo, “5G Radio Access: Requirements, Concept and Technologies”, *NTT DOCOMO White Paper*, no. July, pp. 1–13, 2014.
- [9] M. Agiwal, A. Roy, and N. Saxena, “Next generation 5G wireless networks: A comprehensive survey”, *IEEE Communications Surveys and Tutorials*, vol. 18, no. 3, pp. 1617–1655, 2016, ISSN: 1553877X. DOI: 10.1109/COMST.2016.2532458.
- [10] J. G. Andrews, S. Buzzi, W. Choi, S. V. Hanly, A. Lozano, A. C. Soong, and J. C. Zhang, “What will 5G be?”, *IEEE Journal on Selected Areas in Communications*, vol. 32, no. 6, pp. 1065–1082, 2014, ISSN: 07338716. DOI: 10.1109/JSAC.2014.2328098.

- [11] *3GPP Release 15 Overview*. [Online]. Available: <https://spectrum.ieee.org/telecom/wireless/3gpp-release-15-overview> (visited on 07/07/2020).
- [12] *Cooper's Law*. [Online]. Available: <http://www.arraycomm.com/technology/coopers-law/> (visited on 09/14/2020).
- [13] J. G. Andrews, X. Zhang, G. D. Durgin, and A. K. Gupta, "Are we approaching the fundamental limits of wireless network densification?", *IEEE Communications Magazine*, vol. 54, no. 10, pp. 184–190, 2016, ISSN: 01636804. DOI: 10.1109/MCOM.2016.7588290. arXiv: 1512.00413.
- [14] V. Chandrasekhar, J. G. Andrews, and A. Gatherer, "Femtocell networks: A survey", *IEEE Communications Magazine*, vol. 46, no. 9, pp. 59–67, 2008, ISSN: 01636804. DOI: 10.1109/MCOM.2008.4623708. arXiv: 0803.0952.
- [15] F. Al-Turjman, E. Ever, and H. Zahmatkesh, "Small cells in the forthcoming 5G/IoT: Traffic modelling and deployment overview", *IEEE Communications Surveys and Tutorials*, vol. 21, no. 1, pp. 28–65, 2019, ISSN: 1553877X. DOI: 10.1109/COMST.2018.2864779.
- [16] D. Muirhead, M. A. Imran, and K. Arshad, "A Survey of the Challenges, Opportunities and Use of Multiple Antennas in Current and Future 5G Small Cell Base Stations", *IEEE Access*, vol. 4, pp. 2952–2964, 2016, ISSN: 21693536. DOI: 10.1109/ACCESS.2016.2569483.
- [17] "5G; NR; Base Station (BS) radio transmission and reception (3GPP TS 38.104 version 15.3.0 Release 15)", Tech. Rep. 38.104, 2018. [Online]. Available: https://www.etsi.org/deliver/etsi%7B%5C_%7Dts.
- [18] W. Roh, J. Y. Seol, J. H. Park, B. Lee, J. Lee, Y. Kim, J. Cho, K. Cheun, and F. Aryanfar, "Millimeter-wave beamforming as an enabling technology for 5G cellular communications: Theoretical feasibility and prototype results", *IEEE Communications Magazine*, vol. 52, no. 2, pp. 106–113, 2014, ISSN: 01636804. DOI: 10.1109/MCOM.2014.6736750.
- [19] M. Marcus and B. Pattan, "Millimeter wave propagation: Spectrum management implications", *IEEE Microwave Magazine*, vol. 6, no. 2, pp. 54–62, 2005, ISSN: 15273342. DOI: 10.1109/MMW.2005.1491267.
- [20] Z. Pi and F. Khan, "An Introduction to Millimeter-Wave Mobile Broadband Systems", *IEEE Communications Magazine*, no. June, pp. 101–107, 2011.
- [21] U. T. Virk and K. Haneda, "Modeling Human Blockage at 5G Millimeter-Wave Frequencies", *IEEE Transactions on Antennas and Propagation*, vol. 68, no. 3, pp. 2256–2266, 2020, ISSN: 15582221. DOI: 10.1109/TAP.2019.2948499.
- [22] K. Zhao, J. Helander, D. Sjöberg, S. He, T. Bolin, and Z. Ying, "User Body Effect on Phased Array in User Equipment for the 5G mmWave Communication System", *IEEE Antennas and Wireless Propagation Letters*, vol. 16, pp. 864–867, 2017, ISSN: 15361225. DOI: 10.1109/LAWP.2016.2611674.
- [23] S. Rangan, T. S. Rappaport, and E. Erkip, "Millimeter-wave cellular wireless networks: Potentials and challenges", *Proceedings of the IEEE*, vol. 102, no. 3, pp. 366–385, 2014, ISSN: 00189219. DOI: 10.1109/JPROC.2014.2299397. arXiv: 1401.2560.

- [24] N. Docomo, “DOCOMO 5G White Paper Requirements , Concept and Technologies”, Docomo, N T T, Tech. Rep. July, 2014.
- [25] Ericsson, “5G Radio Access What is 5G ?”, Ericsson, Tech. Rep. February, 2016, p. 10. [Online]. Available: <http://www.ericsson.com/res/docs/whitepapers/wp-5g.pdf>.
- [26] Huawei Technologies, “5G Inaugural Issue, Research and Innovation”, *Huawei Innovation Research Program*, vol. 01, no. 1, pp. 1–100, 2015, ISSN: 1549-8417. DOI: 10.1097/01209203-200503000-00001. [Online]. Available: <http://discovery.ucl.ac.uk/37134/>.
- [27] —, “5G: New Air Interface and Radio Access Virtualization”, Tech. Rep. April, 2015, pp. 1–11.
- [28] Nokia Networks, “Looking ahead to 5G”, Tech. Rep., 2013, pp. 1–16.
- [29] Qualcomm Technologies, “5G Waveform & Multiple Access Techniques”, Qualcomm Technologies, INC, Tech. Rep., 2015.
- [30] K. Tateishi, D. Kunta, A. Harada, Y. Kishryama, S. Parkvall, E. Dahlman, and J. Furuskog, “Field experiments on 5G radio access using 15-GHz band in outdoor small cell environment”, *IEEE International Symposium on Personal, Indoor and Mobile Radio Communications, PIMRC*, vol. 2015-Decem, pp. 851–855, 2015. DOI: 10.1109/PIMRC.2015.7343416.
- [31] Y. Tao, L. Liu, S. Liu, and Z. Zhang, “A survey: Several technologies of non-orthogonal transmission for 5G”, *China Communications*, vol. 12, no. 10, pp. 1–15, 2015, ISSN: 16735447. DOI: 10.1109/CC.2015.7315054.
- [32] T. O. Olwal, K. Djouani, and A. M. Kurien, “A Survey of Resource Management Toward 5G Radio Access Networks”, *IEEE Communications Surveys and Tutorials*, vol. 18, no. 3, pp. 1656–1686, 2016, ISSN: 1553877X. DOI: 10.1109/COMST.2016.2550765.
- [33] L. Hanzo, O. Alamri, M. El-Hajjar, and N. Wu, “Problem Formulation, Objectives and Benefits”, in *Near-Capacity Multi-Functional MIMO Systems*, 2009, ch. 1, pp. 1–48, ISBN: 9780470779651. DOI: 10.1002/9780470744710.ch1.
- [34] H. Holma, A. Toskala, K. Ranta-Aho, J. Pirskanen, and J. Kaikkonen, “High-Speed Packet Access Evolution (HSPA+) in 3GPP Release 7”, *WCDMA for UMTS: HSPA Evolution and LTE: Fourth Edition*, no. December, pp. 445–461, 2008. DOI: 10.1002/9780470512531.ch15.
- [35] T. L. Marzetta, “Noncooperative cellular wireless with unlimited numbers of base station antennas”, *IEEE Transactions on Wireless Communications*, vol. 9, no. 11, pp. 3590–3600, 2010, ISSN: 15361276. DOI: 10.1109/TWC.2010.092810.091092.
- [36] L. Sanguinetti, A. L. Moustakas, and M. Debbah, “Interference management in 5G reverse TDD HetNets with wireless backhaul: A large system analysis”, *IEEE Journal on Selected Areas in Communications*, vol. 33, no. 6, pp. 1187–1200, 2015, ISSN: 07338716. DOI: 10.1109/JSAC.2015.2416991. arXiv: 1407.6481.

- [37] S. Singh and J. G. Andrews, "Joint resource partitioning and offloading in heterogeneous cellular networks", *IEEE Transactions on Wireless Communications*, vol. 13, no. 2, pp. 888–901, 2014, ISSN: 15361276. DOI: 10.1109/TWC.2013.120713.130548. arXiv: 1303.7039.
- [38] S. Talwar, D. Choudhury, K. Dimou, E. Aryafar, B. Bangerter, and K. Stewart, "Enabling technologies and architectures for 5G wireless", *IEEE MTT-S International Microwave Symposium Digest*, pp. 12–15, 2014, ISSN: 0149645X. DOI: 10.1109/MWSYM.2014.6848639.
- [39] A. P. Bianzino, C. Chaudet, D. Rossi, and J. L. Rougier, "A survey of green networking research", *IEEE Communications Surveys and Tutorials*, vol. 14, no. 1, pp. 3–20, 2012, ISSN: 1553877X. DOI: 10.1109/SURV.2011.113010.00106.
- [40] R. L. G. Cavalcante, S. Stańczak, M. Schubert, A. Eisenblätter, and U. Türke, "Toward Energy-Efficient 5G Wireless Communications Technologies", no. november, pp. 24–34, 2014. arXiv: 1407.0344. [Online]. Available: <http://arxiv.org/abs/1407.0344>.
- [41] F. Boccardi, R. Heath, A. Lozano, T. L. Marzetta, and P. Popovski, "Five disruptive technology directions for 5G", *IEEE Communications Magazine*, vol. 52, no. 2, pp. 74–80, 2014, ISSN: 01636804. DOI: 10.1109/MCOM.2014.6736746. arXiv: 1312.0229.
- [42] M. Tehrani, M. Uysal, and H. Yanikomeroglu, "Device-to-device communication in 5G cellular networks: Challenges, solutions, and future directions", *IEEE Communications Magazine*, vol. 52, no. 5, pp. 86–92, 2014, ISSN: 01636804. DOI: 10.1109/MCOM.2014.6815897.
- [43] S. Chen and J. Zhao, "The requirements, challenges, and technologies for 5G of terrestrial mobile telecommunication", *IEEE Communications Magazine*, vol. 52, no. 5, pp. 36–43, 2014, ISSN: 01636804. DOI: 10.1109/MCOM.2014.6815891.
- [44] A. Asadi, Q. Wang, and V. Mancuso, "A survey on device-to-device communication in cellular networks", *IEEE Communications Surveys and Tutorials*, vol. 16, no. 4, pp. 1801–1819, 2014, ISSN: 1553877X. DOI: 10.1109/COMST.2014.2319555. arXiv: 1310.0720.
- [45] X. Lin, J. G. Andrews, A. Ghosh, and R. Ratasuk, "An overview of 3GPP device-to-device proximity services", *IEEE Communications Magazine*, vol. 52, no. 4, pp. 40–48, 2014, ISSN: 01636804. DOI: 10.1109/MCOM.2014.6807945.
- [46] R. Mijumbi, J. Serrat, J. L. Gorricho, N. Bouten, F. De Turck, and R. Boutaba, "Network function virtualization: State-of-the-art and research challenges", *IEEE Communications Surveys and Tutorials*, vol. 18, no. 1, pp. 236–262, 2016, ISSN: 1553877X. DOI: 10.1109/COMST.2015.2477041. arXiv: 1509.07675.
- [47] S. Sezer, S. Scott-Hayward, P. Chouhan, B. Fraser, D. Lake, J. Finnegan, N. Viljoen, M. Miller, and N. Rao, "Are we ready for SDN? Implementation challenges for software-defined networks", *IEEE Communications Magazine*, vol. 51, no. 7, pp. 36–43, 2013, ISSN: 01636804. DOI: 10.1109/MCOM.2013.6553676.

- [48] C. X. Wang, J. Bian, J. Sun, W. Zhang, and M. Zhang, "A survey of 5g channel measurements and models", *IEEE Communications Surveys and Tutorials*, vol. 20, no. 4, pp. 3142–3168, 2018, ISSN: 1553877X. DOI: 10.1109/COMST.2018.2862141.
- [49] Y. Liu, C. X. Wang, J. Huang, J. Sun, and W. Zhang, "Novel 3-D Nonstationary MmWave Massive MIMO Channel Models for 5G High-Speed Train Wireless Communications", *IEEE Transactions on Vehicular Technology*, vol. 68, no. 3, pp. 2077–2086, 2019, ISSN: 00189545. DOI: 10.1109/TVT.2018.2866414.
- [50] W. Hong, Z. H. Jiang, C. Yu, J. Zhou, P. Chen, Z. Yu, H. Zhang, B. Yang, X. Pang, M. Jiang, Y. Cheng, M. K. Al-Nuaimi, Y. Zhang, J. Chen, and S. He, "Multibeam Antenna Technologies for 5G Wireless Communications", *IEEE Transactions on Antennas and Propagation*, vol. 65, no. 12, pp. 6231–6249, 2017, ISSN: 0018926X. DOI: 10.1109/TAP.2017.2712819.
- [51] X. Zhang, W. Cheng, and H. Zhang, "Full-Duplex Transmission in PHY and MAC Layers for 5G Mobile Wireless Networks", *IEEE Wireless Communications*, vol. 22, no. October, pp. 112–121, 2015.
- [52] E. Dahlman, S. Parkvall, and J. Sköld, "LTE Radio Access: An Overview", in *4G: LTE/LTE-Advanced for Mobile Broadband (Second Edition)*, 2014, pp. 103–119, ISBN: 9780124199859. DOI: 10.1016/B978-0-12-419985-9.00007-6. [Online]. Available: <http://linkinghub.elsevier.com/retrieve/pii/B9780124199859000076>.
- [53] P. Pirinen, "Challenges and possibilities for flexible duplexing in 5G networks", *2015 IEEE 20th International Workshop on Computer Aided Modelling and Design of Communication Links and Networks, CAMAD 2015*, pp. 6–10, 2016. DOI: 10.1109/CAMAD.2015.7390471.
- [54] D. Kim, H. Lee, and D. Hong, "A Survey of In-Band Full-Duplex Transmission: From the Perspective of PHY and MAC Layers", *IEEE Communications Surveys and Tutorials*, vol. 17, no. 4, pp. 2017–2046, 2015, ISSN: 1553877X. DOI: 10.1109/COMST.2015.2403614.
- [55] T. Riihonen, S. Werner, and R. Wichman, "Mitigation of loopback self-interference in full-duplex MIMO relays", *IEEE Transactions on Signal Processing*, vol. 59, no. 12, pp. 5983–5993, 2011, ISSN: 1053587X. DOI: 10.1109/TSP.2011.2164910.
- [56] G. Zheng, "Joint beamforming optimization and power control for full-duplex MIMO two-way relay channel", *IEEE Transactions on Signal Processing*, vol. 63, no. 3, pp. 555–566, 2015, ISSN: 1053587X. DOI: 10.1109/TSP.2014.2376885. arXiv: 1411.6021.
- [57] S. Han, I. Chih-Lin, Z. Xu, C. Pan, and Z. Pan, "Full duplex: Coming into reality in 2020?", *2014 IEEE Global Communications Conference, GLOBECOM 2014*, no. 2014, pp. 4776–4781, 2014. DOI: 10.1109/GLOCOM.2014.7037562.
- [58] Z. Zhang, K. Long, A. V. Vasilakos, and L. Hanzo, "Full-Duplex Wireless Communications: Challenges, Solutions, and Future Research Directions", *Proceedings of the IEEE*, vol. 104, no. 7, pp. 1369–1409, 2016, ISSN: 15582256. DOI: 10.1109/JPROC.2015.2497203.

- [59] I. Stevanovic, A. Skrivervik, and J. Mosig, "Smart antenna systems for mobile communications", Tech. Rep. January, 2003, p. 120. [Online]. Available: <http://123seminaronly.com/Seminar-Reports/050/109618796-Smart-Antennas.pdf>.
- [60] C. A. Balanis, *Antenna Theory: Analysis and Design*, 3rd ed. John Wiley & Sons, Inc, 2005.
- [61] P. Xia, S. K. Yong, J. Oh, and C. Ngo, "A practical SDMA protocol for 60 GHz millimeter wave communications", *Conference Record - Asilomar Conference on Signals, Systems and Computers*, pp. 2019–2023, 2008, ISSN: 10586393. DOI: 10.1109/ACSSC.2008.5074786.
- [62] P. Cao and J. S. Thompson, "Practical multi-user transmission design in millimeter wave cellular networks: Is the joint SDMA-TDMA technique the answer?", *IEEE Workshop on Signal Processing Advances in Wireless Communications, SPAWC*, vol. 2016-Augus, 2016. DOI: 10.1109/SPAWC.2016.7536854.
- [63] A. I. Sulyman and M. Hefnawi, "Adaptive MIMO beamforming algorithm based on gradient search of the channel capacity in OFDM-SDMA systems", *IEEE Communications Letters*, vol. 12, no. 9, pp. 642–644, 2008, ISSN: 10897798. DOI: 10.1109/LCOMM.2008.080708.
- [64] ———, "Performance Evaluation of Capacity-Aware MIMO Beamforming Schemes in OFDM-SDMA Systems", *IEEE Transactions on Communications*, vol. 58, no. January, pp. 79–83, 2010.
- [65] F.-L. Luo and C. Zhang, "Signal Processing for 5G: Algorithms and Implementations", in *Non-Orthogonal Multiple Access (NOMA): Concept and Design*, Wiley-IEEE Press, 2016, pp. 143–168, ISBN: 9781119116493.
- [66] T. S. Rappaport, F. Gutierrez, E. Ben-Dor, J. N. Murdock, Y. Qiao, and J. I. Tamir, "Broadband millimeter-wave propagation measurements and models using adaptive-beam antennas for outdoor Urban cellular communications", *IEEE Transactions on Antennas and Propagation*, vol. 61, no. 4, pp. 1850–1859, 2013, ISSN: 0018926X. DOI: 10.1109/TAP.2012.2235056.
- [67] Y. M. Tsang, A. S. Poon, and S. Addepalli, "Coding the beams: Improving beamforming training in mmWave communication system", *GLOBECOM - IEEE Global Telecommunications Conference*, pp. 1–6, 2011. DOI: 10.1109/GLOCOM.2011.6134486. arXiv: 1104.1007.
- [68] P. Xia, S. K. Yong, J. Oh, and ChiuNgo, "Multi-stage iterative antenna training for millimeter wave communications", *GLOBECOM - IEEE Global Telecommunications Conference*, pp. 4740–4745, 2008. DOI: 10.1109/GLOCOM.2008.ECP908.
- [69] F. Dai and J. Wu, "Efficient broadcasting in ad hoc wireless networks using directional antennas", *IEEE Transactions on Parallel and Distributed Systems*, vol. 17, no. 4, pp. 335–347, 2006, ISSN: 10459219. DOI: 10.1109/TPDS.2006.46.

- [70] M. Beriooli, A. Molinaro, S. Morosi, and S. Scalise, "Aerospace communications for emergency applications", *Proceedings of the IEEE*, vol. 99, no. 11, pp. 1922–1938, 2011, ISSN: 00189219. DOI: 10.1109/JPROC.2011.2161737.
- [71] D. Rodriguez-Avila, J. Trajkovikj, and A. Skrivervik, "Study on "mm wave antennas for 5G communications" report I", Tech. Rep., 2015, pp. 1–42.
- [72] Y. Azar, G. N. Wong, K. Wang, R. Mayzus, J. K. Schulz, H. Zhao, F. Gutierrez, D. Hwang, and T. S. Rappaport, "28 GHz propagation measurements for outdoor cellular communications using steerable beam antennas in New York city", *IEEE International Conference on Communications*, pp. 5143–5147, 2013, ISSN: 15503607. DOI: 10.1109/ICC.2013.6655399.
- [73] M. Samimi, K. Wang, Y. Azar, G. N. Wong, R. Mayzus, H. Zhao, J. K. Schulz, S. Sun, F. Gutierrez, and T. S. Rappaport, "28 GHz angle of arrival and angle of departure analysis for outdoor cellular communications using steerable beam antennas in New York City", *IEEE Vehicular Technology Conference*, 2013, ISSN: 15502252. DOI: 10.1109/VTCSpring.2013.6691812.
- [74] H. Zhao, R. Mayzus, S. Sun, M. Samimi, J. K. Schulz, Y. Azar, K. Wang, G. N. Wong, F. Gutierrez, and T. S. Rappaport, "28 GHz millimeter wave cellular communication measurements for reflection and penetration loss in and around buildings in New York city", *IEEE International Conference on Communications*, no. Icc, pp. 5163–5167, 2013, ISSN: 15503607. DOI: 10.1109/ICC.2013.6655403.
- [75] M. Shafi, J. Zhang, H. Tataria, A. F. Molisch, S. Sun, T. S. Rappaport, F. Tufvesson, S. Wu, and K. Kitao, "Microwave vs. Millimeter-Wave Propagation Channels: Key Differences and Impact on 5G Cellular Systems", *IEEE Communications Magazine*, vol. 56, no. 12, pp. 14–20, 2018, ISSN: 15581896. DOI: 10.1109/MCOM.2018.1800255.
- [76] F. Khan and J. Pi, "Millimeter-wave Mobile Broadband : Unleashing 3-300GHz Spectrum", 2011.
- [77] G. R. Maccartney, J. Zhang, S. Nie, and T. S. Rappaport, "Path loss models for 5G millimeter wave propagation channels in urban microcells", *GLOBECOM - IEEE Global Telecommunications Conference*, pp. 3948–3953, 2013. DOI: 10.1109/GLOCOM.2013.6831690.
- [78] W. Roh, "Performances and Feasibility of mmWave Beamforming Prototype for 5G Cellular Communications", *IEEE International Conference on Communications*, pp. 1–29, 2013.
- [79] M. Peter, "Measurement results and final mmMAGIC channel models", *Deliverable D2*, vol. 2, p. 12, 2017. [Online]. Available: https://bscw.5g-mmmagic.eu/pub/bscw.cgi/d202656/mmMAGIC%7B%5C_%7DD2-2.pdf.
- [80] M. R. Akdeniz, Y. Liu, S. Rangan, and E. Erkip, "Millimeter wave picocellular system evaluation for urban deployments", *2013 IEEE Globecom Workshops, GC Wkshps 2013*, pp. 105–110, 2013. DOI: 10.1109/GLOCOMW.2013.6824970. arXiv: arXiv:1304.3963v1.

- [81] I. A. Hemadeh, K. Satyanarayana, M. El-Hajjar, and L. Hanzo, "Millimeter-Wave Communications: Physical Channel Models, Design Considerations, Antenna Constructions, and Link-Budget", *IEEE Communications Surveys and Tutorials*, vol. 20, no. 2, pp. 870–913, 2018, ISSN: 1553877X. DOI: 10.1109/COMST.2017.2783541.
- [82] Y. Huo, X. Dong, and W. XU, "5G Cellular User Equipment : From Theory to Practical Hardware Design", *IEEE Access*, vol. 5, pp. 13 992–14 010, 2017. DOI: 10.1109/ACCESS.2017.2727550.
- [83] K. Bechta, M. Rybakowski, F. Hsieh, and D. Chizhik, "Modeling of radio link budget with beamforming antennas for evaluation of 5G systems", *IEEE 5G World Forum, 5GWF 2018 - Conference Proceedings*, pp. 427–432, 2018. DOI: 10.1109/5GWF.2018.8516969.
- [84] A. Roessler, "Pre-5G and 5G: Will the mmWave link work?", *Microwave Journal*, no. December, 2017.
- [85] Y. Cao, K. S. Chin, W. Che, W. Yang, and E. S. Li, "A Compact 38 GHz Multibeam Antenna Array with Multifolded Butler Matrix for 5G Applications", *IEEE Antennas and Wireless Propagation Letters*, vol. 16, pp. 2996–2999, 2017, ISSN: 15361225. DOI: 10.1109/LAWP.2017.2757045.
- [86] M. Ansari, H. Zhu, N. Shariati, and Y. J. Guo, "Compact Planar Beamforming Array with Endfire Radiating Elements for 5G Applications", *IEEE Transactions on Antennas and Propagation*, vol. 67, no. 11, pp. 6859–6869, 2019, ISSN: 15582221. DOI: 10.1109/TAP.2019.2925179.
- [87] Q. Wu, J. Hirokawa, J. Yin, C. Yu, H. Wang, and W. Hong, "Millimeter-Wave Multibeam Endfire Dual-Circularly Polarized Antenna Array for 5G Wireless Applications", *IEEE Transactions on Antennas and Propagation*, vol. 66, no. 9, pp. 4930–4935, 2018, ISSN: 0018926X. DOI: 10.1109/TAP.2018.2851667.
- [88] Y. Li, J. Wang, and K. M. Luk, "Millimeter-Wave MultiBeam Aperture-Coupled Magnetolectric Dipole Array With Planar Substrate Integrated Beamforming Network for 5G Applications", *IEEE Transactions on Antennas and Propagation*, vol. 65, no. 12, pp. 6422–6431, 2017, ISSN: 0018926X. DOI: 10.1109/TAP.2017.2681429.
- [89] M. Imbert, J. Romeu, M. Baquero-Escudero, M. T. Martinez-Ingles, J. M. Molina-Garcia-Pardo, and L. Jofre, "Assessment of LTCC-Based Dielectric Flat Lens Antennas and Switched-Beam Arrays for Future 5G Millimeter-Wave Communication Systems", *IEEE Transactions on Antennas and Propagation*, vol. 65, no. 12, pp. 6453–6473, 2017, ISSN: 0018926X. DOI: 10.1109/TAP.2017.2767821.
- [90] Y. Yashchyshyn, K. Derzakowski, G. Bogdan, K. Godziszewski, D. Nyzovets, C. H. Kim, and B. Park, "28 GHz Switched-Beam Antenna Based on S-PIN Diodes for 5G Mobile Communications", *IEEE Antennas and Wireless Propagation Letters*, vol. 17, no. 2, pp. 2018–2021, 2018.
- [91] H. A. Diawuo and Y. B. Jung, "Broadband Proximity-Coupled Microstrip Planar Antenna Array for 5G Cellular Applications", *IEEE Antennas and Wireless Propagation Letters*, vol. 17, no. 7, pp. 1286–1290, 2018, ISSN: 15361225. DOI: 10.1109/LAWP.2018.2842242.

- [92] S. J. Park and S. O. Park, "LHCP and RHCP Substrate Integrated Waveguide Antenna Arrays for Millimeter-Wave Applications", *IEEE Antennas and Wireless Propagation Letters*, vol. 16, pp. 601–604, 2017, ISSN: 15361225. DOI: 10.1109/LAWP.2016.2594081.
- [93] Y.-H. Yang, B.-H. Sun, G.-X. Zhang, and L. Shen, "TFSIW-Excited Dual-Polarized Array Antenna With 30° Beam-Pointing for Millimeter-Wave Applications", *IEEE Transactions on Antennas and Propagation*, vol. 67, no. 8, pp. 5740–5745, 2019.
- [94] X. Pang, W. Hong, T. Yang, and L. Li, "Design and implementation of an active multi-beam antenna system with 64 RF channels and 256 antenna elements for massive MIMO application in 5G wireless communications", *China Communications*, vol. 11, no. 11, pp. 16–23, 2014, ISSN: 16735447. DOI: 10.1109/CC.2014.7004520.
- [95] W. Roh, J. Y. Seol, J. H. Park, B. Lee, J. Lee, Y. Kim, J. Cho, K. Cheun, and F. Aryanfar, "Millimeter-wave beamforming as an enabling technology for 5G cellular communications: Theoretical feasibility and prototype results", *IEEE Communications Magazine*, vol. 52, no. 2, pp. 106–113, 2014, ISSN: 01636804. DOI: 10.1109/MCOM.2014.6736750.
- [96] Y. Aslan, J. Puskely, J. H. Janssen, M. Geurts, A. Roederer, and A. Yarovoy, "Thermal-aware synthesis of 5g base station antenna arrays: An overview and a sparsity-based approach", *IEEE Access*, vol. 6, pp. 58 868–58 882, 2018, ISSN: 21693536. DOI: 10.1109/ACCESS.2018.2873977.
- [97] R. W. Heath, N. Gonzalez-Prelcic, S. Rangan, W. Roh, and A. M. Sayeed, "An Overview of Signal Processing Techniques for Millimeter Wave MIMO Systems", *IEEE Journal on Selected Topics in Signal Processing*, vol. 10, no. 3, pp. 436–453, 2016, ISSN: 19324553. DOI: 10.1109/JSTSP.2016.2523924. arXiv: 1512.03007.
- [98] A. Brunner, "Possibilities of Dimensioning Doubly Curved Reflectors for Azimuth-Search Radar Antennas", *IEEE Trans. Antennas Propag.*, vol. 19, no. 1, pp. 52–57, 1971, ISSN: 15582221. DOI: 10.1109/TAP.1971.1139860.
- [99] R. S. Elliott and G. J. Stern, "A New Technique for Shaped Beam Synthesis of Equispaced Arrays", no. 10, pp. 156–163, 1984.
- [100] I. Ahmed, H. Khammari, A. Shahid, A. Musa, K. S. Kim, E. De Poorter, and I. Moerman, "A survey on hybrid beamforming techniques in 5G: Architecture and system model perspectives", *IEEE Communications Surveys and Tutorials*, vol. 20, no. 4, pp. 3060–3097, 2018, ISSN: 1553877X. DOI: 10.1109/COMST.2018.2843719.
- [101] S. Kutty and D. Sen, "Beamforming for Millimeter Wave Communications: An Inclusive Survey", *IEEE Communications Surveys and Tutorials*, vol. 18, no. 2, pp. 949–973, 2016, ISSN: 1553877X. DOI: 10.1109/COMST.2015.2504600.
- [102] A. F. Molisch, V. V. Ratnam, S. Han, Z. Li, S. L. H. Nguyen, L. Li, and K. Haneda, "Hybrid Beamforming for Massive MIMO: A Survey", *IEEE Communications Magazine*, vol. 55, no. 9, pp. 134–141, 2017, ISSN: 01636804. DOI: 10.1109/MCOM.2017.1600400. arXiv: 1609.05078.

- [103] A. Adhikary, J. Nam, J. Y. Ahn, and G. Caire, “Joint spatial division and multiplexing-The large-scale array regime”, *IEEE Transactions on Information Theory*, vol. 59, no. 10, pp. 6441–6463, 2013, ISSN: 00189448. DOI: 10.1109/TIT.2013.2269476.
- [104] R. Mendez-Rial, C. Rusu, N. Gonzalez-Prelcic, A. Alkhateeb, and R. W. Heath, “Hybrid MIMO Architectures for Millimeter Wave Communications: Phase Shifters or Switches?”, *IEEE Access*, vol. 4, pp. 247–267, 2016, ISSN: 21693536. DOI: 10.1109/ACCESS.2015.2514261. arXiv: 1512.03032.
- [105] A. Alkhateeb, Y. H. Nam, J. C. Zhang, and R. W. Heath, “Massive MIMO Combining with Switches”, *IEEE Wireless Communications Letters*, vol. 5, no. 3, pp. 232–235, 2016, ISSN: 21622345. DOI: 10.1109/LWC.2016.2522963. arXiv: 1601.07468.
- [106] S. Han, C. L. I, Z. Xu, and C. Rowell, “Large-scale antenna systems with hybrid analog and digital beamforming for millimeter wave 5G”, *IEEE Communications Magazine*, vol. 53, no. 1, pp. 186–194, 2015, ISSN: 01636804. DOI: 10.1109/MCOM.2015.7010533.
- [107] V. Venkateswaran, F. Pivit, and L. Guan, “Hybrid RF and digital beamformer for cellular networks: Algorithms, microwave architectures, and measurements”, *IEEE Transactions on Microwave Theory and Techniques*, vol. 64, no. 7, pp. 2226–2243, 2016, ISSN: 00189480. DOI: 10.1109/TMTT.2016.2569583. arXiv: 1510.02822.
- [108] R. J. Mailloux, *Phased array antenna handbook*, 2nd. Artech House, 2005.
- [109] A. K. Bhattacharyya, “Projection matrix method for shaped beam synthesis in phased arrays and reflectors”, *IEEE Transactions on Antennas and Propagation*, vol. 55, no. 3 I, pp. 675–683, 2007, ISSN: 0018926X. DOI: 10.1109/TAP.2007.891570.
- [110] F. Ares, R. S. Elliott, and E. Moreno, “Design of planar arrays for obtaining efficient footprint patterns with an arbitrary footprint boundary”, *IEEE Transactions on Antennas and Propagation*, vol. 42, no. 11, pp. 880–882, 1994. DOI: 10.1109/EUMA.1993.336737.
- [111] J. R. Mautz and R. F. Harrington, “Computational Methods for Antenna Pattern Synthesis”, *IEEE Transactions on Antennas and Propagation*, vol. 23, no. 4, pp. 507–512, 1975.
- [112] W. L. Stutzman, “Synthesis of Shaped-Beam Radiation Patterns Using the Iterative Sampling Method”, *IEEE Transactions on Antennas and Propagation*, vol. 19, no. 1, pp. 36–41, 1971, ISSN: 15582221. DOI: 10.1109/TAP.1971.1139892.
- [113] K. Yang, Z. Zhao, and Q. H. Liu, “An iterative FFT based flat-top footprint pattern synthesis method with planar array”, *Journal of Electromagnetic Waves and Applications*, vol. 26, no. 14-15, pp. 1956–1966, 2012, ISSN: 09205071. DOI: 10.1080/09205071.2012.722752.
- [114] W. P. Keizer, “Low-sidelobe pattern synthesis using iterative fourier techniques coded in MATLAB”, *IEEE Antennas and Propagation Magazine*, vol. 51, no. 2, pp. 137–150, 2009, ISSN: 10459243. DOI: 10.1109/MAP.2009.5162038.

- [115] W. T. Li, Y. Q. Hei, J. Yang, and X. W. Shi, "Synthesis of multiple-pattern planar arrays with A hybrid generalised iterative fast Fourier transform algorithm", *IET Microwaves, Antennas and Propagation*, vol. 10, no. 1, pp. 16–24, 2015, ISSN: 17518733. DOI: 10.1049/iet-map.2014.0595.
- [116] Y. Liu, X. Huang, K. D. Xu, Z. Song, S. Yang, and Q. H. Liu, "Pattern Synthesis of Unequally Spaced Linear Arrays Including Mutual Coupling Using Iterative FFT via Virtual Active Element Pattern Expansion", *IEEE Transactions on Antennas and Propagation*, vol. 65, no. 8, pp. 3950–3958, 2017, ISSN: 0018926X. DOI: 10.1109/TAP.2017.2708081.
- [117] O. M. Bucci, D. Giuseppe, G. Mazzarella, and G. Panariello, "Antenna Pattern Syntehsis: a new general approach", *Proceedings of the IEEE*, vol. 82, no. 3, pp. 358–371, 1994.
- [118] O. M. Bucci, M. D'Urso, T. Isernia, P. Angeletti, and G. Toso, "Deterministic synthesis of uniform amplitude sparse arrays via new density taper techniques", *IEEE Transactions on Antennas and Propagation*, vol. 58, no. 6, pp. 1949–1958, 2010, ISSN: 0018926X. DOI: 10.1109/TAP.2010.2046831.
- [119] A. Morabito, T. Isernia, and L. Di Donato, "Optimal synthesis of phase-only reconfigurable linear sparse arrays having uniform-amplitude excitations", *Progressin Electromagnetics Research*, vol. 124, pp. 405–423, 2012.
- [120] J. L. Araque Quijano, M. Righero, and G. Vecchi, "Sparse 2-D array placement for arbitrary pattern mask and with excitation constraints: A simple deterministic approach", *IEEE Transactions on Antennas and Propagation*, vol. 62, no. 4, pp. 1652–1662, 2014, ISSN: 0018926X. DOI: 10.1109/TAP.2013.2288363.
- [121] D. W. Boeringer and D. H. Werner, "Particle swarm optimization versus genetic algorithms for phased array synthesis", *IEEE Transactions on Antennas and Propagation*, vol. 52, no. 3, pp. 771–779, 2004, ISSN: 0018926X. DOI: 10.1109/TAP.2004.825102.
- [122] F. Ares, S. Rengarajan, E. Villanueva, E. Skochinski, and E. Moreno, "Application of genetic algorithms and simulated annealing technique in optimising the aperture distributions of antenna arrays patterns", *Electronics Letters*, vol. 32, no. 3, pp. 148–149, 1996, ISSN: 1098-6596. arXiv: arXiv:1011.1669v3.
- [123] F. J. Villegas, "Parallel genetic-algorithm optimization of shaped beam coverage areas using planar 2-D phased arrays", *IEEE Transactions on Antennas and Propagation*, vol. 55, no. 6 II, pp. 1745–1753, 2007, ISSN: 0018926X. DOI: 10.1109/TAP.2007.898601.
- [124] S. Boyd, "Antenna array pattern synthesis via convex optimization", *IEEE Transactions on Signal Processing*, vol. 45, no. 3, pp. 526–532, 1997.
- [125] J. Mattingley and S. Boyd, "Real-time convex optimization in signal processing: Recent advances that make it easier to design and implement algorithms", *IEEE Signal Processing Magazine*, no. May, pp. 50–61, 2010, ISSN: 1053-5888. [Online]. Available: http://ieeexplore.ieee.org/xpls/abs%7B%5C_%7Dall.jsp?arnumber=5447065.

- [126] J. I. Echeveste, M. A. González De Aza, and J. Zapata, “Shaped Beam Synthesis of Real Antenna Arrays via Finite-Element Method, Floquet Modal Analysis, and Convex Programming”, *IEEE Transactions on Antennas and Propagation*, vol. 64, no. 4, pp. 1279–1286, 2016, ISSN: 0018926X. DOI: 10.1109/TAP.2016.2526038.
- [127] Y.-X. Zhang, Y.-C. Jiao, and L. Zhang, “Antenna Array Directivity Maximization With Side Lobe Level Constraints Using Convex Optimization”, *IEEE Transactions on Antennas and Propagation*, no. c, pp. 1–1, 2020, ISSN: 0018-926X. DOI: 10.1109/tap.2020.3026886.
- [128] S. Boyd, *Convex Optimization*, 7th. Cambridge University Press, 2009, ISBN: 9780521833783. DOI: 10.1201/9781420049503-c34.
- [129] M. C. Grant and S. P. Boyd, *CVX: Matlab Software for Disciplined Convex Programming*, 2012. [Online]. Available: <http://cvxr.com/cvx>.
- [130] H. G. Hoang, H. D. Tuan, and B. N. Vo, “Low-dimensional SDP formulation for large antenna array synthesis”, *IEEE Transactions on Antennas and Propagation*, vol. 55, no. 6 II, pp. 1716–1725, 2007, ISSN: 0018926X. DOI: 10.1109/TAP.2007.898573.
- [131] S. P. Wu, S. Boyd, and L. Vandenberghe, “FIR filter design via semidefinite programming and spectral factorization”, *Proceedings of the IEEE Conference on Decision and Control*, vol. 1, no. December, pp. 5–10, 1996, ISSN: 01912216. DOI: 10.1109/cdc.1996.574313.
- [132] B. Fuchs, “Array Synthesis Problems”, *IEEE Trans. Antennas Propag.*, vol. 62, no. 2, pp. 634–640, 2014.
- [133] J. H. McClellan, T. W. Parks, and L. R. Rabiner, “A computer program for designing optimum FIR linear phase digital filters”, *IEEE Transaction on audio and electroacustics*, vol. AU-21, no. 6, pp. 506–525, 1973.
- [134] Y. Liu, J. Bai, K. D. Xu, Z. Xu, F. Han, Q. H. Liu, and Y. Jay Guo, “Linearly Polarized Shaped Power Pattern Synthesis With Sidelobe and Cross-Polarization Control by Using Semidefinite Relaxation”, *IEEE Transactions on Antennas and Propagation*, vol. 66, no. 6, pp. 3207–3212, 2018, ISSN: 0018926X. DOI: 10.1109/TAP.2018.2816782.
- [135] K. M. Tsui and S. C. Chan, “Pattern synthesis of narrowband conformal arrays using iterative second-order cone programming”, *IEEE Transactions on Antennas and Propagation*, vol. 58, no. 6, pp. 1959–1970, 2010, ISSN: 0018926X. DOI: 10.1109/TAP.2010.2046865.
- [136] B. Fuchs, A. Skrivervik, and J. R. Mosig, “Shaped beam synthesis of arrays via sequential convex optimizations”, *IEEE Antennas and Wireless Propagation Letters*, vol. 12, pp. 1049–1052, 2013, ISSN: 15361225. DOI: 10.1109/LAWP.2013.2280043.
- [137] —, “Synthesis of uniform amplitude focused beam arrays”, *IEEE Antennas and Wireless Propagation Letters*, vol. 11, pp. 1178–1181, 2012, ISSN: 15361225. DOI: 10.1109/LAWP.2012.2221452.

- [138] F. Yang, S. Yang, Y. Chen, S. Qu, and J. Hu, "Efficient Pencil Beam Synthesis in 4-D Antenna Arrays Using an Iterative Convex Optimization Algorithm", *IEEE Transactions on Antennas and Propagation*, vol. 67, no. 11, pp. 6847–6858, 2019, ISSN: 15582221. DOI: 10.1109/TAP.2019.2922817.
- [139] D. P. Scholnik and J. O. Coleman, "Formulating wideband array-pattern optimizations", *IEEE International Symposium on Phased Array Systems and Technology*, pp. 489–492, 2000, ISSN: 0031-2746. DOI: 10.1109/past.2000.859003.
- [140] S. Rajagopal, "Beam broadening for phased antenna arrays using multi-beam subarrays", *IEEE International Conference on Communications*, pp. 3637–3642, 2012, ISSN: 15503607. DOI: 10.1109/ICC.2012.6363657.
- [141] S. E. Nai, W. Ser, Z. L. Yu, and H. Chen, "Beampattern synthesis for linear and planar arrays with antenna selection by convex optimization", *IEEE Transactions on Antennas and Propagation*, vol. 58, no. 12, pp. 3923–3930, 2010, ISSN: 0018926X. DOI: 10.1109/TAP.2010.2078446.
- [142] D. Pinchera, M. D. Migliore, M. Lucido, F. Schettino, G. Panariello, J. E. Ball, and N. H. Younan, "A Compressive-Sensing Inspired Alternate Projection Algorithm for Sparse Array Synthesis", 2017, ISSN: 20799292. DOI: 10.3390/electronics6010003.
- [143] A. K. Pandey, "Design of a Cosecant Square-Shaped Beam Pattern SAR Antenna Array Fed with Square Coaxial Feeder Network", in *Proceedings of the 43rd European Microwave Conference Design*, European Microwave Association, 2013, pp. 1699–1702, ISBN: 9782874870316. DOI: 10.23919/EuMC.2013.6687003.
- [144] M. Koubeissi, L. Freytag, C. Decroze, and T. Monediere, "Design of a Cosecant-Squared Pattern Antenna Fed by a New Butler Matrix Topology for Base Station at 42 GHz", *IEEE Antennas Wireless Propag. Lett.*, vol. 7, pp. 354–357, 2008.
- [145] Z.-c. Hao and M. He, "Developing Millimeter-Wave Planar Antenna With a Cosecant Squared Pattern", *IEEE Trans. Antennas Propag.*, vol. 65, no. 10, pp. 5565–5570, 2017.
- [146] H. Chu, P. Li, and Y.-x. Guo, "A Beam-Shaping Feeding Network in Series Configuration for Antenna Array With Cosecant-Square Pattern and Low Sidelobes", *IEEE Antennas Wireless Propag. Lett.*, vol. 18, no. 4, pp. 742–746, 2019. DOI: 10.1109/LAWP.2019.2901948.
- [147] L. Qiu, K. Xiao, S. L. Chai, H. Y. Qi, and J. J. Mao, "A Double-Layer Shaped-Beam Traveling-Wave Slot Array Based on SIW", *IEEE Trans. Antennas Propag.*, vol. 64, no. 11, pp. 4639–4647,
- [148] H. Qi, F. Zhao, L. Qiu, K. Xiao, and S. Chai, "Design of a Feed Network for Cosecant Squared Beam based on Suspended Stripline", in *Proceedings of the International Symposium on Antennas & Propagation*, Antenna Society of the Chinese Institute of Electronics, 2013, pp. 1005–1007.

- [149] R. V. Gatti and R. Sorrentino, "Slotted waveguide antennas with arbitrary radiation pattern", in *IEEE Antennas and Propagation Society Symposium*, 2004, pp. 821–824, ISBN: 1580539920.
- [150] A. Garcia Tejero, "Design of a beamforming network for sectorial coverage in mm-Waves cell station Master Thesis", PhD thesis, École polytechnique fédérale de Lausanne, 2018.
- [151] R. Glogowski, "Planar Antennas for Ka-Band Space Applications", vol. 6098, 2013.
- [152] S. Karimkashi and G. Zhang, "A dual-polarized series-fed microstrip antenna array with very high polarization purity for weather measurements", *IEEE Trans. Antennas Propag.*, vol. 61, no. 10, pp. 5315–5319, 2013, ISSN: 0018926X. DOI: 10.1109/TAP.2013.2273813.
- [153] L. Qiu, H. Y. Qi, F. Zhao, K. Xiao, and S. L. Chai, "A Shaped-Beam Stripline-Fed Aperture-Coupled Stacked Patch Array", *IEEE Trans. Antennas Propag.*, vol. 64, no. 7, pp. 3172–3176, 2016, ISSN: 0018926X. DOI: 10.1109/TAP.2016.2554201.
- [154] H. A. Diawuo and Y.-b. Jung, "Broadband Proximity-Coupled Microstrip Planar Antenna Array for 5G Cellular Applications", *IEEE Antennas Wireless Propag. Lett.*, vol. 17, no. 7, pp. 1286–1290, 2018.
- [155] L. G. Maloratsky and R. Collins, "Reviewing the basics of Suspended Striplines", *Microwave Journal*, vol. 45, no. 10, p. 82, 2002.
- [156] T. Itoh, "Overview of Quasi-Planar Transmission Lines", *IEEE Transactions on Microwave Theory and Techniques*, vol. 31, no. 2, 1989.
- [157] D. M. Pozar, *Microwave Engineering*, 4th. JohnWiley & Sons, Inc., 2011.
- [158] D. Pozar and D. Schaubert, "Techniques for Improving Element Bandwidth", in *Microstrip Antennas: The analysis and design of microstrip antennas and arrays*, D. M. Pozar and D. H. Schaubert, Eds., New York: IEEE Press, NY, 1995, ch. 4, pp. 155–201.
- [159] F. Croq and D. M. Pozar, "Millimeter-Wave design of wide-band aperture-coupled stacked microstrip antennas", *IEEE Trans. Antennas Propag.*, vol. 39, no. 12, pp. 1770–1776, 1991.
- [160] P. L. Sullivan and D. H. Schaubert, "Analysis of an Aperture Coupled Microstrip Antenna", *IEEE Transactions on Antennas and Propagation*, vol. 34, no. 8, pp. 977–984, 1986, ISSN: 15582221. DOI: 10.1109/TAP.1986.1143929.
- [161] J. Zürcher and F. E. Gardiol, *Broadband patch antennas-a SSFIP update*. Artech House, 1995.
- [162] S. D. Targonski, R. B. Waterhouse, and D. M. Pozar, "Design of wide-band aperture-stacked patch microstrip antennas", *IEEE Transactions on Antennas and Propagation*, vol. 46, no. 9, pp. 1245–1251, 1998, ISSN: 0018926X. DOI: 10.1109/8.719966.
- [163] D. Pozar and S. Targonski, "Improved coupling for aperture coupled microstrip antennas", *IEEE Trans. Antennas Propag.*, vol. 27, no. 13, pp. 1129–1131, 1991, ISSN: 0018926X. DOI: 10.1109/8.511831.

- [164] H. Iizuka, K. Sakakibara, and N. Kikuma, "Millimeter-wave transition from waveguide to two microstrip lines using rectangular patch element", *IEEE Transactions on Microwave Theory and Techniques*, vol. 55, no. 5, pp. 899–905, 2007, ISSN: 00189480. DOI: 10.1109/TMTT.2007.895139.
- [165] J. F. Zürcher, R. Głogowski, and J. R. Mosig, "A new power divider architecture for suspended strip line", in *Proceedings of European Conference on Antennas and Propagation, EuCAP, 2012*, pp. 418–422, ISBN: 9781457709180. DOI: 10.1109/EuCAP.2012.6206226.
- [166] D. Wu and K. Seo, "Waveguide to microstrip line transition and power divider", *Electronics Letters*, vol. 44, no. 7, pp. 7–8, 2008, ISSN: 00251569. DOI: 10.1049/el.
- [167] M. Davidovitz, "Wide-Band and waveguide-to-microstrip transition and power divider", *IEEE Microwave and guided wave letters*, vol. 6, no. 1, pp. 13–15, 1996.
- [168] S. B. Cohn, "Properties of ridge wave guide", *Proceedings of the I.R.E.*, pp. 783–788, 1947.
- [169] Agilent-Technologies, "Agilent Network Analysis Applying the 8510 TRL Calibration for Non-Coaxial Measurements", Tech. Rep., 2001, pp. 1–24. [Online]. Available: <http://scholar.google.com/scholar?hl=en%7B%5C&%7DbtnG=Search%7B%5C&%7Dq=intitle:Applying+the+8510+TRL+Calibration+for+Non-Coaxial+Measurements%7B%5C#%7D0>.
- [170] A. Massa, G. Oliveri, P. Rocca, and F. Viani, "System-by-design: A new paradigm for handling design complexity", *8th European Conference on Antennas and Propagation, EuCAP 2014*, no. EuCAP, pp. 1180–1183, 2014. DOI: 10.1109/EuCAP.2014.6901983.
- [171] Y. Aslan, J. Puskely, A. Roederer, and A. Yarovoy, "Multiple Beam Synthesis of Passively Cooled 5G Planar Arrays Using Convex Optimization", *IEEE Transactions on Antennas and Propagation*, vol. 68, no. 5, pp. 3557–3566, 2020, ISSN: 15582221. DOI: 10.1109/TAP.2019.2955885.

Danelys Rodríguez Avila

École Polytechnique Fédérale de Lausanne [EPFL]
School of Engineering [STI]
Microwaves and Antennas Group [MAG]
Lausanne (Switzerland)
Email: danelys.rodriguez@epfl.ch

Education and qualification

PhD candidate

École Polytechnique Fédérale de Lausanne [EPFL] (Lausanne, Switzerland)
2015 - Present
MSc thesis: *A Portable Picocell Antenna for 5G*

MSc Telecommunications and Telematics

José Antonio Echeverría Insitute of Technology [CUJAE] (Havana, Cuba)
January 2012- October 2014, GPA: 5/5

MSc thesis: *Design contributions in radiating systems for LTE, WiMAX, Bluetooth, WLAN and digital television applications*

Postgraduate course in Basic Training for University Teachers

José Antonio Echeverría Insitute of Technology [CUJAE] (Havana, Cuba)
October 2011 - January 2013, GPA: 5/5

BSc Telecommunication and Electronic Engineering

José Antonio Echeverría Insitute of Technology [CUJAE] (Havana, Cuba)
September 2006 - June 2011, GPA: 4.5/5

BSc thesis: *Microstrip antennas with left-handed metamaterials for WLAN*

Other courses

5G Phased Arrays

TU Delft (Netherlands). June 2018

Millimeter-Wave Antennas Design and Technologies

IETR (Rennes, France). July 2016

Frequency Domain Techniques

University of Florence (Italy). September 2015

Digital Television Technologies Training

Telecom. Research & Development Inst. [LACETEL] (Havana, Cuba). September 2013 - January 2014

Technical Training of Digital Television

National Engineering Lab. for DTV [DTNEL] (Havana, Cuba). November 2014

Digital Television International Forum

(Havana, Cuba). November 2014

Research Areas

Mm-waves antennas, design and synthesis of phased arrays, hybrid beamforming networks.

Publications

- D. Rodríguez-Avila, A. K. Skrivervik, *Efficient cosecant-squared broadband subarray for mm-Waves portable picocell station*, Submitted to IEEE Antennas and Wireless Propagation Letters
- D. Rodríguez-Avila, A. K. Skrivervik, *Subarray antenna fed by analog beamforming network for 5G picocell applications*, 2020 14th European Conference on Antennas and Propagation (EuCAP), Copenhagen, Denmark, 2020, pp. 1-4,
- D. Rodríguez-Avila, A. K. Skrivervik, *Stacked patch antenna and hybrid beamforming network for 5G picocell applications*, 2019 13th European Conference on Antennas and Propagation (EuCAP), Krakow, Poland, 2019, pp. 1-5
- D. Rodríguez-Avila, S. Pereira García, Y. Paz Marrero, A. Saavedra de Vera, F. Marante Rizo, J. Vassallo Sanz, A. Tazón y Puentes, *Multiband CPW-fed slot antennas*, 2016 10th European Conference on Antennas and Propagation (EuCAP), Davos, 2016, pp. 1-4
- F.A. Fernández Carcasés, D.A. Rodas Sansón, D. Rodríguez-Avila, *Enhanced-bandwidth planar LPDA with conical arms*, 2016 10th European Conference on Antennas and Propagation (EuCAP), Davos, 2016, pp. 1-4
- D. Rodríguez-Avila, Y. Paz Marrero, A. Saavedra de Vera, F. Marante Rizo, A. Tazón y Puentes, J. Vassallo Sanz, *Printed quadband CPW-fed slot antenna*, Microwave and Optical Technology Letters. 2015, Vol.58 N1, p. 145-151
- D. Rodríguez-Avila, E. González Gutiérrez, M. Coto Mederos, F. Marante Rizo, *Dual band proximity microstrip antenna*, Electrical Engineering, Automatic Control and Communications Journal [Rielac] (Cuba), 2014, Vol.XXXV 2/2014, p. 11-24
- D. Rodríguez-Avila, E. González Gutiérrez, M. Coto Mederos, F. Marante Rizo, *Multiband microstrip antennas design considerations*, Telematics Journal (Cuba), 2014, Vol.13 N2
- D. Rodríguez-Avila, Y. Santos Belett, F. Marante Rizo, *Impact review of metamaterial microstrip antennas*, Telematics Journal (Cuba), 2014, Vol.13 N2
- D.A. Rodas Sansón, F.A. Fernández Carcasés, D. Rodríguez-Avila, F. Marante Rizo, *Printed VHF logarithmic antenna*, XVII Engineering and Architecture Scientific Congress (Cittel14), Havana (Cuba), November 2014
- D. Rodríguez-Avila, H.M. Águila Acosta, F. Marante Rizo, *Digital television antenna design*, XIII FORDES Technology Week, Converging Technologies: Present and Future, Havana (Cuba), November 2013
- D. Rodríguez-Avila, J. Cabrera Suárez, F. Marante Rizo, *Wideband microstrip balun design*, XIII FORDES Technology Week, Converging Technologies: Present and Future, Havana (Cuba), November 2013

Teaching

Guidance and supervision of 14 BSc theses and 1 MSc thesis

Lectures

- Microwaves, the Basics of Wireless Communications* (teaching assistant) [EPFL]. 2015-2020
- Lab. in Microwaves* (teaching assistant) [EPFL]. 2019-2020
- Project Course in Information Technologies* (teaching assistant) [EPFL]. 2019-2020
- Digital television laboratory* (coordinator and lecturer) [CUJAE]. 2014
- Television fundamentals* (lecturer) [CUJAE]. 2012-2014
- Radiating systems* (lecturer) [CUJAE]. 2012-2014
- Wired transmissions* (lecturer) [CUJAE]. 2013

Other

Languages:

Spanish: native

English: full working proficiency

German: basic

Portuguese: basic

Relevant computer skills and programming languages: HFSS, CST, AWR Microwave Office, Matlab, AutoCad, VHDL.

Hobbies and interests: Music, choral singing, dancing, hiking, spending time with family and friends, arts.

Last updated: February 27, 2021